Supersymmetry Phenomenology in the Context of Neutrino Physics and the Large Hadron Collider LHC

Dissertation
zur
Erlangung des Doktorgrades (Dr. rer. nat.)
der
Mathematisch-Naturwissenschaftlichen Fakultät
der
Rheinischen Friedrich-Wilhelms-Universität Bonn

vorgelegt von
Marja Hanussek
aus
Köln

Bonn 2012

Angefertigt mit Genehmigung der Mathematisch-Naturwissenschaftlichen Fakultät der Rheinischen Friedrich-Wilhelms-Universität Bonn

1. Gutachter:	Prof. Dr. Herbert K. Dreiner
2. Gutachter:	Prof. Dr. Manuel Drees
Tag der Promotion:	04.09.2012
Erscheinungsjahr:	2012

Experimentally, it is well established that the Standard Model of particle physics requires an extension to accommodate the neutrino oscillation data, which indicates that at least two neutrinos are massive and that two of the neutrino mixing angles are large. Massive neutrinos are naturally present in a supersymmetric extension of the Standard Model which includes lepton–number violating terms (the B_3 MSSM). Furthermore, supersymmetry stabilizes the hierarchy between the electroweak scale and the scale of unified theories or the Planck scale. In this thesis, we study in detail how neutrino masses are generated in the B_3 MSSM. We present a mechanism how the experimental neutrino oscillation data can be realized in this framework. Then we discuss how recently published data from the Large Hadron Collider (LHC) can be used to constrain the parameter space of this model. Furthermore, we present work on supersymmetric models where R–parity is conserved, considering scenarios with light stops in the light of collider physics and scenarios with near–massless neutralinos in connection with cosmological restrictions.

Acknowledgements

I would like to thank several people and institutions. Without their experience and support, this thesis would not have been possible. First, I would like to thank my supervisor Herbi Dreiner for his support and encouragement. Likewise, I am much obliged to my second phd advisor Manuel Drees. Furthermore, I thank Klaus Desch and Claus Kiefer for agreeing to be part of my thesis committee. I would also like to express my gratitude to Ben Allanach, Manuel Drees, Herbi Dreiner, Sebastian Grab, Jong Soo Kim, Steve C. H. Kom, Christoph Luhn and Subir Sarkar for enjoyable collaboration. Special thanks to Jong Soo Kim for his support and for reading parts of the thesis. I benefited a lot from discussions with various other people including Nicolas Bernal, Howie Haber, Florian Staub, Tim Stefaniak, Jamie Tattersall, Peter Wienemann and Karina Williams. Many thanks to all members of the Theory group as well as our secretaries for good atmosphere and support. My work and many fruitful visits to conferences or institutions was funded by the Konrad–Adenauer–Stiftung, the Bonn Cologne Graduate School and the Deutsche Telekom Stiftung, for which I am very grateful. I would also like to thank the SCIPP at the University of California Santa Cruz, the DAMTP at the University of Cambridge, the TASI summer school and the ARC Centre of Excellence for Particle Physics at the University of Adelaide for hospitality while part of this work was completed.

Contents

Chapter 1

Introduction

The experimental observation of neutrino oscillations, and thus of neutrino masses, is an indication that the Standard Model of particle physics (SM) is incomplete [1–7]. Experimentally, neutrinos must be relatively light. Direct laboratory measurements restrict their masses to be below $\mathcal{O}(10\,\mathrm{MeV} - 1\,\mathrm{eV})$ [8–11], depending on the flavor. Cosmological observations even give upper bounds of $\mathcal{O}(0.1\,\mathrm{eV})$ on the sum of the neutrino masses [12–14]. Furthermore, the atmospheric and solar neutrino oscillation data are best fit if the squared neutrino mass differences are $\mathcal{O}(10^{-3}\mathrm{eV}^2)$ and $\mathcal{O}(10^{-5}\mathrm{eV}^2)$, respectively [6, 7]. This implies that at least two neutrinos must be massive.

In principle, it is easy to extend the SM Lagrangian by a Dirac neutrino mass term [5]. However, right-handed neutrinos and new Yukawa couplings of $\mathcal{O}(\lesssim 10^{-12})$ are in this case needed. Such tiny couplings seem to be very unnatural and might point towards a dynamical mechanism, that explains the small neutrino masses. Furthermore, the right–handed neutrinos can have an unspecified Majorana neutrino mass. Most prominently discussed are extensions of the SM involving the see–saw mechanism, by introducing right-handed neutrinos and fixing the new Majorana neutrino mass scale to be large, *cf.* Refs. [15–17]. By setting the arbitrary Majorana mass scale to be large, light neutrinos with mass of order $\mathcal{O}(0.1\,\mathrm{eV})$ can be obtained even with $\mathcal{O}(1)$ Yukawa couplings. There are other see–saw mechanisms [18–25], which involve different additional particles that determine/control the see–saw scale. The see–saw mechanism can also be naturally incorporated into supersymmetry (SUSY) [26–29].

Supersymmetry is one of the most promising extensions of the SM. It is the unique extension of the Lorentz spacetime symmetry when allowing for graded Lie algebras [30, 31]. In the minimal supersymmetric extension of the SM, the MSSM, every SM particle gets a superpartner and the Higgs sector is extended by an additional Higgs $\mathrm{SU}(2)_L$ doublet, *cf.* Table 1.1 [27–29]. Supersymmetry also provides a solution to the hierarchy problem of the SM [32–36]. More importantly here: in SUSY, neutrino masses can be generated through a see–saw mechanism with the neutralinos without having to introduce additional particles, if lepton number is violated [37–43]. This is well–motivated because the most general gauge invariant and renormalizable MSSM Lagrangian contains lepton number violating (LNV) operators.

However, the most general MSSM Lagrangian also allows for terms which violate baryon number. If both baryon and lepton number violating operators are present, the proton is likely to decay with a rate which is in contradiction to experimental bounds[1] [44–46]. Most commonly, one therefore introduces the discrete symmetry R–parity [47] (or, equivalently, proton–hexality P_6[2] [48]) which forbids all lepton and baryon number violating (BNV) terms and thus ensures

[1] For example, the combination of couplings $\lambda'_{112}\lambda''_{112}$ would lead to proton decay via tree-level strange squark exchange at an unacceptable rate, unless $|\lambda'_{112}\lambda''_{112}|$ is smaller than about 10^{-25} for a squark mass in the 800 GeV range [44].

[2] Note that proton–hexality additionally ensures that dangerous dimension 5 operators such as $QQQL$ are

Matter & Higgs superfields		spin 0	spin 1/2	$SU(3)_C$, $SU(2)_L$, $U(1)_Y$
squarks, quarks	$Q_i^{a,x}$	$\tilde{Q}_i^{a,x} \equiv (\tilde{u}_{L_i}^x \quad \tilde{d}_{L_i}^x)$	$(u_{L_i}^x \quad d_{L_i}^x)$	$(\mathbf{3}, \mathbf{2}, \frac{1}{6})$
	$\bar{U}_i^x$	$\tilde{\bar{U}}_{R_i}^x$	$u_{R_i}^{x\dagger}$	$(\bar{\mathbf{3}}, \mathbf{1}, -\frac{2}{3})$
	$\bar{D}_i^x$	$\tilde{\bar{D}}_i^x$	$d_{R_i}^{x\dagger}$	$(\bar{\mathbf{3}}, \mathbf{1}, \frac{1}{3})$
sleptons, leptons	L_i^a	$\tilde{L}_i^a \equiv (\tilde{\nu}_i \quad \tilde{e}_{L_i})$	$(\nu_i \quad e_{L_i})$	$(\mathbf{1}, \mathbf{2}, -\frac{1}{2})$
	$\bar{E}_i$	$\tilde{\bar{E}}_{R_i}$	$e_{R_i}^{\dagger}$	$(\mathbf{1}, \mathbf{1}, 1)$
Higgs, higgsinos	H_u^a	$H_u^a \equiv (H_u^+ \quad H_u^0)$	$(\tilde{H}_u^+ \quad \tilde{H}_u^0)$	$(\mathbf{1}, \mathbf{2}, +\frac{1}{2})$
	H_d^a	$H_d^a \equiv (H_d^0 \quad H_d^-)$	$(\tilde{H}_d^0 \quad \tilde{H}_d^-)$	$(\mathbf{1}, \mathbf{2}, -\frac{1}{2})$
Gauge superfields		spin 1	spin 1/2	$SU(3)_C$, $SU(2)_L$, $U(1)_Y$
B boson, bino	V_1	B_μ^0	$\tilde{B}^0$	$(\mathbf{1}, \mathbf{1}, 0)$
W bosons, winos	V_2	W_μ^A	$\tilde{W}^A$	$(\mathbf{1}, \mathbf{3}, 0)$
Gluon, gluino	V_3	g_μ^X	$\tilde{g}^X$	$(\mathbf{8}, \mathbf{1}, 0)$

Table 1.1: The particle spectrum of the MSSM in terms of superfields and their decomposition into SM particles and their superpartners, the latter denoted with a tilde. $i = 1, 2, 3$ are the usual generation indices of quarks, leptons and their superpartners, $a = 1, 2$ ($A = 1, 2, 3$) are the indices of the $SU(2)_L$ fundamental (adjoint) representation and $x = 1, ...8$ ($X = 1, ..$) are the $SU(3)_C$ color indices in the fundamental (adjoint) representation. The fermionic superfield components are two–component Weyl spinors. The $SU(3)_C$, $SU(2)_L$, $U(1)_Y$ quantum numbers are given in the last column. After electroweak (EW) symmetry breaking, the neutral higgsinos and EW gauginos mix to form the neutralinos χ^0 and similarily the charged higgsinos and EW gauginos form the charginos $\chi^\pm$.

proton stability:

$$\mathrm{R_p} = (-1)^{2\mathrm{S}+3\mathrm{B}+\mathrm{L}} \tag{1.1}$$

Instead of $\mathrm{R_p}$, one can equally introduce the well–motivated discrete symmetry baryon triality ($\mathrm{B_3}$) [48–50] which also forbids the BNV terms but allows for lepton number violation. $\mathrm{P_6}$ and $\mathrm{B_3}$ are the only discrete Z^N symmetries of the MSSM which can be written as a remnant of a broken anomaly free gauge symmetry [48, 49], and which also ensure that dimension five BNV operators that might lead to proton decay are forbidden.

Since in a generic $\mathrm{B_3}$ MSSM, the number of free parameters in the SUSY breaking sector is too large to perform a systematic study, we work in the $\mathrm{B_3}$ constrained MSSM ($\mathrm{B_3}$ cMSSM) [51], which imposes simplifying assumptions on the scalar and gaugino masses and couplings at the high energy unification scale $M_X \sim 10^{16}$ GeV. As a result, there are 5 free parameters in the SUSY breaking sector. We reduce the number of parameters in the LNV sector by rotating away the bilinear LNV terms at the unification scale M_X, such that there are only 36 trilinear LNV parameters at M_X left. Note however, that the bilinear terms will be re–generated at lower energy scales via renormalisation group (RG) effects [39]. The generation of neutrino masses through non–zero LNV parameters directly at the electroweak (EW) scale (therefore without the complications from RG effects) has been studied in Refs. [42, 52]. Generation of neutrino

forbidden. However, on a renormalizable level $\mathrm{R_p}$ and $\mathrm{P_6}$ allow for the same terms in the superpotential.

masses via bilinear LNV couplings and the corresponding collider signatures have also been studied. We refer interested readers to Refs. [53–61] and references therein.

In the B_3 cMSSM, the size of the neutrino masses is proportional to the square of the trilinear LNV parameters. Therefore, one can use the upper bound on the neutrino masses from cosmological observations [12–14] to derive bounds on the LNV parameters, which we examine in § 5. These bounds were previously shown to be very strict, as low as $\mathcal{O}(10^{-6})$. We show that they are significantly weakened in regions of cMSSM parameter space specified by certain values of the universal trilinear scalar coupling (A_0) at M_X.

Apart from the upper bound on the sum of neutrino masses, there is also a bound on the effective number of neutrino generations N_ν^{eff} from cosmology. Additional relativistic particles such as sterile neutrinos contribute to the relativistic degrees of freedom and thus speed up the expansion rate of the universe; consequently neutron-proton decoupling occurs earlier and the mass fraction of primordial ^{4}He is increased [62]. Recent results are consistent with the three neutrino generations present in the SM and MSSM [63–68]; however, there is a tendency to slightly larger values. We interpret this in the light of a near–massless neutralino contributing to N_ν^{eff} in § 9. It has been shown that very light or even massless neutralinos in the R_p MSSM are consistent with all current experiments, given non-universal gaugino masses, cf. Refs. [69–77]. Furthermore, a very light neutralino is consistent with astrophysical bounds from supernovae and cosmological bounds on dark matter [73, 77–81]. Here we study the cosmological constraints on this scenario from Big Bang nucleosynthesis (BBN) [67, 68]. We take gravitinos into account, but restrict ourselves to the R_p–conserving MSSM, without including LNV effects, which would lead to mixing between neutralinos and neutrinos. We find that a very light neutralino is even favoured by current observations.

The just mentioned mixing between neutralinos and neutrinos leads to one massive neutrino at tree–level in the B_3 MSSM [37–43]. Higher order corrections need to be included to give mass to at least one more neutrino in order to be consistent with the non–zero values of the neutrino mass squared differences, Δm^2_{21} and Δm^2_{31}. The radiative origin of the second neutrino mass scale implies that a strong hierarchy of $\mathcal{O}(100)$ between the neutrino masses is to be expected, cf. Ref. [43]. However, the data require a neutrino mass ratio of the heaviest two neutrinos of at most $\mathcal{O}(5)$. Thus a mechanism is needed to suppress the tree–level mass scale for viable models. Ref. [43] used sets of five parameters [two trilinear LNV couplings together with the three mixing angles that describe the lepton Yukawa matrix]. The LNV parameters were chosen such that their contributions to the tree–level neutrino masses partially cancel against each other. We present an alternative mechanism, first mentioned in Ref. [82], where the tree–level neutrino mass can vanish in a more generic fashion in certain regions of cMSSM parameter space, specified by the trilinear soft supersymmetry breaking parameter A_0 in § 4.

In § 6 we focus especially on these parameter regions, and aim to reproduce the neutrino oscillation data using a small set of LNV couplings. Compared with Ref. [43], these regions might be considered more preferable in the sense that they avoid suppression of tree level neutrino masses through specific cancellations between LNV parameters. We furthermore wish to analyze the general structures that lead to potential solutions, since it is not possible to systematically list *all* solutions. By introducing parameters coupled to different generations, we attempt to understand how different trilinear LNV terms interplay with each other to generate the observed mass pattern. For a quantitative analysis, it is essential to have a complete 1–loop treatment of the LNV sector, since this significantly influences the generation of neutrino masses. Therefore we have extended the spectrum calculator `SOFTSUSY` to calculate neutrino masses at the full 1–loop level, see § 6.1.2 and Ref. [83].

Having investigated different ansaetze for the LNV sector of the B_3 MSSM, we then turn to the implications of these models for collider signatures at the Large Hadron Collider (LHC). The LHC has been collecting data since 2010. A main objective of both multi–purpose experiments ATLAS and CMS at the LHC is the search for new physics beyond the SM. Many of these extensions, in particular SUSY, include new heavy colored states and a weakly interacting lightest new particle escaping detection. Thus the most generic signal among these models are several hard jets and large transverse missing momentum ($\not{p}_T$). ATLAS and CMS grouped their multi–jet and missing transverse momentum searches into 0, 1, 2 lepton studies [84–95], in order to be sensitive to different SUSY models and to avoid an overlap between these studies. Most studies were recently updated to the full dataset of about 5 fb^{-1} recorded in 2011 at a center–of–mass energy of 7 TeV. So far, no excess above SM expectations has been observed and strict bounds on any supersymmetric model or another relevant new physics model providing a similar collider signal can be derived. ATLAS and CMS mainly concentrate on SUSY searches which are based on the R_p–conserving MSSM.

In the B_3 MSSM, there are several notable differences compared to the R_p–conserving MSSM. The lightest supersymmetric particle (LSP) decays via the LNV interactions and cosmological constraints do not apply [96]. Note that in the LNV MSSM a stau LSP is as well motivated as a neutralino LSP [51, 97–100]. These LSP decays lead to distinct collider signatures at the LHC, which can be significantly different from models with R_p conservation [101]. Also, if the LNV couplings are relatively large, supersymmetric particles (sparticles) can be produced singly at a collider, possibly on resonance[3] [102–105]. Additionally, large LNV couplings can significantly change the renormalization group running of the sparticle masses, such that at the electroweak scale the selectron or smuon (sneutrino) can become lighter than the neutralino or the stau and thus become the LSP [99, 106, 107]. This can dramatically change the SUSY collider signatures, because (heavy) sparticles normally cascade decay down to the LSP [99, 107, 108]. There have been several ATLAS and CMS searches as well as phenomenological studies for $\not{R}_p$ models, mostly based on resonant slepton production, multi–lepton signatures or displaced vertices [109–115]. However, most of these studies constrain models where the L–violating couplings are either very large (for single slepton production), very small (for displaced vertices) or where we have single coupling dominance and four body decays (4 lepton signature) [116]. Apart from these studies, the results of the ATLAS 1 lepton, multi–jet and $\not{p}_T$ study with 1 fb^{-1} of data were used to restrict a bilinear R–parity violating model [58], which takes into account constraints from neutrino data [90].

In § 7, we re–interpret the ATLAS studies with jets, $\not{p}_T$ and 0, 1 or 2 isolated leptons [84, 90, 93] in the light of the hierarchical B_3 MSSM, where we relate the LNV couplings to the Higgs–Yukawa couplings, as first proposed in Ref. [117]. This reduces the number of free LNV parameters to six, cf. § 2.1.1. We take into account experimental results on neutrino oscillations, which amounts to five constraints (neutrino mixing angles and mass-squared differences). When additionally fixing the overall neutrino mass scale, this enables us to unambiguously determine the magnitude of the six LNV parameters, removing (almost) all degrees of freedom from the LNV sector. Consequently, the decay properties of the LSP in the hierarchical B_3 MSSM depend only on the experimental neutrino data. We expect no difference in the production and decay chains of supersymmetric particles compared to the R_p MSSM, since the magnitude of the L–violating couplings is fairly small (of order 10^{-5}) in order to be in accordance with neutrino

[3] For example, single resonant slepton production at the LHC via λ'_{ijk}, Eq. (2.3): An excess over the SM backgrounds is visible if $\lambda'_{ijk} \gtrsim \mathcal{O}(10^{-3})$, depending also on the sparticle masses [102–105].

data. However, due to the LSP decays there is less $\not{p}_T$ and more jets and/or leptons. Therefore, the exclusion limits on the B_3 cMSSM are somewhat weaker than on the R_p–conserving cMSSM using the currently available experimental searches which are optimized for the latter, as we show in § 7.

The parameter space of the conventional R_p–conserving cMSSM is becoming more and more excluded by the LHC searches. The fact that no signal has yet been found allows to derive quite stringent bounds on the masses of some strongly interacting superparticles. In particular, first generation squarks and gluinos below about 1.5 TeV are excluded if their masses are roughly equal [84]. Squark and gluino masses above 1.5 TeV seem already somewhat high, considering that the main motivation for postulating the existence of superparticles is to stabilize the electroweak hierarchy against radiative corrections. However, to one loop order essentially only third generation (s)quarks appear in the loop corrections to Higgs mass parameters. Moreover, the analyses published by CMS and ATLAS so far are not sensitive to direct pair production of *only* third generation squarks, if the other squarks and gluinos are sufficiently heavy [118–122][4]. Hence stop masses of a few hundred GeV are still allowed, and in fact favored by fine–tuning arguments.

There are phenomenological reasons to be interested in quite light stops in the R_p–conserving MSSM. One obvious disadvantage of the B_3 MSSM described in the last paragraphs is that it cannot account for dark matter because the LSP decays. In contrast, in the R_p–conserving MSSM the LSP is stable and the lightest neutralino can be a viable dark matter candidate [29, 124], being weakly interacting and stable (if $R-$parity, or a similar symmetry, is exact). However, for most combinations of parameters the computed LSP relic density is either too large (if the LSP is bino–like, which is preferred in many constrained models) or too small (if it is higgsino– or wino–like). One (of several [29, 124]) solutions is to have a bino–like neutralino with mass splitting of a few tens of GeV to the lightest stop. In this case co–annihilation [125] between these two states can lead to an acceptable relic density [126]. This type of scenario is well motivated for several reasons. If supersymmetry breaking is transmitted to the visible sector at some high energy scale, Yukawa contributions to the renormalization group evolution tend to reduce stop masses relative to the masses of first generation squarks [29, 124]. Also, the mixing between the $SU(2)$ doublet left $(L-)$type and $SU(2)$ singlet right $(R-)$type squarks is proportional to the mass of the corresponding quark, and is therefore most important for top squarks. This mixing will further reduce the mass of the lighter eigenstate (and increase that of the heavier eigenstate).

Thus motivated, we study in § 8 the effects at a hadron collider of a scenario where the lighter stop mass eigenstate $\tilde{t}_1$ is the only strongly interacting light sparticle, with rather small mass splitting to the neutralino LSP. We assume that charginos as well as all other neutralinos are heavier than $\tilde{t}_1$ and the sfermion and gluino masses are $\mathcal{O}$(few TeV). The dominant sparticle production mechanism is then stop pair production. The loop induced two–body decay $\tilde{t}_1 \to c\,\tilde{\chi}_1^0$ is the dominant decay mode [127–129] because other decays are kinematically closed or strongly phase space suppressed. Because of the small mass splitting to the LSP the soft fragmentation and decay products of the stops cannot be reconstructed as jets and thus the usual signals will be swamped by background.

[4] One reason is that the cross section for producing a pair of third generation squarks is much smaller than that for producing first generation squarks, since no "flavor excitation" contributions exist for third generation squarks. However, very recently ATLAS published [123] an analysis of a search for light sbottom pairs using about 2 fb^{-1} of data, which excludes $\tilde{b}_1$ with mass below 400 GeV if $\tilde{b}_1$ decays with unit branching ratio into the lightest neutralino, assuming the mass of that neutralino is sufficiently small.

In Ref. [130] it was proposed to consider stop pair production in association with a hard jet, $\tilde{t}_1\,\tilde{t}_1^* j$. This inevitably leads to the notion of a monojet [131], *i.e.* a final state containing a single high momentum jet, whose p_T is mostly balanced by the invisible LSPs, plus some soft particles. In [132] the SM background for monojets was evaluated in the context of searching for extra dimensions; these results were used in [130] to show that the monojet signature from stop pair production can be seen above the SM background up to stop masses of 200 GeV or larger. In [130] the selection cuts could not be optimized. In § 8, we develop a set of selection cuts optimized for searching for relatively light $\tilde{t}_1$ squarks nearly degenerate with the neutralino LSP. We perform a signal and background simulation at hadron level and simulate the most important detector effects by using a fast detector simulation. In addition, we also include $t\bar{t}$ as an important background for the monojet signal, which had been omitted in previous works.

Note that a further motivation to reconsider stop pair production in association with a hard jet arises in the context of testing a supersymmetry relation involving superpotential couplings. An alternative production process to $\tilde{t}_1\,\tilde{t}_1^* j$ based on the associate production of a $\tilde{t}_1\,\tilde{t}_1^*$ pair with a $b\bar{b}$ pair [133] has large mixed EW–QCD contributions[5] for relatively light higgsinos. These are sensitive to the $\tilde{t}_1 - \tilde{\chi}_1^\pm - b$ coupling. However, reconstructing this coupling requires that the masses of the lighter stop and the lightest neutralino are known, so that the pure QCD contribution, where the $b\bar{b}$ pair originates from gluon splitting, can be subtracted. Determining the stop mass from an independent, QCD dominated process would be advantageous for this purpose.

1.1 Publications

Large parts of the work presented here have already been published. The dependence of neutrino masses on B_3 cMSSM parameter space (§ 4) and bounds on the LNV couplings from the cosmological upper bound on the sum of neutrino masses (§ 5.3) have been analyzed in Ref. [134]. In Ref. [83] we describe how we implemented the 1–loop neutrino sector in `SOFTSUSY`-3.2, cf. § 6.1.2. Phenomenologically viable neutrino masses and mixings within the B_3 cMSSM (§ 6) have been obtained in Ref. [135]. The collider analysis of the hierarchical B_3 cMSSM described in § 7 has been published in Ref. [136]. The light stop search with monojet events (§ 8) and the investigation of cosmological bounds on a very light neutralino (§ 9) can be found in Refs. [137] and [138], respectively.

[5] These can even exceed the pure QCD prediction, since there are $2 \to 3$ diagrams with an on–shell higgsino–like chargino decaying into a stop and a b jet.

Chapter 2

The Baryon Triality (B_3) MSSM

The most general gauge invariant superpotential at the renormalizable level with the field content of the MSSM, cf. Table 1.1, can be written as [45, 139, 140]

$$\mathcal{W} \;=\; \mathcal{W}_{\not{R}_p} + \mathcal{W}_{R_p}, \tag{2.1}$$

where $\mathcal{W}_{R_p}(\mathcal{W}_{\not{R}_p})$ contain terms that conserve (violate) the discrete symmetries R–parity (R_p) as well as proton hexality (P_6). In the notation of Table 1.1, which follows Ref. [51] and `SOFTSUSY` [141, 142] closely, they are

$$\mathcal{W}_{R_p} \;=\; \epsilon_{ab}\,[(Y_E)_{jk} H_d^a L_j^b \bar{E}_k + (Y_D)_{jk} H_d^a Q_j^b \bar{D}_k + (Y_U)_{jk} Q_j^a H_u^b \bar{U}_k - \mu H_d^a H_u^b], \tag{2.2}$$

$$\mathcal{W}_{\not{R}_p} \;=\; \epsilon_{ab}\,[\frac{1}{2}\lambda_{ijk} L_i^a L_j^b \bar{E}_k + \lambda'_{ijk} L_i^a Q_j^b \bar{D}_k + \lambda''_{ijk} \bar{U}_i \bar{D}_j \bar{D}_k - \kappa_i L_i^a H_u^b], \tag{2.3}$$

where $i,j,k \in \{1,2,3\}$ are generation indices, $a,b \in \{1,2\}$ ($\epsilon_{12}=1$) are indices of the $SU(2)_L$ fundamental representation, while the corresponding $SU(3)_c$ indices are suppressed. $(Y_E)_{jk}$, $(Y_U)_{jk}$ and $(Y_D)_{jk}$ are the Higgs–Yukawa couplings of the lepton and the up– and down–type quarks, respectively, and μ is the bilinear Higgs mixing parameter. λ_{ijk} and λ'_{ijk} (λ''_{ijk}) are the trilinear LNV (BNV) couplings and κ_i is the bilinear LNV parameter. To avoid operators that could result in dangerously fast proton decay [44, 140, 143], we impose the discrete symmetry baryon triality (B_3) [48–50]. Under this symmetry, baryon number is conserved while there is lepton number violation (LNV). The superpotential is given by

$$\mathcal{W}_{B_3} \;=\; \mathcal{W}_{R_p} + \mathcal{W}_{\rm LNV}, \tag{2.4}$$

where the last term on the right is obtained by setting $\lambda''=0$ in $\mathcal{W}_{\not{R}_p}$. We note that R_p, B_3 and P_6 are the only discrete Z^N symmetries which can be written as a remnant of a broken anomaly free gauge symmetry [48, 49]. In the rest of this paper, B_3 is assumed to be conserved.

Beside the superpotential, also the soft-breaking Lagrangian of the B_3 conserving MSSM exhibits lepton number violating operators [51]

$$-\mathcal{L}^{\rm soft}_{\rm LNV} = \epsilon_{ab}\,[\frac{1}{2} h_{ijk} \tilde{L}_i^a \tilde{L}_j^b \tilde{\bar{E}}_k + h'_{ijk} \tilde{L}_i^a \tilde{Q}_j^b \tilde{\bar{D}}_k - \tilde{D}_i \tilde{L}_i^a H_u^b] + m^2_{L_i H_d} \tilde{L}^\dagger_{ia} H_d^a + h.c., \tag{2.5}$$

where again $i,j,k=1,2,3$ are generation indices and we use the notation of Table 1.1. Beside the term proportional to $m^2_{H_d \tilde{L}_i}$, the operators in Eq. (2.5) are the soft-breaking analog of the terms in $\mathcal{W}_{\rm LNV}$, Eq. (2.4). We state also the complete R_p–conserving soft SUSY breaking

Lagrangian in order to fix the notation [51, 141],

$$\begin{aligned} -\mathcal{L}_{\mathrm{R_p}}^{\mathrm{soft}} &= \epsilon_{ab}\left[(h_E)_{jk}\tilde{H}_d^a\tilde{L}_j^b\tilde{\bar{E}}_k + (h_D)_{jk}\tilde{H}_d^a\tilde{Q}_j^b\tilde{\bar{D}}_k + (h_U)_{jk}\tilde{Q}_j^a H_u^b\tilde{\bar{U}}_k - \tilde{B}H_d^a H_u^b \;+\; \mathrm{h.c.}\right] \\ &+ m_{H_d}^2 H_d^\dagger H_d + m_{H_u}^2 H_u^\dagger H_u + \tilde{Q}_i{}^\dagger (m_{\tilde{Q}}^2)_{ij}\tilde{Q}_j + \tilde{\bar{L}}_i(m_{\tilde{L}}^2)_{ij}\tilde{\bar{L}}_j^\dagger + \tilde{\bar{E}}_i(m_{\tilde{E}}^2)_{ij}\tilde{\bar{E}}_j^\dagger \\ &+ \tilde{\bar{D}}_i(m_{\tilde{D}}^2)_{ij}\tilde{\bar{D}}_j^\dagger + \tilde{\bar{U}}(m_{\tilde{U}}^2)_{ij}\tilde{\bar{U}}^\dagger + \left[\frac{1}{2}M_1\tilde{B}^0\tilde{B}^0 + \frac{1}{2}M_2\tilde{W}^A\tilde{W}^A + \frac{1}{2}M_3\tilde{g}\tilde{g} + \mathrm{h.c}\right] \end{aligned} \tag{2.6}$$

Here, $(m_{\tilde{F}}^2)_{ij}$ are the soft-breaking scalar masses. $(h_E)_{jk}$, $(h_D)_{jk}$, $(h_U)_{jk}$ as well as $\tilde{B}$ are the soft breaking trilinear and bilinear terms, respectively. M_1, M_2 and M_3 are the $\mathrm{U}(1)_Y$, $SU(2)_L$ and $SU(3)_c$ gaugino masses, respectively. Again, the $SU(3)_c$ indices are suppressed.

2.1 Constraining the Parameter Space

The B_3 MSSM model has more than 200 free parameters [144]. In order to perform a systematic study, we restrict ourselves to the well motivated framework of the B_3 constrained MSSM (cMSSM) [36, 51], which provides simple boundary conditions for the MSSM parameters at the unification scale M_X. The cMSSM model is specified by the parameter set

$$M_0, \quad M_{1/2}, \quad A_0, \quad \mathrm{sgn}(\mu), \quad \tan\beta, \tag{2.7}$$

denoting the universal scalar mass, the universal gaugino mass, the universal trilinear scalar coupling at the unification scale M_X, and the sign of the bilinear Higgs mixing parameter μ and the ratio of Higgs vacuum expectation values (VEVs) v_u/v_d at the electroweak scale M_Z. The magnitude of μ is determined dynamically by radiative electroweak symmetry breaking (REWSB) [145].

Additionally, there are 36 B_3 conserving (but $\mathrm{R_p}$–violating) parameters

$$\mathbf{\Lambda} \subset \{\lambda_{ijk}, \lambda'_{ijk}\}\,. \tag{2.8}$$

Note that we allow for trilinear but not bilinear LNV parameters at the unification scale, because we work in a basis where the bilinear LNV couplings κ_i and $\tilde{D}_i$ are both zero at M_X. It is possible to rotate away the κ_i terms in the superpotential at any given energy scale by an orthogonal rotation of the fields $\mathcal{L}_\alpha \equiv (H_d, L_i)$ [37, 146]. The corresponding bilinear soft-breaking terms proportional to $\tilde{D}_i$, Eq. (2.5), can be rotated away in conjunction with κ_i if $\tilde{D}_i$ and κ_i are aligned. This condition is fulfilled at M_X in the bt cMSSM if the underlying supergravity superpotential f satisfies the quite natural condition [51]

$$f(z_i; y_\alpha) = f_1(z_i) + f_2(y_\alpha)\,, \tag{2.9}$$

where the superfields z_i belong to the observable sector and the superfields y_α to the hidden sector ("universal SUSY breaking").

However, when evolving the parameters down to the weak scale, κ_i, $\tilde{D}_i \neq 0$ are re–generated via the RGEs [39]. The leading terms are given by [51]

$$16\pi^2\frac{d\kappa_i}{dt} = -3\mu\lambda'_{ijk}(Y_D)_{jk} - \mu\lambda_{ijk}(Y_E)_{jk} - 3\kappa_i\left[\frac{g_1^2}{5} + g_2^2 - (Y_U)_{33}^2 - \frac{(Y_E)_{33}^2}{3}\delta_{3i}\right] \tag{2.10}$$

and

$$
\begin{aligned}
16\pi^2 \frac{d\tilde{D}_i}{dt} &= -3(Y_D)_{jk}(2\mu\, h'_{ijk} + \tilde{B}\lambda'_{ijk}) - (Y_E)_{jk}(2\mu\, h_{ijk} + \tilde{B}\lambda_{ijk}) \\
&\quad -3\tilde{D}_i \left[\frac{g_1^2}{5} + g_2^2 - (Y_U)^2_{33} - \frac{(Y_E)^2_{33}}{3}\delta_{3i}\right] + 6\kappa_i \left[\frac{g_1^2}{5} M_1 + g_2^2 M_2\right] \\
&\quad +6\kappa_i \left[(Y_U)_{33}(h_U)_{33} + \frac{(Y_E)_{33}}{3}(h_E)_{33}\,\delta_{3i}\right] . \qquad (2.11)
\end{aligned}
$$

Here $t \equiv \ln(Q/\mu_0)$ with Q the renormalization scale and μ_0 an arbitrary reference scale. $h'_{ijk} \equiv A_0 \times \lambda'_{ijk}$ at M_X, *cf.* Eq. (2.5). g_1 and g_2 are the $\mathrm{U}(1)_Y$ and $SU(2)_L$ gauge couplings, respectively. We see in Eqs. (2.10) and (2.11) that the RGEs differ, and therefore κ_i and $\tilde{D}_i$ will no longer be aligned at the weak scale [39]. The complete low energy spectrum is obtained by running the RGEs down from M_X to M_Z. Note that we work in the CP-conserving limit throughout this work.

2.1.1 The Hierarchical B_3 cMSSM

The Hierarchical B_3 cMSSM further constrains the LNV sector of the B_3 cMSSM by making a hierarchical ansatz for the LNV trilinear couplings by relating them to the corresponding Higgs–Yukawa couplings [117]: In the B_3 cMSSM, the down–type Higgs superfield and the SU(2) doublet lepton superfield have the same gauge quantum numbers [37]. They are indistinguishable because lepton number is broken. Thus, the L–violating trilinear terms in Eq. (2.3) resemble the Higgs–Yukawa terms in the R–parity conserving superpotential, Eq. (2.2). We therefore make the following ansatz at M_X [117], which can be motivated in the framework of Froggatt-Nielsen models [146]

$$
\begin{aligned}
\lambda'_{ijk} &\equiv \ell'_i \cdot (Y_D)_{jk} \,, \qquad (2.12) \\
\lambda_{ijk} &\equiv \ell_i \cdot (Y_E)_{jk} - \ell_j \cdot (Y_E)_{ik} \,. \qquad (2.13)
\end{aligned}
$$

Here, ℓ_i, ℓ'_i are c-numbers. Eq. (2.13) has the required form to maintain the anti-symmetry of the λ_{ijk} in the first two indices. Assuming a specific form of the Higgs–Yukawa couplings, the number of free LNV parameters is reduced from 36 to 6. We have given our ansatz in the weak–current basis. However, after EW symmetry breaking, we must rotate to the mass–eigenstate basis as we discuss in § 2.2 and § 3.4.

2.2 Quark Mixing

The RGE evolution of the parameters in the B_3 cMSSM from M_X to M_{EW} depends on the Higgs–Yukawa coupling matrices Y_E, Y_D and Y_U, cf. Eqs. (2.10) and (2.11). In particular, the RGEs of the LNV violating parameters are coupled via the non–diagonal matrix elements of the Higgs–Yukawa couplings. Also, the LNV parameters in the hierarchical B_3 cMSSM are directly proportional to the Higgs–Yukawa coupling matrices, cf. Eqs. (2.12) and (2.13). Therefore a knowledge of the latter is crucial for the analysis of neutrino masses in the B_3 MSSM.

The initial parameter set of the B_3 cMSSM model at M_X is given in the electroweak basis so that for the RGE evolution the Higgs–Yukawa couplings (or the quark– and lepton–mass matrices) are also needed in the electroweak basis. However, from experiment we only know the

masses and Cabbibo–Kobayashi–Maskawa (CKM) [147, 148] matrix

$$\mathbf{V}_{CKM} = \mathbf{U}_{\mathbf{L}}^{\dagger}\, \mathbf{D}_{\mathbf{L}} \tag{2.14}$$

at $M_{\rm EW}$. Here $\mathbf{U}_{\mathbf{L}}^{\dagger}$ ($\mathbf{D}_{\mathbf{L}}^{\dagger}$) rotate the left–handed up– (down–) quark fields from the mass eigenstate basis to the electroweak basis. For simplicity, we take $\mathbf{Y}_D$ and $\mathbf{Y}_U$ to be real and symmetric and thus the rotation matrices for the right–handed quark fields are identical to the ones for left–handed quark fields, $\mathbf{U_R} = \mathbf{U_L}$ and $\mathbf{D_R} = \mathbf{D_L}$ ("left–right symmetric mixing").

When determining the neutrino masses, we will consider two limiting cases at $M_{\rm EW}$, following Ref. [51, 149, 150]:

- "**up–type mixing**" the quark mixing is only in the up–quark sector,

$$\begin{aligned} &\mathbf{U_{L,R}} = \mathbf{V}_{CKM}, \quad \mathbf{D_{L,R}} = \mathbf{1}\,, \\ &Y_D \times v_d = \mathrm{diag}(m_d, m_s, m_b)\,, \\ &Y_U \times v_u = \mathbf{V}_{CKM} \cdot \mathrm{diag}(m_u, m_c, m_t) \cdot \mathbf{V}_{CKM}^{T}\,. \end{aligned} \tag{2.15}$$

- "**down–type mixing**" the mixing is only in the down–quark sector,

$$\begin{aligned} &\mathbf{D_{L,R}} = \mathbf{V}_{CKM}, \quad \mathbf{U_{L,R}} = \mathbf{1}\,, \\ &Y_D \times v_d = \mathbf{V}_{CKM} \cdot \mathrm{diag}(m_d, m_s, m_b) \cdot \mathbf{V}_{CKM}^{T}\,, \\ &Y_U \times v_u = \mathrm{diag}(m_u, m_c, m_t)\,. \end{aligned} \tag{2.16}$$

Here m_d, m_s, m_b (m_u, m_c, m_t) denote the masses of the down–type (up–type) quarks.

The choice between up– and down–type mixing can have a strong effect on the final results for the LNV couplings $\mathbf{\Lambda} \in \{\lambda'_{ijk}\}$ with $j \neq k$, as we will show in § 5.3 (see Tab. 5.1). The reason is that the generated tree level neutrino mass is proportional to the off–diagonal matrix element $(Y_D)^2_{jk}$, *cf.* the discussion in § 3 and § 4. Our results (for the tree–level neutrino mass) in § 5.3 can be easily translated to scenarios which lie between the limiting cases of Eqs. (2.15) and (2.16). One only needs to know the respective Yukawa matrix elements $(Y_D)_{jk}$.

The choice of mixing can have significant impact on the required magnitude of the λ'_{ijk} couplings at the unification scale, especially for the case $j \neq k$. This is because in our model the bilinear LNV couplings, κ_i, that enter the tree–level mass $(\mathcal{M}_\nu^{\rm eff})^{\rm tree}$ via Eq. (3.5) are generated via renormalization group evolution. For example, there are contributions of the form

$$\frac{d\kappa_i}{dt} \;\propto\; \mu\, \lambda'_{ijk} \times (Y_D)_{jk}, \tag{2.17}$$

where $t = \ln(Q/\mu_0)$, with Q the renormalization scale and μ_0 an arbitrary reference scale. We see that the relative index structure of the non–vanishing R–parity violating and conserving Yukawa couplings is essential for the resulting magnitude of κ_i.

Chapter 3

Neutrino Masses and Mixings in the B_3 MSSM

The LNV terms of the B_3 MSSM detailed in Eq. (2.3) and Eq. (2.5) lead to the dynamical generation of neutrino masses. For example, the bilinear terms in Eq. (2.3) mix the Higgsinos, the supersymmetric partners of the Higgs bosons, with the neutrino fields and thus generate one non–vanishing neutrino mass at tree–level [37–43], cf. Sect 3.1. In order to fit neutrino oscillation data, which implies at least two massive neutrinos, it is necessary to include the 1–loop contributions to m_ν. In fact, these corrections must be sizable as the mass ratio of the two heaviest neutrinos is of order one, *cf.* § 3.5.

We here identify the dominant 1–loop contributions. A complete list of all one–loop contributions is given in Ref. [41], where they are formulated in a basis–independent manner. Many of the one–loop contributions are proportional to the mass insertions that mix the neutrinos with the neutralinos. They are thus aligned to the tree–level neutrino mass matrix and do not lead to more than one massive neutrino.

The dominant one–loop contributions which are not aligned to the tree–level mass matrix are on the one hand due to loops involving two LNV vertices and are thus either proportional to λ^2 or to λ'^2, *cf.* Fig. 3.1 We will review these contributions in § 3.2. On the other hand, loops with virtual neutral scalars (*i.e.* Higgses and sneutrinos) and neutralinos, which are shown in Fig. 3.2, can also give large contributions to neutrino masses. These loops are proportional to the mass difference between CP-even and CP-odd sneutrinos, *cf.* § 3.3.

We discuss how the neutrino mixing angles are obtained from the PMNS matrix in § 3.4 and finally we state the most recent experimental data on neutrino oscillations and the cosmological upper bound on neutrino masses in § 3.5.

3.1 Tree–Level Contributions

Since lepton number is violated in the B_3 MSSM, the lepton doublet superfields L_i carry the same quantum numbers as the down–type H_d doublet superfield. As a result, the neutralinos and neutrinos mix:

$$\mathcal{L}_{\mathcal{M}_N} = -\frac{1}{2}(-i\tilde{B}, -i\tilde{W}^3, \tilde{H}_d^0, \tilde{H}_u^0, \nu_i)\mathcal{M}_N \begin{pmatrix} -i\tilde{\mathcal{B}} \\ -i\tilde{\mathcal{W}}^3 \\ \tilde{H}_d^0 \\ \tilde{H}_u^0 \\ \nu_j \end{pmatrix} . \tag{3.1}$$

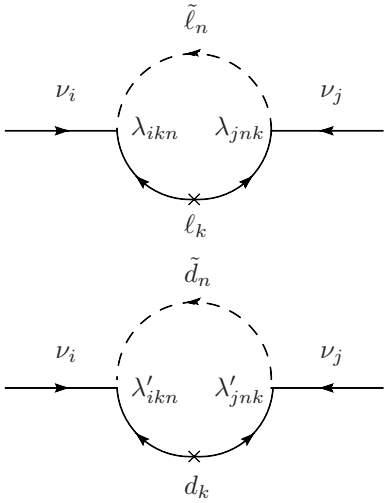

Figure 3.1: Loop contributions to the neutrino mass matrix via a non-vanishing product of B_3 couplings $\lambda_{ikn} \times \lambda_{jnk}$ (upper figure) and $\lambda'_{ikn} \times \lambda'_{jnk}$ (lower figure). See § 3.2 for more details.

In the above expression, $\mathcal{M}_N$ is a 7×7 mass matrix. As we are interested in models with a strong hierarchy between the mass scales of the neutralinos and the neutrinos, it is convenient to write $\mathcal{M}_N$ as

$$\mathcal{M}_N \quad = \quad \begin{pmatrix} \mathcal{M}_{\chi^0} & m \\ m^T & m_\nu \end{pmatrix}, \tag{3.2}$$

where m_ν is the 3×3 mass matrix in the neutrino sector and $\mathcal{M}_{\chi^0}$ is the 4×4 mass matrix in the neutralino sector. m denotes the 3×4 mixing matrix which arises through R–parity violation. Analogously to the standard see-saw mechanism [15–17] (with the neutralinos taking over the role of the right-handed neutrinos), an effective 3×3 neutrino mass matrix $\mathcal{M}_\nu^{\rm eff}$ can then be defined [38, 151]

$$\mathcal{M}_\nu^{\rm eff} \quad \equiv \quad m_\nu - m \mathcal{M}_{\chi^0}^{-1} m^T. \tag{3.3}$$

At tree–level, in which $m_\nu = 0$, it is given by [38, 151]

$$(\mathcal{M}_\nu^{\rm eff})_{ij}^{\rm tree} \quad = \quad \frac{\mu(M_1 g_2^2 + M_2 g^2)}{2 v_u v_d (M_1 g_2^2 + M_2 g^2) - 2\mu M_1 M_2} \Delta_i \Delta_j \tag{3.4}$$

where

$$\Delta_i \quad \equiv \quad v_i - v_d \frac{\kappa_i}{\mu}, \qquad i = 1, 2, 3\,. \tag{3.5}$$

Here v_i and v_d are vacuum expectation values (VEVs) of the sneutrino and (H_d) higgs fields. The former are determined in the minimization of the neutral scalar potential, cf. § 3.1.1. An

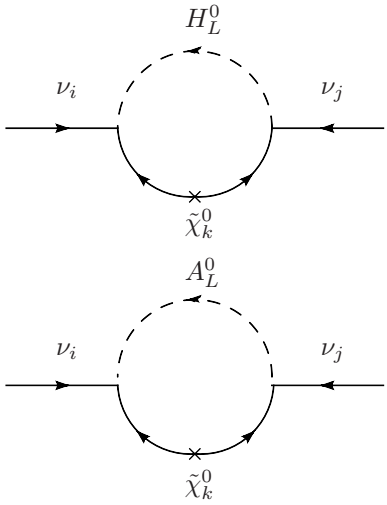

Figure 3.2: Loop contributions to the neutrino mass matrix via a non–exact cancellation of loops with CP-even and CP-odd neutral scalars. Note, that there is a relative minus sign between the two diagrams. See § 3.3 for more details.

effective neutrino mixing matrix U_ν can then be defined via the relation

$$U_\nu^T \mathcal{M}_\nu^{\rm eff} U_\nu \quad = \quad {\rm diag}[m_{\nu_i}], \qquad i = 1,2,3. \tag{3.6}$$

The rank–1 structure of $(\mathcal{M}_\nu^{\rm eff})^{\rm tree}$ leads to only one non–zero neutrino mass, which can at $M_{\rm EW}$ be simplified to [51]

$$m_\nu^{\rm tree} \approx -\frac{16\pi\alpha_{\rm GUT}}{5}\frac{\sum_{i=1}^3 \Delta_i^2}{M_{1/2}}\,, \tag{3.7}$$

if we take into account the gaugino universality assumption at M_X, leading to $M_2 = \frac{3}{5}\frac{\alpha_2^2}{\alpha_1^2}M_1 = \frac{\alpha_2^2}{\alpha_{GUT}^2}M_{1/2}$ at $M_{\rm EW}$ [51]. Here $\alpha_{\rm GUT} = g_{\rm GUT}^2/4\pi \approx 0.041$ is the unified gauge coupling constant [51].

3.1.1 Radiative Electroweak Symmetry Breaking

In the B_3 MSSM, sneutrinos can acquire vevs v_i because of the mixing between the lepton superfields L_i and the Higgs superfield H_d ($i = 1,2,3$). The sneutrino vevs v_i (as well as the bilinear Higgs parameter $|\mu|$ and its corresponding soft breaking term $\tilde{B}$) are determined by the minimization conditions for the neutral scalar potential, which has been discussed in detail in Ref. [51] for the LNV case.

At tree level, the sneutrino vevs can be written as [51]

$$(M_{\tilde{\nu}}^2)_{ij} v_j \quad = \quad -\left[m_{L_i H_d}^2 + \mu\kappa_i\right] v_d + \tilde{D}_i v_u\,, \tag{3.8}$$

with

$$(M^2_{\tilde{\nu}})_{ij} \;=\; (m^2_{\tilde{L}})_{ij} + \kappa_i\kappa_j + \frac{1}{2}M_Z^2\cos 2\beta\,\delta_{ij} + \frac{(g^2+g_2^2)}{2}\sin^2\beta\sum_l v_l^2\,\delta_{ij}\;, \tag{3.9}$$

where $g = \sqrt{3/5}\,g_1$. $m^2_{L_iH_d}$ originates from the LNV soft-breaking Lagrangian, Eq. (2.5). It mixes the down–type Higgs fields, H_d, with the lepton doublet scalars, $\tilde{L}_i$, and is zero at M_X. That is, because we take within cMSSM the mass matrix of the fields $\tilde{\mathcal{L}}_\alpha = (H_d, \tilde{L}_i)$ to be diagonal and proportional to M_0 at M_X. However, $m^2_{L_iH_d} \neq 0$ is subsequently generated via the RGEs, *cf.* Eq. (4.6).

Higher order corrections [152–154] to sneutrino VEVs can amount to $\mathcal{O}(10\%)$ and should therefore be included in a quantitative discussion of neutrino masses in the B_3 MSSM.

3.2 Contributions from $\lambda\lambda$- and $\lambda'\lambda'$-Loops

In large regions of parameter space, the dominant loop contributions are those which are directly proportional to the product of two LNV trilinear couplings, as we will see in § 4. The corresponding squark-quark and slepton-lepton loops are shown in Fig. 3.1. The resulting neutrino mass contributions are [40]

$$\begin{aligned}(m_\nu^{\mathbf{\Lambda\Lambda}})_{ij} \;&=\; \frac{1}{32\pi^2}\sum_{k,n}\lambda_{ikn}\lambda_{jnk}m_{\ell_k}\sin 2\tilde{\phi}^\ell_n\ln\left(\frac{m^2_{\tilde{\ell}_{1n}}}{m^2_{\tilde{\ell}_{2n}}}\right)\\ &+\; \frac{3}{32\pi^2}\sum_{k,n}\lambda'_{ikn}\lambda'_{jnk}m_{d_k}\sin 2\tilde{\phi}^d_n\ln\left(\frac{m^2_{\tilde{d}_{1n}}}{m^2_{\tilde{d}_{2n}}}\right)\;,\end{aligned} \tag{3.10}$$

where m_{ℓ_k} (m_{d_k}) are the lepton (down-quark) masses of generation k, and $\tilde{\phi}^\ell_n$ ($\tilde{\phi}^d_n$) the mixing angles that describe the rotation of the left– and right–handed slepton (down-squark) current eigenstates of generation n to the two mass eigenstates, $m_{\tilde{\ell}_{1n}}$ and $m_{\tilde{\ell}_{2n}}$ ($m_{\tilde{d}_{1n}}$ and $m_{\tilde{d}_{2n}}$), respectively. Note that the squared sfermion masses are linear functions of the cMSSM parameters M_0^2 and $M_{1/2}^2$, see for example Ref. [155]. For the calculation of Eq. (3.10) and all following calculations, we have used the two-component spinor formalism as described in Ref. [156].

For the first two sfermion generations, the sfermion mixing angles are small and we approximate Eq. (3.10) by using the mass insertion approximation (MIA) as described in Ref. [43]. The slepton (and down-squark) mass eigenstates are replaced by the respective left– and right–handed eigenstates with mass $m_{\tilde{\ell}_{Ln}}$ and $m_{\tilde{\ell}_{Rn}}$. The mixing angle can then be approximated by

$$\sin 2\tilde{\phi}^\ell_n = \frac{2(M^{LR}_{\tilde{\ell}})^2_n}{m^2_{\tilde{\ell}_{Ln}} - m^2_{\tilde{\ell}_{Rn}}}\;, \tag{3.11}$$

where

$$(M^{LR}_{\tilde{\ell}})^2_n = m_{\ell_n}\left[\frac{(h_E)_{nn}}{(Y_E)_{nn}} - \mu\tan\beta\right] \tag{3.12}$$

denotes the left–right mixing matrix element of the charged sleptons of generation n [51].

A similar formula is obtained for $\sin 2\tilde{\phi}^d_n$. One only needs to replace in Eq. (3.11) and Eq. (3.12) $\ell \leftrightarrow d$, $\tilde{\ell} \leftrightarrow \tilde{d}$, $(Y_E)_{nn} \leftrightarrow (Y_D)_{nn}$ and $(h_E)_{nn} \leftrightarrow (h_D)_{nn}$.

3.3 Contributions from Neutral Scalar–Neutralino–Loops

Contributions arising from loops with neutral scalars and neutralinos can also play an important role for neutrino mass generation, *cf.* Refs. [40, 157, 158]. Most important is the contribution from sneutrino–antisneutrino mixing, as we will see in Eq. (3.18).

If CP is conserved, sneutrinos $\tilde{\nu}_i$ and antisneutrinos $\tilde{\nu}_i^*$ mix to form CP–invariant mass eigenstates

$$\tilde{\nu}_i^+ \equiv \frac{1}{\sqrt{2}}(\tilde{\nu}_i + \tilde{\nu}_i^*)\,, \tag{3.13}$$

$$\tilde{\nu}_i^- \equiv \frac{1}{i\sqrt{2}}(\tilde{\nu}_i - \tilde{\nu}_i^*)\,. \tag{3.14}$$

If lepton number is conserved, the $\tilde{\nu}_i^\pm$ masses are degenerate and the CP-even (CPE) and CP-odd (CPO) contributions to the neutrino mass from neutral scalar–neutralino–loops cancel, *cf.* Fig. 3.2.

In contrast, if lepton number is violated, the $\tilde{\nu}_i^\pm$ masses are in general different, so the cancellation is no longer exact. This is due to the fact that the CPE and CPO neutrinos mix differently with the CPE and CPO Higgs fields, respectively. The size of this contribution to the neutrino masses is roughly proportional to the mass splitting $\Delta m^2_{\tilde{\nu}_i} = m^2_{\tilde{\nu}_i^+} - m^2_{\tilde{\nu}_i^-}$, *cf.* Eq. (3.18) and Refs. [40, 157, 158].

The neutral scalar–neutralino-loops, shown in Fig. 3.2, lead to the following contributions to the neutrino mass matrix [43]

$$(m_\nu^{\tilde{\nu}\tilde{\nu}})_{ij} = \frac{1}{32\pi^2}\sum_{k=1}^{4}\sum_{L=1}^{5} m_{\tilde{\chi}_k^0}(gN_{1k} - g_2 N_{2k})^2 \times \Big[Z^+_{(2+i)L} Z^+_{(2+j)L} \mathrm{B}_0(0, m^2_{H^0_L}, m^2_{\tilde{\chi}_k^0}) - Z^-_{(2+i)L} Z^-_{(2+j)L} \mathrm{B}_0(0, m^2_{A^0_L}, m^2_{\tilde{\chi}_k^0}) \Big]\,, \tag{3.15}$$

where $m_{\tilde{\chi}_k^0}$ $(k = 1\ldots4)$ are the neutralino masses and N is the 4×4 neutralino mixing matrix in the bino, wino, Higgsino basis [159]. The two-point Passarino-Veltman function is conventionally denoted B_0 [160]. $m_{H^0_L}$ $(m_{A^0_L})$ with $L = 1,\ldots,5$ are the mass eigenvalues of the CPE (CPO) neutral Higgs bosons and CPE (CPO) sneutrino fields. They can be obtained with the help of the unitary matrix Z^+ (Z^-), which diagonalizes the mass matrices of the CPE (CPO) neutral scalars, *i.e.*

$$(Z^+)^T \mathcal{M}_{\mathrm{CPE}} Z^+ = \mathrm{diag}(m^2_{h^0}, m^2_{H^0}, m^2_{\tilde{\nu}_1^+}, m^2_{\tilde{\nu}_2^+}, m^2_{\tilde{\nu}_3^+}) \equiv \mathrm{diag}(m^2_{H^0_L}) \tag{3.16}$$

and

$$(Z^-)^T \mathcal{M}_{\mathrm{CPO}} Z^- = \mathrm{diag}(m^2_{G^0}, m^2_{A^0}, m^2_{\tilde{\nu}_1^-}, m^2_{\tilde{\nu}_2^-}, m^2_{\tilde{\nu}_3^-}) \equiv \mathrm{diag}(m^2_{A^0_L})\,; \tag{3.17}$$

see Ref. [43] for additional details.

In order to analyze the dependence of this contribution on the cMSSM parameters, we make

use of the fact that in the B_3 cMSSM model, Eq. (3.15) can be approximated by [42]

$$(m_\nu^{\tilde{\nu}\tilde{\nu}})_{ij} \approx \frac{1}{32\pi^2}\sum_{k=1}^{4} m_{\tilde{\chi}_k^0}^3 (gN_{1k} - g_2 N_{2k})^2 \times \frac{\Delta m^2_{\tilde{\nu}_i}}{(m^2_{\tilde{\nu}_i} - m^2_{\tilde{\chi}_k^0})^2} \ln\left(\frac{m^2_{\tilde{\chi}_k^0}}{m^2_{\tilde{\nu}_i}}\right)\delta_{ij} \tag{3.18}$$

by expanding around $m^2_{H^0_{L>2}}$ and $m^2_{A^0_{L>2}}$. The mass splitting, $\Delta m^2_{\tilde{\nu}_i}$, in Eq. (3.18) between CPE and CPO sneutrinos of generation i is then given by [158]

$$\Delta m^2_{\tilde{\nu}_i} = \frac{-4\tilde{B}^2 M_Z^2 m^2_{\tilde{\nu}_i} \sin^2\beta}{(m^2_{H^0} - m^2_{\tilde{\nu}_i})(m^2_{h^0} - m^2_{\tilde{\nu}_i})(m^2_{A^0} - m^2_{\tilde{\nu}_i})} \times \frac{(\tilde{B}v_i - \tilde{D}_i v_d)^2}{(v_d^2 + v_i^2)(\tilde{B}^2 + \tilde{D}_i^2)}\,. \tag{3.19}$$

3.4 The PMNS Matrix, Charged Lepton Masses and Neutrino Mixing Angles

The observable Pontecorvo–Maki–Nakagawa–Sakata (PMNS) matrix [161–163] is defined to be

$$U_{\rm PMNS} = U_{\ell L}^T U_\nu. \tag{3.20}$$

The charged lepton mixing matrix $U_{\ell L}$ can be obtained by treating the charged lepton–chargino mass matrix $\mathcal{M}_C$ in a similar fashion as the neutrino–neutralino mass matrix. In particular an effective charged lepton mass matrix $\mathcal{M}_\ell^{\rm eff}$ as well as its corresponding charged lepton mixing matrices $U_{\ell L(R)}$ can be defined, which rotate the left– (right–) handed charged leptons. Consistent with our notation, $\mathcal{M}_C$ is defined in the same way as in Ref. [142]. To an excellent approximation, the charged lepton masses can be obtained by

$$U_{\ell L}^\dagger \mathcal{M}_\ell^{\rm eff} U_{\ell R} = {\rm diag}[m_{\ell i}], \qquad i = 1,2,3. \tag{3.21}$$

To obtain a complete 1–loop description of the PMNS matrix, one–loop corrections to $\mathcal{M}_\ell^{\rm eff}$ need to be included[1]. In our numerical simulations, we impose the condition that the charged lepton mixing matrix is diagonal at the electroweak scale. This implies that one–loop corrections to the charged lepton mixing matrix would only indirectly influence the $U_{\rm PMNS}$ matrix. The unification–scale Yukawa couplings are adjusted such that the charged lepton mixing matrix is always diagonal at the electroweak scale. One–loop corrections to U_ℓ would further (slightly) alter the unification-scale Yukawa couplings, which in turn affects the RGEs of the LNV parameters. However, these changes are negligible compared to the current experimental uncertainties in the neutrino sector [142], therefore we neglect one–loop corrections to the charged lepton mixing matrix.

In this basis, the PMNS matrix is determined only by the form of the effective neutrino mixing U_ν. We consider this advantageous, as this allows for a more transparent understanding and better control of how different LNV parameters contribute to the neutrino masses and mixings. Thus, the PMNS matrix can be expressed in terms of the neutrino mixing angles θ_{ij} [164]

$$U_{\rm PMNS} \equiv \begin{pmatrix} c_{\theta_{12}}c_{\theta_{13}} & s_{\theta_{12}}c_{\theta_{13}} & s_{\theta_{13}} \\ -s_{\theta_{12}}c_{\theta_{23}} - c_{\theta_{12}}s_{\theta_{23}}c_{\theta_{13}} & c_{\theta_{12}}c_{\theta_{23}} - s_{\theta_{12}}s_{\theta_{23}}s_{\theta_{13}} & s_{\theta_{23}}c_{\theta_{13}} \\ s_{\theta_{12}}s_{\theta_{23}} - c_{\theta_{12}}c_{\theta_{23}}s_{\theta_{13}} & -c_{\theta_{12}}s_{\theta_{23}} - s_{\theta_{12}}c_{\theta_{23}}s_{\theta_{13}} & c_{\theta_{23}}c_{\theta_{13}} \end{pmatrix}. \tag{3.22}$$

[1] In `SOFTSUSY`, the R_p–conserving 1–loop corrections are implemented, but not the LNV ones.

where $c_{\theta_{ij}} \equiv \cos(\theta_{ij})$, $s_{\theta_{ij}} \equiv \sin(\theta_{ij})$, and we assume CP–conservation.

3.5 Experimental Neutrino Data

Assuming three active oscillating neutrinos, the best global fit values of the combined global analysis of atmospheric, solar, reactor and accelerator data is given by [6, 165],

$$\begin{aligned}
\sin^2(\theta_{12}) &= 0.31 \pm 0.02, && (3.23)\\
\sin^2(\theta_{23}) &= 0.51 \pm 0.06, && (3.24)\\
\sin^2(\theta_{13}) &< 0.03, && (3.25)\\
\Delta m^2_{21} &= 7.59 \pm 0.2 \times 10^{-5}\ \text{eV}^2, && (3.26)\\
\Delta m^2_{31} &= \begin{cases} -2.34 \pm 0.1 \times 10^{-3}\ \text{eV}^2 \\ \ \ 2.45 \pm 0.1 \times 10^{-3}\ \text{eV}^2 \end{cases}, && (3.27)
\end{aligned}$$

where the errors are given at the 1σ level, and

$$\Delta m^2_{ij} \equiv m^2_{\nu_i} - m^2_{\nu_j}. \tag{3.28}$$

m_{ν_i} denote the neutrino masses in order of largest electron-neutrino admixture. There are two large mixing angles θ_{12} and θ_{23} and a small angle θ_{13}. This implies that at least two neutrinos have non–zero mass. The (as–yet) undetermined sign of Δm^2_{31} means that two mass orderings are possible. They are known as the normal ($\Delta m^2_{31} > 0$) and the inverted ($\Delta m^2_{31} < 0$) hierarchies.

Deviating from Ref [6], an explicit non–zero θ_{13} value has recently been indicated by T2K, Daya Bay and RENO [166–168]. We here display the best–fit value by Daya Bay,

$$\sin^2(2\theta_{13}) = 0.09 \pm 0.02. \tag{3.29}$$

which is within the bound set by Eq. (3.25). Note that there has recently been an updated global fit in Ref. [7]. However, this new global fit is not used in our results yet.

The observations and measurements from neutrino oscillations determine the differences of neutrino masses squared, *cf.* Eqs. (3.26), (3.27). Direct laboratory measurements restrict the absolute masses of the neutrinos to be below $\mathcal{O}(10\,\text{MeV} - 1\,\text{eV})$ [5, 8–11]. Limits dependent on the Majorana nature of neutrinos also exist from non–observation of neutrinoless double beta decay ($0\nu\beta\beta$), which is of $\mathcal{O}(0.5\,\text{eV})$ [169–172]. Note, there is a claim of evidence for a neutrino mass of 0.39 eV in a $0\nu\beta\beta$ experiment [173].

A stringent upper limit can be obtained from cosmological restrictions on the sum of the neutrino masses. The neutrinos act as hot dark matter and can suppress cosmic density fluctuations on small scales through free-streaming. In order for its relic abundance to be small enough to be consistent with the observed small-scale structure, we require

$$\sum m_{\nu_i} \lesssim 0.4\,\text{eV}\,, \tag{3.30}$$

at 99.9% confidence level, obtained from Refs. [12–14]. The exact limit depends on details of the analysis. Typically these analyses include data from the Wilkinson Microwave Anisotropy Probe (WMAP) [174], Large Scale Structure [175–178] and Type Ia supernovae [179, 180].

In the following, we will make use of three limiting cases of neutrino mass hierarchies. In the

first two cases, we assume that the lightest neutrino is massless and impose normal and inverted hierarchy, respectively. In the third case, we consider almost–degenerate neutrino masses with normal hierarchy mass ordering, saturating the cosmological limit stated in Eq. (3.30).

For the normal ($m_1 < m_2 < m_3$) and inverted ($m_3 < m_1 < m_2$) hierarchies, neutrino masses are respectively given by

- normal hierarchy (NH):

$$\begin{aligned} m_1 &\approx 0 \text{ eV}, \\ m_2 &= 8.71 \times 10^{-3} \text{ eV}, \\ m_3 &= 4.95 \times 10^{-2} \text{ eV}, \\ m_3/m_2 &\sim 5.7\,. \end{aligned} \tag{3.31}$$

- inverted hierarchy (IH):

$$\begin{aligned} m_1 &= 4.84 \times 10^{-2} \text{ eV}, \\ m_2 &= 4.92 \times 10^{-2} \text{ eV}, \\ m_3 &\approx 0 \text{ eV}, \\ m_2/m_1 &\sim 1\,. \end{aligned} \tag{3.32}$$

We will use the masses given in Eqs.(3.31) and (3.32) as best–fit values for the three neutrino masses for the NH and IH cases, respectively. For the degenerate case ($m_1 \approx m_2 \approx m_3$), we assume that the sum of the three active neutrino masses equals 0.4 eV.

For illustrative purposes, we often refer to the tri–bi–maximal mixing (TBM) approximation [181], where

$$\sin^2(\theta_{12}) = \frac{1}{3}, \quad \sin^2(\theta_{23}) = \frac{1}{2} \quad \sin^2(\theta_{13}) = 0 \tag{3.33}$$

is assumed. The first two quantities differ from their best fit values by 7% and 2% respectively. We discuss how this difference as well as the non–zero θ_{13} can be accommodated via small deviations from the TBM structure in § 6. In the TBM approximation, the PMNS mixing matrix [161–163] is explicitly given by

$$U_{TBM} \equiv \begin{pmatrix} \sqrt{\frac{2}{3}} & \sqrt{\frac{1}{3}} & 0 \\ -\sqrt{\frac{1}{6}} & \sqrt{\frac{1}{3}} & \sqrt{\frac{1}{2}} \\ \sqrt{\frac{1}{6}} & -\sqrt{\frac{1}{3}} & \sqrt{\frac{1}{2}} \end{pmatrix}. \tag{3.34}$$

Since the defining equations in Eq. (3.33) involve squares, more than one phase convention exists for the resulting mixing matrix.

Chapter 4

Dependence of the ν–Masses on B_3 cMSSM Parameters

In the literature it has frequently been assumed that the tree–level contribution to the neutrino mass, Eq. (3.7), in the B_3 cMSSM model dominates over the loop contributions, *cf.* for example Refs. [43, 51]. However, as has been noted in Ref. [82], in certain regions of B_3 cMSSM parameter space, the tree–level neutrino mass vanishes. We find that there is in particular a strong dependence of the tree–level neutrino mass on the trilinear SUSY breaking parameter A_0.

We demonstrate this effect in Fig. 4.1, where we display the tree–level neutrino mass (solid red line) as a function of A_0. The other B_3 cMSSM parameters are given by Point I with $\lambda'_{233}|_{\rm GUT} = 10^{-5}$, *cf.* § 4.1.1. We see that the tree–level mass, $m_\nu^{\rm tree}$, vanishes around $A_0 \approx 910$ GeV. In the vicinity of this minimum, $m_\nu^{\rm tree}$ drops by several orders of magnitude over a wide range of A_0, and it is therefore not a (large) fine–tuning effect. In this case the loop contributions will dominate the neutrino mass matrix, resulting in much weaker bounds on the involved $\mathbf{\Lambda}$ coupling, *cf.* § 5.3. Thus the bound crucially depends on the choice of A_0.

We emphasize that the range of A_0 for which weaker bounds may be obtained is quite large. In an interval of $\Delta A_0 \approx 100\,\text{GeV}$ around the minimum, we obtain bounds on λ'_{233} that are at least one order of magnitude smaller than the bound derived at for example $A_0 = 0$ GeV. Much weaker bounds can therefore be obtained without a lot of fine tuning.

In this chapter, we aim to explain in detail the origin of this cancellation, considering as an explicit example mostly the case $\mathbf{\Lambda} \in \{\lambda'_{ijk}\}$. We focus on the dependence of $m_\nu^{\rm tree}$ on the cMSSM parameter A_0, because it is always possible to find a value of A_0 [for a given set of parameters $\tan\beta$, $M_{1/2}$, M_0, and $\text{sgn}(\mu)$] such that the tree–level neutrino mass vanishes. All arguments can analogously be applied to a λ_{ijk} coupling, as discussed in § 4.4. Note for the further discussion that we can always obtain a positive $\mathbf{\Lambda}$ by absorbing a possible sign of $\mathbf{\Lambda}$ via a re–definition $L \to -L$ and $E \to -E$ of the lepton doublet and lepton singlet superfields, respectively. We also note that the generated neutrino masses scale roughly with $\mathbf{\Lambda}^2$, *cf.* the following discussion. Although we concentrate in this work on the B3 cMSSM model, the mechanisms described will also work in more general $\not{R}_{\rm p}$ models.

4.1 Preliminaries

4.1.1 Benchmark Scenarios

We center our analysis around the following B_3 cMSSM parameter points with exactly one non–zero LNV parameter $\Lambda \in \{\lambda'_{ijk}, \lambda_{ijk}\}$ at the unification scale M_X,

Particles	Masses (GeV)			
$\tilde{g}$	1146			
$\tilde{\chi}_1^{\pm}, \tilde{\chi}_2^{\pm}$	380	570		
$\tilde{\chi}_1^0, \tilde{\chi}_2^0, \tilde{\chi}_3^0, \tilde{\chi}_4^0$	204	380	552	571
$\tilde{u}_1, \tilde{c}_1, \tilde{t}_1$	1050	1050	1005	
$\tilde{u}_2, \tilde{c}_2, \tilde{t}_2$	1012	1012	858	
$\tilde{d}_1, \tilde{s}_1, \tilde{b}_1$	1053	1053	971	
$\tilde{d}_2, \tilde{s}_2, \tilde{b}_2$	1008	1008	1002	
$\tilde{e}_1, \tilde{\mu}_1, \tilde{\tau}_1$	353	353	346	
$\tilde{e}_2, \tilde{\mu}_2, \tilde{\tau}_2$	217	217	163	
$\tilde{\nu}_e, \tilde{\nu}_\mu, \tilde{\nu}_\tau$	343	343	331	
$h^0, A^0, H^0, H^{\pm}$	112	607	608	612

Table 4.1: Mass spectrum of the benchmark Point I in the R_p conserving limit. From top to bottom, the particles are the gluino, charginos, neutralinos, up–like squarks (2 rows), down–like squarks (2 rows), charged sleptons (2 rows), sneutrinos and the Higgses. The charginos and neutralinos are ordered according to their masses. For a scalar sparticle, a subscript 1(2) denotes that it is primarily 'left'('right') handed, *i.e.* the superpartner of a left(right) chiral fermion. This is the convention used in `SOFTSUSY`. From left to right, the 4 Higgses are the light CP–even Higgs, CP–odd Higgs, heavy CP–even Higgs and the charged Higgs.

Point I: $M_{1/2} = 500$ GeV, $M_0 = 100$ GeV, $\tan\beta = 20$, $\mathrm{sgn}(\mu) = +1$, $A_0 = 900$ GeV, $\mathbf{\Lambda} = \lambda'_{233}$

Point II: $M_{1/2} = 500$ GeV, $M_0 = 100$ GeV, $\tan\beta = 20$, $\mathrm{sgn}(\mu) = +1$, $A_0 = 200$ GeV, $\mathbf{\Lambda} = \lambda_{233}$

Point II differs from Point I only by the choice of the LNV coupling and the size of A_0. We have chosen these points as examples because the tree–level contribution to the neutrino mass is small around Point I and II and therefore one–loop contributions are important. Both points lead to squark masses of $\mathcal{O}(1$ TeV) and slepton masses of around 300 GeV, with a scalar tau (stau) as the LSP. The full spectrum in the R_p–conserving limit (for Point I) is displayed in table 4.1.

We ensured that both points lie in regions of parameter space where various other experimental constraints are fulfilled, such as the lower bound on the lightest Higgs mass from LEP2 [182, 183] or the bound from $b \to s\gamma$ [184] and from $B_s \to \mu^+\mu^-$ [184]. We elaborate this in more detail in § 5.2. Furthermore, we are well above the LEP2 and Tevatron supersymmetric mass bounds, as for example on the charginos.

4.1.2 Numerical Implementation

The numerical calculation of the neutrino mass matrix is done in the following way. We first employ `SOFTSUSY-3.0.12` [141, 142] to obtain the low energy mass spectrum[1]. `SOFTSUSY` employs the full set of renormalization group equations (RGEs) at one loop [51, 82, 185, 186] in order to obtain the B_3 MSSM spectrum at the electroweak scale (M_{EW}). We then use our own add–on

[1] We use as SM inputs for `SOFTSUSY` the following parameters: $M_Z = 91.1876$ GeV ($m_t = 165.0$ GeV) for the pole mass of the Z boson (top quark); $\alpha^{-1}(M_Z) = 127.925$ and $\alpha_s(M_Z) = 0.1176$ for the gauge couplings in the $\overline{MS}$ scheme; $m_b(m_b) = 4.20$ GeV, $m_u(2\mathrm{GeV}) = 0.0024$ GeV, $m_d(2\mathrm{GeV}) = 0.00475$ GeV, $m_s(2\mathrm{GeV}) = 0.104$ GeV and $m_c(m_c) = 1.27$ GeV for the light quark masses in the $\overline{MS}$ scheme.

to calculate the neutrino mass matrix. The tree–level contribution was derived from Eq. (3.4). For the $\lambda\lambda$– and $\lambda'\lambda'$–loops, we employed Eq. (3.10), if third generation sfermions were involved. However, for sfermions of the first two generations we used the MIA as given in Eqs. (3.11) and (3.12). For the neutral scalar–neutralino–loops, we in principle employed Eq. (3.15). However, instead of performing the large numerical cancellation between CPE and CPO neutral scalars directly [square bracket in Eq. (3.15)], we used an MIA to calculate the deviation from exact cancellation in the R-parity conserving (RPC) limit, following Ref. [43]. The resulting formula is quite lengthy and we refer the interested reader to Ref. [43] for details. We have cross checked our program with the help of Eq. (3.18) and Eq. (3.19). All our calculations are performed in the CP-conserving limit. We employ `micrOMEGAs2.2` [187] for the evaluation of $\mathrm{BR}(B_s \to \mu^+\mu^-)$, $\mathrm{BR}(b \to s\gamma)$ and $\delta a_\mu^{\mathrm{SUSY}}$.

4.2 A_0 Dependence of the Tree–Level Neutrino Mass

We now discuss the dependence of the tree–level neutrino mass at M_{EW} as a function of A_0 at M_{GUT}. Recall from § 3.1 that

$$m_\nu^{\mathrm{tree}} \propto \Delta_i^2 = \left(v_i - v_d \frac{\kappa_i}{\mu}\right)^2 . \tag{4.1}$$

From the RGE of κ_i, Eq. (2.10), we obtain as the dominant contribution

$$\kappa_i \propto \mu\lambda'_{ijk}(\mathbf{Y}_D)_{jk} \equiv \mu\lambda'_{ijk}\frac{(m_d)_{jk}}{v_d} \tag{4.2}$$

at all energy scales, where $(m_d)_{jk}$ denotes a matrix element of the down quark mass matrix. Therefore,

$$v_d\frac{\kappa_i}{\mu} \propto \lambda'_{ijk}\cdot(m_d)_{jk}\,, \tag{4.3}$$

without further dependence on cMSSM parameters.

Thus, the dependence of the tree–level neutrino mass, Eq. (4.1), on the cMSSM parameters is solely through the sneutrino vev v_i[2]. In Fig. 4.1, the dashed green line explicitly shows the dependence of $|v_i|\,,\ i=2$ on A_0. It possesses a clear minimum which is close to the minimum of m_ν^{tree}.

This behavior can be understood by taking a look at the (tree–level) formula for the vev v_i, Eq. (3.8). For $\mathbf{\Lambda} \in \{\lambda'_{ijk}\}$ it can be written as

$$v_i = \frac{1}{(M^2_{\tilde\nu})_{ii}}\left[\tilde D_i v_u - (m^2_{L_iH_d} + \mu\kappa_i)v_d\right]\,, \tag{4.4}$$

with

$$(M^2_{\tilde\nu})_{ii} = (m^2_{\tilde L})_{ii} \ + \ \frac{1}{2}M_Z^2\cos 2\beta\,. \tag{4.5}$$

Here, we have neglected terms proportional to κ_i^2 and v_i^2, because they are much smaller than $(m^2_{\tilde L})_{ii}$ and M_Z^2. Note that we only obtain one non–zero sneutrino vev because λ'_{ijk} violates only

[2] Note that there is one exception, namely the direct proportionality $m_\nu^{\mathrm{tree}} \propto 1/M_{1/2}$, *cf.* Eq. (3.7). However, compared to v_i, the impact of this term on m_ν^{tree} and thus on the bounds of the trilinear LNV couplings is much weaker.

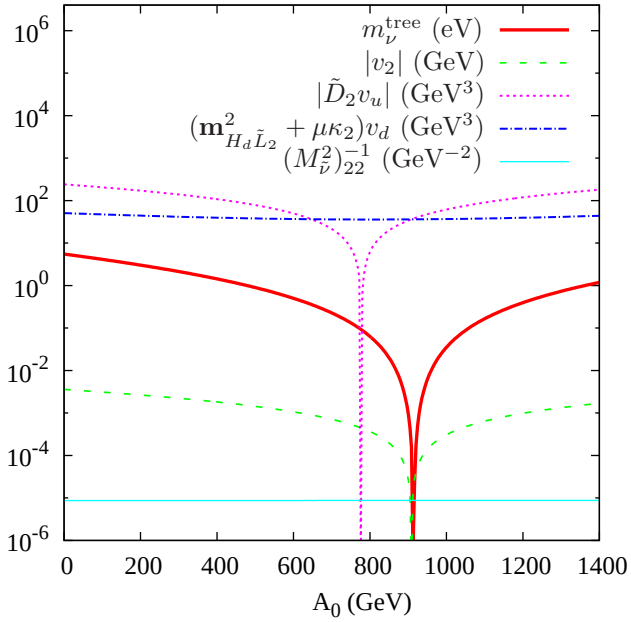

Figure 4.1: A_0 dependence of $m_\nu^{\rm tree}$ and the terms determining the sneutrino vev v_2, Eq. (4.4), at the REWSB scale (used in `SOFTSUSY` to calculate the sneutrino vev). Since the scale affects the parameters only logarithmically, there are only minor changes when running to $M_{\rm EW}$. The other B_3 cMSSM parameters are that of Point I with $\lambda'_{233}|_{\rm GUT} = 10^{-5}$, § 4.1.1.

one lepton flavor.

In many regions of parameter space the sneutrino vev in Eq. (4.1) is at least two orders of magnitude larger than the term $v_d\kappa_i/\mu$. Thus the minimum of the neutrino mass can only occur when the sneutrino vev is drastically reduced. As we shall see, the sneutrino vev becomes very small, when there is a cancellation between the two terms in Eq. (4.4).

The second term of v_i in Eq. (4.4), $(m^2_{L_i H_d} + \mu\kappa_i)v_d$, and the prefactor $1/(M^2_{\tilde{\nu}})_{ii}$ are always positive and depend only weakly on A_0. This can be seen in Fig. 4.1 for $(m^2_{L_i H_d} + \mu\kappa_i)v_d$ (dotted–dashed blue line) and also for $1/(M^2_{\tilde{\nu}})_{ii}$ (solid turquoise line). This behavior can be easily understood:

The soft breaking parameter, $m^2_{L_i H_d}$, Eq. (2.5), is zero at M_X and is generated at lower scales via [51]

$$16\pi^2 \frac{dm^2_{L_i H_d}}{dt} = -\lambda'_{ijk}(Y_D)_{jk}\mathcal{F}(\tilde{m}^2) - 6h'_{ijk}(h_D)_{jk}\,, \tag{4.6}$$

where $\mathcal{F}(\tilde{m}^2)$ is a linear function of the soft-breaking scalar masses squared and of the down–type Higgs mass parameter squared. h'_{ijk} $[(h_D)_{jk}]$ is the soft-breaking analog of λ'_{ijk} $[(Y_D)_{jk}]$ with $h'_{ijk} = \lambda'_{ijk} \times A_0$ $[(h_D)_{jk} = (Y_D)_{jk} \times A_0]$ at $M_{\rm GUT}$. The second term in Eq. (4.6) thus depends on A_0^2. However, $\mathcal{F}(\tilde{m}^2)$ is in general much larger than A_0^2 due to several contributions from soft breaking masses [51]. Therefore, varying A_0 does not significantly change the magnitude of $m^2_{L_i H_d}$ as long as A_0 is not much larger than the sfermion masses.

Concerning the term $\mu\kappa_i$ in $(m^2_{L_i H_d} + \mu\kappa_i)v_d$, we note from the RGE for κ_i, Eq. (2.10), that the only A_0 dependence of κ_i stems from its proportionality to μ. μ at $M_{\rm EW}$ can be approximated

by [155]

$$\mu^2 = c_1 M_0^2 + c_2 M_{1/2}^2 + c_3 A_0^2 + c_4 A_0 M_{1/2} - \frac{M_Z^2}{2} \,. \tag{4.7}$$

Here c_1 and c_2 are numbers of $\mathcal{O}(1)$ whereas c_3 and c_4 are only of $\mathcal{O}(10^{-1} - 10^{-2})$[3]. Therefore, except for $A_0 \gg M_0, M_{1/2}$, the order of magnitude of μ remains constant when varying A_0.

We conclude that $(m^2_{L_i H_d} + \mu\kappa_i) v_d$ depends only weakly on A_0 and therefore, $\tilde{D}_i$ is decisive for the A_0 dependence of the vev v_i and thus of m_ν^{tree}. If the first term in Eq. (4.4), $\tilde{D}_i v_u$, is positive and only slightly larger than the (nearly constant) second term, $(m^2_{L_i H_d} + \mu\kappa_i) v_d$, v_i can equal $v_d \kappa_i / \mu$ and we get $m_\nu^{\text{tree}} = 0$, *cf.* Eq. (4.1).

The strong A_0 dependence of the magnitude of $\tilde{D}_i v_u$ is also displayed in Fig. 4.1 (dotted magenta line). We observe that $|\tilde{D}_i v_u|$ is often larger than $(m^2_{L_i H_d} + \mu\kappa_i) v_d$ (dotted–dashed blue line). However, near the tree–level neutrino mass minimum (solid red line), it drops below $(m^2_{L_i H_d} + \mu\kappa_i) v_d$ and v_i can equal $v_d \frac{\kappa_i}{\mu}$. In this case m_ν^{tree}, Eq. (4.1), vanishes.

In order to understand this behavior of $\tilde{D}_i$, we need to understand how $\tilde{D}_i$ is generated via the RGEs. Recall that $\tilde{D}_i = 0$ at M_X within the B_3 cMSSM model. The generation of $\tilde{D}_i$ primarily depends on the running of the trilinear soft breaking mass h'_{ijk} [51],

$$16\pi^2 \frac{d\tilde{D}_i}{dt} = -6\mu (Y_D)_{jk} h'_{ijk} + \dots \,. \tag{4.8}$$

We find the contribution in Eq. (2.11) proportional to $\tilde{B}$ is typically much smaller[4] and we here focus on the effects due to h'_{ijk}. The dominant terms of the corresponding RGE are given by [51, 107]

$$16\pi^2 \frac{dh'_{ijk}}{dt} = \frac{16}{3} g_3^2 \left(2 M_3 \lambda'_{ijk} - h'_{ijk}\right) + \dots \,, \tag{4.9}$$

where g_3 (M_3) denotes the SU(3) gauge coupling (gaugino mass). At M_X this equation simplifies to

$$16\pi^2 \frac{dh'_{ijk}}{dt} = \frac{16}{3} g^2_{\text{GUT}} (2 M_{1/2} - A_0)\, \lambda'_{ijk} + \dots \,. \tag{4.10}$$

Keeping for now all parameters except A_0 fixed (with $\text{sgn}(\mu) = +1$ and $\lambda'_{ijk} > 0$[5]), we can classify the running of h'_{ijk}, Eq. (4.9) and Eq. (4.10), in the following way (see also Ref. [107] for a detailed discussion):

(a) $\mathbf{A_0 \ll 2 M_{1/2}}$ (including negative values of A_0): Since the right hand side (RHS) of the RGE for h'_{ijk}, Eq. (4.9), is always positive and large, h'_{ijk} is quickly reduced from its initial value of $A_0 \times \lambda'_{ijk}$ and even becomes negative when running to lower energies. This

[3] All c_i depend also weakly on $\tan\beta$. However, this becomes only relevant for very small $\tan\beta$ [155].

[4] Only in parameter regions with small $\tan\beta$ and small $M_{1/2}$, a term proportional to $\tilde{B}$, Eq. (2.11), becomes equally important. This is because $\tilde{B}$ increases with decreasing $\tan\beta$ [51] whereas $\mu \times h'_{ijk}$ decreases with decreasing $M_{1/2}$, *cf.* Eq. (4.7) and Eq. (4.9). The term proportional to $\tilde{B}$ in Eq. (2.11) is then enhanced with respect to the term proportional to h'_{ijk}. However, in this parameter region v_i will typically end up being negative because $\tilde{D}_i$ is further reduced than the other term in v_i, such that the latter dominates. Then there can be no cancellation in the tree–level neutrino mass, Eq. (4.1).

[5] From Eq. (2.10) it is easy to see that this implies $\text{sgn}(\kappa_i) = +1$ below M_{GUT}.

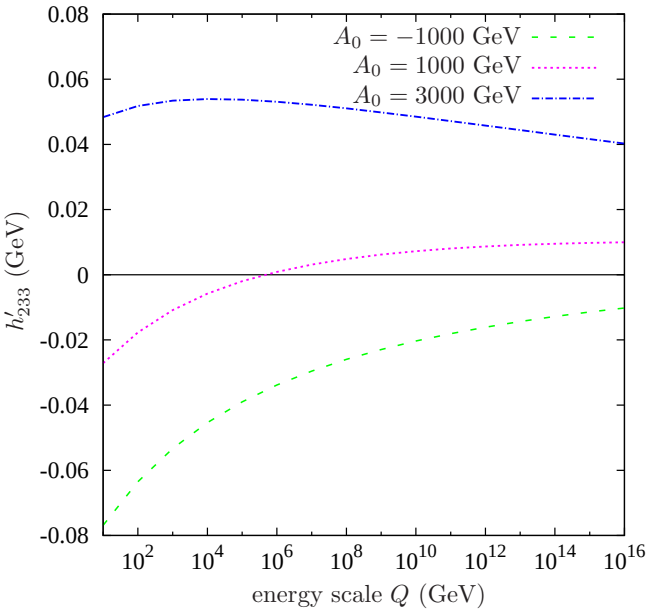

Figure 4.2: Running of h'_{233} for various values of A_0. The other B_3 cMSSM parameters are that of Point I, § 4.1.1, with $\lambda'_{233}|_{\rm GUT} = 10^{-5}$ and $M_{1/2} = 500$ GeV.

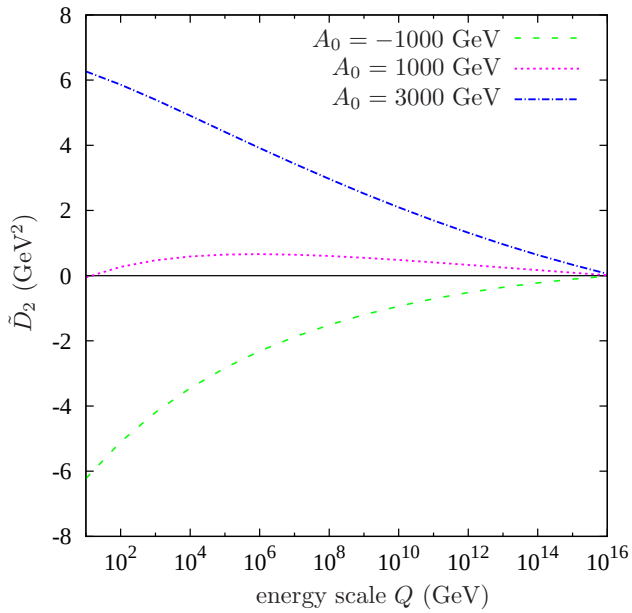

Figure 4.3: Running of the bilinear coupling $\tilde{D}_2$, Eq. (4.8), for the same parameter sets as those in Fig. 4.2.

behavior is displayed in Fig. 4.2 (dashed green line), where the running of h'_{233} is shown for different boundary conditions at $M_{\rm GUT}$.

(b) $\mathbf{A_0 \approx 2M_{1/2}}$: If the size of A_0 is comparable to $2M_{1/2}$, h'_{ijk} will be fairly constant at

high energies, *cf.* the dotted magenta line in Fig. 4.2. However, when running to lower energies it will still start decreasing, but more slowly than in case (a). This is due to the fact that M_3 and λ'_{ijk} themselves increase significantly (by factors of approx. 2.5 and 3, respectively; see Ref. [107]) when running to lower energies. Thus the term $2M_3\lambda'_{ijk}$ eventually dominates in Eq. (4.9) even if initially $A_0 \gtrsim 2M_{1/2}$. This leads to a small, negative h'_{ijk} at low energies.

(c) $\mathbf{A_0 \gg 2M_{1/2}}$: h'_{ijk} is large at M_X and is further increased when running to lower energies. This is due to the negative RHS of the RGE for h'_{ijk}, Eq. (4.9); see also the dotted–dashed blue line in Fig. 4.2.
Caveat: Since the term $2M_3\lambda'_{ijk}$ in Eq. (4.9) increases by a factor of approximately $8 \approx 3 \cdot 2.5$ when running from M_X to $M_{\rm EW}$ [as mentioned in (b)], h'_{ijk} only strictly displays the behavior of case (c) when $A_0 \gtrsim 20M_{1/2}$. Otherwise, h'_{ijk} will decrease once the term $2M_3\lambda'_{ijk}$ dominates.

Because $\tilde{D}_i$ is zero at $M_{\rm GUT}$ and, according to Eq. (4.8), also proportional to the integral of h'_{ijk} over $\ln(Q)$, points (a) - (c) have the following consequences for $\tilde{D}_i$:

(a) $\mathbf{A_0 \ll 2M_{1/2}}$: Since h'_{ijk} always becomes negative below some energy scale close to M_X, the RHS of Eq. (4.8) is positive. This leads to a large negative $\tilde{D}_i$ at M_Z as can be seen in Fig. 4.3 (dashed green line). Consequently, all terms except $\tilde{D}_i v_u$ become negligible in v_i, Eq. (4.4), and thus $|v_i|$ at $M_{\rm EW}$ is large, dominating the tree–level neutrino mass, Eq. (4.1).

(b) $\mathbf{A_0 \approx 2M_{1/2}}$: Due to the initially negative RHS of Eq. (4.8) at energies close to M_X (where $h'_{ijk} \approx A_0 \times \lambda'_{ijk}$), $\tilde{D}_i$ first increases when running to lower energies but then starts decreasing once h'_{ijk} becomes negative, *cf.* the dotted magenta lines in Fig. 4.2 and Fig. 4.3. At some energy scale Q, $\tilde{D}_i$ becomes small such that v_i, Eq. (4.4), can equal $v_d \frac{\kappa_i}{\mu}$. A cancellation between these two terms in $m_\nu^{\rm tree}$, Eq. (4.1), at the scale Q will then occur. This corresponds to a vanishing tree–level neutrino mass if $Q = M_{\rm EW}$.

(c) $\mathbf{A_0 \gg 2M_{1/2}}$: The RHS of Eq. (4.8) is always negative with a large magnitude such that we get a large positive $\tilde{D}_i$ at the weak scale, *cf.* the dotted–dashed blue line in Fig. 4.3. As in case (a), $\tilde{D}_i v_u$ provides the main contribution to $|v_i|$, Eq. (4.4). Therefore, $|v_i|$ is large and dominates $m_\nu^{\rm tree}$, Eq. (4.1).

Summarizing, the tree–level neutrino mass has a minimum in the parameter region where the size of A_0 is comparable to $2M_{1/2}$. This is mainly due to the running of the parameters $\tilde{D}_i$ and h'_{ijk} that affect the sneutrino vevs; in particular due to a partial cancellation in Eq. (4.9). Note that in Fig. 4.1 the tree–level neutrino mass vanishes at $A_0 \approx 910$ GeV, which is indeed close to $2M_{1/2}$.

In Fig. 4.4, we show two dimensional cMSSM parameter scans of the tree–level neutrino mass. The other cMSSM parameters are those of Point I, § 4.1.1, with $\lambda'_{233}|_{\rm GUT} = 10^{-5}$. One scan parameter is always A_0 in order to show how the position of the minimum, which was described in the last section, changes with the other cMSSM parameters. Fig. 4.4(i) shows the A_0–$M_{1/2}$ plane. We can clearly see that the position of the neutrino mass minimum is at $A_0 \approx 2M_{1/2}$ as was concluded above. Fig. 4.4(ii) presents the A_0–M_0 plane and Figs. 4.4(iii) and (iv) present the A_0–tanβ plane for positive and negative sgn(μ), respectively. As we will explain in the

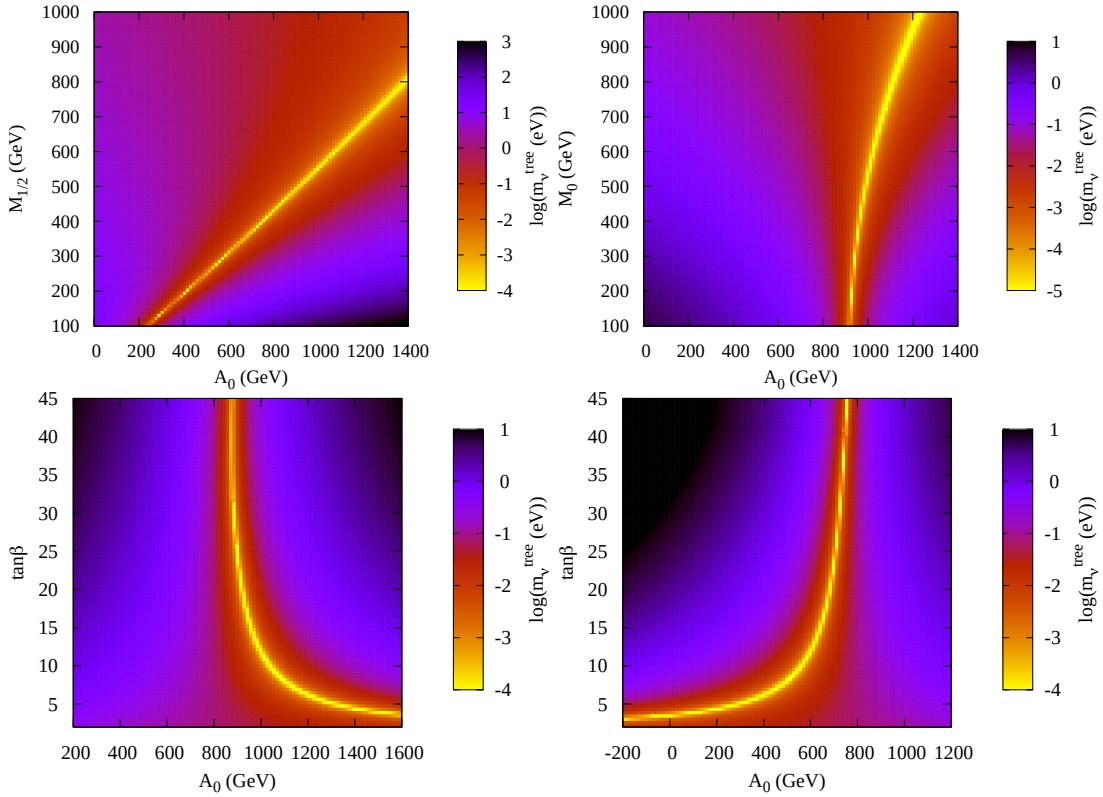

Figure 4.4: Two dimensional plots of the tree–level neutrino mass. In plot (i) [top, left], we depict the $A_0 - M_{1/2}$ plane, in plot (ii) [top, right], we depict the $A_0 - M_0$ plane, in plot (iii) [bottom, left], we depict the $A_0 - \tan\beta$ plane for $\mathrm{sgn}(\mu) = +1$ and in plot (iv) [bottom, right], we depict the $A_0 - \tan\beta$ plane for $\mathrm{sgn}(\mu) = -1$. The plots are centered around parameter Point I, § 4.1.1, with $\lambda'_{233}|_{\mathrm{GUT}} = 10^{-5}$. The yellow regions signify parts of the parameter space where the neutrino mass becomes smaller than 10^{-4}eV [plots (i),(iii),(iv)] or smaller than 10^{-5}eV [plot (ii)] .

following subsection, the position of the minimum is shifted towards higher values of A_0 for small $\tan\beta$. However, in this case a change of $\mathrm{sgn}(\mu)$ also has a significant impact.

4.3 Dependence on Further B_3 cMSSM Parameters

In § 4.2, we described in detail the dependence of the tree–level neutrino mass, Eq. (3.7), on the B_3 cMSSM parameter A_0. In this section, we explain now in more detail the dependence of the tree–level neutrino mass and the loop induced masses on the remaining B_3 cMSSM parameters.

4.3.1 $M_{1/2}$ Dependence

The tree–level neutrino mass minimum can be explained equivalently in terms of its dependence on $M_{1/2}$ instead of its dependence on A_0. This is because varying $M_{1/2}$ has a similar effect on the running of h'_{ijk}, Eq. (4.9) and Eq. (4.10), as varying A_0. This is clear from the arguments (a)-(c) in § 4.2. We could just rephrase the case differentiation as

(a) $\mathbf{M_{1/2} \gg A_0/2}$.

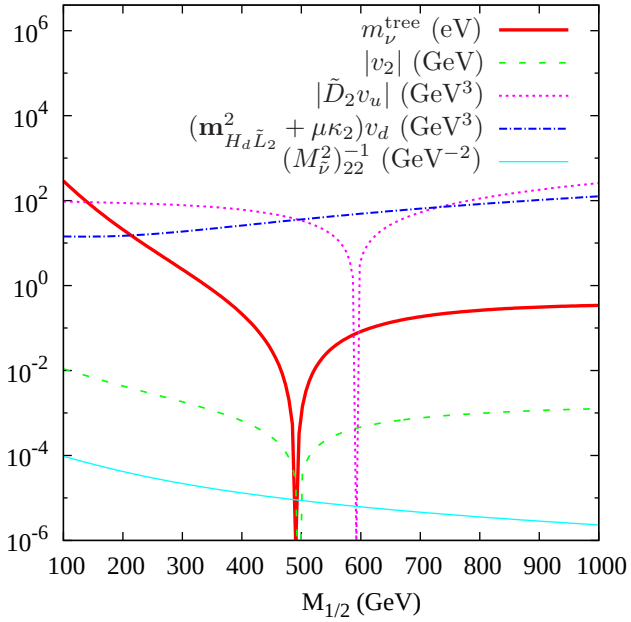

Figure 4.5: Same as Fig. 4.1, but now for the cMSSM parameter $M_{1/2}$ instead of A_0.

(b) $\mathbf{M_{1/2} \approx A_0/2}$.

(c) $\mathbf{M_{1/2} \ll A_0/2}$.

However, when varying $M_{1/2}$ there are *additional effects* coming on the one hand from the dependence of μ^2, $(M^2_{\tilde{\nu}})_{ii}$ and $m^2_{L_i H_d}$ on $M_{1/2}$. These quantities are linear functions of $M^2_{1/2}$. For μ^2 this can bee seen from Eq. (4.7). For $(M^2_{\tilde{\nu}})_{ii}$ and $m^2_{L_i H_d}$ this follows because the respective RGEs are functions of the squared sfermion masses [51]. One obtains for example [155]

$$(M^2_{\tilde{\nu}})_{ii} \approx M_0^2 + 0.52 M^2_{1/2} + \frac{1}{2} M_Z^2 \cos 2\beta \,. \tag{4.11}$$

On the other hand, there is also a direct proportionality of $m_\nu^{\rm tree}$ to $M^{-1}_{1/2}$, *cf.* Eq. (3.7). All these additional effects do not significantly influence the position of the tree–level neutrino mass minimum, *i.e.* $A_0 \approx 2M_{1/2}$ still holds for $\mathbf{\Lambda} \in \{\lambda'_{ijk}\}$; see § 4. However, the effects add a global slope to the terms (as a function of $M_{1/2}$), which contribute to the tree level mass. This behavior can be seen in Fig. 4.5.

We show in Fig. 4.5 the same contributions as in Fig. 4.1, but now as a function of $M_{1/2}$ instead of A_0. Here A_0 has been fixed to 900 GeV. On the one hand, we observe that the quantities $\tilde{D}_i v_u$ (dotted magenta line) and $(m^2_{L_i H_d} + \mu\kappa_i) v_d$ (dotted-dashed blue line) are nearly constant for low values of $M_{1/2}$, but they have a positive slope for large values of $M_{1/2}$. This is mainly due to their dependence on μ; *cf.* Eq. (2.11) [Eq. (2.10)] for $\tilde{D}_i$ [κ_i]. On the other hand $(M^{-2}_{\tilde{\nu}})_{ii}$ (solid turquoise line) has a negative slope for all values of $M_{1/2}$ because of Eq. (4.11). Overall this leads to a steep decrease of the tree–level neutrino mass (solid red line) in the region of low $M_{1/2}$, whereas in the region of large $M_{1/2}$, the various contributions' dependence on $M_{1/2}$ roughly cancels, see Fig. 4.5.

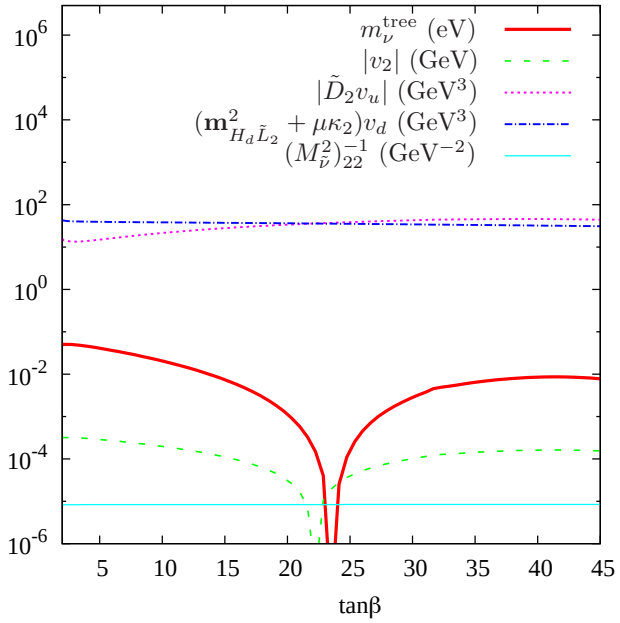

Figure 4.6: Same as Fig. 4.1, but now for the cMSSM parameter $\tan\beta$ instead of A_0.

Going beyond the plot, for $M_{1/2} \to \infty$ the tree–level mass scales with $M_{1/2}^{-1}$, as follows from the different contributions to $m_\nu^{\rm tree}$ in Eq. (3.7). Such a behavior is expected, because SUSY decouples from the SM sector in the limit $M_{1/2} \to \infty$.

4.3.2 $\tan\beta$ Dependence

Varying $\tan\beta$ most importantly affects the tree–level neutrino mass via the term $\tilde{D}_i v_u$ in Eq. (4.4). The RGE for $\tilde{D}_i$, Eq. (4.8), is proportional to the down–type Yukawa coupling $(\mathbf{Y}_D)_{jk} \equiv (\mathbf{m}_d)_{jk}/v_d$. Therefore,

$$\tilde{D}_i v_u \propto c_1 + c_2 \frac{v_u}{v_d} \equiv c_1 + c_2 \tan\beta \ , \tag{4.12}$$

at $M_{\rm EW}$. The factors c_1 and c_2 depend on the other cMSSM parameters but their magnitude is approximately independent of $\tan\beta$. However, there is a dependence of $\mathrm{sgn}(c_2)$ on $\tan\beta$ via the RGE of h'_{ijk}. Especially in case (b) of § 4.2, *i.e.* in the region around the tree–level neutrino mass minimum, this becomes relevant [6].

This (weak) $\tan\beta$ dependence of $|\tilde{D}_i v_u|$ is illustrated in Fig. 4.6 for our B_3 cMSSM parameter set Point I; see § 4.1.1. One observes that the dotted magenta line ($|\tilde{D}_i v_u|$) increases between $\tan\beta = 2$ and $\tan\beta \approx 40$. Here, $\mathrm{sgn}(c_2) > 0$. Above $\tan\beta \approx 40$, $|\tilde{D}_i v_u|$ starts decreasing, *i.e.* $\mathrm{sgn}(c_2) < 0$. This is due to the enhancement of the down–type Yukawa coupling when increasing $\tan\beta$, since this reduces h'_{ijk} further and further until it becomes negative. This decrease of $|\tilde{D}_i v_u|$ is only partially visible in Fig. 4.6 since the parameter region with high $\tan\beta$ is excluded due to tachyons.

One can also see in Fig. 4.6 that the other term determining the sneutrino vev, $(m^2_{L_i H_d} +$

[6] In case (a), c_2 remains always negative and in case (c), c_2 is positive.

$\mu\kappa_i)v_d$, which is displayed as a dotted-dashed blue line, is fairly constant regarding $\tan\beta$. This contribution to the sneutrino vev is subtracted from the first term, $\tilde{D}_i v_u$ (dotted magenta line), so that the sneutrino vev becomes zero when the two lines intersect; see Eq. (4.4).

We observe this intersection in Fig. 4.6 at $\tan\beta \approx 22$, thus yielding the tree–level neutrino mass minimum in this region. In theory, there could even arise *two* minima because above $\tan\beta \approx 40$ $\tilde{D}_i v_u$ starts decreasing again, leading to another intersection with $(m^2_{L_i H_d} + \mu\kappa_i)v_d$. However, as mentioned before, this usually happens in an excluded region of parameter space.

As is also illustrated in Fig. 4.6, there is quite a sizable difference between the two terms which determine the sneutrino vev, *i.e.* $(m^2_{L_i H_d} + \mu\kappa_i)v_d$ (dotted–dashed blue line) and $\tilde{D}_i v_u$ (dotted magenta line) in the region of low $\tan\beta$. If we are looking for a neutrino mass minimum in this region of parameter space, we need to adjust A_0 towards higher values, which will increase h'_{ijk} [*cf.* Eq. (4.9)]. Therefore, increasing A_0 will shift the dotted magenta line upwards until it intersects with the dotted-dashed blue line at the desired low $\tan\beta$ value. This shift of the tree–level neutrino mass minimum to higher A_0 is clearly visible in Fig. 4.4 (iii). For $\tan\beta = 20$, the minimum lies at $A_0 \approx 900$ GeV whereas for $\tan\beta = 5$, it has shifted to $A_0 \approx 1300$ GeV. In short, the shift is due to a decrease of the down–type Yukawa coupling for low $\tan\beta$ leading to a decrease of the RHS of Eq. (4.8). This decrease needs to be balanced by increasing A_0; recall that $h'_{ijk} = \lambda'_{ijk} \times A_0$ at M_X in Eq. (4.8).

4.3.3 $\mathrm{sgn}(\mu)$ Dependence

A change of $\mathrm{sgn}(\mu)$ notably affects the tree–level neutrino mass via the RGE running of $\tilde{D}_i$ [Eq. (4.8)], in which the overall sign of the RGE is changed. Therefore, the sign of $\tilde{D}_i$ itself is reversed at any energy scale but its magnitude is mostly unaffected. Consequently, the A_0 value where $\tilde{D}_i = 0$ is still mostly the same after a sign change.

However, at the position of the tree–level neutrino mass minimum, $\tilde{D}_i$ needs to be slightly larger than zero in order to cancel the other terms contributing to the tree–level mass, *cf.* § 4.2 and § 4.3.2. When we are at a parameter point where the tree–level neutrino mass minimum occurs for positive μ (*i.e.* $\tilde{D}_i$ is small and positive), a sign change to $\mathrm{sgn}(\mu) = -1$ will yield a $\tilde{D}_i$ which is small and negative. The other contributing terms undergo no overall sign change. If we would like to obtain a neutrino mass minimum now, $\tilde{D}_i$ needs to be increased in order to become slightly larger than zero again. This can be achieved by *decreasing* A_0, § 4.2, (or, equivalently, *increasing* $M_{1/2}$, § 4.3.1) since this increases $\tilde{D}_i$ via h'_{ijk} in its RGE, Eq. (4.8), when μ is negative. Therefore, the tree–level minimum will occur at smaller values of A_0 (or equivalently larger values of $M_{1/2}$) when we change $\mathrm{sgn}(\mu) = +1$ to $\mathrm{sgn}(\mu) = -1$.

This effect becomes more important when we go to regions of low $\tan\beta$. Here the influence of h'_{ijk} on $\tilde{D}_i$, Eq. (4.8), becomes weaker due to the decrease of the down–type Yukawa coupling, as we discussed in § 4.3.2. In order to still obtain a positive $\tilde{D}_i$ after reversing $\mathrm{sgn}(\mu)$, h'_{ijk} has to decrease in a more substantial fashion than for large $\tan\beta$. Therefore, the parameter point where the tree–level neutrino mass minimum is located will shift to smaller A_0 when changing $\mathrm{sgn}(\mu) = +1$ to $\mathrm{sgn}(\mu) = -1$, especially for $\tan\beta \lesssim 10$.

Overall, the sign change of μ leads to a "mirroring" of the tree–level mass minimum curve in the A_0–$\tan\beta$ plane around $A_0 = 800$ GeV$(\approx 2M_{1/2})$ because of a reversal of the sign of the RGE for $\tilde{D}_i$. This can be seen in Fig. 4.4 (iii) and (iv): for $\mathrm{sgn}(\mu) = +1$ the minimum shifts to higher values of A_0 with decreasing $\tan\beta$, whereas for $\mathrm{sgn}(\mu) = -1$ the minimum shifts to lower values of A_0.

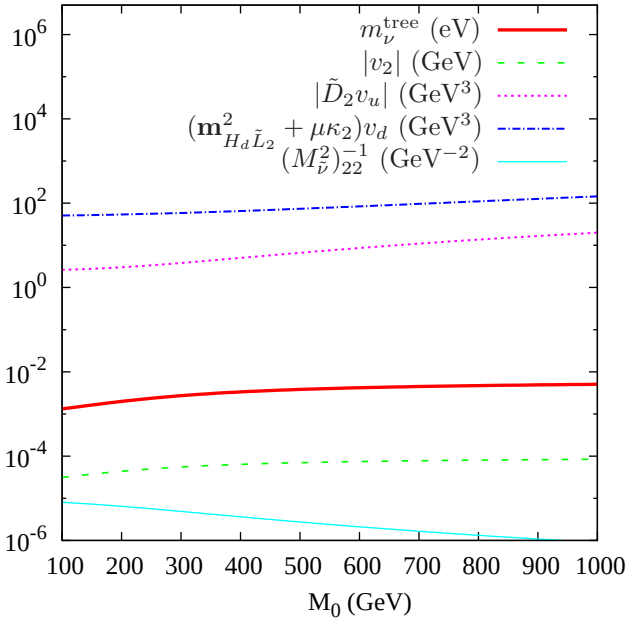

Figure 4.7: Same as Fig. 4.1, but now for the cMSSM parameter M_0 instead of A_0.

4.3.4 M_0 Dependence

Varying M_0 does not greatly affect the tree–level neutrino mass. However, similar effects as those described in § 4.3.1 as *additional effects*, arise due to the dependence of several parameters on M_0^2, *cf.* for example Eq. (4.7) and Eq. (4.11). This can be seen in Fig. 4.7, where we again show the terms, which enter the tree–level neutrino mass formula, Eq. (3.7). We can see that most of the quantities depend only weakly on M_0. This results in a nearly constant tree–level neutrino mass, *cf.* solid red line in Fig. 4.7.

However, the above mentioned M_0^2 dependences lead to a moderate shift of the tree–level neutrino mass minimum towards higher values of A_0 when increasing M_0. Explaining this in detail is fairly lengthy because the M_0 dependence of the parameters determining the tree–level neutrino mass is not as straightforward as the dependence on other cMSSM parameters. However, the effect is shown numerically in Fig. 4.4 (ii). At large M_0, the interval around the minimum in the A_0 direction where the the tree–level neutrino mass is considerably reduced (and therefore the bounds on λ'_{ijk} are substantially weakened) is significantly broadened.

It should be noted that there is a similar *mirror effect* when changing $\mathrm{sgn}(\mu)$ as for $\tan\beta$. For $\mathrm{sgn}(\mu) = -1$, the minimum shifts towards *lower* values of A_0 when increasing M_0.

4.4 Changes for $\mathbf{\Lambda} \in \lambda_{ijk}$

We now consider the case of $\mathbf{\Lambda} \in \{\lambda_{ijk}\}$ instead of $\mathbf{\Lambda} \in \{\lambda'_{ijk}\}$. Since λ_{ijk} only couples lepton superfields to each other (as opposed to the λ'_{ijk} operator which also involves quark superfields), the RGEs in § 4.2 are reduced by a (color) factor of 3 [51, 82]. In addition, the down quark Yukawa matrix elements, $(Y_D)_{jk}$, need to be replaced by the respective lepton Yukawa matrix elements, $(Y_E)_{jk}$. Otherwise, the structure of the RGEs remains the same.

The only RGE where there are more extensive relevant changes is that for h_{ijk} (which replaces

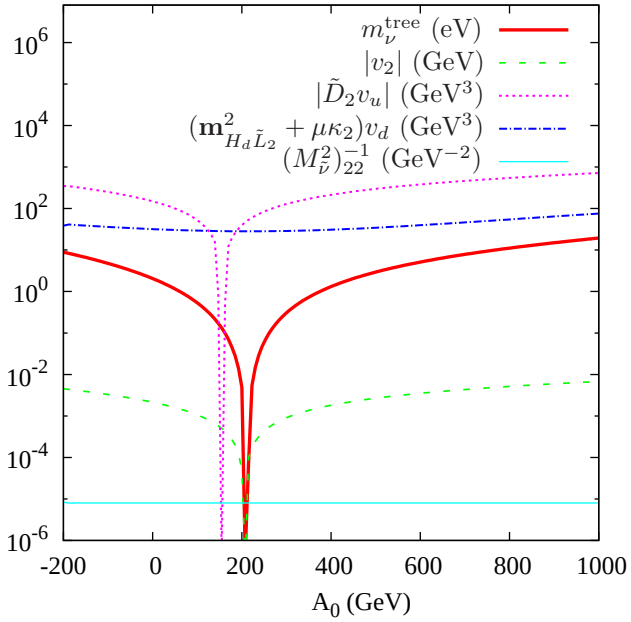

Figure 4.8: Same as Fig. 4.1, but now for the B_3 cMSSM Point II, § 4.1.1, with $\lambda_{233}|_{\rm GUT} = 10^{-4}$.

h'_{ijk}); *cf.* Eq. (2.5). Eq. (4.9) must be replaced by [51]

$$16\pi^2 \frac{dh_{ijk}}{dt} = \frac{9}{5} g_1^2 (2M_1 \lambda_{ijk} - h_{ijk}) + 3 g_2^2 (2M_2 \lambda_{ijk} - h_{ijk}) + \dots \,, \tag{4.13}$$

with $h_{ijk} = A_0 \times \lambda_{ijk}$ at $M_{\rm GUT}$. This looks exactly the same as the RGE for h'_{ijk}, Eq. (4.9), only with g_3 and M_3 replaced by g_α and M_α ($\alpha = 1, 2$). However, it is important to realize that the running of g_α and M_α is different from the running of g_3 and M_3. As was mentioned in § 4.2, the latter quantities *increase* when running to lower energy scales whereas the former *decrease* [28].

This has important consequences for the position of the tree–level neutrino mass minimum. The terms $g_\alpha^2 M_\alpha \lambda_{ijk}$ of Eq. (4.13) now decrease [as opposed to $g_3^2 M_3 \lambda'_{ijk}$ in Eq. (4.9)]. It is thus necessary to choose A_0 smaller in order to have a smaller h_{ijk} at $M_{\rm GUT}$ and at lower scales to compensate for this. Quantitatively, we checked numerically that we now need $A_0 \approx M_{1/2}/2$ ($\mathbf{\Lambda} \in \{\lambda_{ijk}\}$) to achieve a vanishing tree–level neutrino mass rather than $A_0 \approx 2M_{1/2}$ ($\mathbf{\Lambda} \in \{\lambda'_{ijk}\}$) as was the case in § 4.2.

For illustrative purpose, we show in Fig. 4.8 the A_0 dependence of the tree–level neutrino mass (solid red line) and of the terms determining the sneutrino vev v_2 for a non-vanishing coupling λ_{233} at M_X. Fig. 4.8 is equivalent to Fig. 4.1 beside the fact that we now employ the parameter Point II with $\lambda_{233}|_{\rm GUT} = 10^{-4}$ instead of the parameter Point I with $\lambda'_{233}|_{\rm GUT} = 10^{-5}$, *cf.* § 4.1.1. The qualitative behavior of all terms is the same in both figures. However, in Fig. 4.8 the minima are shifted to lower values of A_0 compared to Fig. 4.1.

We conclude that the line of argument explaining the minimum of the tree–level neutrino mass in the case of $\mathbf{\Lambda} \in \{\lambda'_{ijk}\}$ still holds for $\mathbf{\Lambda} \in \{\lambda_{ijk}\}$. However, the position of the minimum now shifts to $A_0 \approx M_{1/2}/2$. The change of the prefactor is due to the fact that λ_{ijk} couples only leptonic fields to each other. Consequently, only superfields carrying SU(2) and U(1) charges,

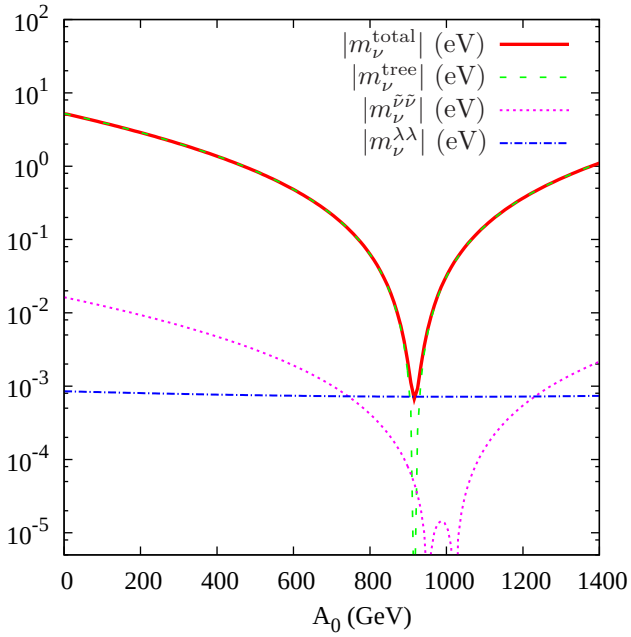

Figure 4.9: A_0 dependence of the different contributions to the neutrino mass at the REWSB scale for the B_3 cMSSM Point I, § 4.1.1, with $\lambda'_{233}|_{\text{GUT}} = 10^{-5}$. Note that only the absolute values of the contributions to the neutrino mass are displayed. m_ν^{tree} and $m_\nu^{\lambda\lambda}$ are negative whereas $m_\nu^{\tilde{\nu}\tilde{\nu}}$ is mostly positive. $m_\nu^{\tilde{\nu}\tilde{\nu}}$ is only negative between the two minima of $|m_\nu^{\tilde{\nu}\tilde{\nu}}|$; see § 4.5 for details.

but not SU(3) charges, contribute to the relevant RGEs.

4.5 Dependence of the Loop Contributions to ν Masses on cMSSM Parameters

The loop contributions to the neutrino mass matrix are usually several orders of magnitude smaller than the tree–level contribution [43, 51]. However, in the region around the tree–level neutrino mass minimum, the loops dominate as shown in Fig. 4.9 and Fig. 4.10. Therefore, we now briefly discuss the dependence of the loop contributions on the cMSSM parameters.

- *$\lambda\lambda$– and $\lambda'\lambda'$–loops:* This contribution to the neutrino mass, $m_\nu^{\lambda\lambda}$, depends only weakly on the cMSSM parameters, in particular it depends logarithmically on the relevant sfermion mass. For example, varying A_0 from 0 to 1400 GeV (-200 GeV to 1000 GeV) around Point I (Point II) leaves the magnitude of $m_\nu^{\lambda\lambda}$ nearly unchanged[7]; *cf.* the dotted–dashed blue line in Fig. 4.9 (Fig. 4.10). However, increasing M_0 or $M_{1/2}$ results in a decreasing $m_\nu^{\lambda\lambda}$: as the SUSY spectrum gets heavier the sfermions in the loops decouple.

- *Neutral scalar–neutralino–loops:* This contribution to the neutrino mass, $m_\nu^{\tilde{\nu}\tilde{\nu}}$, as a function of A_0 possesses a minimum which lies in the vicinity of the m_ν^{tree} minimum. However, there is no exact alignment.

[7] In principle, there is an A_0 dependence that stems from left-right mixing of the sfermions inside the loop, *cf.* the first term in Eq. (3.12). However, in most regions of parameter space we have $\mu \tan\beta \gg A_0$. In this case only the second term in Eq. (3.12) plays a role.

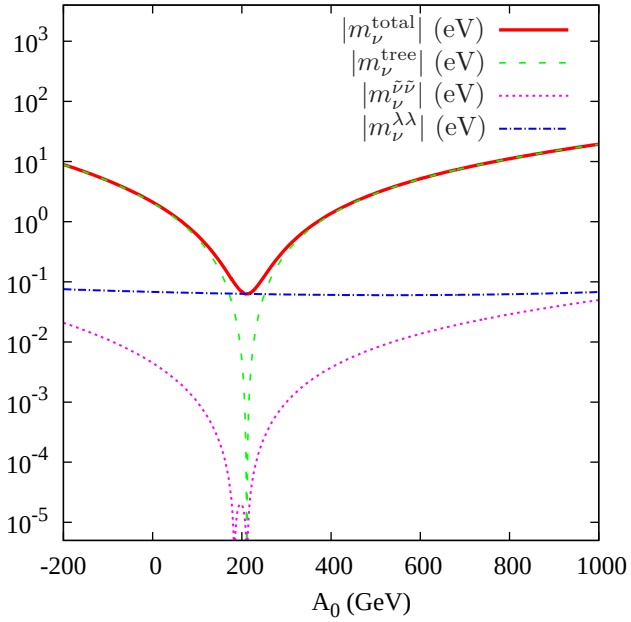

Figure 4.10: Same as Fig. 4.9, but for the B_3 cMSSM Point II, § 4.1.1, with $\lambda_{233}|_{\text{GUT}} = 10^{-4}$.

According to Eqs. (3.18) and (3.19), the dominant loop contribution from neutral scalar–neutralino–loops to the neutrino mass matrix, $(m_\nu^{\tilde{\nu}\tilde{\nu}})_{ii}$, is proportional to

$$(m_\nu^{\tilde{\nu}\tilde{\nu}})_{ii} \propto \; (\tilde{D}_i v_d - \tilde{B} v_i)^2 \times f(m^2_{\tilde{\chi}^0_k}, m^2_{\tilde{\nu}_i}, m^2_{H_0}, m^2_{A_0}, m^2_{h_0}) \,, \tag{4.14}$$

where f is a function of the neutralino, sneutrino and Higgs masses squared, respectively. The A_0 dependence of Eq. (4.14) is mainly determined by $\tilde{D}_i$, since the A_0 dependence of v_i is governed by $\tilde{D}_i(A_0)$,

$$v_i(A_0) \propto \tilde{D}_i(A_0) + c \,, \tag{4.15}$$

where the term c depends mainly on the other cMSSM parameters but barely on A_0, as discussed in § 4.2. Therefore $(m_\nu^{\tilde{\nu}\tilde{\nu}})_{ii}$ is roughly proportional to $\tilde{D}_i^2$. The behavior of $\tilde{D}_i$ has been discussed in detail in § 4.2 in the context of the tree–level neutrino mass. We have shown that there is always a value of A_0 where $\tilde{D}_i$ becomes zero. Thus the neutral scalar–neutralino loops display a similar minimum as the tree–level neutrino mass. The position of the minimum is close to the tree–level one, but not exactly aligned. This can be seen by comparing the dotted magenta line and dashed green line in Fig. 4.9 and Fig. 4.10. However, since Eq. (4.14) is only an approximate formula [for the exact formula, *cf.* Eq. (3.15)], the real curve is slightly shifted downwards such that its minimum reaches negative values. Therefore $|(m_\nu^{\tilde{\nu}\tilde{\nu}})_{ii}|$ in Fig. 4.9 and Fig. 4.10 appears to have two minima.

It is also immediately obvious from Eq. (4.14) that the scalar–neutralino–loops are roughly proportional to $[\mathbf{\Lambda} \times (Y_D)_{jk}]^2$ like the tree–level mass. Again, increasing M_0 or $M_{1/2}$ will in general decrease $m_\nu^{\tilde{\nu}\tilde{\nu}}$, because the SUSY mass spectrum gets heavier.

- NLO corrections to the sneutrino vevs are typically at least one order of magnitude smaller

than the tree–level quantities determining the sneutrino vevs, $m^2_{L_i H_d} \times v_d/(M_{\tilde{\nu}})^2_{ii}$ and $\tilde{D}_i \times v_u/(M_{\tilde{\nu}})^2_{ii}$, in Eq. (3.8) [152]. For illustration, one could consider this as a $\mathcal{O}(10\%)$ correction to $m^2_{L_i H_d}$. This shift upwards of the dotted–dashed blue line in Fig. 4.1 slightly changes the position of the tree–level neutrino mass minimum, but does not alter any of the conclusions drawn in this section. Since the effects that we investigate in this chapter arise mainly from the contribution $\tilde{D}_i v_u$ to the sneutrino vevs (see § 4.2), these corrections are not important for the qualitative analysis performed here. In chapter 6.1.2, we discuss how these NLO corrections can be implemented in the spectrum generator `SOFTSUSY`.

For parameter Points I and II, § 4.1.1, the A_0 interval, ΔA_0, where the loops dominate is relatively small, *cf.* Fig. 4.9 and Fig. 4.10. However, there are other parameter regions where the loops dominate in intervals of $\Delta A_0 = \mathcal{O}(100\,\text{GeV})$! This is for example the case if one varies A_0 around the benchmark point SPS1a [188].

4.6 Implications for Model Building

The tree–level neutrino mass depends strongly on the trilinear soft-breaking A_0–parameter (and also similarly on the gaugino masses). We concluded that in regions of parameter space with $A_0 \approx 2M_{1/2}$ ($A_0 \approx M_{1/2}/2$) for $\lambda'_{ijk}|_{\text{GUT}} \neq 0$ ($\lambda_{ijk}|_{\text{GUT}} \neq 0$), a cancellation between the different contributions to the tree–level mass can occur. This can weaken the bounds on LNV parameters arising from the cosmological upper bound on neutrino masses significantly, since the overall neutrino mass scale is reduced. We will investigate this in § 5.3.

The work presented in this chapter can also help to find new supersymmetric scenarios that are consistent with the observed neutrino masses and mixings. We have shown how the (typically large) hierarchy between the tree–level and 1–loop neutrino masses can be reduced systematically . One can use this mechanism to match the ratio between tree–level and 1–loop induced masses to the observed neutrino mass hierarchy, both for hierarchical neutrino masses and for a degenerate spectrum. We further develop this idea in § 6. However, in § 4.5 it was mentioned that loop corrections to the sneutrino vevs can lead to a seizable correction of the absolute value of the neutrino masses. Also, there are further contributions to 1–loop neutrino masses besides the dominant $\Lambda\Lambda$ and neutral scalar–neutralino loops discussed here. Hence, § 6.1.2 is devoted to a discussion of the implementation of a full 1–loop treatment of the neutrino sector within the spectrum calculator `SOFTSUSY`, in order to obtain a precise description of neutrino masses for comparison with experimental data.

Chapter 5

Bounds on the B_3 cMSSM

5.1 Low–energy bounds on the trilinear LNV couplings of the B_3 cMSSM

Once a set of LNV couplings is specified, a natural question arises as to whether the model is compatible with the large number of low energy observables (LEOs) on lepton–number violation. If a considered model predicts LEO values close to current experimental limits, future (non–)observations could (dis–)favor this model.

An extended set of relevant bounds on LNV LEOs is presented in Refs. [44, 189, 190]. Typically these constraints are more important for LNV couplings involving lighter generations. The reasons are two fold: Firstly, the fermion mass term in the $\lambda\lambda$ and $\lambda'\lambda'$–loops in Eq. (3.10) implies that, in order to generate a neutrino mass contribution of the same size, LNV couplings involving a light family index k need to be much larger than corresponding couplings with heavy family indices to compensate for the mass suppression. Secondly, experimental constraints generally provide more stringent limits on LNV couplings invocationlving light generations.

In the models presented in later sections, we compare our best fit parameter values with the limits presented in Ref. [44], as well as a $0\nu\beta\beta$ bound on λ'_{111} from Ref. [191–194]. The bounds which are most relevant for the discussion of our results are displayed below:

[b1] $\mu \to eee$ decay:

$$\begin{aligned} \lambda_{nij}\lambda_{n11} &\lesssim 6.6 \cdot 10^{-7} \left(\frac{m_{\tilde{\nu}_n}}{100\,\mathrm{GeV}}\right)^2, \quad i,j = 12,21 \\ \lambda'_{211}\lambda'_{111} &\lesssim 1.3 \cdot 10^{-41} \end{aligned}$$

[b2] $\mu - e$ conversion in nuclei:

$$\begin{aligned} \lambda_{nij}\lambda'_{n11} &\lesssim 2.1 \cdot 10^{-8} \left(\frac{m_{\tilde{\nu}_n}}{100\,\mathrm{GeV}}\right)^2, \quad i,j = 12,21 \\ \lambda'_{2n1}\lambda'_{1n1} &\lesssim 4.3 \cdot 10^{-8} \left(\frac{m_{\tilde{q}_n}}{100\,\mathrm{GeV}}\right)^2, \quad n = 2,3 \\ \lambda'_{21n}\lambda'_{11n} &\lesssim 4.5 \cdot 10^{-8} \left(\frac{m_{\tilde{q}_n}}{100\,\mathrm{GeV}}\right)^2, \quad n = 2,3 \\ \lambda'_{211}\lambda'_{111} &\lesssim 4.3 \cdot 10^{-8} \cdot \Delta^{-1}, \\ \Delta &\equiv \left(\frac{100\,\mathrm{GeV}}{m_{\tilde{u}}}\right)^2 - \left(\frac{2Z+N}{2N+Z}\frac{100\,\mathrm{GeV}}{m_{\tilde{d}}}\right)^2 \end{aligned}$$

For $^{48}_{22}$Ti, $(2Z+N)/(2N+Z) = 70/74$. This comes from the ratio of the number of valence up–quarks to that of the down–quarks in a nuclei. See Ref. [195].

[b3] μ decay:

$$\lambda_{12k} \lesssim 0.08 \left(\frac{m_{e_{kR}}}{100\,\mathrm{GeV}}\right)$$

[b4] Leptonic τ decay:

$$\lambda_{23k}, \lambda_{13k} \lesssim 0.08 \left(\frac{m_{e_{kR}}}{100\,\mathrm{GeV}}\right)$$

[b5] Forward–backward asymmetry of Z decay:

$$\begin{aligned} \lambda_{i3k}(i \neq k \neq 3) &\lesssim 0.25 \left(\frac{m_{\tilde{\nu}_\tau}}{100\,\mathrm{GeV}}\right) \\ \lambda_{i2k}(i \neq k \neq 2) &\lesssim 0.11 \left(\frac{m_{\tilde{\nu}_\mu}}{100\,\mathrm{GeV}}\right) \end{aligned}$$

[b6] Leptonic K–meson decay (here $i, j = 12, 21$):

$$\begin{aligned} \lambda_{n11}\lambda'_{nij} &\lesssim 1.0 \cdot 10^{-8} \left(\frac{m_{\tilde{\nu}_n}}{100\,\mathrm{GeV}}\right)^2, \\ \lambda_{n22}\lambda'_{nij} &\lesssim 2.2 \cdot 10^{-7} \left(\frac{m_{\tilde{\nu}_n}}{100\,\mathrm{GeV}}\right)^2, \\ \lambda_{n12}\lambda'_{nij} &\lesssim 6 \cdot 10^{-9} \left(\frac{m_{\tilde{\nu}_n}}{100\,\mathrm{GeV}}\right)^2, \\ \lambda_{n21}\lambda'_{nij} &\lesssim 6 \cdot 10^{-9} \left(\frac{m_{\tilde{\nu}_n}}{100\,\mathrm{GeV}}\right)^2, \end{aligned}$$

[b7] $\mu \to e\gamma$:

$$\begin{aligned} \lambda_{nl2}\lambda_{nl1} &< 8.2 \cdot 10^{-5} \cdot \\ &\quad \cdot \left[2\left(\frac{100\,\mathrm{GeV}}{m_{\tilde{\nu}_L}}\right)^2 - \left(\frac{100\,\mathrm{GeV}}{m_{\tilde{l}_L}}\right)^2\right]^{-1} \\ \lambda_{23n}\lambda_{13n} &< 2.3 \cdot 10^{-4} \cdot \\ &\quad \cdot \left[2\left(\frac{100\,\mathrm{GeV}}{m_{\tilde{\nu}_L}}\right)^2 - \left(\frac{100\,\mathrm{GeV}}{m_{\tilde{l}_R}}\right)^2\right]^{-1} \\ \lambda'_{2nl}\lambda'_{1nl} &< 7.6 \cdot 10^{-5} \left(\frac{m_{\tilde{d}_{lR}}}{100\,\mathrm{GeV}}\right)^2, \quad n = 1, 2 \end{aligned}$$

[b8] $0\nu\beta\beta$ (here $\tilde{f} = \tilde{e}_L, \tilde{u}_L, \tilde{d}_R$):

$$|\lambda'_{111}| \lesssim 5 \cdot 10^{-4} \left(\frac{m_{\tilde{f}}}{100\mathrm{GeV}}\right)^2 \left(\frac{m_{\tilde{g}/\tilde{\chi}}}{100\mathrm{GeV}}\right)^{1/2}.$$

These bounds are given in the mass basis, with the reference sparticle mass scale set at 100 GeV. In order to compare our model values with these bounds, we rotate to the mass basis

and include the correct mass dependence for all constraints derived from tree–level (4–fermion) operators.

5.2 Bounds on the B_3 cMSSM parameter space

We also need to take into account various other constraints on the B_3 cMSSM parameter space such as the absence of tachyons [51] or the lower bound on the lightest Higgs mass from LEP2 [182, 183]. However, we reduce the LEP2 bound by 3 GeV in order to account for numerical uncertainties of `SOFTSUSY` [196–198]. For instance, in the decoupling limit (where the light Higgs, h^0, is SM-like) a lower bound of

$$m_{h^0} > 111.4\,\text{GeV} \tag{5.1}$$

We check in all numerical analyses presented in this work that we lie within the 2σ window for the branching ratio of $b \to s\gamma$ [184],

$$2.74 \times 10^{-4} < \text{BR}(b \to s\gamma) < 4.30 \times 10^{-4}\,, \tag{5.2}$$

and we are below the experimental upper bound on the branching ratio of $B_s \to \mu^+\mu^-$ [184], *i.e.*

$$\text{BR}(B_s \to \mu^+\mu^-) < 4.7 \times 10^{-8}\,. \tag{5.3}$$

The 2σ window of the SUSY contribution to the anomalous magnetic moment of the muon [199–202] excludes fairly large regions of cMSSM parameters space, which we show for example in Figs. 5.1 and 5.2:

$$8.6 \times 10^{-10} < \delta a_\mu^{\text{SUSY}} < 40.6 \times 10^{-10}\,. \tag{5.4}$$

For more details see Ref. [107] and references therein. Note that there is a significant correlation in cMSSM models between the muon anomalous magnetic moment and $B_s \to \mu^+\mu^-$ [203].

5.3 Bounds on the trilinear LNV Couplings from ν–Masses

In this section, we calculate upper bounds on all trilinear LNV couplings $\mathbf{\Lambda} \in \{\lambda_{ijk}, \lambda'_{ijk}\}$ at M_X from the cosmological upper bound on the sum of neutrino masses as given in Eq. (3.30). We use the same benchmark points and numerical tools as in § 4. Beside the tree–level neutrino mass, we also include the dominant contributions to the neutrino mass matrix at one–loop as described in § 3.2 and § 3.3. Note that in good approximation

$$m_\nu|_{\text{EW}} \propto \mathbf{\Lambda}^2|_{\text{GUT}}\,, \tag{5.5}$$

for both tree–level as well as 1–loop neutrino masses, as explained in § 4.2 [2] and § 4.5. Based on this approximation we employ an iterative procedure to account for effects beyond Eq. (5.5).

In § 5.3.1, we first compare our bounds with those given in Ref. [51], where the cMSSM parameters of the benchmark point SPS1a [188] (in addition to $\mathbf{\Lambda}$) were used. We choose the same cMSSM parameters beside A_0 in order to show how the bounds change in the vicinity of the tree–level neutrino mass minimum, *cf.* § 4.2. We then perform in § 5.3.3 two dimensional

[2] This is directly clear since the LNV parameters $\tilde{D}_i$, κ_i and $m^2_{L_i H_d}$ that determine the sneutrino vev are generated proportional to $\mathbf{\Lambda}$ at M_X, *cf.* § 4.2. From $m_\nu^{\text{tree}} \propto v_i^2$ we then obtain the relationship in Eq. (5.5).

	Up mixing			Down mixing		
A_0 (GeV)	-100	500	550	-100	500	550
λ'_{111}	2.0×10^{-3}	2.7×10^{-2}	8.3×10^{-2}	9.7×10^{-4}	1.3×10^{-2}	5.3×10^{-2}
λ'_{211}	2.0×10^{-3}	2.7×10^{-2}	8.3×10^{-2}	9.7×10^{-4}	1.4×10^{-2}	5.3×10^{-2}
λ'_{311}	2.0×10^{-3}	2.7×10^{-2}	8.3×10^{-2}	9.6×10^{-4}	1.3×10^{-2}	5.3×10^{-2}
λ'_{121}, λ'_{112}	$(1.3\times10^{-1})^t$	$(1.7\times10^{-1})^t$	$(1.7\times10^{-1})^t$	4.3×10^{-4}	6.0×10^{-3}	2.7×10^{-2}
λ'_{221}, λ'_{212}	$(1.3\times10^{-1})^t$	$(1.7\times10^{-1})^t$	$(1.7\times10^{-1})^t$	4.3×10^{-4}	6.0×10^{-3}	2.7×10^{-2}
λ'_{321}, λ'_{312}	$(1.3\times10^{-1})^t$	$(1.7\times10^{-1})^t$	$(1.7\times10^{-1})^t$	4.3×10^{-4}	5.9×10^{-3}	2.6×10^{-2}
λ'_{131}	$(1.4\times10^{-1})^t$	$(1.9\times10^{-1})^t$	$(1.9\times10^{-1})^t$	6.9×10^{-4}	9.5×10^{-3}	4.2×10^{-2}
λ'_{231}	$(1.4\times10^{-1})^t$	$(1.9\times10^{-1})^t$	$(1.9\times10^{-1})^t$	6.9×10^{-4}	9.5×10^{-3}	4.3×10^{-2}
λ'_{331}	$(1.4\times10^{-1})^t$	$(1.9\times10^{-1})^t$	$(1.9\times10^{-1})^t$	6.8×10^{-4}	9.3×10^{-3}	4.2×10^{-2}
λ'_{122}	9.1×10^{-5}	1.3×10^{-3}	5.3×10^{-3}	8.9×10^{-5}	1.2×10^{-3}	5.2×10^{-3}
λ'_{222}	9.1×10^{-5}	1.3×10^{-3}	5.3×10^{-3}	8.9×10^{-5}	1.2×10^{-3}	5.2×10^{-3}
λ'_{322}	9.0×10^{-5}	1.3×10^{-3}	5.3×10^{-3}	8.8×10^{-5}	1.2×10^{-3}	5.2×10^{-3}
λ'_{132}	2.4×10^{-2}	$(1.9\times10^{-1})^t$	$(1.9\times10^{-1})^t$	5.8×10^{-5}	8.0×10^{-4}	3.9×10^{-3}
λ'_{232}	2.4×10^{-2}	$(1.9\times10^{-1})^t$	$(1.9\times10^{-1})^t$	5.8×10^{-5}	8.0×10^{-4}	3.9×10^{-3}
λ'_{332}	2.4×10^{-2}	$(1.9\times10^{-1})^t$	$(1.9\times10^{-1})^t$	5.8×10^{-5}	7.9×10^{-4}	3.8×10^{-3}
λ'_{113}	4.2×10^{-3}	5.5×10^{-2}	1.9×10^{-1}	6.3×10^{-4}	8.7×10^{-3}	3.8×10^{-2}
λ'_{213}	4.2×10^{-3}	5.5×10^{-2}	1.9×10^{-1}	6.3×10^{-4}	8.7×10^{-3}	3.8×10^{-2}
λ'_{313}	4.2×10^{-3}	5.4×10^{-2}	1.7×10^{-1}	6.2×10^{-4}	8.6×10^{-3}	3.7×10^{-2}
λ'_{123}	5.9×10^{-4}	8.7×10^{-3}	2.4×10^{-2}	5.3×10^{-5}	7.4×10^{-4}	3.4×10^{-3}
λ'_{223}	5.9×10^{-4}	8.7×10^{-3}	2.4×10^{-2}	5.3×10^{-5}	7.4×10^{-4}	3.4×10^{-3}
λ'_{323}	5.8×10^{-4}	8.5×10^{-3}	2.4×10^{-2}	5.3×10^{-5}	7.2×10^{-4}	3.4×10^{-3}
λ'_{133}	2.3×10^{-6}	3.2×10^{-5}	1.3×10^{-4}	2.3×10^{-6}	3.2×10^{-5}	1.3×10^{-4}
λ'_{233}	2.3×10^{-6}	3.2×10^{-5}	1.3×10^{-4}	2.3×10^{-6}	3.2×10^{-5}	1.3×10^{-4}
λ'_{333}	2.3×10^{-6}	3.1×10^{-5}	1.3×10^{-4}	2.3×10^{-6}	3.1×10^{-5}	1.3×10^{-4}

Table 5.1: Upper bounds on the trilinear couplings λ'_{ijk}, Eq. (2.3), at M_X for several values of A_0 (second row). The other cMSSM parameters are those of SPS1a [188]. We assume up-mixing (down-mixing) in column 2-4 (5-7), *cf.* § 2.2. Bounds arising from the absence of tachyons are in parentheses and marked by a superscript t: $()^t$.

parameter scans around the benchmark scenarios Point I and Point II (*cf.* § 4.1.1) to show more generally how the bounds depend on the B_3 cMSSM parameters.

In our parameter scans we exclude parameter regions where a tachyon occurs [51] or where the lower bound on the lightest Higgs mass from LEP2 [182, 183] is violated. In the figures, we also show contour lines for the 2σ window of the SUSY contribution to the anomalous magnetic moment of the muon [200]. We have checked that the complete parameter space which we investigate in the following is consistent with the experimental bounds from $b \to s\gamma$ [184], and from $B_s \to \mu^+\mu^-$ [184] and that we are well above the LEP2 and Tevatron supersymmetric mass bounds; see § 5.2 for details.

5.3.1 Comparison with Previous Results

In Ref. [51], bounds on single couplings $\mathbf{\Lambda}$ at $M_{\rm GUT}$ in the B_3 cMSSM model from the tree–level neutrino mass were determined for the cMSSM parameters of SPS1a, in particular $A_0 = -100$

A_0 (GeV)	-100	200	120
λ_{211}	1.1×10^{-1}	2.7×10^{-1}	$(7.1\times10^{-1})^t$
λ_{311}	1.1×10^{-1}	2.7×10^{-1}	$(7.1\times10^{-1})^t$
λ_{231}	$(5.5\times10^{-1})^t$	$(6.7\times10^{-1})^t$	$(7.1\times10^{-1})^t$
λ_{122}	4.7×10^{-4}	1.7×10^{-3}	4.9×10^{-3}
λ_{322}	4.7×10^{-4}	1.7×10^{-3}	4.9×10^{-3}
λ_{132}	$(5.5\times10^{-1})^t$	$(6.7\times10^{-1})^t$	$(7.1\times10^{-1})^t$
λ_{123}	$(5.1\times10^{-1})^t$	$(6.3\times10^{-1})^t$	$(6.7\times10^{-1})^t$
λ_{133}	2.7×10^{-5}	1.0×10^{-4}	2.8×10^{-4}
λ_{233}	2.7×10^{-5}	1.0×10^{-4}	2.8×10^{-4}

Table 5.2: Upper bounds on the trilinear couplings λ_{ijk}, at M_X for different values of A_0 (first row). The othercMSSM parameters are those of SPS1a [188]. Bounds arising from the absence of tachyons are marked by $()^t$.

GeV. It was claimed that neutrino masses put an upper bound of $\mathcal{O}(10^{-3} - 10^{-6})$ on most of the trilinear couplings in Eq. (2.3). However, the possibility of obtaining much weaker bounds on the coupling $\mathbf{\Lambda}$ in the region of the tree–level neutrino mass minimum was not exploited. We present here an update of these results by using Eq. (3.30) and including the dominant 1–loop contributions. We then explore the cMSSM parameter dependence of the bounds.

In Tab. 5.1 and Tab. 5.2 ($\mathbf{\Lambda} \in \{\lambda'_{ijk}\}$ and $\mathbf{\Lambda} \in \{\lambda_{ijk}\}$, respectively), we compare the previous results with bounds (at $M_{\rm GUT}$) that we obtain for identical B_3 cMSSM parameter points, where only the choice of A_0 differs. In order to obtain corresponding bounds at $M_{\rm EW}$ one needs to take into account the RGE evolution of the couplings. Quantitatively this results in multiplying the bounds in Tab. 5.1 (Tab. 5.2) by roughly a factor of 3.5 (1.5), *cf.* Ref. [51, 82, 150, 190, 204].

In addition to $A_0 = -100$ GeV (SPS1a), we choose two parameter points which lie $\Delta A_0 \approx 10$ GeV and $\Delta A_0 \approx 60-70$ GeV, away from the neutrino mass minimum. In Tab. 5.1 ($\mathbf{\Lambda} \in \{\lambda'_{ijk}\}$), we choose $A_0 = 500$ GeV (column 3 and 6) and $A_0 = 550$ GeV (column 4 and 7). In Tab. 5.2 ($\mathbf{\Lambda} \in \{\lambda_{ijk}\}$), we choose $A_0 = 200$ GeV (column 3) and $A_0 = 120$ GeV (column 4). This enables us to examine the dependence of the bounds on A_0 around the tree–level mass minimum.

Note that at SPS1a and when varying A_0, the neutrino mass minimum for $\lambda'_{ijk} \neq 0$ lies at $A_0 = 563$ GeV. This value is mostly independent of the choice of the indices i, j, k. This is clear because the condition for the minimum to occur, $A_0 \approx 2M_{1/2}$, does not depend on i, j, k, *cf.* § 4. Similarly, for $\lambda_{ijk}|_{\rm GUT} \neq 0$ the minimum is expected at $A_0 \approx M_{1/2}/2$. For the SPS1a parameters we thus obtain $A_0 \approx 127$ GeV[3].

We first concentrate on Tab. 5.1. Comparing the columns for $A_0 = -100$ GeV and then for $A_0 = 500$ GeV, *i.e.* approaching the minimum up to $\Delta A_0 = 63$ GeV, the bounds from too large neutrino masses are weakened by a factor of 13–15. When we go even closer, *i.e.* $A_0 = 550$ GeV and $\Delta A_0 = 13$ GeV, the bounds are weakened by a factor of 40–64 compared to $A_0 = -100$ GeV. As we discuss below, in the case of up-mixing, some couplings in Tab. 5.1 (column 2-4) can not be restricted at all by too large neutrino masses. In this case we show the bounds at $M_{\rm GUT}$ [marked by $()^t$], that one obtains from the absence of tachyons; see also Ref. [51].

[3] This value is smaller than would be expected by estimating $A_0 \approx M_{1/2}/2 = 250$ GeV, because we are considering a parameter point with relatively low $\tan\beta$ ($\tan\beta = 10$ for SPS1a). As discussed in § 4.3, this leads to a shift of the tree–level neutrino mass minimum towards lower values of A_0, *cf.* Fig. 4.4 (iii).

We differentiate in Tab. 5.1 between up– and down–type quark mixing, *cf.* § 2.2. Different quark mixing has important consequences for the bounds on the couplings λ'_{ijk} if $j \neq k$. As is clear from § (4.2), the tree–level neutrino mass is generated proportional to $\lambda'_{ijk} \times (Y_D)_{jk}$. Thus, no tree–level mass is generated at this level when we consider $j \neq k$ and up–type mixing (which implies a diagonal Y_D). But, an additional λ'_{ikk} coupling will be generated via RGE running at lower scales, *cf.* Ref. [51]. This coupling will still generate a tree–level neutrino mass, which is however suppressed by the additional one–loop effect [4].

This effect can be seen in Tab. 5.1, if we compare for example the upper bounds on λ'_{223} and λ'_{233} for up– and down–type quark mixing. The ratio between these bounds is roughly 200 in the case of up–type mixing whereas there is only one order of magnitude difference for down–type mixing.

In the latter case, the ratio between the λ'_{223} and λ'_{233} bounds originates mainly from the ratio

$$\frac{(Y_D)_{23}}{(Y_D)_{33}} = \frac{(\mathbf{V}_{CKM})_{23}}{(\mathbf{V}_{CKM})_{33}}\,, \tag{5.6}$$

since the tree–level mass is generated via $\lambda'_{223} \times (Y_D)_{23}$ and $\lambda'_{233} \times (Y_D)_{33}$, respectively.

To conclude, the bounds from the generation of neutrino masses (at least in the case of down–type mixing) are usually the strongest bounds on the couplings λ'_{ijk} at $M_{\rm GUT}$. As considered in Ref. [51], they range from $\mathcal{O}(10^{-4})$ to $\mathcal{O}(10^{-6})$ for the parameter point SPS1a (column 5 in Tab. 5.1). However, there is a large window around the tree-level neutrino mass minimum, where bounds may be obtained that are between one and two orders of magnitude weaker than those in Ref. [51]. Around the minimum, the couplings are only bounded from above by $\mathcal{O}(10^{-2})$ to $\mathcal{O}(10^{-4})$ (*cf.* column 7 in Tab. 5.1). Thus, other low energy bounds become competitive [44, 190, 205–209].

We now discuss in Tab. 5.2 the case of a non-vanishing coupling λ_{ijk} at $M_{\rm GUT}$. Contrary to Tab. 5.1, in the case considered in Tab. 5.2 the quark mixing assumption does not affect the bounds since λ_{ijk} couples only to lepton superfields. Due to the antisymmetry $\lambda_{ijk} = -\lambda_{jik}$ there are only 9 independent couplings.

We observe in Tab. 5.2 that if $i \neq j \neq k \neq i$ there are no bounds from too large neutrino masses. The only bound we obtain stems from the absence of tachyons. This is because we assume a diagonal lepton Yukawa matrix Y_E as stated in § 2.2 and therefore, only couplings of the form λ_{ikk} can generate a neutrino mass [5].

For these couplings, the bounds at $M_{\rm GUT}$ for $A_0 = -100$ GeV (column 2) range from 1.1×10^{-1} (λ_{211} and λ_{311}) to 2.7×10^{-5} (λ_{133} and λ_{233}). If we approach the tree–level mass minimum, *i.e.* going from column 2 to column 4 with $A_0 = 120$ GeV, the bound is weaker than the tachyon bound (λ_{211} and λ_{311}) or it is weakened to 2.8×10^{-4} (λ_{133} and λ_{233}). The bounds from neutrino masses are thus decreased by roughly a factor of 10.

Comparing the bounds on λ_{ikk} at $M_{\rm GUT}$, one can see nicely how the choice of k influences the strength of the bound. The bounds resemble the hierarchy between the lepton Yukawa couplings $(Y_E)_{kk}$ analogously to Eq. (5.6). Therefore, the bounds are strongest for $k = 3$.

In contrast to Tab. 5.1, the bounds are only reduced by one order of magnitude when we approach the tree-level mass minimum. This is because the loop contributions play an important role for the bounds in Tab. 5.2, as we discuss in the following section.

[4] Note that also the loop contributions are strongly suppressed, because the $\lambda'\lambda'$–loops are proportional to $\lambda'_{ijk} \times \lambda'_{ikj}$, Eq. (3.10), and the neutral scalar loops are aligned with the tree-level mass, *cf.* § 4.5.

[5] This would change drastically if the Y_E were strongly mixed [51].

5.3.2 Influence of Loop Contributions

We now shortly discuss the influence of the neutrino mass loop contributions on the bounds. Typically, one expects that the closer we approach the tree–level neutrino mass minimum the more important the loop contributions become. This is because the loops are not aligned to the tree–level mass, *cf.* § 4.5.

However, in the case of the neutral scalar loops there is still partial alignment, because both the tree–level mass minimum and the minima of the neutral scalar loops crucially depend on the vanishing of the bilinear LNV parameter $\tilde{D}_i$, *cf.* § 4.5. Therefore, it is the $\lambda'\lambda'$–loops and $\lambda\lambda$–loops, § 3.2, that are relevant whenever the loop contributions become dominant over the tree–level contributions.

We now give a few examples. For $\mathbf{\Lambda} \in \{\lambda_{ijk}\}$, Tab. 5.2, the loop contributions dominate over the tree–level mass in a range of $\Delta A_0 \approx \pm 50$ GeV around the tree–level mass minimum at $A_0 = 127$ GeV. Therefore, the bounds in this region are much more restrictive (*i.e.* the value of the bounds *decreases*) when taking into account the loop contributions. For example,

$$\frac{\lambda_{233}^{\rm tot}}{\lambda_{233}^{\rm tree}} \approx 0.3\,, \tag{5.7}$$

for $A_0 = 120$ GeV; column 4 in Tab. 5.2. Here, $\lambda_{233}^{\rm tot}$ is the bound on λ_{233} at M_X if we take into account both tree–level and loop–contributions to the neutrino mass. In contrast, $\lambda_{233}^{\rm tree}$ would be the bound if we only employ the tree-level mass.

Further away from the minimum, the influence of the loop contributions is weaker. The bounds are strengthened by approximately 5% for $A_0 = 200$ GeV (column 3 of Tab. 5.2) and $< 1\%$ for $A_0 = -100$ GeV (column 2 of Tab. 5.2).

The loop contributions are less important for the bounds in Tab. 5.1, *i.e.* $\mathbf{\Lambda} \in \{\lambda'_{ijk}\}$. For example, even near the tree-level mass minimum (column 4 and 7 with $A_0 = 550$ GeV), the bounds become only stronger by up to 20% if we take the loop induced neutrino masses in addition to the tree–level mass into account.

5.3.3 Dependence of Bounds on B_3 cMSSM Parameters

In this section, we discuss the dependence of the bounds on $\Lambda \in \{\lambda_{ijk}, \lambda'_{ijk}\}$ at $M_{\rm GUT}$ on the B_3 cMSSM parameters. For that purpose we perform two-dimensional parameter scans around the benchmark scenarios, Point I and Point II, of § 4.1.1. For the calculation of the bounds all contributions to the neutrino mass considered in § 3 are included. We will focus here on the couplings λ'_{233} and λ_{233}, because these couplings have the strongest constraints from neutrino masses, *cf.* Tab. 5.1 and Tab. 5.2.

We have analyzed in § 4 how the neutrino mass changes with the cMSSM parameters. Due to its approximate proportionality to $\mathbf{\Lambda}^2$, *cf.* Eq. (5.5), the analysis in § 4 is directly transferable to the cMSSM dependence of bounds on the LNV trilinear couplings. Therefore, the parameter scans presented in this section, *i.e.* Fig. 5.1 and Fig. 5.2, resemble closely those in Fig. 4.4, § 4.

We show in Fig. 5.1 [Fig. 5.2] how the bounds on λ'_{233} [λ_{233}] at $M_{\rm GUT}$ vary with cMSSM parameters. We present in Figs. 5.1 (i)–(iii) [Figs. 5.2 (i)–(iii) the A_0–$M_{1/2}$, A_0–tanβ, and A_0–M_0 planes, respectively. The bounds are shown on a logarithmic scale. The blackened out regions designate areas of parameter space which are rejected due to tachyons in the model or violation of the LEP2 bound on the lightest Higgs mass, *cf.* Eq. (5.1). Furthermore, we include contour lines of the 2σ window for the SUSY contribution to the anomalous magnetic moment

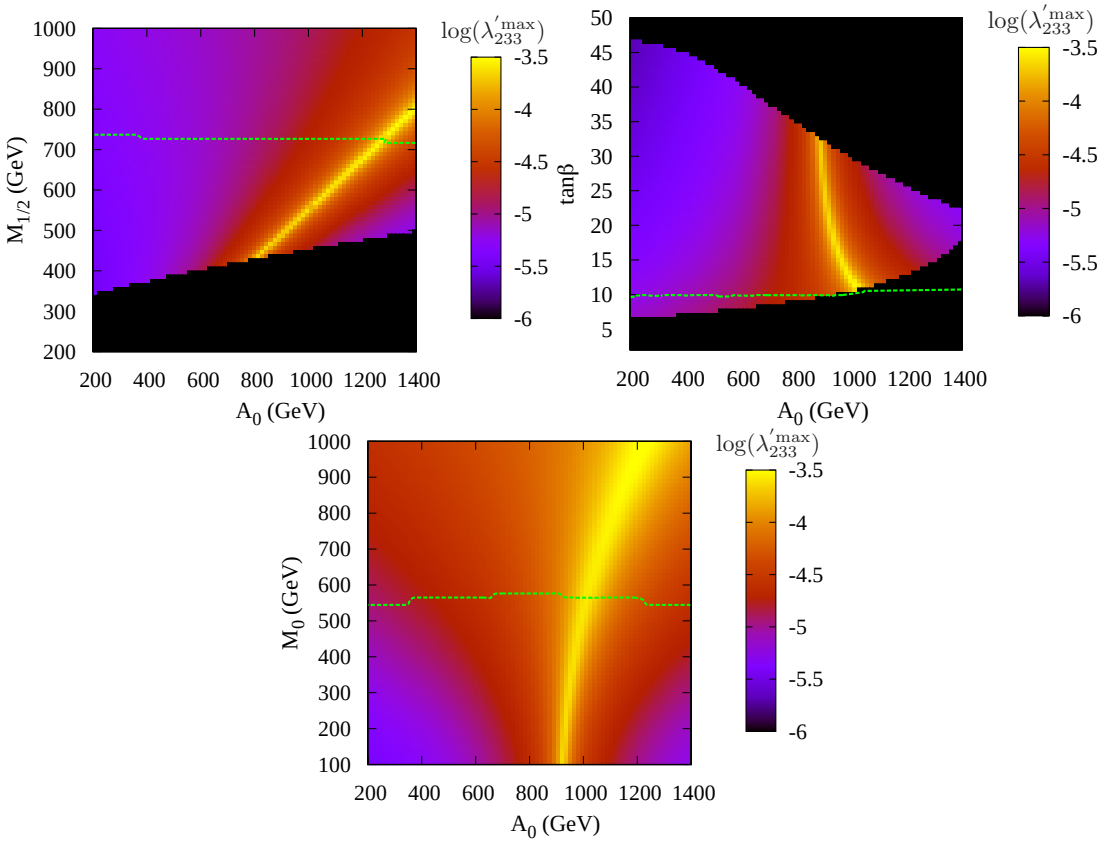

Figure 5.1: Upper bounds on λ'_{233} at M_X from the cosmological bound on the sum of neutrino masses, Eq. (3.30), as a function of cMSSM parameters. In plot (i) [top, left], we depict the $A_0 - M_{1/2}$ plane, in plot (ii) [top, right], we depict the $A_0 - \tan\beta$ plane, in plot (iii) [bottom, left], we depict the $A_0 - M_0$ plane. The parameter space below [above] the green line in plot (i), (i) [plot (iii)] is disfavored by $\delta_\mu^{\rm SUSY}$; see Eq. (5.4). The parameter scans are centered around benchmark Point I, *cf.* § 4.1.1. The blackened-out region denotes parameter points where tachyons occur or where the LEP2 Higgs bound is violated.

of the muon, Eq. (5.4). Imposing Eq. (5.4) disfavors the parameter space below [above] the green contour line in Figs. 5.1 (i) and (ii), 5.2 (i) and (ii) [Fig. 5.1 (iii) and Fig. 5.2 (iii)].

We observe in Fig. 5.1 that the strictest bounds on λ'_{233} from too large neutrino masses are of $\mathcal{O}(10^{-6})$. However, there are sizable regions of parameter space where the bounds are considerably weakened. For example, in the A_0–$M_{1/2}$ plane, Fig. 5.1 (i), the bounds are of $\mathcal{O}(10^{-6})$ only in approximately half of the parameter space whereas in the other half, the bounds are $\mathcal{O}(10^{-5})$ or weaker. In roughly 10% of the allowed region in Fig. 5.1, the bounds even lie at or above $\mathcal{O}(10^{-4})$! In this region, the loop contributions to the heaviest neutrino mass are essential for determining the bounds since the corresponding tree–level neutrino mass vanishes, *cf.* also the discussion in § 5.3.2.

We can see in Fig. 5.2 a similar behavior for the parameter dependence of the bounds on λ_{233}. Here, the strongest bounds are now of $\mathcal{O}(10^{-5})$. However, for example in the A_0–M_0 plane, Fig. 5.2 (iii), the bounds are as strong as $\mathcal{O}(10^{-5})$ in only about 25% of the parameter plane. The remaining 75% have bounds of $\mathcal{O}(10^{-4})$ (50%) or even $\mathcal{O}(10^{-3})$ (25%)!

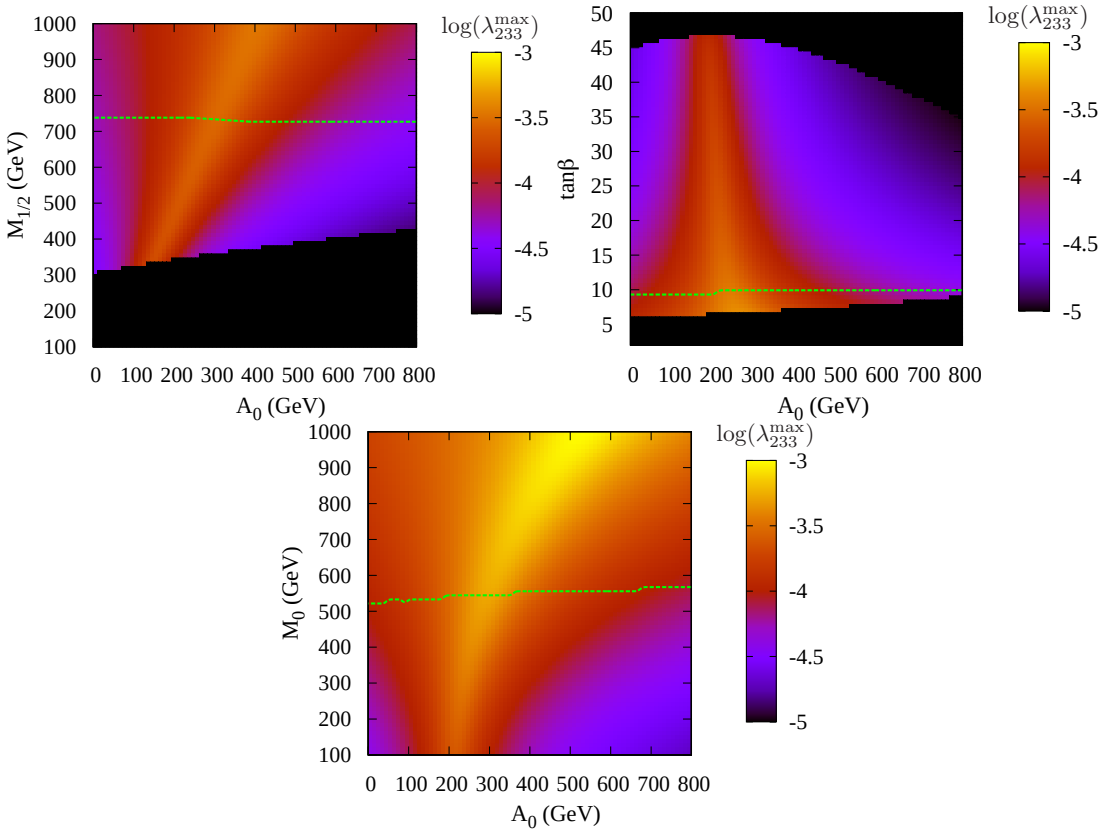

Figure 5.2: Same as Fig. 5.1, but for λ_{233} at M_X and for the benchmark scenario Point II, *cf.* § 4.1.1.

Up to now, we have analyzed how the bounds on the trilinear LNV couplings λ'_{233} and λ_{233} vary with the cMSSM parameters. However, from the analysis in § 5.3.1, we can easily deduce how most of these bounds change for different couplings λ'_{ijk} and λ_{ijk}, *i.e* for different indices i, j, k. For λ'_{ijk} the index i does not significantly influence the bound, because the employed Yukawa coupling, $(Y_D)_{jk}$, via which the tree–level mass is generated, does not depend on i. But, the situation is totally different when we change the indices j, k. In general, for λ'_{ijk} (and down–mixing) the bounds will display the hierarchy of the down–type Yukawa couplings. Therefore, bounds for couplings λ'_{i11} are about three orders of magnitude weaker than bounds for the couplings λ'_{i33} as long as the other B_3 cMSSM parameter are the same. We also observe a similar behavior for λ'_{ijk} with up–mixing and for λ_{ijk} [using $(Y_E)_{jk}$ instead of $(Y_D)_{jk}$], if $j = k$; *cf.* the discussion in § 5.3.1.

To conclude, one can use the Yukawa matrix Y_D (Y_E) to easily translate the bounds in Fig. 5.1 (Fig. 5.2) to bounds on couplings other than λ'_{233} (λ_{233}).

Chapter 6

Phenologically Viable Neutrino Masses and Mixings in the B_3 cMSSM

In this chapter we discuss how the experimental neutrino oscillation data can be realized in the framework of the B_3 cMSSM. We show how to obtain phenomenologically viable solutions, which are compatible with the recent experimental results in § 6.2. In § 6.3, we present and discuss results for the normal hierarchy, inverted hierarchy and degenerate cases which illustrate the possible size and structure of the LNV couplings. Our aim is to obtain the correct masses and mixing angles with a small number of LNV parameters. We furthermore wish to analyze the general structures that lead to potential solutions, since it is not possible to systematically list *all* solutions. By introducing parameters coupled to different generations, we attempt to understand how different trilinear LNV terms interplay with each other to generate the observed mass pattern. We work with a new `SOFTSUSY`-3.2 version, where we implement full 1–loop neutrino masses as described in § 6.1.2. Finally, we shortly discuss some phenomenological implications at the LHC in § 6.4.

6.1 Preliminaries

6.1.1 Choice of cMSSM benchmark point

As has been noted in § 4, there are preferred regions of B_3 cMSSM parameter space in which the neutrino oscillation data can be more easily accommodated. This is illustrated once more in Fig. 6.1 for one single LNV coupling. However, now we also include the full 1–loop contributions to neutrino masses as calculated with our newly published `SOFTSUSY`-3.2 in the figure. Recall that there is only one tree–level neutrino mass, the second (and third) neutrino mass scale is set by the 1–loop contributions[1]. From Fig. 6.1 (a) [(b)] we see that for a given λ [λ'], in the parameter region $100 \lesssim A_0/\text{GeV} \lesssim 300$ [$870 \lesssim A_0/\text{GeV} \lesssim 930$], the tree–level neutrino mass is sufficiently suppressed relative to the 1–loop neutrino mass to match the mild neutrino mass hierarchy required by the data of maximally 5.7, *cf.* Eqs. (3.31), (3.32). This region of parameter space is determined by the fact that the tree–level neutrino mass (solid cyan line in Fig. 6.1) has a zero in A_0 parameter space due to RGE effects. This region exists for every B_3 cMSSM parameter point, cf. § 4, provided that

$$A_0^{(\lambda')} \approx 2\, M_{1/2} \tag{6.1}$$

$$A_0^{(\lambda)} \approx \frac{M_{1/2}}{2} \tag{6.2}$$

[1] Note that at least two lepton flavors need to be violated in order to generate more than one neutrino mass. Therefore, one single LNV coupling will not be sufficient. For the discussion here, however, the simplifying picture of one LNV coupling is sufficient, since the arguments remain valid for more than one LNV coupling.

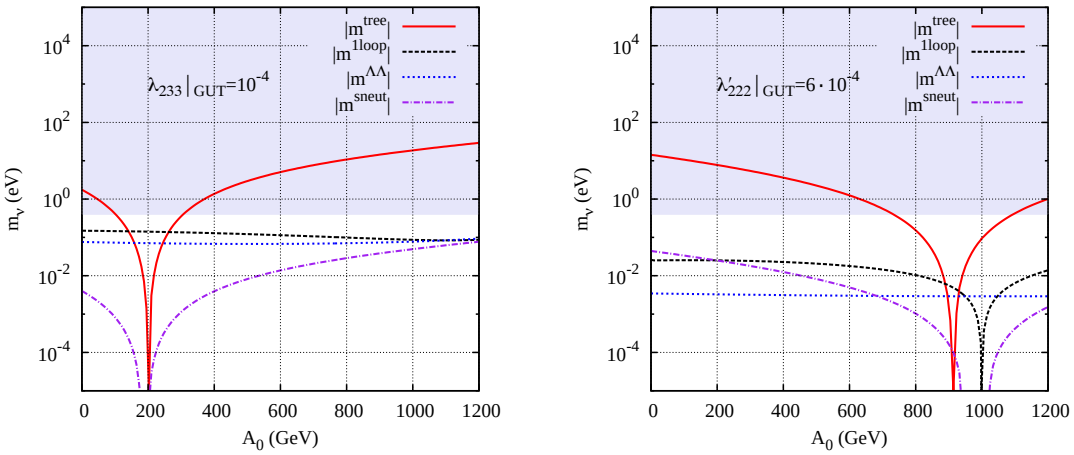

Figure 6.1: A_0 dependence of the different contributions to the neutrino mass at the electroweak symmetry breaking scale for our benchmark point BP, with (top) $\lambda_{233}|_{\rm GUT} = 10^{-4}$, (bottom) $\lambda'_{222}|_{\rm GUT} = 6\cdot10^{-4}$. Note that only the absolute values of the contributions to the neutrino mass are displayed. The equations for $m_\nu^{\rm tree}$ and $m_\nu^{\mathbf{\Lambda\Lambda}}$ are given in Eqs. (3.4) and (3.10), respectively. $m_\nu^{\rm 1loop}$ represents the full 1–loop corrections to the neutrino mass, $m_\nu^{\rm sneut}$ represents the neutral scalar loops. The grey–shaded area is excluded by the cosmological bound.

for non–zero LNV couplings λ'_{ijk} or λ_{ijk}, respectively. Note that the position of the minimum is approximately the same for all indices $i, j, k = 1, 2, 3$. Henceforth we denote the A_0 minimum with respect to λ and λ' by $A_0^{(\lambda)}$ and $A_0^{(\lambda')}$ respectively. In this paper we focus on this region; more details are given in § 6.3.1. Therefore we have only 4 R_p–conserving parameters left, namely $M_{1/2}$, M_0, $\tan\beta$ and $\mathrm{sgn}(\mu)$.

For easy comparison with § 4, we use the same benchmark point (BP):

$$\begin{aligned} M_{1/2} &= 500 \text{ GeV} \\ M_0 &= 100 \text{ GeV} \\ \tan\beta &= 20 \\ \mathrm{sgn}(\mu) &= +1\,, \end{aligned} \tag{6.3}$$

for which we checked various low–energy bounds, cf. § 4.1.1. The spectrum in the R_p conserving limit is displayed in Table 4.1. The squark masses are of order $\mathcal{O}(1\,\text{TeV})$, whereas the slepton masses are around 200–300 GeV. The lightest supersymmetric particle (LSP) is a stau. However the presence of LNV couplings will render the LSP unstable, making cosmological constraints on the nature of the LSP not applicable [101, 150, 210, 211].

It should also be pointed out that it is not possible to suppress tree–level contributions for both λ and λ' simultaneously for a universal A_0 parameter [134], as the two minima do not coincide in the A_0 parameter space, *cf.* Eqs. (6.1), (6.2). Therefore scenarios such as those discussed in Ref. [212], where there is no tree–level neutrino mass at all, are only possible in the B_3 cMSSM if there is only one type of LNV coupling, either λ or λ'.

It is also interesting to note that in the case of λ couplings [Fig. 6.1 (a)], the full 1–loop contributions are well approximated by the $\Lambda\Lambda$ loops, whereas in the case of λ' couplings [Fig. 6.1

(b)], the approximation is less satisfactory, and further 1–loop contributions such as neutral scalar–neutralino loops also play an important role in parts of the parameter space. However, around the $A_0^{(\lambda')}$ minimum, the $\Lambda\Lambda$ loops still give a good order of magnitude estimate.

Note that viable neutrino masses might also be obtained away from the A_0 minimum region by using only off–diagonal LNV couplings, since the tree–level contribution is dominantly generated through diagonal LNV couplings. Thus, scenarios involving only off–diagonal couplings (and up–mixing if using λ' couplings) also lead to a suppression of the tree–level contribution and could thus potentially reduce the dependence on the A_0 minimum.

For concreteness, we work in the flavor basis with up–type mixing, unless stated otherwise. In this basis, the λ'_{ijk} couplings which are off–diagonal in j, k do not contribute significantly to $\mathcal{M}_\nu^{\text{eff}}$ at tree–level, but could be used as parameters to adjust loop level contributions when fitting the data. Note that because Y_E is always diagonal in our model, λ_{ijk} couplings for $i, j \neq k$ can be utilized in a similar fashion. The changes that appear for down–type mixing is discussed in § 6.3.4.

6.1.2 Numerical Tools & the Inclusion of Tadpoles in SOFTSUSY

Our numerical simulation is performed using the new SOFTSUSY-3.2. We refer interested readers to the SOFTSUSY manual [83, 142] for the detailed procedure of obtaining the B_3 MSSM mass spectrum. We use the program package MINUIT2 and a Markov chain Monte Carlo method (Metropolis–Hastings algorithm) for fitting the LNV couplings Λ_{ijk} to the neutrino data as well as for obtaining a good value for A_0 within the minimum region.

We now comment briefly on the additional features we include in SOFTSUSY. We implement the full 1–loop contributions to the neutrino–neutralino sector, cf. the new $\not{R}_p$ SOFTSUSY manual [83]. Our calculation follows closely that of Refs. [42, 43]. However we go beyond their approximations by including also the 1–loop LNV corrections to the sneutrino and Higgs vacuum expectation values (VEVs) v_i, v_d and v_u[2]. This is done by calculating the tadpoles $\frac{\partial \Delta V}{\partial v_A}$ $(A = i, d, u)$ where ΔV denotes the 1–loop contributions to the neutral scalar potential. These $\not{R}_p$ tadpole corrections are included in the SOFTSUSY iteration procedure which minimizes the 5–dimensional EW symmetry breaking neutral scalar potential.

The explicit 1–loop corrections to the 7x7 neutralino–neutrino mass matrix have already been implemented by Ref. [43] in a private add–on code to SOFTSUSY. We cross–check and integrate this code together with the improved REWSB including full $\not{R}_p$ 1–loop contributions into the new SOFTSUSY-3.2 version. We present the relevant parts of the code where the explicit formula for the tadpoles are visible in the appendix (§ B).

The effective 3×3 neutrino mass matrix $\mathcal{M}_\nu^{\text{eff}}$ and the effective neutrino mixing matrix U_ν are calculated at the EWSB scale given an input set of LNV parameters at the unification scale. Note that within SOFTSUSY, the condition that the charged lepton mixing matrix is diagonal is imposed at the electroweak scale. Thus, $U_{\text{PMNS}} = U_\nu$, cf. § 3.4.

6.2 Choice of LNV parameters

In this section, we choose specific representative scenarios for the LNV sector which will be used for the numerical fit of the neutrino masses and mixings in § 6.3. First, as a motivation to and a guide line in finding models, we discuss the general neutrino mass matrix in the TBM

[2] Tree–level results and R_p 1–loop contributions are already included in SOFTSUSY

approximation. As we have seen in § 3.5, this is a very good approximation to the data. Later, when performing our numerical fits, we use the experimental values listed in Eqs. (3.23)–(3.25). In § 6.2.1 we limit the discussion to "diagonal LNV parameters" λ_{ijj} and λ'_{ijj}. In § 6.2.2 we discuss the more general case which includes "non–diagonal couplings", *i.e.* λ_{ijk} and λ'_{ijk} with $j \neq k$.

Since any LNV coupling λ_{ijk}, λ'_{ijk} could potentially contribute to the effective neutrino mass matrix, we expect a large number of possible solutions to Eqs. (3.23)–(3.27). It is well beyond the scope of this paper to attempt to determine them completely. Instead we wish to classify the types of solutions with a potentially minimal set of parameters. We thus make a series of simplifying assumptions, restricting ourselves to a subset of couplings. We will suggest 5 different scenarios (denoted **S1** to **S5**), each making use of LNV coupling combinations from different types (λ and λ') and generations, which we will make explicit as we proceed.

In order to obtain the neutrino mass matrix, we solve the equation

$$U_{TBM}^{\dagger} M_{\nu}^{TBM} U_{TBM} = \mathrm{diag}[m_{\nu\alpha}]\,, \tag{6.4}$$

for M_{ν}^{TBM}. Here the neutrino masses $m_{\nu\alpha} (\alpha = 1,2,3)$ fit the mass–squared differences and U_{TBM} is given in Eq. (3.34).

It is natural to split up the resulting neutrino mass matrix into three separate contributions, each of which is proportional to one neutrino mass:

$$\begin{aligned} M_{\nu}^{TBM} &\equiv M_1 + M_2 + M_3 \\ &= \frac{m_{\nu 1}}{3}\begin{pmatrix} 2 & -1 & 1 \\ -1 & 1/2 & -1/2 \\ 1 & -1/2 & 1/2 \end{pmatrix} + \frac{m_{\nu 2}}{3}\begin{pmatrix} 1 & 1 & -1 \\ 1 & 1 & -1 \\ -1 & -1 & 1 \end{pmatrix} + \frac{m_{\nu 3}}{2}\begin{pmatrix} 0 & 0 & 0 \\ 0 & 1 & 1 \\ 0 & 1 & 1 \end{pmatrix} \qquad (6.5) \\ &= \frac{1}{6}\begin{pmatrix} 4m_{\nu 1} + 2m_{\nu 2} & 2\alpha_{21} & -2\alpha_{21} \\ 2\alpha_{21} & m_{\nu 1} + 2m_{\nu 2} + 3m_{\nu 3} & -2\alpha_{21} + 3\alpha_{31} \\ -2\alpha_{21} & -2\alpha_{21} + 3\alpha_{31} & m_{\nu 1} + 2m_{\nu 2} + 3m_{\nu 3} \end{pmatrix}, \qquad (6.6) \end{aligned}$$

where the off–diagonal entries are written in terms of

$$\alpha_{ij} \equiv \frac{\Delta m_{ij}^2}{m_{\nu i} + m_{\nu j}}\,. \tag{6.7}$$

We observe that all three contributions M_α are of the symmetric form

$$(M_\alpha)_{ij} \propto c_i^{(\alpha)} c_j^{(\alpha)}\,. \tag{6.8}$$

If U_{TBM} is orthogonal, this always follows from Eq. (6.4), independent of its exact form. The supersymmetric tree–level neutrino mass matrix displays an identical structure if one assigns

$$c_i^{(tree)} \sim \lambda'_{ijk} (Y_D)_{jk}\,, \tag{6.9}$$

or

$$c_i^{(tree)} \sim \lambda_{ijk} (Y_E)_{jk}\,. \tag{6.10}$$

This follows from a first–order approximation of Eq. (3.4), making use of RGE considerations such as Eq. (2.17)[3]. The dominant 1–loop level contribution to the neutrino mass matrix does not strictly display the same structure, as can be seen from Eq. (3.10). However, for diagonal couplings ($j = k$), one can make a similar assignment as in the tree–level case,

$$c_j^{(loop)} \sim \lambda'_{jkk}(m_d)_k \tag{6.11}$$

or

$$c_j^{(loop)} \sim \lambda_{jkk}(m_\ell)_k \,, \tag{6.12}$$

cf. Eq. (3.10). We discuss the generalisation to non–diagonal couplings in § 6.2.2.

For simplicity, we mainly focus on solutions which directly reflect the form of Eq. (6.6) (**S1** to **S4**)[4], namely

$$\begin{aligned} c_1^{(1)} = -2c_2^{(1)} = 2c_3^{(1)} &= \sqrt{\frac{2m_{\nu_1}}{3}}, \\ c_1^{(2)} = c_2^{(2)} = -c_3^{(2)} &= \sqrt{\frac{m_{\nu 2}}{3}}, \\ c_1^{(3)} = 0, \quad c_2^{(3)} = c_3^{(3)} &= \sqrt{\frac{m_{\nu 3}}{2}} \,. \end{aligned} \tag{6.13}$$

This can minimally be achieved by allowing for exactly one LNV parameter for each coefficient $c_i^{(\alpha)}$[5]. The three matrices in Eq. (6.6) can then be described by 8 coefficients

$$\{c_{1,2,3}^{(1)},\, c_{1,2,3}^{(2)},\, c_{2,3}^{(3)}\} \,, \tag{6.14}$$

where we have made use of the fact that $c_1^{(3)} = 0$ in both the TBM case *and the best–fit case*, under the assumption that $\theta_{13} = 0$. Since we need only two mass scales to describe the neutrino data, we shall assume that the lightest neutrino is massless in the NH and IH cases. Depending on the scenario (NH, IH, DEG), we thus need either five, six or eight non–zero coefficients $c_i^{(\alpha)}$.

To illustrate possible alternatives, we show how "non–diagonal" couplings might contribute to neutrino masses in another example (**S5**).

While we have presented the TBM approximation to display the general coupling structure we are aiming for, in the numerical analysis below we solve Eq. (6.4) not in the TBM approximation but instead for the best–fit neutrino data given in Eqs. (3.23)–(3.27). This results in slightly

[3] Note that in Eq. (6.10), $j = k$ to excellent approximation due to our assumption that the charged lepton mass matrix is diagonal at the electroweak scale, *cf.* § 2.2. Thus, Y_E is near-diagonal up to small corrections.

[4] It is possible to obtain other solutions to Eq. (6.4) by forming linear combinations of the M_α's given in Eq. (6.6). As an example we here present the NH solution with $c_3^{(3)} = 0$ used in **S4** NH:

$$\begin{aligned} c_1^{(2)} &= \sqrt{\frac{m_{\nu 2}}{3} + \frac{m_{\nu 3}}{2}}, \\ c_2^{(2)} &= \frac{\frac{m_{\nu 2}}{3} + \frac{m_{\nu 3}}{2}}{\frac{m_{\nu 2}}{3}}, \quad c_3^{(2)} = \frac{\frac{m_{\nu 2}}{3} + \frac{m_{\nu 3}}{2}}{\frac{m_{\nu 3}}{2} - \frac{m_{\nu 2}}{3}}, \\ c_1^{(3)} &= \frac{c_2^{(3)}}{2} = \sqrt{\frac{\frac{m_{\nu 2}}{3}\frac{m_{\nu 3}}{2}}{\frac{m_{\nu 2}}{3} + \frac{m_{\nu 3}}{2}}}, \quad c_3^{(3)} = 0. \end{aligned}$$

[5] In the "off-diagonal" scenarios, some deviation from this statement is necessary, as will be explained in § 6.2.2.

different values for $c_j^{(i)}$. However, the deviation from the TBM case is less than 7% for each $c_j^{(i)}$.

6.2.1 Diagonal LNV scenarios

Scenarios involving only diagonal LNV couplings Λ_{ijk} with $j = k$ are the most straightforward to consider. With these we can generate all neutrino mass matrix entries with a minimal set of LNV couplings. The non–diagonal case requires additional couplings, as we discuss below, *cf.* § 6.2.2. We first discuss normal hierarchy and inverted hierarchy scenarios and then the degenerate case.

- **Normal Hierarchy:**

  Since the first part of the neutrino mass matrix, M_1, is zero for NH, we need only five LNV couplings to generate $M_\nu \equiv M_2 + M_3$. In order to keep these two contributions M_2, M_3 (corresponding to the two non–zero neutrino mass eigenvalues) as independent as possible, we use λ couplings for one and λ' couplings for the other matrix. If we now choose A_0 such that it lies in the minimum region for either λ or λ' (we denote this by $A_0^{(\lambda)}$ and $A_0^{(\lambda')}$ respectively), *cf.* § 6.1.1, we can generate one neutrino mass eigenvalue at tree–level and one at loop–level in a nearly independent fashion. This implies that the mass scales can be easily adjusted. We focus on the case $A_0^{(\lambda')} \sim 2\, M_{1/2}$, where the contribution from λ' couplings to the tree–level mass matrix is suppressed, because as we will show, for the IH scenarios only this choice of A_0 is possible. We briefly mention changes for the case $A_0^{(\lambda)} \sim M_{1/2}/2$ in NH scenarios during the discussion in § IV D.

  Motivated by the observation that the first row/column of M_3 is zero (*i.e.* $c_1^{(3)} = 0$), and also $\lambda_{111} = 0$ due to antisymmetry, we fit

  $$(M_3)_{ij} \sim \lambda_{i11}\lambda_{j11}\ , \tag{6.15}$$

  (*i.e.* $c_i^{(3)} \sim \lambda_{i11}$). We then automatically obtain the structure of M_3. Because we have chosen $A_0^{(\lambda')} \sim 2M_{1/2}$, this matrix is dominated by the tree–level contribution. In order to generate M_2 independently of M_3 (at 1–loop level), we choose

  $$(M_2)_{ij} \sim \lambda'_{ikk}\lambda'_{jkk}\ , \tag{6.16}$$

  where k is fixed. We present all three cases $k = 1, 2, 3$ in Table 6.1, denoted **S1**, **S2** and **S3**, respectively.

  Additionally, we present one further scenario where we depart from the correspondence $c_i^{(\alpha)} \sim \Lambda_i$. The motivation for this is to consider a neutrino scenario where third generation couplings are dominant, in analogy to the hierarchy of the SM Yukawa couplings. This scenario is particularly interesting because it represents a lower limit on the required size of the LNV couplings under the assumption that no further mechanism exists to contribute to the neutrino masses. We discuss this aspect in more detail in section 6.3.2. In order to be able to fit the matrices M_2, M_3 only with third generation couplings λ_{i33} and λ'_{i33}, one of those matrices needs to fulfill $(M_i)_{3k} = 0$ due to the antisymmetry of λ in the first two indices. To achieve this, we build a suitable superposition of the matrices M_2 and M_3. We denote the new coefficients by $\tilde{c}_i^{(\alpha)}$ in **S4** of Table 6.1.

- **Inverse Hierarchy:**

  As mentioned in the case of Normal Hierarchy, λ_{ijj} couplings will always lead to one row/column of zeros in the generated neutrino mass matrix. Since in the case of Inverse Hierarchy, the two non–zero matrices M_1 and M_2 are both non–zero in all entries, we take this as motivation to fit M_1 and M_2 with λ' couplings only (however, for completeness we also present one scenario with both λ and λ' couplings, *cf.* next paragraph). With only λ' couplings present, we set the value of A_0 to $A_0^{(\lambda')} \sim 2\, M_{1/2}$, such that all tree–level contributions are suppressed, and the two mass scales are both generated at loop level. Otherwise the neutrino mass hierarchy would be much larger than experimentally observed, *cf.* § 6.1.1. We display the three possibilities arising from

$$(M_1)_{ij} \sim \lambda'_{ikk}\lambda'_{jkk}\,, \tag{6.17}$$
$$(M_2)_{ij} \sim \lambda'_{ill}\lambda'_{jll}\,, \tag{6.18}$$

  where $l < k$[6] in Table 6.1. These models are labelled (IH) **S1**, **S2** and **S3**.

  If we choose $\lambda_{i\ell\ell}$ couplings instead of $\lambda'_{i\ell\ell}$ in Eq. (6.18), this would again generate a (unwanted) row/column of zeros in M_2. Therefore, in this case we need to combine, for example, λ_{i33} with λ_{322} in order to generate non–zero entries for the third row/column of M_2. Such a combination of couplings generates a matrix of the form $c_i^{(2)} c_j^{(2)}$, where $c_{1,2}^{(2)}$ and $c_3^{(2)}$ originate from λ_{i33} and λ_{322} at tree–level respectively, because these couplings generate κ_i via the RGEs, *cf.* Eqs. (3.4) and (2.17). In order to ensure that M_2 is generated at tree–level, we still set $A_0^{(\lambda')} = 2M_{1/2}$, such that we are able to fit Eq. (6.6). This case is also listed under **S4** in Table 6.1.

- **Degenerate Masses:**

  Since for degenerate masses, all three matrices $M_{1,2,3}$ are non–zero and of similar magnitude, this scenario is a combination of choices made for NH and IH. As explained for the case of NH, we choose

$$(M_3)_{ij} \sim \lambda_{i11}\lambda_{j11}\,. \tag{6.19}$$

  To generate M_1 and M_2, we fit in analogy to the IH case

$$(M_1)_{ij} \sim \lambda'_{ikk}\lambda'_{jkk} \tag{6.20}$$
$$(M_2)_{ij} \sim \lambda'_{ill}\lambda'_{jll}\,. \tag{6.21}$$

  These models are listed in Table 6.1 as (DEG) **S1**, **S2** and **S3**. Here, as in the IH case, only the parameter choice $A_0^{(\lambda')}$ is possible in order to suppress the λ' contribution to the tree–level neutrino mass.

[6] Note that in principle, there would be 6 possibilities. However, numerically the values of the LNV parameters are affected only at $\mathcal{O}(1)$ level if we swap the assignment of λ' couplings to $c_i^{(1)}$ or $c_i^{(2)}$, *i.e.* $c_i^{(1)} \sim \lambda'_{i33}$, $c_i^{(2)} \sim \lambda'_{i22}$ looks very similar to $c_i^{(1)} \sim \lambda'_{i22}$, $c_i^{(2)} \sim \lambda'_{i33}$. This is obvious because the $c_i^{(1)}$ and $c_i^{(2)}$ differ from each other by maximally a factor 2.

	Normal Hierarchy (NH)	Inverse Hierarchy (IH)	Degenerate (DEG)
S1	$c_i^{(1)} \sim 0$ $c_i^{(2)} \sim \lambda'_{i11}$ $c_i^{(3)} \sim \lambda_{i11}$	$c_i^{(1)} \sim \lambda'_{i11}$ $c_i^{(2)} \sim \lambda'_{i22}$ $c_i^{(3)} \sim 0$	$c_i^{(1)} \sim \lambda'_{i11}$ $c_i^{(2)} \sim \lambda'_{i22}$ $c_i^{(3)} \sim \lambda_{i11}$
S2	$c_i^{(1)} \sim 0$ $c_i^{(2)} \sim \lambda'_{i22}$ $c_i^{(3)} \sim \lambda_{i11}$	$c_i^{(1)} \sim \lambda'_{i11}$ $c_i^{(2)} \sim \lambda'_{i33}$ $c_i^{(3)} \sim 0$	$c_i^{(1)} \sim \lambda'_{i11}$ $c_i^{(2)} \sim \lambda'_{i33}$ $c_i^{(3)} \sim \lambda_{i11}$
S3	$c_i^{(1)} \sim 0$ $c_i^{(2)} \sim \lambda'_{i33}$ $c_i^{(3)} \sim \lambda_{i11}$	$c_i^{(1)} \sim \lambda'_{i22}$ $c_i^{(2)} \sim \lambda'_{i33}$ $c_i^{(3)} \sim 0$	$c_i^{(1)} \sim \lambda'_{i22}$ $c_i^{(2)} \sim \lambda'_{i33}$ $c_i^{(3)} \sim \lambda_{i11}$
S4	$c_i^{(1)} \sim 0$ $\tilde{c}_i^{(2)} \sim \lambda'_{i33}$ $\tilde{c}_i^{(3)} \sim \lambda_{i33}$	$c_i^{(1)} \sim \lambda'_{i33}$ $c_i^{(2)} \sim \lambda_{i33}$ & λ_{322} $c_i^{(3)} \sim 0$	–
S5	$c_i^{(1)} \sim 0$ $c_i^{(2)} \sim \lambda'_{i23}$ & λ'_{i32} $c_i^{(3)} \sim \lambda_{i11}$	–	$c_i^{(1)} \sim \lambda'_{i33}$ $c_i^{(2)} \sim \lambda_{i33}$ & λ_{322} $c_i^{(3)} \sim \lambda_{231}$ & λ_{213} & λ_{312} (& λ_{313})

Table 6.1: Overview of the "diagonal" (**S1** – **S4**) and "non–diagonal" (**S5**) scenarios used for our numerical analysis.

6.2.2 Non–diagonal LNV scenarios

In this section, we depart from the diagonal coupling scenarios and discuss the effects of introducing "non–diagonal" couplings.

When allowing for non–diagonal LNV couplings λ'_{ikl} (λ_{ikl}), $l \neq k$, we generally need more couplings than in the diagonal case. This is because at 1–loop level[7], neutrino masses are dominantly generated proportional to $\lambda'_{ikl}\lambda'_{ilk}$ ($\lambda_{ikl}\lambda_{ilk}$). Thus, the assignment of one LNV coupling to one $c_i^{(\alpha)}$ parameter (Eq. (6.8)) is not possible for the part of the neutrino mass matrix generated at 1–loop level. Instead, we require

$$c_i^{(\alpha)} c_j^{(\alpha)} \sim \frac{1}{2} \cdot (\lambda'_{ikl}\lambda'_{jlk} + \lambda'_{ilk}\lambda'_{jkl})\ (m_d)_k\ (m_d)_l \tag{6.22}$$

where k, l are fix (similarly for λ couplings). This effectively doubles the number of LNV parameters if we choose $k \neq l$. Phenomenologically, one can distinguish between two cases:

(a) $\lambda'_{ikl} \approx \lambda'_{ilk}$ (same order of magnitude)

(b) $\lambda'_{ikl} \gg \lambda'_{ilk}$ or vice versa (strong hierarchy)

In the first case (a), the size of the couplings will not differ significantly from the diagonal case.

[7] Our choice to take the charged lepton mass matrix at the electroweak scale to be diagonal ensures that in good very approximation an off–diagonal coupling λ_{ijk} with $j \neq k$ does not generate a tree–level neutrino mass, since the bilinears κ_i are generated proportionally to $\lambda_{ijk}(Y_E)_{jk}$ and are thus zero for $j \neq k$. This argument still roughly holds if there are small off–diagonal entries in the Higgs Yukawa coupling, so in approximation this is also valid for couplings λ'_{ijk} with $j \neq k$, especially for the case of up–mixing.

For illustrative purposes, we will present numerical results for a non–diagonal scenario similar to the **S3** NH example, which we list under **S5** NH in Table 6.1. Here, we take as starting values $\lambda'_{i23} = \lambda'_{i32}$ and thus, a simplified form of Eq. (6.22) is $c_i^{(2)} \sim \lambda'_{i32}$, similar to the assignment in the diagonal case.

In the latter case (b), the size of the couplings become very different from those in the diagonal scenarios. In particular, some of the couplings can become very large. This is potentially of great interest experimentally. However, various low–energy bounds could potentially be violated. This can be illustrated with the help of the following example with degenerate neutrino masses, which we list under **S5** DEG in Table 6.1. Here, the first two neutrino masses are generated as in the case of **S4** IH (however, now for normal mass ordering): M_2 is generated at tree–level via diagonal λ_{i33} and λ_{322} couplings, and M_1 is generated at loop–level via λ'_{i33} couplings. However, now we additionally generate M_3 at 1–loop level via the 3 off–diagonal λ couplings λ_{231}, λ_{213} and λ_{312}. The latter do not lead to tree–level neutrino masses because the leptonic Higgs–Yukawa coupling is (nearly) diagonal and thus the tree–level generating term $\lambda_{ijk}(Y_E)_{jk}$ is (practically) zero. As we will see, the benchmark point we use leads to a very large λ_{231} beyond the perturbativity limit. For this reason, a different BP point, labelled as BP2, will be introduced for this scenario in § 6.3.3[8].

To obtain a qualitative understanding of the relative size of the couplings, first note that λ_{133} contributes to both M_2 and M_3 due to the antisymmetry, $\lambda_{133} \equiv -\lambda_{313}$. We choose the $A_0^{(\lambda')}$ minimum, and thus generate M_2 at tree level. The value of λ_{133} is therefore fixed, and is forced to be small due to its coupling with the large tau Yukawa coupling $(Y_E)_{33}$. The matrices M_1 and M_3 are then generated at loop level. The coupling product $\lambda_{231}\lambda_{313} = -\lambda_{231}\lambda_{133}$ is responsible for generating $(M_3)_{23}$. This implies that λ_{231} needs to be large in order to compensate for the smallness of λ_{313}. When now fitting $(M_3)_{22} \sim \lambda_{231}\lambda_{213}$, the large λ_{231} then leads to a hierarchically smaller λ_{213} in order to be consistent with the experimental result. Similarly, λ_{231} leads to a small λ_{312} by their contribution to $(M_3)_{33}$ via $\lambda_{312}\lambda_{321}(A_{12}^l + A_{21}^l)$ as shown in Eq. (3.10).

6.3 Numerical Results

In this section, we present the numerical results. We first describe our minimization procedure. Then we present our best–fit solutions for the normal hierarchy, inverted hierarchy and the degenerate case, respectively. We discuss the results for diagonal and off–diagonal LNV scenarios and how changes to the benchmark point can effect the results..

6.3.1 Minimization Procedure

Our goal is to find numerical values for each LNV scenario specified in Table 6.1, such that we obtain the experimentally observed neutrino data, Eqs. (3.23)–(3.27), at the $1\,\sigma$ level by means of least–square fitting. In order to achieve this also in degenerate scenarios, which necessarily

[8] Note that the coupling λ_{133} contributes to both M_2 and M_3 due to the antisymmetry, $\lambda_{133} \equiv -\lambda_{313}$. We fix its value when fitting M_2. Therefore, effectively there are only 3 off-diagonal couplings to fit M_3, which is nonetheless sufficient. We set the A_0 minimum to λ', such that M_2 is generated at tree–level (leading to small λ_{i33} couplings) whereas M_1, M_3 are generated at loop level. For this reason, a strong hierarchy between λ_{313} and λ_{231} arises when fitting $(M_3)_{23} \sim \lambda_{231}\lambda_{313}$, because λ_{231} has to compensate for the smallness of λ_{313}. When now fitting $(M_3)_{22} \sim \lambda_{231}\lambda_{213}$, the large λ_{231} coupling also leads to a strong hierarchy to λ_{213} in order to not exceed the experimental values (similarly for $(M_3)_{33}$ and λ_{312}).

involve some fine–tuning (as we discuss in § 6.3.2), we use a multistep procedure as outlined below.

We take as initial values for each set of LNV parameters at the unification scale M_X

$$\Lambda_{ikk} \sim c_i^{(\alpha)} \frac{1}{(Y_f)_{kk}} \tag{6.23}$$

(no summation over k) as specified in Table 6.1. f denotes a down quark for a λ' and a charged lepton for a λ coupling. The proportionality factor is estimated from the upper bound on the LNV couplings which comes from the upper bound on the neutrino mass from WMAP measurements, *cf.* Ref. [134].

Next, we perform a pre–iteration within our modified version of `SOFTSUSY`, where we make the simplifying assumption that the generation of the tree–level (by $\Lambda = \lambda$) and 1–loop level (by $\Lambda = \lambda'$) neutrino mass matrices M_α in Eq. (6.6) are independent of each other. So for each M_α we separately fit the relevant Λ_{ijk}. In our iteration procedure we set

$$\Lambda_{ijk}|_{new} = \sqrt{\frac{(M_\alpha^{obs})_{ii}}{(M_\alpha^{softsusy})_{ii}}} \Lambda_{ijk}|_{old} \,. \tag{6.24}$$

Here $M_\alpha^{softsusy}$ is the effective neutrino mass matrix (at 1–loop level) obtained via the seesaw–mechanism with `SOFTSUSY` . In the first step we use the initial values corresponding to Eq. (6.23). We obtain $(M_\alpha^{obs})_{ii}$ by inverting Eq. (6.4), without using the TBM approximation. For $m_{\nu\alpha}$ we use the experimental best–fit values. And for the diagonalization matrix U, we implement the general form, using θ_{12}, θ_{23} from the experimental best–fit, as well as $\theta_{13} = 0$. In Eq. (6.24) there is also no sum over i.

This gives a very good order of magnitude estimate for all LNV couplings and thus a suitable starting point for our least–square fit. However, so far each set of couplings $\Lambda_{ijk} \sim c_i^{(\alpha)}/(Y_f)_{kk}$ has only been fit separately for each α, while keeping the other LNV couplings equal to zero. When fitting all LNV couplings simultaneously, they can affect each other via the RGEs and through contributions to the other M_α^{obs}. Note that these effects are easily controllable for NH and IH scenarios. However, in the case of DEG scenarios, some strong cancellations occur for some entries of the effective neutrino mass matrix, *e.g.* the $(M_\nu)_{13} = (M_1)_{13} + (M_2)_{13}$ entry in Eq. (6.6). Here, both individual entries $(M_\alpha)_{13}$ are of the order of the generated neutrino mass, but the resulting $(M_\nu)_{13}$ entry is at least 3 orders of magnitude smaller. This will become relevant in the next step of our procedure.

After these first approximations, we next fit all LNV parameters specified for each scenario in Table 6.1 simultaneously. We calculate the full 7×7 neutralino–neutrino mass matrix with `SOFTSUSY`. The 3×3 neutrino mass matrix is then obtained via the seesaw mechanism, and is used in order to extract predictions for the neutrino masses and mixing angles.

We define a χ^2 function

$$\chi^2 \equiv \frac{1}{N_{obs}} \sum_{i=1}^{N_{obs}} \left(\frac{f_i^{softsusy} - f_i^{obs}}{\delta_i} \right)^2 \tag{6.25}$$

where f_i^{obs} are the central values of the N_{obs} experimental observables defined in Eqs. (3.23)–(3.27), $f_i^{softsusy}$ are the corresponding numerical predictions and δ_i are the $1\,\sigma$ experimental

uncertainties. We minimize Eq. (6.25) with a stepping method of the program package MINUIT2 for the NH/IH case. In the DEG scenarios, MINUIT2 initially does not converge due to the points made in the last paragraph. Therefore, we first use the Hastings–Metropolis algorithm to obtain a $\chi^2 < \mathcal{O}(10)$. Subsequently, the same MINUIT2 routine as in the NH/IH case is used. We accept a minimization result as successful if our minimization procedure yields $\chi^2 < 1$.

Simultaneously, we ensure that the conditions (cf. § 3.5)

$$\sum_i m_{\nu_i} \lesssim 0.4 \text{ eV}$$
$$\sin^2(\theta_{13}) < 0.047 \tag{6.26}$$

are fulfilled.

6.3.2 Discussion of the Results for Diagonal LNV Scenarios

We present our numerical results in Table 6.2. In the three columns, we show our best–fit solutions for normal hierarchy, inverse hierarchy and degenerate masses, respectively. In the five rows, we show our solutions for the various scenarios enlisted in Table 6.1. **S1**–**S4** are the "diagonal" LNV scenarios, while **S5** involves non–diagonal couplings, as discussed in the previous section. In order to illustrate the low energy bounds most relevant to our scenarios, we also display models which do not satisfy all constraints. These solutions are highlighted in bold and the violated bound(s) are also stated. In this subsection, we restrict ourselves to the diagonal LNV scenarios; the off–diagonal LNV scenarios will be discussed in the following subsection.

We first discuss some general features of the best fit parameter sets. Focusing on the three scenarios **S1**–**S3**, some ratios among the LNV couplings are displayed in Table 6.3. We see that the results reflect the basic structure of our ansätz Eq. (6.23). In particular, the relative signs among different LNV couplings are reproduced. However, the relative magnitude among the couplings are expected to deviate somewhat from Eqs. (6.23) and (6.13). One reason is that our LNV couplings should mirror the structure of Eq. (6.13) at the electroweak scale, while in Table 6.2 and Table 6.3 the couplings are given at the unification scale. So RG running needs to be taken into account. However the change in the LNV couplings when going to the unification scale is not uniform for all couplings. Also, we fit the oscillation data given in § 3.5 instead of the TBM approximation, such that the $c_i^{(\alpha)}$ differ from Eq. (6.13) already by up to 7% percent.

We also see from Table 6.3 that the LNV parameters in the IH scenarios follow the pattern of $c_i^{(\alpha)}$ more closely than those in the NH and DEG scenarios. For the IH scenarios, the tree level contribution is suppressed by choosing A_0 appropriately. The neutrino mass matrix entries are dominated by loop contributions and the associated couplings should then reflect the near TBM structure as well as the orthogonality of the vectors $c^{(\alpha)}$. However for the NH and DEG scenarios, the significant contributions from both tree and loop masses mean that while the $c_i^{(\alpha)}$ have the expected ratios for each α after pre–iteration, once contributions from different α's are combined for the full iteration they interfere with each other. For example, the presence of λ couplings changes the position of the $A_0^{(\lambda')}$ minimum, making the contributions of the λ' couplings to the tree level masses less suppressed, thus leading to the larger deviation.

It is clear from Eq. (6.23) that the magnitude of diagonal LNV couplings should decrease from first to third generation (while generating the same neutrino masses), because the LNV couplings have to balance out the effect of the Higgs–Yukawa–couplings, which increase with generation.

	Normal Hierarchy	Inverse Hierarchy	Degenerate
S1	$\lambda'_{111} = \mathbf{1.12 \cdot 10^{-2}}$ **[b2],[b8]** $\lambda'_{211} = \mathbf{8.76 \cdot 10^{-3}}$ $\lambda'_{311} = -1.48 \cdot 10^{-2}$ $\lambda_{211} = \mathbf{1.52 \cdot 10^{-2}}$ **[b2]** $\lambda_{311} = 1.37 \cdot 10^{-2}$	$\lambda'_{111} = \mathbf{3.94 \cdot 10^{-2}}$ **[b1],[b2],[b8]** $\lambda'_{211} = \mathbf{-1.88 \cdot 10^{-2}}$ **[b1],[b2]** $\lambda'_{311} = 1.94 \cdot 10^{-2}$ $\lambda'_{122} = 1.21 \cdot 10^{-3}$ $\lambda'_{222} = 1.27 \cdot 10^{-3}$ $\lambda'_{322} = -1.31 \cdot 10^{-3}$	$\lambda'_{111} = \mathbf{5.85 \cdot 10^{-2}}$ **[b1],[b2],[b7],[b8]** $\lambda'_{211} = \mathbf{-3.63 \cdot 10^{-2}}$ **[b1],[b2],[b6],[b7]** $\lambda'_{311} = \mathbf{3.35 \cdot 10^{-2}}$ **[b6]** $\lambda'_{122} = 2.18 \cdot 10^{-3}$ $\lambda'_{222} = 1.63 \cdot 10^{-3}$ $\lambda'_{322} = -2.09 \cdot 10^{-3}$ $\lambda_{211} = \mathbf{2.55 \cdot 10^{-2}}$ **[b2],[b6]** $\lambda_{311} = \mathbf{2.28 \cdot 10^{-2}}$ **[b6]**
S2	$\lambda'_{122} = 5.08 \cdot 10^{-4}$ $\lambda'_{222} = 3.88 \cdot 10^{-4}$ $\lambda'_{322} = -6.97 \cdot 10^{-4}$ $\lambda_{211} = 1.52 \cdot 10^{-2}$ $\lambda_{311} = 1.37 \cdot 10^{-2}$	$\lambda'_{111} = \mathbf{3.99 \cdot 10^{-2}}$ **[b1],[b2],[b8]** $\lambda'_{211} = \mathbf{-1.81 \cdot 10^{-2}}$ **[b1],[b2]** $\lambda'_{311} = 1.89 \cdot 10^{-2}$ $\lambda'_{133} = 3.09 \cdot 10^{-5}$ $\lambda'_{233} = 3.21 \cdot 10^{-5}$ $\lambda'_{333} = -3.35 \cdot 10^{-5}$	$\lambda'_{111} = \mathbf{6.87 \cdot 10^{-2}}$ **[b1],[b2],[b7],[b8]** $\lambda'_{211} = \mathbf{-2.90 \cdot 10^{-2}}$ **[b1],[b2],[b6],[b7]** $\lambda'_{311} = \mathbf{3.18 \cdot 10^{-2}}$ **[b6]** $\lambda'_{133} = 4.99 \cdot 10^{-5}$ $\lambda'_{233} = 2.98 \cdot 10^{-5}$ $\lambda'_{333} = -7.43 \cdot 10^{-5}$ $\lambda_{211} = \mathbf{2.99 \cdot 10^{-2}}$ **[b2],[b6]** $\lambda_{311} = \mathbf{2.10 \cdot 10^{-2}}$ **[b6]**
S3	$\lambda'_{133} = 1.30 \cdot 10^{-5}$ $\lambda'_{233} = 4.84 \cdot 10^{-6}$ $\lambda'_{333} = -2.28 \cdot 10^{-5}$ $\lambda_{211} = 1.55 \cdot 10^{-2}$ $\lambda_{311} = 1.40 \cdot 10^{-2}$	$\lambda'_{122} = 1.80 \cdot 10^{-3}$ $\lambda'_{222} = -8.29 \cdot 10^{-4}$ $\lambda'_{322} = 8.64 \cdot 10^{-4}$ $\lambda'_{133} = 3.11 \cdot 10^{-5}$ $\lambda'_{233} = 3.22 \cdot 10^{-5}$ $\lambda'_{333} = -3.32 \cdot 10^{-5}$	$\lambda'_{122} = 2.93 \cdot 10^{-3}$ $\lambda'_{222} = -1.98 \cdot 10^{-3}$ $\lambda'_{322} = 5.79 \cdot 10^{-4}$ $\lambda'_{133} = 5.18 \cdot 10^{-5}$ $\lambda'_{233} = 5.78 \cdot 10^{-5}$ $\lambda'_{333} = -5.13 \cdot 10^{-5}$ $\lambda_{211} = 1.71 \cdot 10^{-2}$ $\lambda_{311} = 3.08 \cdot 10^{-2}$
S4	$\lambda'_{133} = -6.80 \cdot 10^{-6}$ $\lambda'_{233} = 2.81 \cdot 10^{-5}$ $\lambda'_{333} = 4.21 \cdot 10^{-5}$ $\lambda_{133} = 1.32 \cdot 10^{-6}$ $\lambda_{233} = 2.70 \cdot 10^{-6}$	$\lambda'_{133} = 3.96 \cdot 10^{-5}$ $\lambda'_{233} = -2.81 \cdot 10^{-5}$ $\lambda'_{333} = 2.89 \cdot 10^{-5}$ $\lambda_{133} = 3.23 \cdot 10^{-6}$ $\lambda_{233} = 3.48 \cdot 10^{-6}$ $\lambda_{322} = -5.64 \cdot 10^{-5}$	
S5	$\lambda'_{123} = 5.76 \cdot 10^{-5}$ $\lambda'_{132} = 5.75 \cdot 10^{-5}$ $\lambda'_{223} = 6.23 \cdot 10^{-5}$ $\lambda'_{232} = 6.24 \cdot 10^{-5}$ $\lambda'_{323} = -5.88 \cdot 10^{-5}$ $\lambda'_{332} = -6.00 \cdot 10^{-5}$ $\lambda_{211} = 1.52 \cdot 10^{-2}$ $\lambda_{311} = 1.39 \cdot 10^{-2}$		$\lambda'_{133} = -3.11 \cdot 10^{-5}$ $\lambda'_{233} = 8.79 \cdot 10^{-5}$ $\lambda'_{333} = -4.14 \cdot 10^{-5}$ $\lambda_{133} = 1.99 \cdot 10^{-6}$ $\lambda_{233} = 4.08 \cdot 10^{-6}$ $\lambda_{322} = -2.57 \cdot 10^{-5}$ $\lambda_{231} = -5.67 \cdot 10^{-2}$ $\lambda_{213} = -2.03 \cdot 10^{-5}$ $\lambda_{312} = 2.54 \cdot 10^{-3}$

Table 6.2: Best–fit points for the LNV parameters at the unification scale M_X for our benchmark point BP and $A_0^{(\lambda')} = 912.3$ GeV, except for **S5** DEG, where BP2 and $A_0^{(\lambda')} = 1059.2$ GeV are used, *cf.* § 6.3.3. The couplings printed in bold violate one of the low–energy bounds [b1]–[b7] which are listed in § 5.1. Note that the values are given at 2 significance level only for better readability. In order to reproduce the results, higher significance is needed as is clear from Eq. (6.28). Readers are encouraged to contact the authors to obtain the exact values.

	Normal Hierarchy	Inverse Hierarchy	Degenerate
data	$c_1^{(2)} : c_2^{(2)} : c_3^{(2)} = 0.94 : 0.99 : -1$ $c_2^{(3)} : c_3^{(3)} = 0.99 : 1$	$c_1^{(1)} : c_2^{(1)} : c_3^{(1)} = 2.09 : -0.98 : 1$ $c_1^{(2)} : c_2^{(2)} : c_3^{(2)} = 0.94 : 0.99 : -1$	$c_1^{(1)} : c_2^{(1)} : c_3^{(1)} = 2.09 : -0.98 : 1$ $c_1^{(2)} : c_2^{(2)} : c_3^{(2)} = 0.94 : 0.99 : -1$ $c_2^{(3)} : c_3^{(3)} = 0.99 : 1$
S1	$\lambda'_{111} : \lambda'_{211} : \lambda'_{311} = 0.75 : 0.59 : -1$ $\lambda_{211} : \lambda_{311} = 1.11 : 1$	$\lambda'_{111} : \lambda'_{211} : \lambda'_{311} = 2.04 : -0.97 : 1$ $\lambda'_{122} : \lambda'_{222} : \lambda'_{322} = 0.93 : 0.97 : -1$	$\lambda'_{111} : \lambda'_{211} : \lambda'_{311} = 1.75 : -1.09 : 1$ $\lambda'_{111} : \lambda'_{211} : \lambda'_{311} = 1.04 : 0.78 : -1$ $\lambda_{211} : \lambda_{311} = 1.19 : 1$
S2	$\lambda'_{122} : \lambda'_{222} : \lambda'_{322} = 0.73 : 0.56 : -1$ $\lambda_{211} : \lambda_{311} = 1.11 : 1$	$\lambda'_{111} : \lambda'_{211} : \lambda'_{311} = 2.12 : -0.96 : 1$ $\lambda'_{133} : \lambda'_{233} : \lambda'_{333} = 0.93 : 0.96 : -1$	$\lambda'_{111} : \lambda'_{211} : \lambda'_{311} = 2.11 : -0.91 : 1$ $\lambda'_{133} : \lambda'_{233} : \lambda'_{333} = 0.67 : 0.40 : -1$ $\lambda_{211} : \lambda_{311} = 1.42 : 1$
S3	$\lambda'_{133} : \lambda'_{233} : \lambda'_{333} = 0.57 : 0.21 : -1$ $\lambda_{211} : \lambda_{311} = 1.11 : 1$	$\lambda'_{122} : \lambda'_{222} : \lambda'_{322} = 2.09 : -0.96 : 1$ $\lambda'_{133} : \lambda'_{233} : \lambda'_{333} = 0.93 : 0.97 : -1$	$\lambda'_{122} : \lambda'_{222} : \lambda'_{322} = 5.06 : -3.41 : 1$ $\lambda'_{133} : \lambda'_{233} : \lambda'_{333} = 1.01 : 1.13 : -1$ $\lambda_{211} : \lambda_{311} = 0.56 : 1$

Table 6.3: Ratios of the LNV parameters at the unification scale M_X for scenarios **S1, S2** and **S3** and the ratios $c_1^{(\alpha)} : c_2^{(\alpha)} : c_3^{(\alpha)}$ inferred from experimental data. For comparison, the ratios $c_1^{(\alpha)} : c_2^{(\alpha)} : c_3^{(\alpha)}$ in the TBM limit are $(2 : -1 : 1)$, $(1 : 1 : -1)$ and $(0 : 1 : 1)$ for $\alpha = 1, 2$ and 3 respectively.

For example, comparing the size of λ'_{ikk} in scenarios **S1**–**S3** in the IH case, one observes that the difference in magnitude of the LNV couplings mirrors the hierarchy of down–type quark masses, $\lambda'_{ijj}/\lambda'_{ikk} \sim (m_d)_k/(m_d)_j$ for fixed index i.

As we see in Table 6.2, models involving first generation couplings (λ'_{111} and λ'_{211}) are disfavored due to strong constraints from $\mu \to eee$ [b1], μ–e conversions [b2] and $0\nu\beta\beta$ [b8]. In addition, the λ_{211} in **S1** NH, **S1** DEG and **S2** DEG violate the two–coupling bound from μ–e conversion [b2] in conjunction with the large λ'_{111} coupling. Limits on leptonic K–meson decay [b6] and $\mu \to e\gamma$ [b7] are also seen to be violated in degenerate scenarios **S1** DEG and **S2** DEG involving diagonal first generation couplings. The second generation LNV Yukawa couplings are of the order of 10^{-3} (10^{-4}) for IH and DEG (NH) scenarios[9] and safely satisfy all low–energy bounds. The third generation couplings take on values between 10^{-5} and 10^{-6}.

Collider implications of the solutions we obtained will be discussed in section 6.4. Generally speaking, the stringent low energy bounds on the first generation couplings could be evaded in models with heavier supersymmetric mass spectra. In these models the relatively large couplings could still lead to interesting collider phenomenology, for example resonant production of sparticles [102–105, 213]. These couplings could also have significant impact on the RG running of the sparticle masses, and result in observable changes to the sparticle spectrum when compared with those in the R_p–conserving limit. In particular, new LSP candidates may be obtained even within the B_3 cMSSM framework [99, 100, 108, 204].

In contrast, third generation couplings are tiny, *e.g.* the **S4** NH model in Table 6.2. However these small couplings could result in a finite decay length for the LSP and hence potential detection of displaced vertices in a collider. See Ref. [43] for numerical estimates.

In Fig. 6.2, we display the changes in χ^2 for a few selected scenarios (**S2** NH, **S3** IH and **S3** DEG) when a LNV coupling is varied within [0.5:1.5] times the best–fit value. We define a "width" for a χ^2 minimum to be

$$w \equiv \frac{\Delta\Lambda|_{\chi^2<3}}{\Lambda|_{\chi^2\approx 0}}\,, \tag{6.27}$$

so that a large (small) w value may be interpreted as less (more) fine–tuning between different

[9] For NH the couplings are smaller because the lighter neutrino mass is smaller in NH than in IH/DEG.

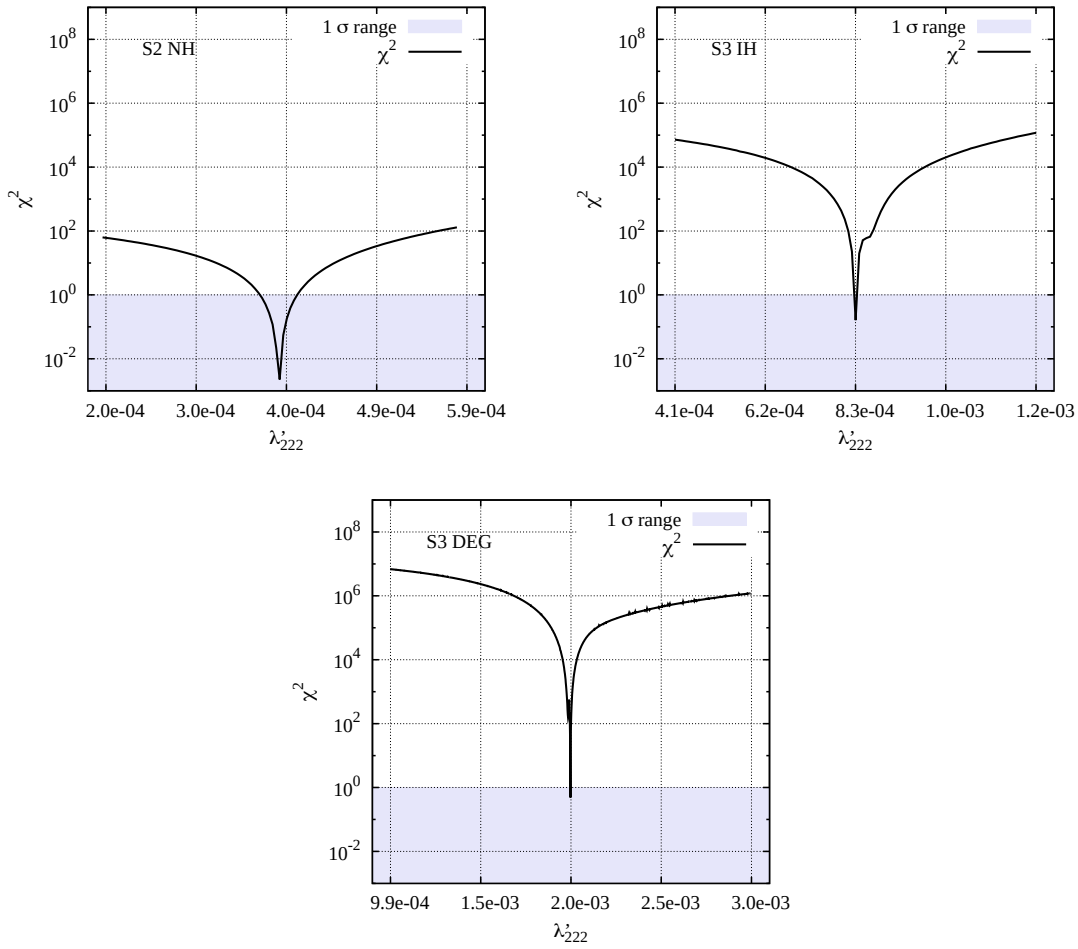

Figure 6.2: Variation of χ^2 as a function of λ'_{222} for scenarios **S2** NH, **S3** IH and **S3** DEG. The glitches in **S3** IH and **S3** DEG are associated with the 'crossing–over' of mass eigenstates when λ'_{222} is varied. See text for more discussion.

LNV couplings.

Clearly the NH case looks significantly better than the IH/DEG cases:

$$\begin{aligned} w(\mathrm{NH}, \Lambda = \lambda'_{222}) &= 1.1 \cdot 10^{-1} \,, \\ w(\mathrm{IH}, \Lambda = \lambda'_{222}) &= 7.4 \cdot 10^{-3} \,, \\ w(\mathrm{DEG}, \Lambda = \lambda'_{222}) &= 4.8 \cdot 10^{-4} \,. \end{aligned} \tag{6.28}$$

In fact, since the neutrino masses in our model are free parameters to be fitted to the data, it is natural for these masses to be non–degenerate. To obtain the two (three) quasi–degenerate masses in the IH (DEG) spectrum thus requires a certain amount of fine–tuning, which should be reflected in the value of w. Recall from Eqs. (6.6) and (6.7) that due to a small (zero) $\sin[\theta_{13}]$ in the near (exact) TBM limit, there are small off–diagonal entries for an inverted or degenerate mass spectrum. Specifically, α_{21} is small in both cases, while α_{31} is also small in a DEG spectrum. As a result, there are small off–diagonal entries for both IH and DEG scenarios

but not for a normal hierarchy, while in our set–up the diagonal and off–diagonal entries of M_α are of the same order for each α. Therefore, a way to understand this fine tuning technically would be by considering the size of the off–diagonal entries of $\mathcal{M}_\nu^{\rm eff}$. We discuss the three cases separately.

In the case of NH, the off–diagonal entries in $\mathcal{M}_\nu^{\rm eff}$ will be of the same order as the diagonal values. In this case, the experimental observables are fairly insensitive to changes of up to $\mathcal{O}(10\%)$ in the LNV sector, *cf.* Eq. (6.28).

For IH, we have two nearly degenerate mass eigenstates. Therefore, the tree–level and the loop contribution have to be of the same order, with a near–cancellation occurring between the off–diagonal entries of M_1 and M_2. This results in a significantly larger width of the χ^2 minimum than in the NH case.

For the same reason, in the DEG cases even larger fine–tuning is required in order to obtain *three* nearly degenerate neutrino masses. Actually, in the limit $M \gg \Delta M \sim \Delta m^2/M$, where M is the mass scale of the heaviest neutrino, all off–diagonal entries will have a magnitude of $\mathcal{O}(\Delta M)$, and the width w can be approximated by

$$\Lambda^2 \sim M\,, \tag{6.29}$$

$$\frac{\Delta\Lambda}{\Lambda} \sim \frac{1}{2}\frac{\Delta M}{M}. \tag{6.30}$$

A consequence of such fine–tuning is that if $\mathcal{M}_\nu^{\rm eff}$ is deformed slightly (for example due to changes in model parameters or technical aspects such as low convergence threshold in the spectrum calculation), the angles can change a lot since they are especially sensitive to the (small) off–diagonal entries of $\mathcal{M}_\nu^{\rm eff}$. In contrast, the mass values are much more stable, with their sum determined by the diagonal entries of $\mathcal{M}_\nu^{\rm eff}$.

This can be illustrated by changing the implementation of the LNV parameters in the numerical code from 6 significant figures to 3: the masses change by less than 1 percent, whereas the angles change by a factor of order one. Therefore the values displayed in Table 6.2, especially those for the IH and DEG cases, need to be taken with caution. However, listing more digits would result in worse readability, so we ask readers interested in reproducing our results to contact the authors for more precise values.

To see how the experimental observables change as the LNV couplings are varied, we show in Figs. 6.3, 6.4 and 6.5 the variation of the mixing angles and masses as functions of λ'_{222}. Recall that the χ^2 variation of the fit for λ'_{222} is displayed in Fig. 6.2. For illustrative purposes these figures also show the variation of another LNV coupling for each of these scenarios, such that two sets of couplings, each corresponding to one M_α, are presented[10].

We first discuss the scenario **S2** NH, which is illustrated in Fig. 6.3. In the upper two plots, one sees that the variation of λ'_{222} mainly affects θ_{12} and somewhat also m_2, whereas θ_{23} and m_3 are left relatively unchanged. In the lower two plots, where λ_{211} is varied, the observables are reversely affected. This is because the two non–zero mass matrices, $M_2 \sim m_{\nu 2}$ and $M_3 \sim m_{\nu 3}$, are controlled by the λ and λ' couplings separately (*i.e.* by the tree–level and loop level contribution, respectively). Obviously, in NH $\sin^2\theta_{12}$ is determined only by M_2, whereas in IH and DEG, the form of M_1 is also relevant. Therefore, NH is the easiest scenario to fit, because the observables can be directly related to independent sets of couplings. The mixing $\sin^2\theta_{13}$

[10] We refrain from showing an additional set for the third M_α in the DEG case, because it does not give rise to any new insights.

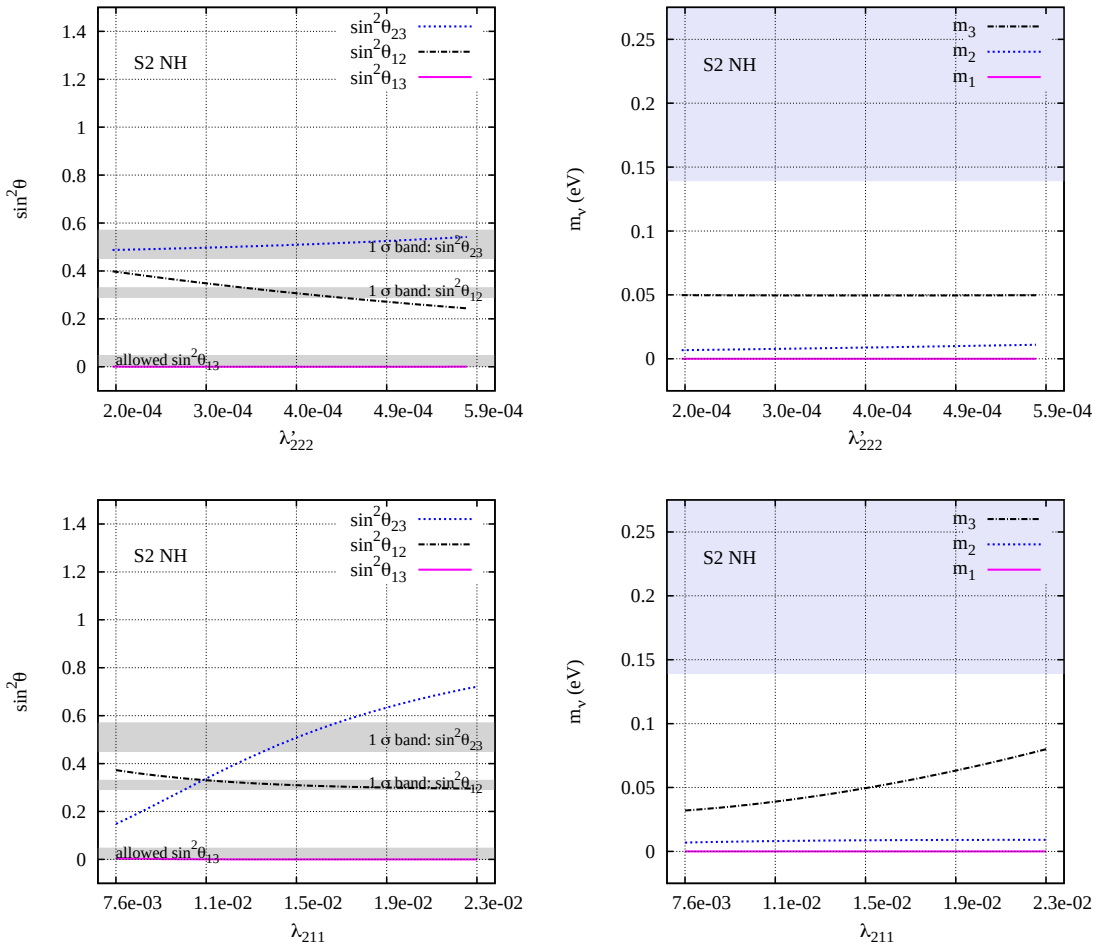

Figure 6.3: Variation of the mixing angles (left) and the mass eigenvalues (right) as functions of λ'_{222} (top) and λ_{211} (bottom) for scenario **S2** NH. The best fit values for λ'_{222} and λ_{211} are located at the centre of the plots. On the plots of mixing angles, the grey bands are experimentally viable regions for (from top to bottom) $\sin^2\theta_{23}$, $\sin^2\theta_{12}$ and $\sin^2\theta_{13}$. On the plots of mass eigenvalues, values inside the grey bands are disfavoured by cosmological considerations.

remains practically unchanged due to our ansätz in Eq. (6.23), which is designed to give a tiny θ_{13}.

For scenario **S3** IH (Fig. 6.4), we see that here, no clean correlation exists between which LNV parameter is varied and which observable is affected. θ_{12} and m_2 change drastically and are affected by both $\lambda'_{i22} \sim M_1$ and $\lambda'_{i33} \sim M_2$. The sharp change in $\sin^2\theta_{12}$ around the best–fit point corresponds to "cross–overs" of mass eigenstates m_1 and m_2 as λ'_{222} or λ'_{233} is varied. The fact that the best–fit solution lies in this steeply changing region simply reflects the fact that for IH the two heavy neutrinos have similar masses. Incidentally, the small "suppression" at $\lambda'_{222} \sim -8.4 \cdot 10^{-4}$ in the corresponding χ^2 plot in Fig. 6.2 near the best–fit point corresponds to a region where Δm^2_{21} coincides with the experimental value during this cross–over. However to a reasonable approximation the flavour content of the two mass eigenstates are now swapped, hence $\sin^2\theta_{12}$ is different from its best–fit value.

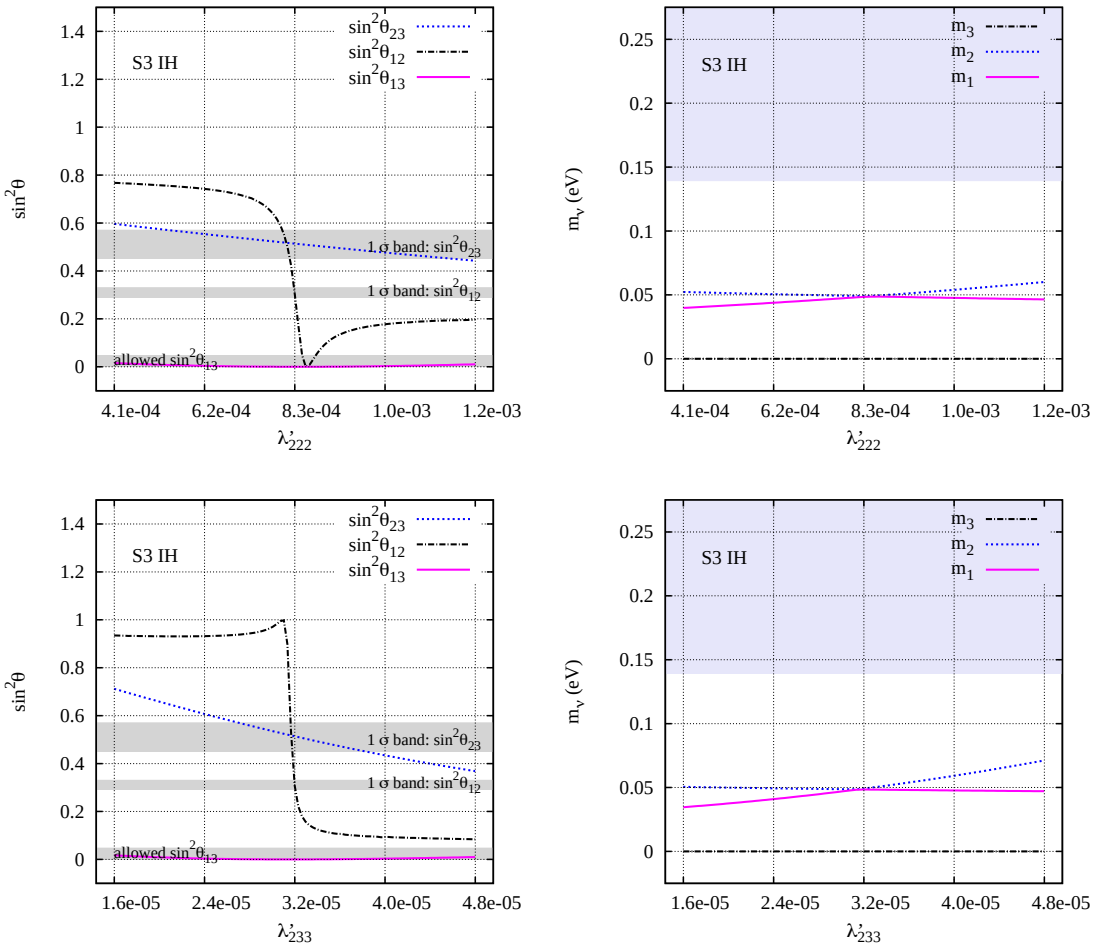

Figure 6.4: Variation of the mixing angles (left) and the mass eigenvalues (right) as functions of λ'_{222} (top) and λ'_{233} (bottom) for scenario **S3** IH. The best–fit values of λ'_{222} and λ'_{233} are located at the centre of the plots. On the plots of mixing angles, the grey bands are experimentally viable regions for (from top to bottom) $\sin^2\theta_{23}$, $\sin^2\theta_{12}$ and $\sin^2\theta_{13}$. On the plots of mass eigenvalues, values inside the grey bands are disfavoured by cosmological considerations.

On the other hand, it is clear that m_3 does not sit close to the cross–over region. Moreover, since m_3 basically contains only μ and τ flavours around the best–fit region, the proportion of μ and τ content of the other two mass eigenstates must be the same in order for them to be orthogonal to m_3. As a consequence, the cross–over of these two states only changes $\sin^2\theta_{23}$ mildly. As in the case of **S2** NH, $\sin^2\theta_{13}$ is designed to have a tiny value.

For the scenario **S3** DEG (Fig. 6.5), the fact that the three mass scales are very close to each other means that complete separation of the three contributions is in practice very difficult. As in **S3** IH, the best–fit point lies close to a region where cross–over of mass eigenstates take place. In this case, two cross–overs take place near the best–fit point. For example, the non–trivial variation of $\sin^2\theta_{12}$ with λ'_{233} immediately to the right of the best–fit point corresponds to a second cross–over of the mass eigenvectors. The fact that all three masses are quasi–degenerate also explains the large transition of all three mixing angles. In particular, even though the

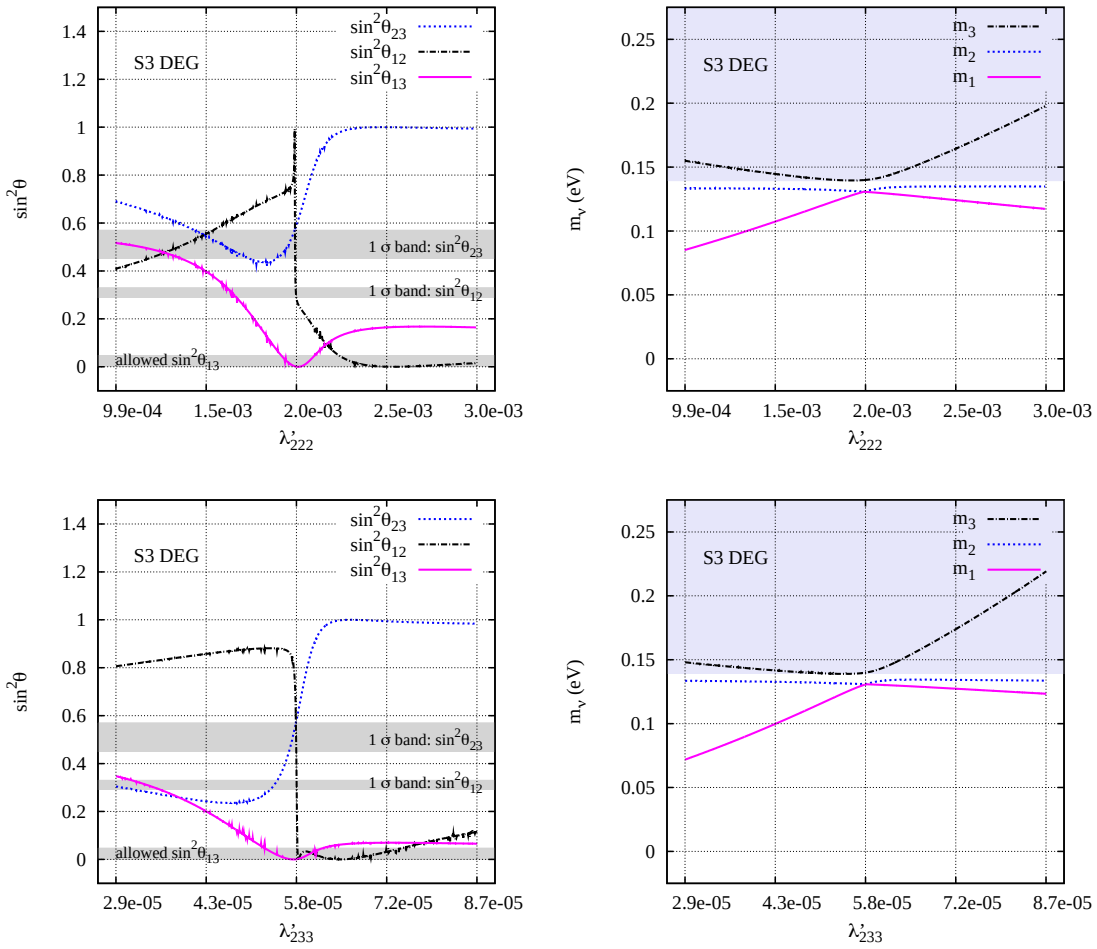

Figure 6.5: Variation of the mixing angles (left) and the mass eigenvalues (right) as functions of λ'_{222} (top) and λ'_{233} (bottom) for scenario **S3** DEG. The best fit values for λ'_{222} and λ'_{233} are located at the centre of the plots. On the plots of mixing angles, the grey bands are experimentally viable regions for (from top to bottom) $\sin^2\theta_{23}$, $\sin^2\theta_{12}$ and $\sin^2\theta_{13}$. On the plots of mass eigenvalues, values inside the grey bands are disfavoured by cosmological considerations.

coupling set is chosen to have a small $\sin^2\theta_{13}$, immediately away from the best–fit point the mass ordering is changed, resulting in the different $\sin^2\theta_{13}$ behaviour compared with the NH and IH cases.

Furthermore, due to the strong fine–tuning, the χ^2 suppression expected as in the IH scenarios is buried within the rapidly increasing χ^2 value. We note in passing that due to this fine–tuning, the numerical results are less stable than those in the NH and IH scenarios. This results in the fluctuations seen in the figures[11].

We now go on to discuss the scenarios **S4**, which represent scenarios with the smallest possible LNV couplings to still describe the oscillation data correctly. In the **S4** NH scenario, recall that the antisymmetry of the λ_{i33} couplings generates zeros in M_3 which do not correspond

[11] In fact, the tolerance parameter in `SOFTSUSY` needs to be set to high precision ($\mathcal{O}(10^{-6})$) in order to produce results comparable among different platforms.

to the "texture zeros" given in Eq. (6.6). Therefore, linear combinations between the different contributions to the neutrino masses (*i.e.* between $M_2 \sim m_{\nu 2}$ and $M_3 \sim m_{\nu 3}$) are necessary to obtain the desired oscillation parameters. As a result, the ratio of the couplings are not approximated by those displayed in Eq. (6.13) but instead by a linear combination of these, *cf.* Ref.[12]. Still, the behaviour of the observables when the relevant LNV couplings are varied is similar to the scenarios discussed above.

In the **S4** IH scenario, the λ'_{i33} couplings still roughly follow the expected structure and magnitude as before in **S1** to **S3** IH. However, the deviations are slightly larger because of the presence of λ couplings. In contrast to other IH scenarios, in **S4** IH, M_2 is generated at tree–level from λ_{i33} and λ_{322} instead of at 1–loop level from λ'_{i22}. The absence of λ_{333}, due to anti–symmetry of the first two generation indices, means that λ_{322} (or λ_{311}) is needed to "fill up" the third row/column of the tree–level matrix M_2. In this scenario, all diagonal third generation couplings are used. Consequently, the magnitude of our coupling set is the smallest possible among the diagonal inverted hierarchy scenarios.

The ratio of the three λ couplings is approximately

$$(\lambda_{133} : \lambda_{233} : \lambda_{322}) \;\sim\; (1 \;:\; 1 \;:\; -16)\,, \tag{6.31}$$

which is expected as these couplings scales as $1/(Y_E)_{ii}$ $(i = 2, 3)$.

We conclude in both the NH and the IH case that it is not possible to push all LNV couplings below $\mathcal{O}(10^{-5})$. However, at this order of magnitude, displaced vertices might be observed at colliders, depending on the benchmark point, *cf.* § 6.4.

6.3.3 Discussion of the Results for Off–diagonal LNV Scenarios

In **S5** in Table 6.3, we present the solutions for the two off–diagonal LNV scenarios. We see that the NH off–diagonal solution, being an example of non–hierarchical off–diagonal couplings, is very similar to the diagonal NH solutions in structure, *cf.* Eq. (6.31). Obviously, because here the generation indices of the couplings are $i23/i32$ instead of $i22$ (**S2**) or $i33$ (**S3**). The order of magnitude of the couplings is somewhere between the solutions **S2** and **S3**, mirroring the mass hierarchy in the down–quark sector.

In scenario **S5** DEG, the λ_{231} coupling is much larger than the other couplings, representing an example of a strongly hierarchical off–diagonal scenario. In fact,when performing the `SOFTSUSY` pre–iteration for our benchmark point, we found λ_{231} to be of $\mathcal{O}(1)$, which is inconsistent with the requirement of perturbativity, and also violates the low–energy bounds.

To reduce the size of this coupling, a different cMSSM benchmark point is therefore chosen. Employing a larger $\tan\beta$ and also $\mathrm{sgn}(\mu) = -1$ is useful, as the former implies larger down–type quark Yukawa couplings, while the latter also increases certain loop contributions to neutrino

[12] It is possible to obtain other solutions to Eq. (6.4) by forming linear combinations of the M_α's given in Eq. (6.6). As an example we here present the NH solution with $c_3^{(3)} = 0$ used in **S4** NH:

$$\begin{aligned}
c_1^{(2)} &= \sqrt{\frac{m_{\nu 2}}{3} + \frac{m_{\nu 3}}{2}}, \\
c_2^{(2)} &= \frac{\frac{m_{\nu 2}}{3} + \frac{m_{\nu 3}}{2}}{\frac{m_{\nu 2}}{3}}, \quad c_3^{(2)} = \frac{\frac{m_{\nu 2}}{3} + \frac{m_{\nu 3}}{2}}{\frac{m_{\nu 3}}{2} - \frac{m_{\nu 2}}{3}}, \\
c_1^{(3)} &= \frac{c_2^{(3)}}{2} = \sqrt{\frac{\frac{m_{\nu 2}}{3}\frac{m_{\nu 3}}{2}}{\frac{m_{\nu 2}}{3} + \frac{m_{\nu 3}}{2}}}, \quad c_3^{(3)} = 0.
\end{aligned}$$

Particles	Masses (GeV)			
$\tilde{g}$	1696			
$\tilde{\chi}_1^\pm, \tilde{\chi}_2^\pm$	599	798		
$\tilde{\chi}_1^0, \tilde{\chi}_2^0, \tilde{\chi}_3^0, \tilde{\chi}_4^0$	320	599	785	799
$\tilde{u}_1, \tilde{c}_1, \tilde{t}_1$	1593	1593	1431	
$\tilde{u}_2, \tilde{c}_2, \tilde{t}_2$	1536	1535	1281	
$\tilde{d}_1, \tilde{s}_1, \tilde{b}_1$	1595	1595	1427	
$\tilde{d}_2, \tilde{s}_2, \tilde{b}_2$	1530	1530	1358	
$\tilde{e}_1, \tilde{\mu}_1, \tilde{\tau}_1$	665	665(663)	631(629)	
$\tilde{e}_2, \tilde{\mu}_2, \tilde{\tau}_2$	516(510)	515	382	
$\tilde{\nu}_e, \tilde{\nu}_\mu, \tilde{\nu}_\tau$	659	659(657)	616(614)	
$h^0, A^0, H^0, H^\pm$	116	579	577	585

Table 6.4: Mass spectrum of the benchmark point BP2 in the R_p conserving limit. The notation is the same as Table 4.1. The values in brackets denote changes when the non–zero LNV couplings in **S5** DEG is included. As expected, the dominant coupling λ_{231} changes the second and third generation slepton and the (right–handed) selectron masses, but only by at most 1%.

masses. Of course, assuming a heavier mass spectrum is also helpful. In fact, a scan over the cMSSM parameter space with the condition $\lambda_{231} \lesssim \mathcal{O}(0.1)$, leads to the following benchmark point (BP2):

$$\begin{aligned} M_{1/2} &= 760 \text{ GeV}, \\ M_0 &= 430 \text{ GeV}, \\ \tan\beta &= 40, \\ \text{sgn}(\mu) &= -1. \end{aligned} \tag{6.32}$$

The $A_0^{(\lambda')}$ corresponding to this is 1059.2 GeV. The resulting mass spectrum is displayed in Table 6.4. Compare with the original benchmark point BP, the sparticles in BP2 are somewhat heavier than those in BP. Also, while the LSP in BP is a stau, the relatively small differences between $M_{1/2}$ and M_0 in BP2 results in a neutralino LSP ($\tilde{\chi}_1^0$) instead. This leads to distinctly different collider phenomenology, which will be briefly discussed in the next section.

6.3.4 Effects of changing the benchmark point

So far, we have only considered scenarios under the assumption of up–mixing in the quark sector and using the $A_0^{(\lambda')}$ minimum. In the rest of this section we briefly discuss changes which occur when down–mixing is assumed or using the $A_0^{(\lambda)}$ minimum instead.

- $A_0^{(\lambda)}$ **minimum:** We consider as an example the scenario **S2** NH. The best–fit LNV couplings for $A_0^{(\lambda')} = 912.3$ GeV are given in the second row, first column of Table 6.2. When using the $A_0^{(\lambda)}$ minimum instead (given by $A_0^{(\lambda)} = 200.6$ GeV), the λ'_{i22} couplings generate M_2 at tree–level whereas M_3 is generated by λ_{i11} at 1–loop level (for the $A_0^{(\lambda')}$ it

was the other way round). We obtain as a best fit

$$\begin{aligned} \lambda'_{122} &= 1.11 \cdot 10^{-5} \\ \lambda'_{222} &= 1.49 \cdot 10^{-5} \\ \lambda'_{322} &= -8.99 \cdot 10^{-6} \\ \lambda_{211} &= \mathbf{1.53 \cdot 10^{-1}}\ [\mathbf{b3}], [\mathbf{b5}] \\ \lambda_{311} &= \mathbf{1.59 \cdot 10^{-1}}\ [\mathbf{b4}] \end{aligned} \tag{6.33}$$

The decrease (increase) by a factor 10 of the λ'_{i22} (λ_{i11}) couplings reflects the typical hierarchy between the tree–level and the 1–loop neutrino mass of $\mathcal{O}(10^2)$, *cf.* Fig. 6.1. In contrast to the original **S2** NH scenario, this scenario is not compatible with several low–energy bounds as listed in § 5.1 due to the larger λ_{i11} couplings.

- **down–mixing:** When changing the quark mixing assumption from up–type to down–type mixing, *cf.* § 2.2, the LNV parameters are affected via RG running. However, the changes when running from the unification scale down to the electroweak scale are less than 1 percent for diagonal LNV couplings when switching from up–type to down–type mixing. This is because for λ' couplings involving light generations (*e.g.* λ'_{i11}), RG running is dominated by gauge contributions. For couplings involving the third generation (*e.g.* λ'_{i33}), the fact that the only significant mixing in the CKM matrix is between the first two generations implies that the effect of changing the quark mixing is also small. The bilinear LNV couplings responsible for the tree level neutrino mass matrix are dynamically generated by λ couplings, which are of course not affected directly by changes in the quark mixing assumptions. In models where bilinear couplings are generated by λ' couplings, the effect of changing the quark mixing assumption is more complicated.

  Note also that for non–diagonal couplings, the changes are expected to be much larger than for diagonal couplings. This is because Y_D is diagonal when assuming up–quark mixing, while non–zero off–diagonal entries are present when down–quark mixing is assumed instead. We note that similar observations are made in Ref. [134], where a single non–zero LNV coupling is used to saturate the cosmological bound.

  Nevertheless, these small changes for diagonal LNV couplings can still be important, particularly for the IH and DEG scenarios, which are sensitive to the exact values of the LNV parameters. On top of that, 1–loop contributions involving light quark mass insertions can depend sensitively on the quark mixing assumption. For example, $(Y_D)_{11}$ changes by a factor of ~ 2 when the mixing is changed, which implies large changes in the loop contributions involving λ'_{i11}, which in turn will affect all mass ordering scenarios. In contrast, $(Y_D)_{22}$ changes by a couple of percent, so the impact through the mass insertion is relatively mild.

  In principle, changing the mixing assumption, but retaining the same coupling values, can affect χ^2 dramatically, if the width w of the scenario is small. As a numerical example consider a comparison of the three scenarios depicted in Fig. 6.2. **S2** NH, involves λ'_{i22} with a width w of $\mathcal{O}(10\%)$. Here χ^2 increases from ~ 0 in the up–mixing case to about 3 in the down–mixing case. In contrast, in **S3** IH (DEG), where the width is narrower than 1% (0.1%), changing the quark mixing assumption leads to a χ^2 change of 4 (more than 6) orders of magnitude. These changes can be compensated by refitting the LNV couplings. It is not surprising that refitting a subset of couplings is sufficient. For example, a refit of

S3 IH yields:

$$\begin{aligned}
\lambda'_{122} &= 1.70 \cdot 10^{-3} \\
\lambda'_{222} &= -8.80 \cdot 10^{-4} \\
\lambda'_{322} &= 9.71 \cdot 10^{-4} \\
\lambda'_{133} &= 3.11 \cdot 10^{-5} \\
\lambda'_{233} &= 3.22 \cdot 10^{-5} \\
\lambda'_{333} &= -3.32 \cdot 10^{-5}\,,
\end{aligned} \tag{6.34}$$

where the three λ'_{i22} are refitted. A different solution with a small χ^2 can also be obtained by refitting λ'_{i33} alone. The solution in Eq. (6.34) differs from the original up–type mixing solution by $\mathcal{O}(10\%)$. This is what one might expect, bearing in mind that the changes occurring in the CKM matrix from up–type to down–type mixing are $\sim 20\%$.

6.4 Collider Phenomenology

The neutrino models we have found in the previous sections lead to observable collider signatures. We will examine in detail the collider signatures of the *hierarchical* B_3 cMSSM scenario in § 7. This scenario is quasi identical to the here presented scenario **S4** NH, however, it is motivated by a high energy ansatz, cf. § 2.1.1. The magnitude of the couplings in **S4** NH is of the order 10^{-5} or 10^{-6}. The collider phenomenology of scenarios with couplings of the same magnitude will be very similar to the one discussed in § 2.1.1. However, if the couplings become as large as 10^{-3} or smaller than 10^{-6}, the observation of resonant single slepton production or displaced vertices at the LHC might be possible, which we now shortly discuss.

Resonant slepton production typically requires a coupling strength $\lambda'_{i11} \gtrsim 10^{-3}$ for incoming first generation quarks [102–105, 213]. For higher generation quarks an even larger coupling is required to compensate the reduced parton luminosity. In Table 6.2, we see that our models do not satisfy this requirement. However, by considering a scenario which combines aspects of **S1** NH and **S4** NH, it is possible to have a large λ'_{211} while evading the low energy constraints.For example, if we consider an "intermediate" scenario with $\tilde{c}_i^{(2)} \sim \lambda'_{i11}$ and $\tilde{c}_i^{(3)} \sim \lambda_{i22}$, which can be achieved by using a linear combination of the original $c_i^{(\alpha)}$'s (similar to the construction of **S4** NH), we can evade the bounds which exclude **S1** NH and obtain a NH scenario with resonant smuon production. This is because this scenario leads to $\lambda'_{211} = \mathcal{O}(10^{-3})$, whereas $\lambda'_{111} \sim \mathcal{O}(10^{-4})$ is sufficiently small in order to be consistent with **[b8]**, due to the fact that $\tilde{c}_1^{(2)}/\tilde{c}_2^{(2)} \sim \mathcal{O}(10^{-1})$.

Let us now consider the case of very smal LNV couplings. lThe stau lifetime can be estimated by

$$\begin{aligned}
\tau_{\tilde{\tau}} &= [\Gamma(\tilde{\tau} \to f_1 + f_2)]^{-1} = \frac{16\pi}{N_c \Lambda^2 m_{\tilde{\tau}_2}} \\
&= 3.3 \cdot 10^{-15}\,\mathrm{sec} \frac{1}{N_c} \left(\frac{100\,\mathrm{GeV}}{m_{\tilde{\tau}_2}}\right) \left(\frac{10^{-5}}{\Lambda}\right)^2 .
\end{aligned} \tag{6.35}$$

Here N_c is the colour factor, which is 3 for λ' couplings and 1 for λ couplings. We have ignored

any factors due to stau mixing and have only considered one dominant decay mode [13]. The decay length is then given by

$$\begin{aligned} L_{\tilde{\tau}_2} &= \gamma\beta c\tau_{\tilde{\tau}_2} \\ &= \gamma\beta \cdot 10^{-6} m \cdot \frac{1}{N_c} \left(\frac{100\,\mathrm{GeV}}{m_{\tilde{\tau}_2}}\right) \left(\frac{10^{-5}}{\Lambda}\right)^2 . \end{aligned} \tag{6.36}$$

In **S4** NH the stau mass is 163 GeV and $c\tau_{\tilde{\tau}_2} \sim 3\mu$m. Therefore a small fraction of events, with $\gamma\beta$ near 10 for one of the stau LSPs could lead to detached vertices that are observable at the LHC [214]. For a more detailed discussion of the collider phenomenological aspects, we refer the reader to § 7.2 and Refs. [101–105, 150, 213, 215–218].

[13] For a primarily right–handed stau with a dominant λ_{ij3} coupling, an extra factor of 0.5 should be included to account for the two final state configurations $\nu_i l_j$ and $\nu_j l_i$.

Chapter 7

Testing Neutrino Masses in the Hierarchical B_3 cMSSM with LHC Results

In this chapter, we work in the so–called hierarchical B_3 cMSSM described in § 2.1.1. The aim is to derive exclusion limits on the parameter space from SUSY ATLAS searches. We now shortly describe how the LNV sector of the hierarchical B_3 cMSSM is fixed by taking into account the experimental neutrino data of § 3.5 before discussing the resulting collider signatures (§ 7.2) and the exclusion limits (§ 7.3).

7.1 Fixing the LNV Sector of the Hierarchical B_3 cMSSM

According to § 4.6, we need to fix the soft breaking scalar coupling A_0 in order to obtain a phenomenologically viable mass hierarchy in the neutrino sector. We choose A_0 such that it minimizes the λ' contribution to neutrino masses [Eq. (6.2)]. Thus, in the hierarchical B_3 cMSSM a set of 10 free parameters,

$$M_{1/2},\ M_0,\ \mathrm{sgn}(\mu),\ \tan\beta,\ \ell_i,\ \ell'_i, \tag{7.1}$$

fixes the full B_3 cMSSM.

We fit the lepton–number violating parameters to the most recent neutrino oscillation data, including the mixing angle θ_{13} found by Daya Bay, cf. Eq. (3.29). In the quark sector, we assume up–type–mixing. In Ref. [135], it was shown that the choice of quark mixing (e.g. mixing in the up–type versus mixing in the down–type–sector) does not significantly influence the numerical results at the low energy scale.

As described in § 6, it is possible to obtain the experimentally measured neutrino mass squared differences and mixing angles by independently generating each neutrino mass with a set of three L–violating free parameters. This means that 6 or 9 independent couplings are necessary in order to obtain the full spectrum with either two or three massive neutrinos. However, in the case of neutrinos in normal hierarchy mass ordering with a massless lightest neutrino, it turns out that one can do with only 2 couplings to explain the heaviest neutrino mass, m_{ν_3}, cf. Ref. [135]. This is fortunate, because due to our hierarchical ansatz only ℓ'_i, ℓ_1 and ℓ_2 have a significant impact on the neutrino sector whereas ℓ_3 generates only a negligible contribution to the neutrino masses if it is of the same order of magnitude as the other couplings [1]. Therefore, we generate m_{ν_3} at tree–level via the λ_{ijk} couplings, which are in turn determined by ℓ_1 and ℓ_2. The second neutrino mass, m_{ν_2} is generated via λ'_{ijk} (determined by the ℓ'_i) at one–loop level, whereas the lightest neutrino must remain massless, $m_{\nu_1} \approx 0$.

[1] Because of the antisymmetry of λ_{ijk}, $\lambda_{333} = 0$ and ℓ_3 could only contribute to neutrino masses via λ_{233}. This means that for a sizable contribution, ℓ_3 must be several orders of magnitude larger than ℓ_1 or ℓ_2.

In summary, we have 5 free L-violating parameters which control the neutrino sector, ℓ_i' and ℓ_1, ℓ_2. These can be used to generate non-zero m_{ν_2} and m_{ν_3}, respectively, in accordance with the two mass squared difference and three mixing angles from experiment. It is not easily possible to obtain inverse hierarchy or degenerate neutrino masses in the hierarchical B_3 cMSSM unless ℓ_3 becomes several orders of magnitude larger than the other L-violating parameters.

7.1.1 Numerical tools

The low energy mass spectrum and couplings are calculated with `SOFTSUSY3.3` [83]. The numerical minimization of our neutrino parameter χ^2 function is done with the program package `MINUIT2` [219]. The decay widths of the relevant sparticles are obtained with `IsaJet7.64` [220] and `IsaWig1.200`. However, the decay channels of the neutralino LSP via the sneutrino vevs and the κ_i term are absent in `IsaWig1.200`. Therefore, we calculate decays via the bilinear L–violating couplings with `SPheno3.1` [221]. We combined all decay widths in order to calculate the branching ratio of the sparticles. We use the parton distribution functions MRST2007 LO modified [222]. Our signal events are generated with `Herwig6.510` [223]. The cross sections are normalized with the NLO calculations from `Prospino2.1` [224] assuming equal renormalization and factorization scale. Our events are stored in the Monte Carlo event record format `StdHep5.6.1`. We take into account detector effects by using the fast detector simulation `Delphes1.9` [225], where we choose the default ATLAS–like detector settings. Our event samples are then analyzed with the program package `ROOT` [226] and we calculate the 95% and 68% confidence levels (CL) of the exclusion limits with TRolke [227].

7.1.2 Size of the LNV parameters

For each cMSSM point we fit the L–violating parameters ℓ_i and ℓ_i' to the best–fit Normal Hierarchy neutrino mass data in Eq. (3.31). We perform this fit by minimizing the χ^2 function

$$\chi^2 = \frac{1}{N_{\rm obs}} \sum_{i=1}^{N_{\rm obs}} \left(\frac{f_i^{\rm softsusy} - f_i^{\rm obs}}{\delta_i} \right), \tag{7.2}$$

where $f_i^{\rm obs}$ are the central values of the $N_{\rm obs}$ experimental observables in Eq. (3.31), $f_i^{\rm softsusy}$ are the corresponding numerical predictions and δ_i are the 1σ uncertainties. Details of our numerical procedure can be found in chapter 6 or Ref. [135]. Here, we present an example solution where we translate the best fit values ℓ_i and ℓ_i' into the corresponding values of the trilinear L-violating couplings at the unification scale:

$$\begin{aligned} \lambda_{133} &= 1.72 \cdot 10^{-6} \\ \lambda_{233} &= 2.74 \cdot 10^{-6} \\ \lambda'_{133} &= 1.13 \cdot 10^{-5} \\ \lambda'_{233} &= 3.89 \cdot 10^{-5} \\ \lambda'_{333} &= 3.11 \cdot 10^{-5} \end{aligned} \tag{7.3}$$

We have used $M_0 = 100$ GeV, $M_{1/2} = 500$ GeV, $\tan\beta = 25$, $\mathrm{sgn}(\mu)$ and $A_0^{(\lambda')} \approx 2M_{1/2}$. As one can see, the λ_{i33} and λ'_{i33} couplings are between $\mathcal{O}(10^{-5})$ and $\mathcal{O}(10^{-6})$. All remaining trilinear L–violating couplings are at least one order of magnitude smaller, below $\mathcal{O}(10^{-7})$. The

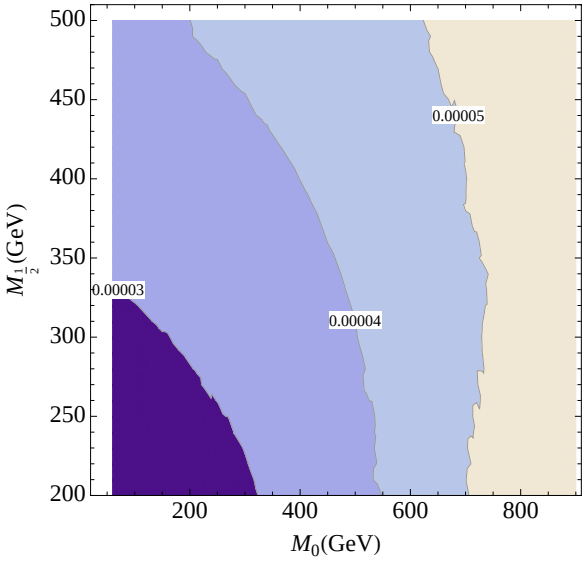

Figure 7.1: Best–fit values of the L–violating coupling λ'_{233} at the unification scale in the M_0–$M_{1/2}$ plane, fixing $A_0^{(\lambda')} \approx 2M_{1/2}$, $\tan\beta = 25$ and $\mathrm{sgn}(\mu) = +1$.

couplings λ'_{233} and λ'_{333} tend to be the largest trilinear L–violating couplings. In Fig. 7.1, we display the best fit value of λ'_{233} in the M_0–$M_{1/2}$ plane. We see that the magnitude of the L–violating couplings does not strongly depend on M_0 and $M_{1/2}$. Furthermore, the relative magnitude of the L–violating couplings to each other remains roughly the same throughout the parameter space.

Recall that the parameter ℓ_3 is not fixed by the neutrino oscillation data in the normal hierarchy scenario. However, we assume that ℓ_3 is of the same order of magnitude as ℓ_1 and ℓ_2, setting $\ell_3 = \ell_2$ in the rest of our paper [2].

We have checked all low energy constraints on the L–violating trilinear couplings [44, 205]. However, in our case the couplings are too small to have an observable impact on any low energy observables.

7.2 Collider signatures

In this section, we investigate possible collider signatures of the hierarchical B_3 cMSSM at the LHC. The best–fit values of the L–violating couplings to neutrino data are too small to have an observable effect on the resonant production of supersymmetric particles. Thus, pair production of colored sparticles via strong interactions is the dominant production channel at the LHC. Only if sleptons and gauginos are much lighter than the colored sparticles, their production rate becomes comparable. The produced sparticles cascade decay into the LSP. In our parameter space, we can have either a stau LSP or a neutralino LSP[3]. The final state collider signature is

[2] ℓ_3 has no relevance for the collider signatures as long as it doesn't become several orders of magnitude larger than ℓ_1 and ℓ_2.

[3] In principle, any sparticle could be the LSP in $\not{R}_p$ models since it is unstable [99]. However, since the L–violating couplings in the hierarchical B_3 cMSSM are small, the particle spectrum remains very similar to the R_p cMSSM and thus the lighter stau is always the lightest sfermion due to large left–right mixing.

determined by the decay properties of the LSP candidate. In the B_3 cMSSM, the LSP is almost always short–lived and decays within the detector via the L-violating interactions [4]. We now describe the final state signatures of stau LSP and neutralino LSP scenarios separately. Then we go on to discuss in which regions of $M_0 - M_{1/2}$ parameter space they occur.

7.2.1 Stau LSP decay

In the parameter region where the lighter stau $\tilde{\tau}_1$ is the LSP, pair produced squarks and gluinos at the LHC cascade decay into the LSP, producing jets and taus (tau–neutrinos) along the way,

$$pp \to \tilde{q}\tilde{q}/\tilde{q}\tilde{g}/\tilde{g}\tilde{g} \to \tilde{\tau}_1\tilde{\tau}_1 + 2j + X, \tag{7.4}$$

where j and X denote jets and additional particles of the process (such as τ or ν_τ), respectively. Note that we can have more than 2 jets in the final state if the process involves gluinos. These additional jets are included in X, which we discuss in more detail in § 7.2.3. For example, right-handed squarks decay into a jet and the lightest neutralino, which then typically decays into a stau and a tau with a branching ratio of one,

$$\tilde{q}_R\,\tilde{q}_R \to jj\tilde{\chi}_1^0\tilde{\chi}_1^0 \to jj\ \tau\tau\ \tilde{\tau}_1\tilde{\tau}_1\,. \tag{7.5}$$

The stau then directly decays into two SM fermions via the trilinear L–violating couplings λ_{133}, λ_{233} and λ'_{3jk}, cf. Fig 7.2. Decays via the λ_{i33} couplings are dominant, even though the decay width via λ'_{3jk} is enhanced by a factor of $N_C = 3$ and the λ'_{3jk} couplings are generally larger. However, the lightest stau is mostly right–handed and thus the coupling of the stau via λ' is suppressed due to the small admixture with the left–handed stau. Additionally, the stau decay via λ'_{333} into a top and bottom quark is kinematically forbidden or suppressed in large regions of parameter space. Stau decays via λ'_{311} and λ'_{322} are heavily suppressed due to the smallness of the couplings.

In principle, the stau can also mix with the charged Higgs boson via κ_3 and decay via the two–body decay mode $\tilde{\tau} \to \tau\nu$. However, we have numerically checked that stau decays via bilinear operators are always sub–dominant in our model. We define a

- **benchmark point BP1** in the stau LSP region with

$$M_0 = 100\ \text{GeV},\ M_{1/2} = 500\ \text{GeV},\ \tan\beta = 25,\ \text{sgn}(\mu) = 1 \text{ and } A_0^{(\lambda')} \approx 2M_{1/2}$$

This benchmark point is characterized by lightest neutralino, lighter stau, gluino and squark masses of 205 GeV, 162 GeV, 1146 GeV and 1012 GeV, respectively. The dominant LSP branching ratios for **BP1** are given by

$$\begin{aligned}
\text{Br}(\tilde{\tau}_1^- \to \tau^-\nu_\text{e}) &= 0.26 \\
\text{Br}(\tilde{\tau}_1^- \to \tau^-\nu_\mu) &= 0.21 \\
\text{Br}(\tilde{\tau}_1^- \to \text{e}^-\nu_\tau) &= 0.26 \\
\text{Br}(\tilde{\tau}_1^- \to \mu^-\nu_\tau) &= 0.21 \\
\text{Br}(\tilde{\tau}_1^- \to \text{s}\,\bar{\text{c}}\,) &= 0.04\,.
\end{aligned} \tag{7.6}$$

[4] Only in a small part of the neutralino LSP region, where $M_{1/2} \lesssim 240$ GeV, the lifetime of the LSP can become larger than $c\tau \gtrsim 15$ mm, cf. Fig 7.6.

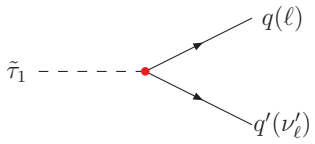

Figure 7.2: Schematic characterization of the stau LSP decay in the hierarchical B_3 cMSSM.

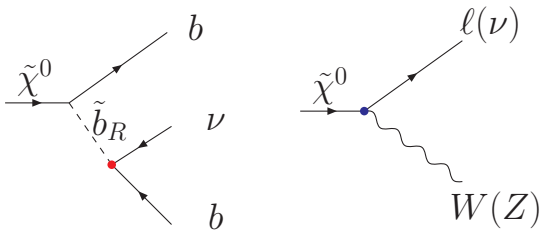

Figure 7.3: Schematic characterization of the three–body (left) and two–body (right) decay modes of the neutralino LSP in the hierarchical B_3 cMSSM.

Note that the branching ratios into different decay channels are roughly independent of the stau mass as long as the final state masses are negligible.

Roughly half of the staus decay into a charged lepton and neutrino, the other half decays into a tau and neutrino. Note that we only denote electrons or muons as leptons in this paper. Since one third of taus decays leptonically, we expect final state collider signatures with either 0, 1 or 2 leptons from the decaying stau LSPs, for 12%, 46% and 42% of events, respectively:

$$\begin{aligned} 0\ell + 2\nu + 2\tau_{\text{had}} + 2j + X \\ 1\ell + 2(4)\nu + 1\tau_{\text{had}} + 2j + X \\ 2\ell + 2(4,6)\nu + 2j + X \end{aligned} \tag{7.7}$$

where ℓ denotes an electron or muon and τ_{had} denotes a hadronically decaying tau. If the lepton[s] in the 1ℓ or 2ℓ channel come from a leptonically decaying tau, the number of neutrinos increases from 2 to 4 [6], as shown in brackets in Eq. (7.7). Due to the Majorana character of the neutralino, both neutralinos can decay into like–charged staus and hence we can have same–sign leptons in the final state.

7.2.2 Neutralino LSP decay

In the hierarchical B_3 cMSSM, the lightest neutralino eigenstate is generally bino–like. The production process is given by

$$pp \to \tilde{q}\tilde{q}/\tilde{q}\tilde{g}/\tilde{g}\tilde{g} \to \tilde{\chi}_1^0\tilde{\chi}_1^0 + 2j + X\,. \tag{7.8}$$

The neutralino LSP can either decay via a trilinear L–violating operator into three SM fermions or via neutralino–neutrino mixing (proportional to the bilinear L–violating couplings and the sneutrino vevs) into a gauge/Higgs boson and a lepton, cf. Fig. 7.3.

For relatively low sfermion masses in the propagator, the trilinear three–body decay modes dominate because the bilinear L–violating couplings are only generated radiatively via RGE

running and the sneutrino vevs are determined to be relatively small from radiative electroweak symmetry breaking. However, in parameter regions with heavy sfermions, the bilinear two–body decay mode becomes dominant because the three body decay mode suffers from phase space suppression and heavy virtual sfermions in the propagator.

First, we discuss the case where the lightest neutralino dominantly decays via the trilinear LNV couplings, for which we define

- **benchmark point BP2** with

$$M_0 = 200 \text{ GeV}, \; M_{1/2} = 400 \text{ GeV}, \; \tan\beta = 25, \; \text{sgn}(\mu) = 1 \text{ and } A_0^{(\lambda')} \approx 2M_{1/2}$$

This benchmark point is characterized by lightest neutralino, lighter stau, gaugino and squark masses of 163 GeV, 213 GeV, 937 GeV and 846 GeV, respectively. We obtain the following LSP branching ratios for **BP2**:

$$\begin{aligned}
\text{Br}(\tilde{\chi}_1^0 \to \overset{(-)}{\nu}_\ell \text{b}\bar{\text{b}}) &= 0.31 \\
\text{Br}(\tilde{\chi}_1^0 \to \overset{(-)}{\nu}_\tau \text{b}\bar{\text{b}}) &= 0.20 \\
\text{Br}(\tilde{\chi}_1^0 \to \text{W}^\pm \ell^\mp) &= 0.21 \\
\text{Br}(\tilde{\chi}_1^0 \to \text{W}^\pm \tau^\mp) &= 0.05 \\
\text{Br}(\tilde{\chi}_1^0 \to \overset{(-)}{\nu}_\tau \text{Z}^0) &= 0.13 \\
\text{Br}(\tilde{\chi}_1^0 \to \overset{(-)}{\nu}_\tau \text{h}^0) &= 0.08
\end{aligned} \tag{7.9}$$

The branching ratio of the three–body decay modes (the $\tilde{\chi}_1^0 \to \nu b\bar{b}$ channel) is roughly 51%. However, for this benchmark point the two–body L–violating decays via bilinear L–violating couplings already have a sizable contribution to the LSP decays. The electron (electron-neutrino) channel is suppressed compared to the muon decay channel because $\lambda'_{133} \sim 0.3\lambda'_{233}$, cf. Eq. (7.3). Therefore, about 90% of our leptons are muons. Summing up the various decay channels and including the gauge boson branching ratios, roughly 72% of neutralinos decay without leptons, 19% with one lepton and 7% with two leptons. This leads to 52%, 27% and 14% of events with 0, 1 and 2 leptons from LSP decays, respectively.

Assuming the cascade decay processes of Eq. (7.8), dominant final state signatures are then given by

$$\begin{aligned}
0\ell + 2\nu + 2b\bar{b} + 2j + X \\
1\ell + 1\nu + b\bar{b} + W_{\text{had}} + 2j + X \\
2\ell + 2\nu + b\bar{b} + 2j + X
\end{aligned} \tag{7.10}$$

Next, we discuss the decay properties of the lightest neutralino in a region where the two–body decays dominate,

- **benchmark point BP3** with

$$M_0 = 600 \text{ GeV}, \; M_{1/2} = 400 \text{ GeV}, \; \tan\beta = 25, \; \text{sgn}(\mu) = 1 \text{ and } A_0^{(\lambda')} \approx 2M_{1/2}$$

The lightest neutralino, lighter stau, gluino and squark masses of **BP2** are 164 GeV, 579 GeV, 961 GeV and 1010 GeV, respectively. Here, the LSP decay channels are the same as for **BP2**;

however, the branching ratios differ drastically:

$$\begin{aligned}
\mathrm{Br}(\tilde{\chi}_1^0 \to \overset{(-)}{\nu}_\ell \mathrm{b}\bar{\mathrm{b}}) &= 0.04 \\
\mathrm{Br}(\tilde{\chi}_1^0 \to \overset{(-)}{\nu}_\tau \mathrm{b}\bar{\mathrm{b}}) &= 0.03 \\
\mathrm{Br}(\tilde{\chi}_1^0 \to \mathrm{W}^\pm \ell^\mp) &= 0.40 \\
\mathrm{Br}(\tilde{\chi}_1^0 \to \mathrm{W}^\pm \tau^\mp) &= 0.14 \\
\mathrm{Br}(\tilde{\chi}_1^0 \to \overset{(-)}{\nu}_\tau \mathrm{Z}^0) &= 0.27 \\
\mathrm{Br}(\tilde{\chi}_1^0 \to \overset{(-)}{\nu}_\tau \mathrm{h}^0) &= 0.12
\end{aligned} \tag{7.11}$$

Since here the scalar masses (M_0) are fairly large, the two–body neutralino decay modes via bilinear L–violating couplings or sneutrino vevs dominate, amounting to 93%. Therefore, there are only half as many neutralinos decaying into the 0ℓ channel as for **BP2**; twice as many decay into the 1ℓ and 2ℓ channel. This results in final state signatures with 0,1 or 2 leptons at 24, 37 and 27%, respectively. Typical final state signatures are given by

$$\begin{aligned}
0\ell + 2\nu + 2Z^0_{\mathrm{had}/\nu\nu} + 2j + X \\
1\ell + 1\nu + Z^0_{\mathrm{had}/\nu\nu} + W_{had} + 2j + X \\
2\ell + 2\nu + Z^0_{\mathrm{had}/\nu\nu} + 2j + X
\end{aligned} \tag{7.12}$$

As mentioned before, the electron decay channel is suppressed by roughly a factor of 10 compared to the muon decay channel. Additionally to the channels mentioned in Eq. (7.12), there are 12% of events with 3 or 4 leptons from LSP decay.

7.2.3 Scan in the $M_0 - M_{1/2}$ plane and kinematical distributions

In the subsequent numerical analysis, we perform a scan in the $M_0 - M_{1/2}$ plane. For this, we define a benchmark region (BR) which contains the three benchmark points defined above (**BP1**, **BP2**, **BP3**):

- **Benchmark region BR** (where M_0, $M_{1/2}$ free):

$$\tan\beta = 25,\ \mathrm{sgn}(\mu) = 1 \text{ and } A_0^{(\lambda')} \approx 2M_{1/2}$$

BP1, **BP2** and **BP3** each lie in distinct sections of the BR: stau LSP region, neutralino LSP region dominated by three-body decays and neutralino LSP region dominated by two–body decays, respectively. This is depicted in Fig 7.4, where the ratio between three– and two–body decay modes of the neutralino LSP is displayed. The two–body $\tilde{\chi}_1^0$ decay modes dominate at large $M_{1/2}$ and M_0. As one can also see in this figure, the stau LSP region within our BR is approximately given by

$$M_{1/2} \geq 3\ M_0 - 80\,\mathrm{GeV}, \tag{7.13}$$

since the lightest neutralino mass is driven to larger values by the large $M_{1/2}$. In general, the lighter stau mass eigenstate is mostly right–handed. In § 7.1.2, we discussed that the absolute magnitude of the L–violating parameters as well as the relative magnitude between them does not vary significantly with M_0 and $M_{1/2}$. This implies that the LSP decay branching ratios are hardly affected by variations of the L–violating parameters within our BR. However, the decay modes are importantly affected by two points, as illustrated in Fig. 7.4:

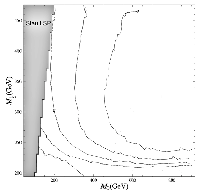

Figure 7.4: The iso curves show the logarithmic ratio between three–body and two–body decay modes of the neutralino LSP in our benchmark region. In the stau LSP region, the two–body stau decay modes via the trilinear RPV couplings are always dominant.

(A) Whether we are in the stau or neutralino LSP region

(B) The ratio between three– and two–body decay modes within the neutralino LSP region.

In the stau LSP region, the 1 and 2 lepton channels are dominant for large regions of parameter space. The 0 lepton channel only becomes significant once the stau becomes heavier than the top–quark. Then, hadronic stau decays via λ'_{i33} contribute significantly and the 1 and 2 lepton studies perform much worse, resulting in a "cutoff" of the sensitive region for stau masses above the top mass. Now, the 0 lepton channel could further exclude parameter space; however, since this region extends well above $M_{1/2} \approx 500$ GeV, we expect that the amount of data collected is not yet large enough to make exclusion possible. In the neutralino LSP region dominated by three–body decays, we expect the 0 lepton channel to be the best, whereas in the case of two–body decays, the 2 lepton channel should perform better.

We now come to a discussion of possible additions to the final state particles from "X" [as contained in Eqs. (7.4) and (7.8)] and the most important distributions for our benchmark region.

Additional jets can arise from gluinos in the hard process, since the gluino decays into quark and (virtual) squark, leading to more jets in the final state [5]. Besides gluino pair and gluino–squark production, gluinos can occur in squark decays if $M_{1/2} \ll M_0$. For example, in **BP3** the gluinos are lighter than the squarks and a sizable fraction of the squarks decay into a gluino and a quark. Thus, we expect a higher jet multiplicity than for **BP1** or **BP2**, where $m_{\tilde{q}} < m_{\tilde{g}}$. This is illustrated in Fig. 7.5 (i). There, we show the distribution of the number of jets for our three benchmark points as well as for a R_p–conserving version of **BP2** and **BP3** with a stable LSP (denoted "**BP2 RPC**" and "**BP3 RPC**", respectively). One can see that for **BP2 RPC**, there are on average only 2-3 jets because here squarks typically decay into a neutralino/chargino and a quark, whereas for **BP3 RPC**, there are 3-4 jets. Comparing **BP2 RPC** to **BP2**, we expect up to 4 additional b–jets from the neutralino LSP decays [Eq. (7.10)], and thus the distribution peaks around $N_{\text{jet}} = 5 - 6$, cf. Fig. 7.5 (i). Similar observations can be made for **BP3**. Here, there are more jets from the (R–parity conserving) decay chain involving gluinos. However, on average there are less jets from neutralino LSP decays, Eq. (7.12), such that the distribution also peaks at $N_{\text{jet}} = 5 - 6$. In the stau LSP case (**BP1**), the distribution peaks at $N_{jets} = 3 - 4$. Here there are only few jets which can be attributed to X (ie. gluino decays), as discussed above.

Further leptons in the final state can emerge in the cascade decays of the SU(2) doublet squarks. The latter decay into charginos and neutralinos with dominant SU(2) gaugino com-

[5] Note that additional jets can also arise from QCD Bremsstrahlung

position, which are typically $\tilde{\chi}_1^\pm$ and $\tilde{\chi}_2^0$ in the cMSSM. $\tilde{\chi}_1^\pm$ and $\tilde{\chi}_2^0$ subsequently decay either into slepton and lepton or gauge boson/Higgs and the lightest neutralino. However, this leads to isolated leptons in only $\sim$15% of events in our case, as is illustrated in Fig. 7.5 (ii) by the N_ℓ distributions for **BP2 RPC** and **BP3 RPC**. The reason for this is that in **BP2**, the $\tilde{\tau}_1$ is much lighter than the other sleptons, whereas the latter are heavier than $\tilde{\chi}_2^0$ and $\tilde{\chi}_1^\pm$. Thus $\tilde{\chi}_2^0$ and $\tilde{\chi}_1^\pm$ dominantly decay into $\tilde{\tau}\tau$ and $\tilde{\tau}\nu$, respectively. About one third of these τ's decay leptonically, leading to final state leptons. In **BP3**, all sleptons are heavier than $\tilde{\chi}_1^\pm$ and $\tilde{\chi}_2^0$ and hence the latter preferably decay into a gauge/Higgs boson and the lightest neutralino. Comparing **BP2 RPC** and **BP3 RPC** with the corresponding $\not{R}_p$ scenarios, we clearly see that there are significantly more leptons for **BP2** and **BP3** due to leptonic decays of $\tilde{\chi}_1^0$. However, there are more entries in the 0 lepton bin for **BP2** and **BP3** than expected from Eqs. (7.10) and (7.12), because some of the leptons are non-isolated or too soft or do not fall into the acceptance region of the tracking system. The same holds for **BP1**, which has overall the largest number of isolated leptons; nevertheless the ratio between events with 1 lepton and 0 leptons is still less than predicted from Eq. (7.7) [6].

In Fig. 7.5 (iii), we present the missing transverse momentum distribution. Here, we clearly see that **BP1** has the hardest distribution among all R_p violating distributions. Note that for the two other R_p violating scenarios the missing transverse energy distribution is much softer compared to the respective R_p conserving scenarios, due to the LSP decays.

7.3 Exclusion limits on the Hierarchical B_3 cMSSM parameter space

In this section, we further constrain the hierarchical B_3 cMSSM parameter space using data from the LHC at $\sqrt{s} = 7$ TeV with an integrated luminosity of up to 5 fb^{-1}. We focus on recent ATLAS studies with 0,1 or 2 isolated leptons, several jets and large missing transverse momentum. A short overview over the ATLAS studies used is given in Table 7.1. Full details of objects reconstruction, definitions of all kinematical observables and event selection cuts of all three analyses can be found in the respective ATLAS publications [84–86] (0 lepton), [90, 91] (1 lepton) and [93] (2 leptons). We have chosen these analyses because they only rely on simple objects such as electrons, muons, jets and missing transverse momentum in the final state. Thus, we do not rely on complicated tau reconstruction and b–tagging algorithms, which are difficult to simulate with the detector simulation `Delphes1.9` [225]. In particular, difficulties arise in reconstructing hadronically decaying taus [101]. Also, the published ATLAS studies for supersymmetry involving taus [228] or b–jets [229] in the final states have smaller cross–sections or smaller efficiencies than the multi–jet, large $\not{p}_T$ and lepton searches. Thus, we expect the "simple" 0-2 lepton analyses to perform better with the current amount of data. So far, the experimental data is in agreement with the SM background expectations. We use their results in order to derive the 68% and 95% CL exclusion regions in the M_0–$M_{1/2}$ parameter space. We plan to investigate exclusion limits arising from third generation studies and multi–lepton studies in a future publication.

ATLAS and CMS have recently published conference notes which found that the lightest Higgs is at least heavier than 117.5 GeV at 95% CL [230, 231]. In the hierarchical B_3 cMSSM, the lightest Higgs is typically rather lighter than 116 GeV, because the value of A_0 is necessarily

[6] Note that for **BP1** additional leptons can arise from non–vanishing branching ratios of $\tilde{\chi}_1^\pm$ and $\tilde{\chi}_1^0$ into first and second generation sleptons and the corresponding leptons.

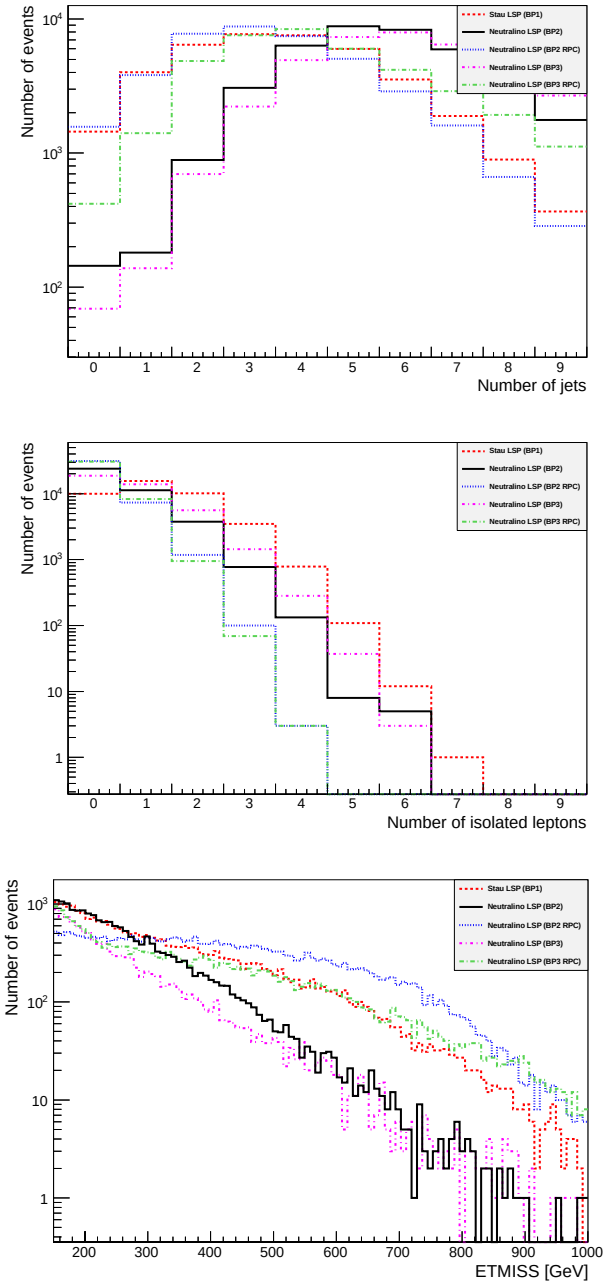

Figure 7.5: We depict (i) the number of jets N_{jet}, (ii) the number of isolated leptons N_ℓ with $p_T > 20$ GeV and (iii) the missing transverse momentum ("ETMISS") for our benchmark points **BP1**, **BP2** and **BP3**. Additionally we display an R_p version of **BP2** and **BP3** ("**BP2 RPC**","**BP3 RPC**"), where the neutralino LSP is kept stable. We generated 40000 events for each benchmark point.

	0lept–SRE–m	1lept–3j	2lept–OS–4j
N_ℓ	0	1	2
N_{jet}	6	3	≥ 4
p^T_{jets}	$>(130, 60, 60, 60, 40, 40)$	$>(100, 25, 25)$	$>(100, 70, 70, 70)$
$\not{p}_T$	> 160	> 250	> 100
$m^{\text{inc}}_{\text{eff}}$	> 1200	> 1200	–
$\frac{\not{p}_T}{m_{\text{eff}}}$	> 0.15	> 0.3	–
$\mathcal{L}$	4.7 fb^{-1}	4.7 fb^{-1}	1.0 fb^{-1}

Table 7.1: The main cuts used in the ATLAS studies used in this collider study. More details concerning the cuts can be found in the relevant ATLAS studies (0 lepton [86], 1 lepton [91] and 2 lepton [93]). N_ℓ denotes the number of isolated leptons, N_{jet} the number of jets and p^T_{jets} specifies the minimal transverse momentum which is required for these jets. $\not{p}_T$ gives the minimal value of missing transverse momentum of the event, $m^{(inc)}_{\text{eff}}$ the minimal (inclusive) effective mass and $\mathcal{L}$ denotes the total integrated luminosity at 7 TeV.

fixed to be positive and similar in magnitude to $2M_{1/2}$, cf. § 7.1. This means that the stop mixing cannot become very large and thus the loop contributions to the lightest Higgs mass are moderate. We have checked various values of $\tan\beta$ and both $\text{sgn}(\mu) = \pm 1$; however, we found that the Higgs mass does not become larger than 117 GeV for M_0, $M_{1/2} < 1$ TeV. Therefore, the exclusion limits derived from this lightest Higgs mass bound would by far exceed the exclusion limits derived from the 0, 1 and 2 lepton channels mentioned above. However, it could be possible to soften the bound if we extend the field content of the hierarchical B_3 MSSM by a singlet, i.e. working in the next-to minimal SSM (NMSSM) [232–234]. We leave this topic for a future investigation at a time when there is more certainty regarding the lightest Higgs mass.

Before applying the model independent cross section limits from the ATLAS searches to our neutrino model, we checked that the Monte Carlo tools are correctly tuned. Therefore, we generated 20000 events for each grid point in the M_0–$M_{1/2}$ plane in the R–parity conserving cMSSM. We determined the 95% CL exclusion region in the M_0–$M_{1/2}$ plane for the ATLAS "1lepton-3j" study (cf. Table 7.1) and verified that our results are compatible with the interpretation from ATLAS within ±30 GeV. We now discuss the 0, 1 and 2 lepton channels in detail.

7.3.1 0 lepton channel

ATLAS has used the 0 lepton channel as one of the first search channels for supersymmetry [84–86]. So far, they have collected a total luminosity of about 4.7 fb^{-1} at the center of mass energy of $\sqrt{s} = 7$ TeV. From the non–observation of an excess, we can derive exclusion limits on the hierarchical B_3 cMSSM. The ATLAS 0 lepton channel is divided into several signal regions (SR). For all signal regions, the cut on $\not{p}_T$ and the minimum requirement on p^T_{jet} of the first two most–energetic jets are identical. However, the number of jets and the minimum p^T_{jet} cut for the remaining jets as well as the cut on m^{inc}_{eff} and on the ratio $\not{p}_T/m_{\text{eff}}$ differ for the different signal regions.

We have examined all signal regions after applying the object reconstruction described in their study and found that we obtain the strictest exclusion limits for the "SRE–m" signal region, which demands 6 jets, $m^{\text{incl}}_{\text{eff}} > 1200$ GeV and $\frac{\not{p}_T}{m_{\text{eff}}} > 0.15$, cf. Table 7.1. We show the resulting plot in the M_0–$M_{1/2}$ plane in Fig. 7.6. The exclusion limit peaks at $M_0 \approx 200$ GeV. This is

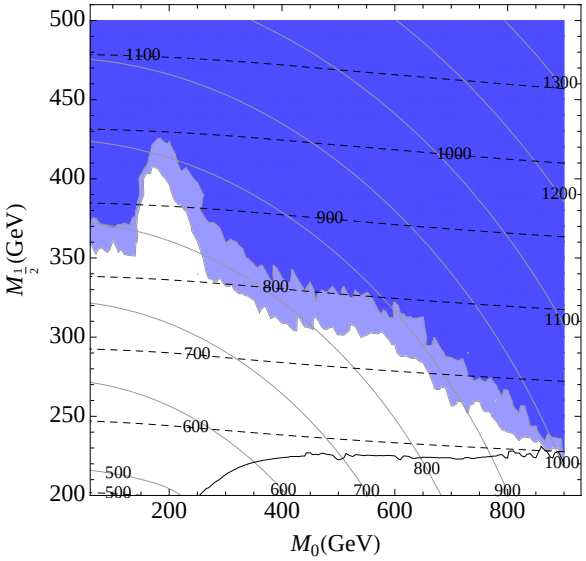

Figure 7.6: Exclusion limit on our benchmark region, where $\tan\beta = 25$, $\mathrm{sgn}(\mu) = 1$ and $A_0^{(\lambda')} \approx 2M_{1/2}$, from the 0 isolated leptons, 6–jets and MET ("0lept–SRE–m") ATLAS study. The white region is excluded at 95% confidence level (CL), the light blue is excluded at 68% CL. The grey lines denote the gluino masses, the dashed black lines denote the squark masses (each in GeV). The black line delineates the region (below) where the lifetime of the LSP becomes larger than $c\tau \gtrsim 15$ mm.

the region where the neutralino LSP decays dominantly via three–body decays $\tilde{\chi}_1^0 \to \nu b\bar{b}$, *c. f.* Fig. 7.4. It was to be expected that the "SRE–m" signal region gives good exclusion limits for this type of scenario, because if both neutralinos decay via $\tilde{\chi}_1^0 \to \nu b\bar{b}$, we expect at least 6 parton level jets (including b–jets). Also, we have only moderate $\not{p}_T$ because of the three–body decay of the neutralino, and therefore more events survive in the "SRE–m" than in the "SRE–t" scenario (where $m_{\mathrm{eff}}^{inc} > 1500$ GeV). Finally, leptons from the cascade decays of SU(2) doublet squarks into $\tilde{\chi}_1^\pm$ and $\tilde{\chi}_0^2$ are suppressed, since the latter dominantly decay into $\tilde{\chi}_1^\pm \to \tilde{\tau}\nu$ and $\tilde{\chi}_2^0 \to \tilde{\tau}\tau$.

For increasing M_0, the exclusion region decreases to lower $M_{1/2}$ values. We can see in Fig. 7.4 that the two–body decay mode of the neutralino becomes more important here. Thus, an increasing number of the neutralino LSPs decay into a gauge boson and a lepton and less b–jets are expected in the final state, so that less events pass the kinematical cuts on the final state jets. Another effect is that for larger M_0, the production cross section decreases.

Directly to the left of the peak at $M_0 \approx 200$ GeV, the limit drops off sharply because here the LSP becomes the $\tilde{\tau}_1$ and there are significantly less events with 6 jets and no leptons. However, $M_{1/2} \lesssim 350$ GeV can still be excluded at 95% CL. We would like to point out that in principle, it is possible to obtain better exclusion limits (up to $M_{1/2} \lesssim 400$ GeV) in the stau LSP case by using a signal region with only 4 or 5 jets. However, the 1 lepton study performs even better and therefore we go not into detail about the results from these signal regions here.

7.3.2 1 lepton channel

Refs. [90, 91] search for multi–jet events with large missing transverse momentum and exactly one isolated lepton. Similarly to the 0 lepton channel in the previous subsection, the 1 lepton

channel was one of the first supersymmetry search channels and the current integrated luminosity is 4.7 fb^{-1} at the center of mass energy of 7 TeV. They consider signal regions with 3– or 4–jets with different kinematic configurations, which are optimized for the R_p cMSSM with a large mass difference between the gluino and the LSP. Additionally, they include a soft–lepton signal region which is sensitive to scenarios with small mass splitting between the sparticles.

Comparing the results for the different signal regions, we observe that the 3–jet signal region ("1lept–3j") provides us with the best overall exclusion limits in the stau LSP region up to $M_{1/2} \sim 500$ GeV (i.e. better than the limits from any other signal region in the 0 to 2 lepton channels). The main kinematic cuts of the 1lept–3j signal region are listed in Table 7.1 and the resulting plot is shown in Fig. 7.7. Almost half of the events in the stau LSP region decay into final states with 1 lepton, cf. § 7.2.1. Note also that the 1 lepton study [91] demands the most stringent cut on $\not{p}_T$ among the 0, 1 and 2 lepton studies. In the stau LSP region with direct (two–body) leptonic decays, much more missing transverse momentum is produced than in the neutralino LSP region. In particular in the neutralino LSP region with dominant three–body decays into $\nu\bar{b}b$, the amount of $\not{p}_T$ is greatly reduced compared to the stau LSP region. Moreover, much less charged leptons arise from the neutralino decay. Additional leptons from the cascade decays are also heavily suppressed. Thus, we have a sharp drop of the acceptance in the crossover region between the stau and neutralino LSP region. For larger M_0 values, eventually the two–body neutralino decay modes become dominant over the three–body decay mode. However, the hard cut on $\not{p}_T$ still rejects many signal events in this region.

Note that the ATLAS signal region with 1 lepton and 4–jets is also sensitive to the neutralino LSP region besides the stau LSP region. This explains why in the old 4–jet signal region with 1 fb^{-1} in the muon channel, ATLAS was able to constrain the bilinear $\not{R}_p$ model presented in Ref. [90] (with two–body neutralino decays) quite well. However, having in mind that in our case we have addtional three–body decays and in the new 5 fb^{-1} study, the cuts are more stringent cuts than the 1 fb^{-1} version and not optimized for our type of scenario, the resulting exclusion limits on the neutralino LSP region are weaker than the limits derived in the 2 lepton channel as shown below.

7.3.3 2 lepton channel

The ATLAS study based on final states with two leptons and missing transverse momentum [93] has not yet been updated to include more than 1 fb^{-1} of data. The search is divided into opposite–sign (OS), same–sign (SS) and flavour–subtraction (FS) signal regions where up to 4 jets are demanded besides exactly 2 leptons and a cut on $\not{p}_T$. We find that we obtain the best exclusion limits with the OS signal regions. The three OS regions differ in the $\not{p}_T$ cut, the number of jets and the corresponding minimal p^T_{jets} cut. As in the case of the 1 lepton channel, the OS studies with the hardest transverse missing momentum cut ("2lept–OS–2j", $\not{p}_T > 250$ GeV) are quite sensitive to the stau LSP region where two staus decay leptonically. However, in the 2 lepton channel the obtained exclusion limits are $\sim$50 GeV weaker than in the "1lept–3j" study. This is due to the stringent cuts on m^{inc}_{eff} and on the ratio $\not{p}_T/m_{\text{eff}}$ in the "1lept–3j" search channel, which yield better signal isolation and background suppression.

The OS and 4–jet channel with a moderate $\not{p}_T$ cut of 100 GEV ("2lept–OS–4j"), described in Table 7.1, provides us with the best exclusion limits for $M_0 \gtrsim 300$ GeV, where the neutralino LSP decays dominantly via two–body decays as shown in Fig. 7.8. We notice a slight dip for smaller M_0 ($M_0 \sim 200$ GeV), where there are dominant three–body neutralino decays. Here, as discussed in the previous subsections, parton–level leptons from the neutralino LSP decays or

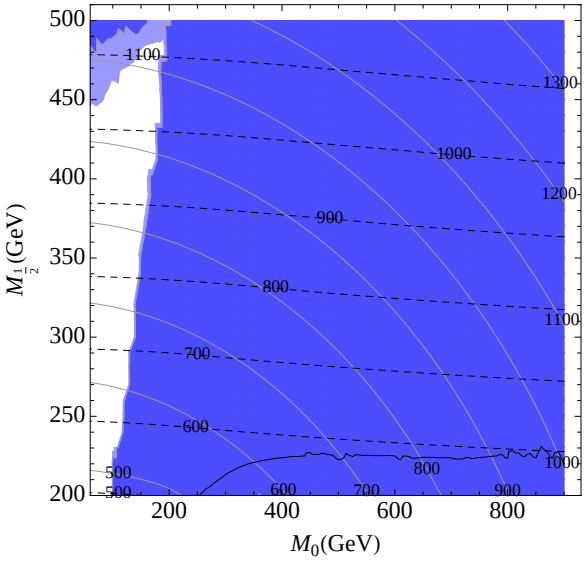

Figure 7.7: Exclusion limit on our benchmark region, where $\tan\beta = 25$, $\mathrm{sgn}(\mu) = 1$ and $A_0^{(\lambda')} \approx 2M_{1/2}$, from the 1 isolated lepton, 3–jets and MET ("1lept–3j") ATLAS study [91]. The white region is excluded at 95% CL, the light blue is excluded at 68% CL. The grey lines denote the gluino masses, the dashed black lines denote the squark masses (each in GeV). The black line delineates the region (below) where the lifetime of the LSP becomes larger than $c\tau \gtrsim 15$ mm.

from the cascade decays of the SU(2) doublet squarks are heavily suppressed and the exclusion limits from the 0 lepton channel are more stringent. For even smaller values of M_0, we are in the stau LSP region and the exclusion limits improve again. However, as discussed in the last paragraph, the cuts are not optimized for a stau LSP scenario. The E_T^{miss} cut is the weakest among all three analyses in Table 7.1 and the kinematic requirements on the jets are harder compared to the "1lept–3j" search channel.

For $M_0 \gg M_{1/2}$, the gluino is generally lighter than the squarks and thus we expect a higher jet multiplicity and in general more jets passing the kinematic cuts. However, much less transverse momentum is generated compared to the R–parity conserving case or the stau LSP region. Thus, the "2lept–OS–4j" yields the better overall exclusion region in the neutralino LSP region with dominant bilinear RPV decays due to the softer E_T^{miss} cut compared to "0lept–SREm". One further remark on the number of leptons in the final state: for $M_{1/2} \ll M_0$, the SU(2) doublet squarks decay via a wino–like gaugino is quite sizable, although we have the competing decay channel via an off–shell gluino. These wino–like gauginos again dominantly decay into gauge bosons providing additional leptons in the final state.

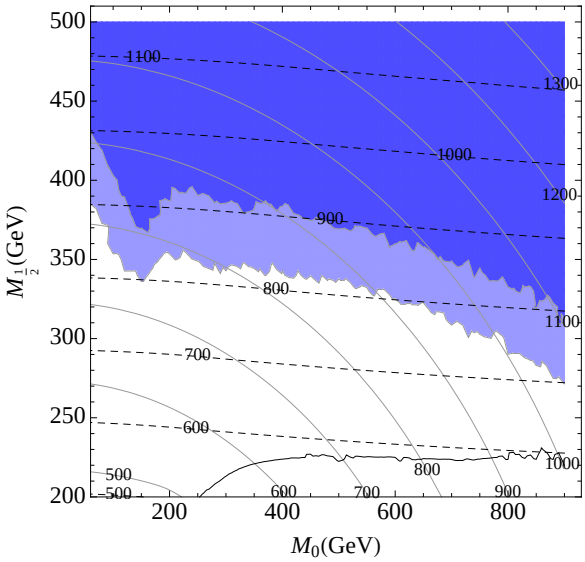

Figure 7.8: Exclusion limit on our benchmark region, where $\tan\beta = 25$, $\mathrm{sgn}(\mu) = 1$ and $A_0^{(\lambda')} \approx 2M_{1/2}$, from the 2 isolated opposite–sign leptons, 4–jets and MET ("2lept–OS–4j") ATLAS study. The white region is excluded at 95% CL, the light blue is excluded at 68% CL. The grey lines denote the gluino masses, the dashed black lines denote the squark masses (each in GeV). The black line delineates the region (below) where the lifetime of the LSP becomes larger than $c\tau \gtrsim 15$ mm.

Chapter 8

Light Stop Searches at the LHC with Monojet Events

We consider light top squarks (stops) in the R_p–conserving MSSM at the LHC. Here, we assume that the lightest neutralino is the lightest supersymmetric particle (LSP) and the lighter stop is the next–to–LSP. We consider stop pair production in association with one QCD jet,

$$pp \to \tilde{t}_1 \tilde{t}_1^* j + X, \tag{8.1}$$

where X stands for the rest of the event. We assume that the mass difference between the lightest stop and the lightest neutralino is a few tens of GeV or less, and that the on–shell $\tilde{t}_1 \to \tilde{\chi}_1^+ b$ and $\tilde{t}_1 \to b \tilde{\chi}_1^0 W$ decays are closed. Due to the small mass splitting to the LSP, four–body decays like $\tilde{t}_1 \to \tilde{\chi}_1^0 \ell^+ \nu_\ell b$ are strongly suppressed. However, the flavor changing neutral current (FCNC) stop decay into a charm–quark and the lightest neutralino,

$$\tilde{t}_1 \to c \tilde{\chi}_1^0 , \tag{8.2}$$

is open. This decay can only occur if $\tilde{t}_1$ has a non–vanishing $\tilde{c}$ component. As pointed out in [127, 128], such a component will be induced radiatively though CKM mixing even if it is absent at tree level. For simplicity we assume that it has branching ratio of 100%.

The small mass difference to the LSP also implies that both charm "jets" in the signal are rather soft.[1] The charm quarks will then not be useful for suppressing backgrounds since soft jets are ubiquitous at the LHC, and may not be detected as jets at all. Thus our signal will be a single high p_T jet with large missing energy,

$$pp \to j \not{p}_T, \tag{8.3}$$

possibly accompanied by one or more soft jet(s) from gluon radiation and the $\tilde{t}_1$ decay products. At the LHC, the largest contribution to stop pair production in association with a jet comes from gluon fusion diagrams, but contributions from qg and $\bar{q}g$ initial states, which become more important for large $\tilde{t}_1$ masses, are nearly as large.[2] Contributions from $q\bar{q}$ annihilation are relatively small. We perform a full leading order analysis, using exact $\mathcal{O}(\alpha_S^3)$ parton–level cross sections for gg, $q\bar{q} \to \tilde{t}_1 \tilde{t}_1^* g$ and $gq \to \tilde{t}_1 \tilde{t}_1^* q$.

Since most events have at least one gluon in the initial state, we expect strong QCD bremsstrahlung due to the large color charge. The QCD radiation increases with increasing stop mass. However, the topology of the signal is still simple compared to standard supersymmetric collider

[1] Unless the stop squarks themselves are highly boosted, which is true only in a tiny fraction of all signal events.
[2] For light stop masses of 120 GeV, the qg contribution is already about 43% of the total cross section. It increases to 47% for 300 GeV stops.

signatures: a single energetic jet, which is essentially back to back to the missing transverse momentum vector.

After shortly introducing our numerical tools, we discuss the major backgrounds in the next section, and describe how to determine them from experimental data, including a discussion of the resulting systematic and statistical errors. Next, we shortly discuss our numerical tools before introducing a specific benchmark scenario. We then show the relevant kinematic distributions and motivate our final cuts. We conclude the chapter with the discovery reach at the LHC in the neutralino–stop mass plane.

8.1 Preliminaries

8.1.1 Benchmark Scenario

In the introduction, we motivated scenarios with a light stop and light neutralino in order to be fully consistent with dark matter and electroweak baryogenesis. However, in this study we do not only want to discuss these scenarios, but also to determine the discovery reach in the stop–neutralino plane, where the mass difference between stop and lightest neutralino is at most a few tens of GeV. On the one hand, scenarios with a heavier stop are expected to have a worse signal to background ratio than those with a very light stop, due to the very quickly decreasing production cross section. However, for heavier stops, producing an additional hard jet reduces the cross section by a smaller factor than for light stops. We choose a scenario with a rather large stop mass, in order to probe the discovery reach found in Ref. [130]:

$$m_{\tilde{t}_1} = 220\text{GeV}, \tag{8.4}$$

as a benchmark scenario. The mass of the lightest neutralino is

$$m_{\tilde{\chi}_1^0} = 210\text{GeV}. \tag{8.5}$$

All remaining sparticles are decoupled.[3]

We require $p_T(\text{jet}) \geq 150$ GeV for the parton–level jet. The total leading order (LO) cross section for our signal then only depends on the stop mass. The cross section for the benchmark point is $\sigma = 4.2$ pb. We have generated $8 \cdot 10^5$ signal events for our benchmark point. LO predictions for cross sections for different stop masses are listed in Table 8.1.

As described at the beginning of this chapter, we assume that all $\tilde{t}_1$ undergo two–body decay

$$\tilde{t}_1 \to c\,\tilde{\chi}_1^0\,. \tag{8.6}$$

We assume that these decays are prompt; a finite impact parameter would greatly facilitate detection of the signal [239].

[3] In order to reduce stop and sbottom loop contributions to electroweak precision variables, in particular to the ρ parameter [235–238], our $\tilde{t}_1$ should be predominantly an $SU(2)$ singlet. However, the stop mixing angle and the identity of the LSP are irrelevant for our analysis. Similarly, the presence of relative light higgsino–like chargino and neutralino states, as required for EW baryogenesis, does not affect our analysis, as long as they are not produced in $\tilde{t}_1$ decays. We primarily use the right–left stop mixing parameter A_t and the gaugino mass M_1 as parameters to obtain the desired values for $m_{\tilde{t}_1}$ and $m_{\tilde{\chi}_1^0}$, respectively.

$m_{\tilde{t}_1}$ [GeV]	120	140	160	180	200	220	240	260	280	300	320
σ [pb]	31	20	13	8.8	6.0	4.2	2.9	2.1	1.5	1.2	0.86

Table 8.1: Total hadronic cross sections in pb for the signal at $\sqrt{s} = 14$ TeV. The cross sections were calculated with `Madgraph4.5.5`, with a parton–level cut $p_T > 150$ GeV on the jet.

8.1.2 Numerical tools

The masses, couplings and branching ratios of the relevant sparticles are calculated with `SPheno-2.2.3` [240], starting from weak–scale inputs for the relevant parameters. We use the CTEQ6L1 parton distribution functions and the one–loop expression for the strong gauge coupling with five active flavors with $\Lambda_{\rm QCD} = 165$ MeV [241]. Our parton–level signal events are generated with `Madgraph4.4.5` [242]. These events are then passed on to `Pythia8.150` [243] for showering and hadronization. As already mentioned, we generate our SM background events directly with `Pythia8.150` fixing the $t\bar{t}$ normalization as in Table 8.2. Apart from the $t\bar{t}$ sample, we employed a parton–level cut on minimum transverse momentum of 150 GeV on our parton–level jet, which will become the "monojet" in our signal and background; the final cut on the p_T of this jet will be much harder, so that the cut on the parton–level jet, which greatly increases the efficiency of generating signal and background events, does not affect our final results. Our events are stored in the Monte Carlo event record format `HepMC 2.04.01` [244]. We take into account detector effects by using the detector simulation `Delphes1.9` [225], where we choose the default ATLAS–like detector settings. Our event samples are then analyzed with the program package `ROOT` [226].

We define jets using the anti$-k_t$ algorithm implemented in FastJet [245], with a cone radius $\Delta R = \sqrt{(\Delta\phi)^2 + (\Delta\eta)^2} = 0.7$, where $\Delta\phi$ and $\Delta\eta$ are the difference in azimuthal angle and rapidity, respectively. All jets have to have $p_T > 20$ GeV. We demand that electrons have $p_T(e) > 10$ GeV and are isolated, i.e. that there is no other charged particle with $p_T > 2.0$ GeV within a cone radius $\Delta R = 0.5$. Since muons can be identified even if they are not isolated and have quite small p_T [246], we include all reconstructed muons with $p_T > 4$ GeV. Note that `Delphes1.9` assumes a track reconstruction efficiency of only 90%, giving a substantial probability that charged leptons are lost. Moreover, we only include true leptons, i.e. we do not attempt to estimate the rate of fake leptons.

In `Delphes1.9`, the same object can in principle be reconstructed as several different objects. *E.g.*, an electron can be reconstructed as an electron as well as a jet. Since such double counting of objects has to be prevented, we use an object removal procedure similar to that outlined in Ref. [247]. However, any jet within ΔR < 0.2 of an electron (including non–isolated electrons) will be removed if

$$p_T(\text{jet}) - p_T(e^{\pm}) < 20\text{GeV}. \tag{8.7}$$

This removes "jets" whose energy is dominated by an electron, but we keep hard, hadronic jets even if they are very close to an electron. Note that contrary to Ref. [247], we keep all isolated electrons and all muons even if they are close to a jet.

8.2 Backgrounds

The dominant SM backgrounds are:

process	$Z(\to \nu\bar{\nu}) + j$	$W(\to e\nu_e, \mu\nu_\mu) + j$	$W(\to \tau\nu_\tau) + j$	$t\bar{t}$
σ [pb]	37	94	47	800

Table 8.2: Total hadronic cross sections in pb for the main SM backgrounds at $\sqrt{s} = 14$ TeV. The cross sections were calculated with `Pythia8.150` apart from $t\bar{t}$ production, which is calculated in Ref. [248]. The $V + j$ ($V = W, Z$) cross sections have been calculated demanding $p_T > 150$ GeV for the parton–level jets.

- $Z(\to \nu\bar{\nu}) + j$ production, *i.e.* Z boson production in association with a jet. The Z boson decays into a pair of neutrinos. If the charm jets in the signal are very soft, this background looks very similar to our signal. We will see in § 8.4 that $Z(\to \nu\bar{\nu}) + j$ is the dominant irreducible background after applying all kinematic cuts. Fortunately its size can be directly determined from data: One can measure $Z(\to \ell^+\ell^-) + j$, where the Z decays into a pair of either electrons or muons. From the known Z branching ratios (BRs) one can then obtain an estimate for the background cross section. However, this procedure will increase the statistical error, since $BR(Z \to \ell^+\ell^-) \simeq BR(Z \to \nu_i\bar{\nu}_i)/3$ after summing over $\ell = e$, μ and all three generations of neutrinos. Moreover, not all $Z \to \ell^+\ell^-$ events are reconstructed correctly. Including efficiencies, Ref. [132] estimated that the calibration sample $Z(\to e^+e^-/\mu^+\mu^-) + j$ is roughly a factor of 5.3 smaller than the $Z(\to \nu\nu) + j$ background in the signal region.[4] Hence, we expect that the error of this background is $\sqrt{5.3} \simeq 2.3$ times larger than the statistical error.

- $W(\to \ell\nu) + j$ production, where the W decays leptonically. Unlike the signal, this background contains a charged lepton ($\ell = e^\pm, \mu^\pm$), and will thus resemble the signal only if the charged lepton is not identified. This can happen when the charged lepton emerges too close to the beam pipe or (in case of electrons) close to a jet. Since the production cross section for $W(\to \ell\nu) + j$ is larger than $Z(\to \nu\bar{\nu}) + j$ by a factor of ~ 3, this will still contribute significantly to the overall background, as we will see in § 8.4. The $W(\to \ell\nu_\ell) + j$ background can be determined by extrapolation using events where the lepton is detected.

- $W(\to \tau\nu) + j$ production, where the W decays into a tau. The reconstructed jets from a hadronically decaying tau are in general not back to back in azimuth to the missing momentum vector. Ref. [132] exploits this feature to suppress the tau decay channel of $W + j$. However, identification of hadronically decaying τ leptons is not easy. This background can be experimentally determined with the help of $W(\to \ell\nu) + j$ events where the charged lepton is detected, using known tau decay properties. We (quite conservatively) assign an overall systematic uncertainty of 10% for the total $W + j$ background, including that from $W \to \ell\nu_\ell$ decays.

- $t\bar{t}$ production (including all top decay channels). Top decays will almost always produce two $b-$jets. Since we require large missing E_T, at least one of the W bosons produced in top decay will have to decay leptonically. Note that this again gives rise to a charged lepton (e, μ) or τ, whereas the signal does not contain isolated charged leptons. However, for hadronically decaying τ's, we can have large missing E_T with no e or μ present. This

[4] Ref. [132] cites a factor of seven between the $Z \to \ell^+\ell^-$ control sample and the *total* background from $V + j$ production ($V = W^\pm, Z$), after applying a lepton veto in the signal. The ratio of 5.3 follows since according to the cuts of [132], about 75% of the $V + j$ background comes from $Z(\to \nu\bar{\nu}) + j$.

background can again be estimated by normalizing to $t\bar{t}$ events where (at least) one charged lepton is detected. Just as for the $W + j$ background, we assume a total systematic error of 10%.

We consider the above default estimates of systematic errors to be conservative, since they do not rely on Monte Carlo simulations. We expect that the SM contribution to the missing transverse energy signal rate will be determined with at least this precision. For example $W^{\pm}+j$ and even $\gamma + j$ samples can also be used for reducing the error on the leading $Z(\to \nu\bar{\nu}) + j$ background, since these classes of events have very similar QCD dynamics [249].

In principle, one should also consider single top production, since semi–leptonic top decays can again give rise to large missing E_T. However, the production cross section for single top production is a factor of ~ 4 smaller than for $t\bar{t}$. Even though $t\bar{t}$ is important for the cut selection, we will see that in the end it only contributes 5% to the total SM background. For these reasons, we neglect single top production as a background. We do not consider pure QCD dijet and trijet production in our analysis, since a large $\not{p}_T$ cut is expected to essentially remove those backgrounds [247, 250, 251]. We also neglect gauge boson pair production as background, since the total cross section is much smaller than that for single gauge boson plus jet production.

There are many SUSY processes leading to a monojet signature, which could be considered to be backgrounds to our signal. LSP pair plus jet production always gives a monojet signature, but has a very small cross section. Associate gluino plus squark production can lead to monojets if the gluino mass is close to that of the neutralino LSP. In addition, squark pair production can give rise to monojets, if both squarks directly decay into the LSP and one of the two jets is lost in the beam direction or the partons from both squarks are reconstructed in the same jet. Recently, [251] considered squark–wino production. However, as we argued in the introduction, in order to avoid bounds from electron and neutron EDM, we assume that most superparticles are quite heavy. Thus, the production rates of these additional supersymmetric processes are strongly suppressed and we need only consider Standard Model backgrounds.

Estimates for the total hadronic cross sections for these SM backgrounds are given in Table 8.2. The cross section for the $t\bar{t}$ background has been taken from [248], which includes NLO corrections as well as resummation of next–to–leading threshold logarithms. All other backgrounds have been calculated to leading order using `Pythia8.150` [243].

We have generated $2 \cdot 10^6$ $Z(\to \nu\bar{\nu}) + j$ events, $2 \cdot 10^6$ $W(\to e\nu_e, \mu\nu_\mu) + j$ events, $2 \cdot 10^6$ $W(\to \tau\nu_\tau) + j$ events as well as 10^7 $t\bar{t}$ events. Note that exact $\mathcal{O}(\alpha\alpha_S)$ parton–level cross sections have been used to generate the hardest jet in the W, $Z+$ jet backgrounds.

8.3 Distributions

In this subsection, we discuss the basic kinematic distributions and jet and particle multiplicities for the signal (our benchmark point) as well as for the background processes. The distributions are not stacked on each other and are shown on a logarithmic scale. All distributions are scaled to an integrated luminosity of 100 fb^{-1} at $\sqrt{s} = 14$ TeV at the LHC.

We show in Fig. 8.1 the number of leptons (electrons and muons) for signal and background. The signal contains very few charged leptons. In principle, semi–leptonic $c \to s\ell\nu_\ell$ decays can produce leptons, but these are usually too soft to satisfy our criteria; in addition, most of the remaining electrons are removed by our isolation criterion. The $Z + j$ background also contains very few leptons, since we only consider $Z \to \nu\bar{\nu}$ decays here. In contrast, the $t\bar{t}$ background can have up to seven charged leptons, mostly from semileptonic $t \to b \to c \to s, d$ decays. Note that

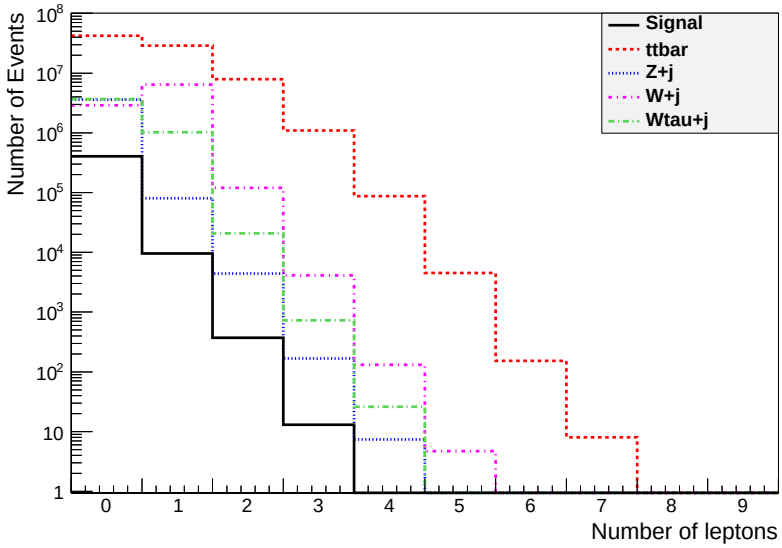

Figure 8.1: Number of leptons for the signal and SM backgrounds assuming an integrated luminosity of 100 fb^{-1} at $\sqrt{s} = 14$ TeV. For the signal we assumed the benchmark scenario of § 8.1.1, *i.e.* $m_{\tilde{\chi}_1^0} = 210$ GeV and $m_{\tilde{t}_1} = 220$ GeV.

we include $t\bar{t}$ events where both t quarks decay fully hadronically. This background therefore peaks at $n_\ell = 0$ charged leptons. The $W + j$ background peaks at $n_\ell = 1$ charged lepton; recall that we have only generated $W \to \ell\nu$ decays here, and that we show the $W + j$ background with $W \to \tau\nu_\tau$ separately. In the latter case a charged lepton can arise from the leptonic decays of the tau.

We will later apply a hard cut on missing E_T. This would remove all $W + j$ events where the W decays hadronically, which we therefore didn't bother to generate. Similarly, $t\bar{t}$ events can pass this cut only if they contain at least one charged lepton.[5] A veto on charged leptons will therefore efficiently remove most of the SM backgrounds, except for the contribution from $Z(\to \nu\bar{\nu}) + j$.

The distribution of the number of identified taus is shown in Fig. 8.2. Leptonically decaying taus cannot be reconstructed; they can, however, be vetoed by charged lepton veto, if the decay lepton is sufficiently energetic. On the other hand, taus decaying hadronically *can* be identified, although tau identification is not very easy at a hadron collider. In case of hadronic tau–decays, only 1–prong events are taken into account for the reconstruction of tau–jets in `Delphes`, where 77% of all hadronically decaying taus are 1–prong events. `Delphes` exploits that the cone of tau jets is narrower than that of QCD jets and they state a tau–tagging efficiency of about 30% for $Z \to \tau^+\tau^-$. We find that the tau tagging efficiency, as estimated by `Delphes`, is much worse for the $t\bar{t}$ background due to the increased hadronic activity. Nevertheless the $t\bar{t}$ background has the second largest percentage of identified taus, exceeded only by $W(\to \tau\nu) + j$; even in the latter case only about 25% of all events contain an identified tau, even though *all* of these events do contain a tau lepton.[6] Note that we include mis–tags of QCD jets as taus, as estimated by

[5] Since the other top (anti)quark might decay fully hadronically, we cannot simply enforce semi–leptonic top decays when simulating this background.

[6] It might well be possible to design a tau *veto* algorithm that performs better than that used by `Delphes`. We have not attempted to do so since at the end the SM background will be dominated by $Z \to \nu\bar{\nu}$ events even

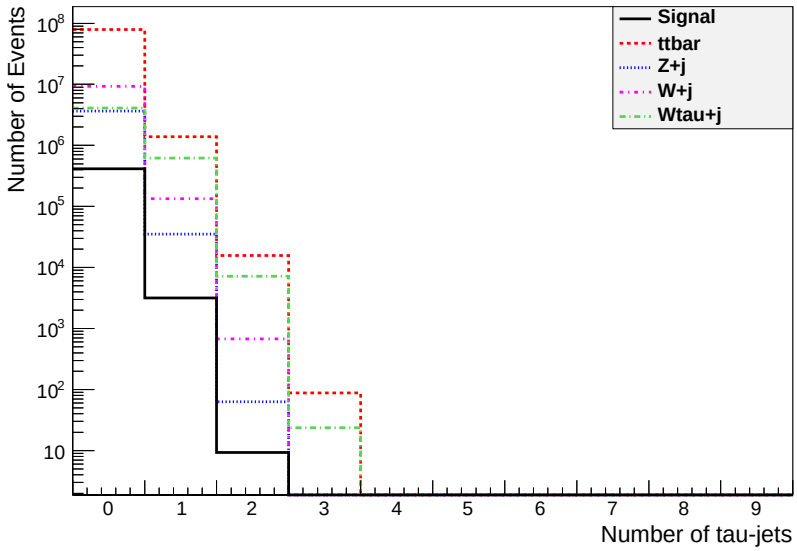

Figure 8.2: Number of isolated hadronic taus for the signal and SM backgrounds. Parameters are as in Fig. 8.1.

`Delphes`. In fact, most $\tau-$jets identified in the signal are fakes.

Fig. 8.3 shows the number of reconstructed jets including $b-$jets. Jets are reconstructed with the anti$-k_t$ jet algorithm with a cone of $\Delta R = 0.7$. We require the jets to have minimum transverse momentum $p_T > 20$ GeV. We see that the signal distribution has its peak around four jets. Jets can be created not only from the hard interaction (e.g. the jet produced explicitly in the signal as well as in the $V + j$ backgrounds, or the jets produced in top decays), but also from QCD radiation in the initial and/or final state. QCD radiation is controlled by the average partonic squared center of mass energy $\hat{s}$ as well as by the color charges in the initial and final states. As expected from the discussion in § 8, we see that the jet multiplicity of the signal is on average larger than for the gauge boson plus jet backgrounds.[7] Not surprisingly, the $t\bar{t}$ background is characterized by the by far largest average jet multiplicity. In previous works, the $t\bar{t}$ background was omitted. Fig. 8.3 indicates that this background can be greatly reduced by cutting against additional jet activity; however, such a cut will reduce the signal more than the $V + j$ backgrounds. Therefore, it is crucial to include the $t\bar{t}$ background in our analysis in order to determine the optimal set of cuts.

Fig. 8.4 shows the number of tagged $b-$jets. A jet is taggable as a $b-$jet if it lies in the acceptance region of the tracking system, i.e. satisfies $|\eta| < 2.5$ in addition to the requirement $p_T > 20$ GeV that all jets have to fulfill, and if it is associated with the parent $b-$quark. `Delphes` assumes a tagging efficiency of about 40% for taggable jets; the total $b-$tagging efficiency is thus less than 40%. `Delphes` also assumes mistagging efficiencies of 10% and 1% for charm–jets and light–flavored (or gluon) jets, respectively. Not surprisingly, the $t\bar{t}$ background contains the

assuming `Delphes` efficiencies.

[7] We have not explicitly matched the parton shower to the matrix element calculation for our signal, i.e. we did not forbid the showering to produce jets that are even harder than the primary jet. However, we will later demand a large cut on the minimum p_T of the hardest jet. Since showering produces such energetic jets exceedingly rarely, the error introduced by our simplified treatment should be small – certainly much smaller than the error due to unknown NLO contributions.

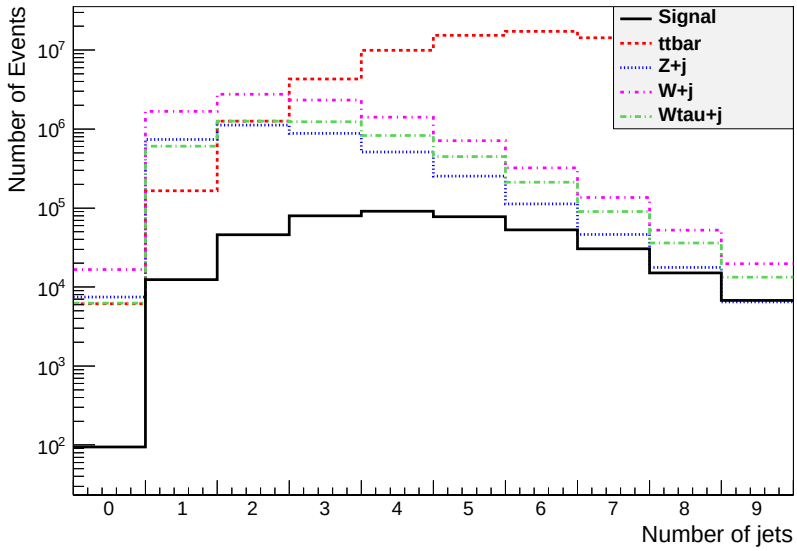

Figure 8.3: Number of jets for the signal and SM backgrounds. Parameters are as in Fig. 8.1.

largest number of $b-$tags, since every $t\bar{t}$ event contains two $b-$quarks arising from top quark decays, and additional $b-$quarks can emerge from gluon splitting. Unfortunately the signal contains $b-$tags slightly more often than the $V + j$ backgrounds do. This is partly due to the presence of two c (anti)quarks, which have a relatively high probability to be mistagged as $b-$jets. Moreover, at the parton–level the jet in signal events is most often a gluon, which can split into a $b\bar{b}$ pair, whereas in $V + j$ events the parton–level jet is most of the time a quark; signal events are therefore more likely to produce a $b\bar{b}$ pair in the QCD shower. Nevertheless a $b-$jet veto will suppress the $t\bar{t}$ background with relatively little loss of signal.

The p_T distribution of the hardest jet is given in Fig. 8.5, where we have also included the $b-$jets. At very large transverse momentum, $p_T(\text{jet}) > 600$ GeV, all curves have similar slopes, since then the hardness of the event is determined by the p_T of the hardest jet rather than the mass of the produced particles. However, at smaller p_T the $V + j$ backgrounds have a significantly softer spectrum than the signal and the $t\bar{t}$ background; once a pair of massive particles is produced, producing a jet with p_T comparable to, or smaller than, twice the mass of these particles is more likely than in events containing only relatively light particles. Finally, the peaks in the distributions for the signal as well as the $V + j$ backgrounds are due to the parton–level cut of 150 GeV on the jet that is produced as part of the hard partonic collision. Recall that we generated $t\bar{t}$ events without requiring an additional parton, and therefore we did not require a minimum $p_T(\text{jet1})$ here at parton–level. As a result, the $t\bar{t}$ contribution peaks at a lower p_T value ($\sim m_t/2$, off the scale shown in Fig. 8.5) than the other processes. We conclude from Fig. 8.5 that a lower cut of about 500 GeV on the hardest jet will improve the statistical significance of the signal.

We see in Fig. 8.6 that the p_T distribution of the second hardest jet is much softer for the signal and the $V + j$ backgrounds than that of the hardest jet. Recall that the first jet is generated at parton level with $p_T > 150$ GeV, whereas the second jet comes from QCD showers, or, in case of the signal, possibly from stop decays; both sources give mostly soft jets, whose spectrum is backed up against the lower cut of 20 GeV we impose on all jets. In contrast, in

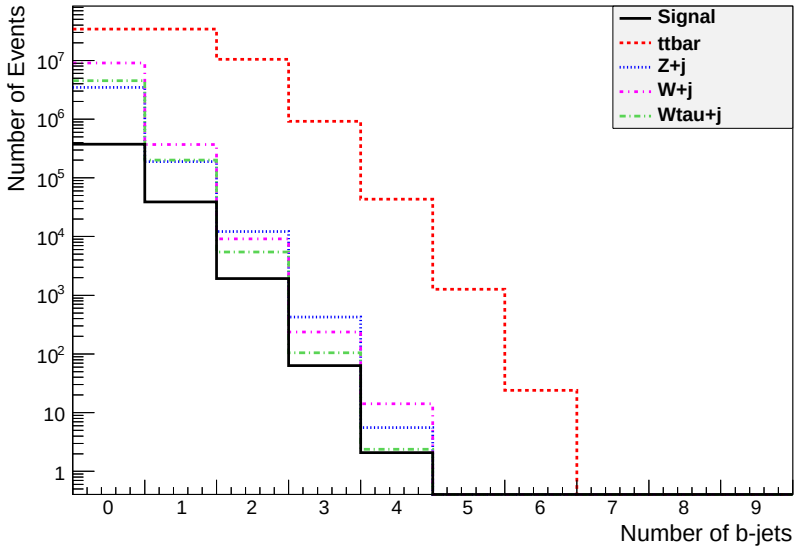

Figure 8.4: Number of tagged $b-$jets for the signal and SM backgrounds. Parameters are as in Fig. 8.1.

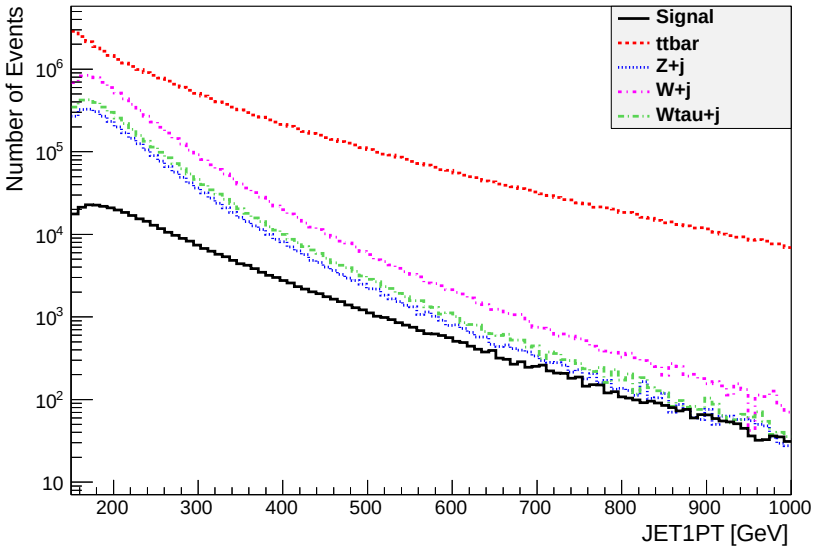

Figure 8.5: p_T distributions of the hardest jet for the signal and SM backgrounds. Parameters are as in Fig. 8.1.

t

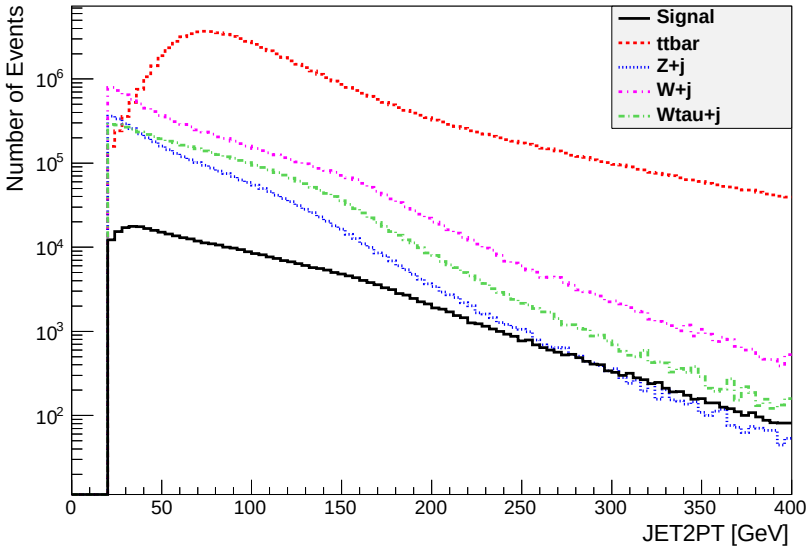

Figure 8.6: p_T distributions of the second hardest jet for the signal and SM backgrounds. Parameters are as in Fig. 8.1.

$t\bar{t}$ events the hardest and second hardest jet usually both originate from top decay. The p_T spectrum of the second hardest jet therefore peaks not much below that of the hardest jet, at $p_T \simeq 75$ GeV.

From Fig. 8.3, we have seen that a veto on the second jet is necessary in order to sufficiently suppress the $t\bar{t}$ background. However, if we vetoed all jets with $p_T > 20$ GeV, we would lose too many signal events. We find that it is a good choice to veto all events where the second hardest jet has $p_T > 100$ GeV. We also examined a veto on the third hardest jet with reduced p_T threshold. This would reduce the $t\bar{t}$ background even further. However, it would also remove many signal events and thus a veto on the third jet does not increase the significance of our signal.

Finally, Fig. 8.7 shows the missing transverse energy distributions of signal and backgrounds. We see that the signal has the slowest fall off. Recall that we did not take into account pure QCD backgrounds such as dijet and trijet events. Thus we need a cut on missing energy in order to suppress these backgrounds [247]. We find that a missing transverse energy cut near 450 GeV maximizes the significance of the signal for our benchmark point. Such a hard cut on the missing E_T, together with the veto on a second hard jet, should suppress the pure QCD background to a negligible level.

8.4 Discovery Potential at the LHC

In the previous Subsection, we have discussed the basic distributions which we use to derive a set of kinematical cuts. Now we discuss the statistical significance for our benchmark point. Then, we will show the discovery potential of our signal in the stop–neutralino mass plane at the LHC for an integrated luminosity of 100 fb^{-1} at $\sqrt{s} = 14$ TeV, using the same set of cuts that optimizes the signal significance for our benchmark point.

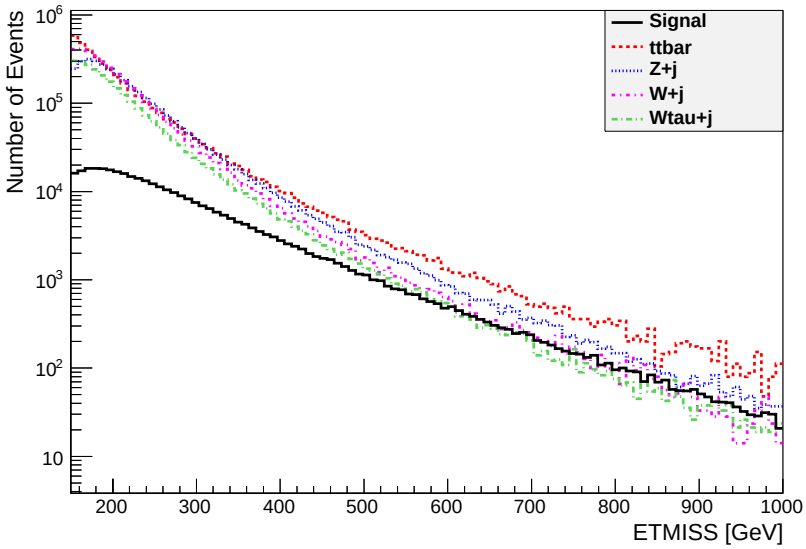

Figure 8.7: Missing transverse energy distributions for the signal and SM backgrounds. Parameters are as in Fig. 8.1.

As motivated by our discussion in § 8.3, we apply the following set of cuts:

- $p_T(\text{jet}_1) \geq 500$ GeV, i.e. we require one hard jet with $p_T \geq 500$ GeV.
- $\not{p}_T > 450$ GeV, i.e. we demand large missing transverse energy.
- $N_{\text{lepton}} < 1$, i.e. we veto all events with a reconstructed electron or muon with $|\eta| < 2.5$. Recall that we only include isolated electrons with $p_T > 10$ GeV, but all muons with $p_T > 4$ GeV.
- $N_{\text{tau}} < 1$, i.e. we veto all events with an identified tau jet with $|\eta| < 2.5$ and $p_T > 20$ GeV.
- $N_{\text{b-jet}} < 1$, i.e. require a veto on all tagged $b-$jets with $p_T > 20$ GeV and $|\eta| < 2.5$.
- $p_T(\text{jet}_2) < 100$ GeV, i.e. we veto the existence of a second hard jet.

The numerical values of the first, second and last cut have been set by optimizing the signal significance for our benchmark point.

In Table 8.3, we list all cuts in the first column. We display the total number of $(Z \to \nu\bar{\nu}) + j$ (second column), $W(\to \ell\nu_\ell) + j$ (third column), $W(\to \tau\nu_\tau) + j$ (fourth column) and $t\bar{t}$ events (fifth column) for an integrated luminosity of 100 fb^{-1} at the LHC with $\sqrt{s} = 14$ TeV. The signal S, the resulting ratio between signal and background (B) events and the estimate significance $S/\delta B$ are given in the sixth, seventh and eighth column, respectively.

The significance of the signal depends on the error δB (8.8) of the background. In Section 8.2, we discussed the individual systematical errors. We also mentioned a data driven method to determine the dominant $Z + j$ background from the $Z(\to \ell\ell) + j$ calibration channel. Our

cut	$Z(\to \nu\bar{\nu}) + j$	$W(\to e\nu_e, \mu\nu_\mu) + j$	$W(\to \tau\nu_\tau) + j$	$t\bar{t}$	signal	S/B	$S/\delta B$
$p_T(j_1) > 500$ GeV	27 619	69 802	35 137	2 206 070	17 797	0.008	0.08
$\not{p}_T > 450$ GeV	22 798	20 738	16 835	63 320	13 350	0.108	1.94
veto on e, μ	22 284	6 363	11 978	23 416	12 810	0.200	4.68
veto on isolated taus	22 221	6 274	9 031	22 848	12 727	0.21	4.96
veto on $b-$jets	21 295	5 968	8 617	11 424	11 064	0.23	6.94
veto on second jet ($p_T(j_2) \leq 100$GeV)	15 415	3 702	5 128	1 408	5 848	0.23	8.17

Table 8.3: Cut flow for the benchmark scenario of § 8.1.1 at the LHC with $\sqrt{s} = 14$ TeV and an integrated luminosity of 100 fb^{-1}. In the second last column, we present the ratio between signal and background number of events. In the last column, we estimate the significance via δB given in Eq. (8.8)

overall error estimate is then given by

$$\delta B = \sqrt{5.3\, B_{Z+j} + \sum_i B_i + \sum_i (0.1 B_i)^2}, \qquad i = t\bar{t}, \mathrm{W}(\to \ell\nu_\ell) + \mathrm{j}, \mathrm{W}(\to \tau\nu_\tau) + \mathrm{j}. \tag{8.8}$$

We start with a cut on the hardest jet (including $b-$tagged jets). After applying this cut, $t\bar{t}$ is the dominant background; it is two orders of magnitude larger than the signal and the remaining SM background, as can be seen in the first row of Table 8.3 and Fig. 8.5. Because of the large $t\bar{t}$ background, the signal significance is still very small. Note that for lower stop masses, a less stiff cut on the hardest jet would be slightly more efficient but we optimize our cuts for heavier stops since we would like to determine the discovery reach.

The rather hard cut on the missing transverse energy strongly suppresses the $W + j$ and $t\bar{t}$ backgrounds, but, coming after the hard cut on the p_T of the first jet, has little effect on the signal and on the $Z + j$ background. This holds for relatively small mass splittings between the lighter stop and the lightest neutralino. In these scenarios (including our benchmark scenario), the charm jets are very soft and rarely reconstructed, leading to large missing transverse energy. As the mass splitting increases, the charm jets become harder and are more often reconstructed, decreasing $\not{p}_T$. We therefore anticipate that the significance of our signal will be worse for larger mass splittings (see below).

As we have shown in Fig. 8.1, the lepton veto should efficiently reduce the SM background, while having little effect on the signal. We can see in Table 8.3 that the leptonic $W + j$ background is reduced by about a factor of three. $W + j$ events involving leptonically decaying taus from the W are also removed. This cut also reduces the $t\bar{t}$ background significantly. Naively, one would assume that after demanding large missing transverse energy, at least one W boson from $t \to b + W$ or in $W + j$ decays leptonically. However, there is a quite substantial probability that a charged lepton is not reconstructed according to the criteria described in § IIIB. Finally, the irreducible $Z + j$ background is not affected by this cut.

The tau veto removes 25% of the $W(\to \tau\nu) + j$ background events. However, nearly all $t\bar{t}$ events pass the cut. Requiring a large missing transverse energy cut and a lepton veto should mostly leave $t\bar{t}$ events with one W decaying into a tau. Even so, only a few $t\bar{t}$ events are removed, since the τ tagging efficiency is very poor for $t\bar{t}$ events.

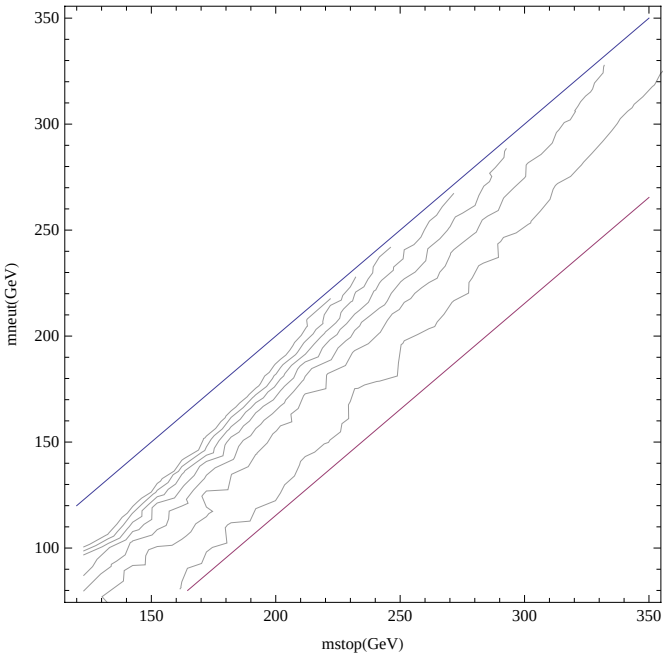

Figure 8.8: Number of signal events after isolation cuts in the stop–neutralino mass plane assuming an integrated luminosity of 100 fb^{-1} at $\sqrt{s} = 14$ TeV. The two parallel straight lines delineate the region where $\tilde{t}_1 \to \tilde{\chi}_1^0 c$ decays are allowed but $\tilde{t}_1 \to \tilde{\chi}_1^0 W^+ \bar{b}$ decays are forbidden. The grey lines correspond to 7000, 6000, 5000, 4000, 3000, 2000 and 1000 signal events (from top to bottom), respectively.

After these four cuts, the signal significance is slightly less than five, with a signal to background ratio of 0.21. At this stage $t\bar{t}$ and $Z + j$ are still the dominant backgrounds. The $b-$jet veto further suppresses the $t\bar{t}$ background by a factor of two. As expected, it has little effect on the $Z + j$ and $W + j$ backgrounds. We saw in Fig. 4 that a relatively large fraction of the signal events contains a tagged $b-$jet. Thus the veto also removes 13% of the signal events. Nevertheless this cut increases the signal significance to 6.94.

The final cut vetoing a second hard jet is of crucial importance to further suppress the $t\bar{t}$ background. We now obtain a significance of 8.17 and a rather good signal to background ratio of about 0.23. Note that the $t\bar{t}$ background is now quite insignificant, being much smaller than the signal. It could be suppressed even further by reducing the p_T threshold in the second jet veto. However, the number of signal events is decreased more strongly by this veto than the $Z + j$ background, such that our overall significance would get worse.

Having discussed the signal significance for our benchmark scenario, we now want to present results for other stop and neutralino masses. As before, we assume that all other sparticles are effectively decoupled. For the sake of simplicity, we apply the same cuts as for the benchmark point, *i.e.* the cuts in Table 8.3.

In Fig. 8.8, we present the number of signal events in the stop–neutralino mass plane applying all cuts of Table 8.3. The number of signal events is normalized to a luminosity of 100 fb^{-1} at $\sqrt{s} = 14$ TeV. We see that even after the stiff cuts listed at the beginning of this Subsection, our $\mathcal{O}(\alpha_S^3)$ signal process yields in excess of 1000 signal events out to quite large stop masses, as long as the mass splitting to the $\tilde{\chi}_1^0$ is small.

In Fig. 8.9, we show the statistical significance in the stop–neutralino mass plane for an

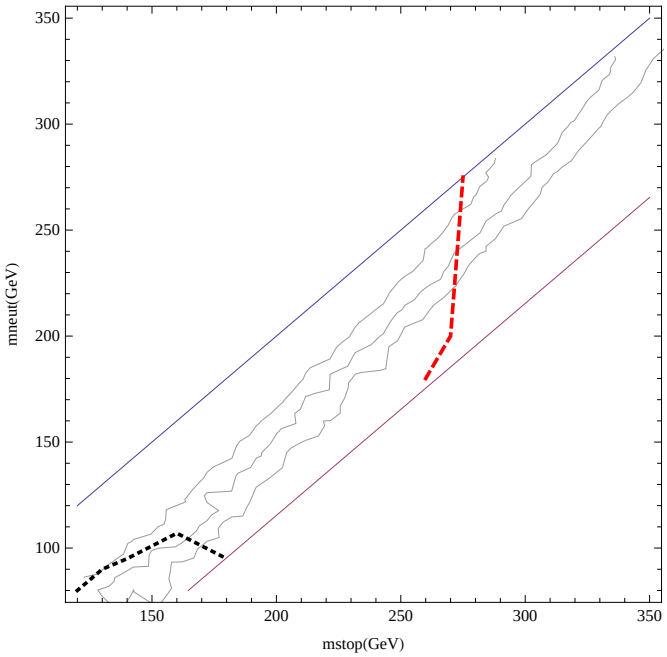

Figure 8.9: Signal significance with background error estimated as in Eq. (8.8) in the stop–neutralino mass plane assuming an integrated luminosity of 100 fb^{-1} at $\sqrt{s} = 14$ TeV. The two parallel straight lines delineate the region where $\tilde{t}_1 \to \tilde{\chi}_1^0 c$ decays are allowed but $\tilde{t}_1 \to \tilde{\chi}_1^0 W^+ \bar{b}$ decays are forbidden. The three grey lines correspond to 5σ, 3σ and 2σ (from top to bottom), respectively. The short-dashed black curve delimits the Tevatron exclusion region, whereas the long-dashed red curve denotes the lower limit of the discovery reach of searches for light stops in events with two $b-$jets and large missing energy.

integrated luminosity of 100 fb^{-1} at $\sqrt{s} = 14$ TeV. We present the discovery reach corresponding to 5σ, 3σ and 2σ, respectively; the latter should be interpreted as the region that can be excluded at 95% c.l. if no signal is found. The stop can dominantly decay into a charm and a neutralino for $m_{\tilde{\chi}_1^0} + m_c < m_{\tilde{t}_1} < m_{\tilde{\chi}_1^0} + m_W + m_b$, the area lying between the two straight lines in Figs. 8.9 and 8.8. The region below the short–dashed black curve is excluded by Tevatron searches at the 95% confidence level [252, 253]. Note that LEP2 experiments could already rule out $\tilde{t}_1$ masses below 100 GeV [254] even for very small mass splitting[8]. In the region to the left of the long–dashed red curve, searches for light stops in events with two $b-$jets and large missing energy [133] should have at least 5σ *statistical* significance.

We see from Fig. 8.9 that the discovery of stop pairs in association with a jet should be possible for stop masses up to 290 GeV and for mass splittings between stop and neutralino of up to 45 GeV. Stop masses up to 360 GeV can be excluded at 2σ if the mass splitting is very small. As mentioned in the discussion of the missing E_T cut as well as in Ref. [130], the significance of our monojet signal gets worse with increasing mass splitting. Increasing the mass splitting increases the average energy of the $c-$jets. This reduces the missing E_T, and increases the probability that the signal fails the veto on a second hard jet. These effects are cumulative: the reduced missing E_T could be compensated by increasing the p_T of the additional parton–level jet. However, this would also increase the p_T of the $\tilde{t}_1 \tilde{t}_1^*$ pair, and hence the average p_T

[8] $\tilde{t}_1$ pair production should be detectable at e^+e^- colliders for arbitrarily small mass splitting to the LSP if one includes the effects of (both perturbative and non–pertubative) gluon radiation [255].

of the $c-$jets from $\tilde{t}_1$ decay.

The region close to the maximal allowed mass splitting (for the assumed loop–level two–body decay of $\tilde{t}_1$) could perhaps be probed through conventional searches for di–jet plus missing E_T events, without demanding the presence of an additional parton–level jet. Alternatively one could reduce the missing E_T cut, and try to suppress the $V + j$ backgrounds by a cut on the minimal multiplicity of charged particles [133]. In both cases some sort of $c-$jet tagging would be helpful and perhaps even crucial. Unfortunately little is known (to us) about the capabilities of the LHC experiments to detect charm jets (or at least to isolate an event sample enriched in charm jets). We have therefore not attempted this approach here.

The dashed red line in Fig. 8.9 indicates that the two $b-$jet plus missing transverse energy signature [133] is degraded less for larger mass splittings compared to our monojet signal. There the presence of two hard $b-$jets allowed to use a much milder missing E_T cut of "only" 200 GeV, and no veto against additional jet activity was used. However, the analysis of [133] isn't really comparable to our present work. First of all, only statistical uncertainties were considered in [133], whereas in the present case the uncertainty of the background, and hence the total significance, is dominated by the systematic errors; for example, after all cuts our benchmark point has a *statistical* significance of about 37, compared to our stated significance of "only" 8.17. Secondly, detector effects were not included in [133]. At least according to `Delphes`, this over–estimates the efficiency of the lepton veto in reducing $W + j$ and top backgrounds. Finally, the red curve shown in Fig. 8.9 holds under the assumption that there is a higgsino–like chargino just 20 GeV above the $\tilde{t}_1$; this increases the cross section for $\tilde{t}_1\,\tilde{t}_1^* b\bar{b}$ production, which receives contributions from $\tilde{t}_1\tilde{\chi}_1^-\bar{b}$ production followed by $\tilde{\chi}_1^- \to \tilde{t}_1^* b$ decays (as well as charge conjugate processes).

As noted above, the total uncertainty of our background estimate is dominated by the systematic error on the W+1 jet background, which we estimate to be 10%. This is compatible with recent preliminary ATLAS results on monojet searches at the 7 TeV LHC [256]. Since with the accumulation of additional data our understanding of $W + 1$ jet production should improve, we consider this estimate, and the resulting estimate of the LHC reach, to be quite conservative. For example, Ref.[132] estimates the *total* uncertainty from all W, $Z + 1$ jet backgrounds to be $7B_{Z+j}$. This would reduce the total uncertainty δB of the background after all cuts from about 715 (our estimate) to about 360, i.e. by a factor of two. Once the total error on the background has been established, Fig. 8.8 can be used to determine the region of parameter space that can be probed at a given significance.

Finally, our estimate of the signal S also has uncertainties. Since we define the significance as $S/\delta B$ the systematic (theoretical) uncertainty on S will only change the signal reach appreciably if the uncertainty is sizable. Since we are employing leading order $\mathcal{O}(\alpha_S^3)$ expressions for the parton–level signal cross section, NLO corrections might indeed be sizable. One often attempts to estimate their magnitude by varying the factorization and renormalization scales. For example, for $m_{\tilde{t}_1} = 120$ GeV, setting both of these scales equal to the stop mass increases the parton–level cross section before cuts to 49 pb; this is a factor 1.6 larger than the value of 31 pb we quote in Table 8.1, which has been computed using the MadGraph default scale choices. Unfortunately no NLO calculation of squark pair production with radiation of an additional jet has been performed as yet. All other theoretical uncertainties (due to details of the QCD shower and fragmentation or the choice of parton distribution functions) are significantly smaller than this estimate of the uncertainty due to NLO corrections.

Chapter 9

Gravitino cosmology with a very light neutralino

In the MSSM, the photon and the Z^0 boson, as well as the two neutral CP–even Higgs bosons, have SUSY spin-1/2 partners which mix. The resulting mass eigenstates are denoted neutralinos, χ_i^0, with $i = 1, \ldots, 4$, and are ordered by mass $m_{\chi_1^0} < \ldots < m_{\chi_4^0}$ [28]. The Particle Data Group quotes a lower mass bound on the lightest neutralino in the R_p–conserving MSSM [164]

$$m_{\chi_1^0} > 46 \text{ GeV}\,, \tag{9.1}$$

which is derived from the LEP chargino search under the assumption of gaugino mass universality:

$$M_1 = \frac{5}{3} \tan^2 \theta_W M_2\,. \tag{9.2}$$

Here θ_W is the electroweak mixing angle. If we relax this latter assumption, the bound (9.1) no longer applies. In fact for any value of M_2, μ, and $\tan\beta$ there is always a M_1

$$M_1 = \frac{M_2 M_Z^2 \sin(2\beta) \sin^2\theta_W}{\mu M_2 - M_Z^2 \sin(2\beta)\cos^2\theta_W} \tag{9.3}$$

$$\simeq 2.5 \text{ GeV} \left(\frac{10}{\tan\beta}\right)\left(\frac{150 \text{ GeV}}{\mu}\right)\,, \tag{9.4}$$

such that the lightest neutralino is massless [71, 77]. A very light or massless neutralino is necessarily predominantly bino–like since the experimental lower bound on the chargino mass, sets lower limits on M_2 and μ [69, 74, 75]. Although Eq. (9.3) holds at tree–level, there is always a massless solution even after including quantum corrections to the neutralino mass [77].

Such a light or even massless neutralino is consistent with all laboratory data. The processes considered include the invisible width of the Z^0, electroweak precision observables, direct pair production, associated production, and rare meson decays. Note that a bino-like neutralino does not couple directly to the Z^0. The other production processes, including the meson decays, thus necessarily involve virtual sleptons or squarks. If these have masses of $\mathcal{O}(200)$ GeV or heavier, then all bounds are evaded — for details on the individual analyses see Refs. [69–77]. The best possible laboratory mass measurement can be performed at a linear collider via selectron pair production with an accuracy of order 1 GeV, depending on the selectron mass [257].

Light neutralinos can lead to rapid cooling of supernovæ, so are constrained by the broad agreement between the expected neutrino pulse from core collapse and observations of SN 1987A [78]. The neutralinos would be produced and interact via the exchange of virtual selectrons and squarks. For a massless neutralino which 'free-streams' out of the supernova, the selectron must be heavier than about 1.2 TeV and the squarks must be heavier than about 360 GeV.

For light selectrons or squarks of mass $\sim 100 - 300$ GeV, the neutralinos instead diffuse out of the supernova just as the neutrinos do and thus play an important role in the supernova dynamics. Hence lacking a detailed simulation which includes the effects of neutralino diffusion, no definitive statement can presently be made [73, 78–80]. Recently the luminosity function of white dwarfs has been determined to high precision [258, 259] and this may imply interesting new bounds on light neutralinos, just as on axions.

If a neutralino is stable on cosmological time scales it can contribute to the dark matter (DM) of the universe. If 'cold', then its mass is constrained from below by the usual Lee-Weinberg bound [260–263] which depends only on the self-annihilation cross-section. This limit has been widely discussed in the literature in the framework of the ΛCDM cosmology [264–267] and various values are quoted for a MSSM neutralino: $M_{\chi_1^0} > 12.6$ GeV [268, 269] and $M_{\chi_1^0} > 9$ GeV [270, 271]. The low mass range is particularly interesting because the DAMA [272] and CoGeNT [273] direct detection experiments have presented evidence for annual modulation signals suggestive of a DM particle with mass of $\mathcal{O}(10)$ GeV.

A light neutralino with a much smaller mass is also viable as 'warm' or 'hot' DM but this possibility has been less discussed. The observed DM density $\Omega_{\rm DM}h^2 \approx 0.11$ can in principle be entirely accounted for with warm dark matter (WDM) in the form of neutralinos having a mass of a few keV [274]. However the usual assumption of radiation domination and entropy conservation prior to big bang nucleosynthesis (BBN) then needs to be relaxed otherwise the relic neutralino density is nominally much larger than required. This scenario requires a (unspecified) late episode of entropy production or, equivalently, reheating after inflation to a rather low temperature of a few MeV. Although models of baryogenesis with such reheating temperatures exist [275, 276], the necessary baryon number violating interactions would result in rapid decay of the proton to (the lighter) neutralinos. This makes such models very difficult to realise in this context, although the situation may be somewhat eased since the maximum temperature during reheating can be higher than the final thermalisation temperature [277].

In this chapter we focus on a light neutralino which acts as hot dark matter (HDM)[1], *i.e.* can suppress cosmic density fluctuations on small scales through free-streaming. In order for its relic abundance to be small enough to be consistent with the observed small-scale structure we require [77] following Ref.[81]:

$$m_{\chi_1^0} \lesssim 0.7 \text{ eV} \,. \tag{9.5}$$

analogous to Eq. (3.30) for neutrinos. Such ultralight neutralinos affect BBN by contributing to the relativistic degrees of freedom and thus speeding up the expansion rate of the universe; consequently neutron-proton decoupling occurs earlier and the mass fraction of primordial ^{4}He is increased [62]. The resulting constraint on new relativistic degrees of freedom is usually presented as a limit on the number of additional effective $SU(2)$ doublet neutrinos:

$$\Delta N_\nu^{\rm eff}(\chi_1^0) \equiv N_\nu^{\rm eff} - 3 \,. \tag{9.6}$$

In § 9.1, we calculate this number in detail and compare it with observational bounds on $\Delta N_\nu^{\rm eff}$ from BBN [281].

Until recently, the BBN prediction and the inferred primordial ^{4}He abundance implied ac-

[1] Note that HDM cannot contribute more than a small fraction of the observed dark matter, so another particle is required to make up the cold dark matter (CDM). Potential candidates include the gravitino [278], the axion [279] or the axino [280].

cording to some authors [65, 66]

$$\Delta N_\nu^{\rm eff} \lesssim 0\,. \tag{9.7}$$

This is however in tension with recent measurements of the cosmic microwave background (CMB) anisotropy by WMAP, which suggest a larger value of [63, 64]

$$\text{WMAP}: \quad \Delta N_\nu^{\rm eff} = 1.34\,^{+0.86}_{-0.88}\,. \tag{9.8}$$

Recent measurements of the primordial ^{4}He abundance are also higher than reported earlier, implying [67, 68]:

$$\text{BBN}: \quad \Delta N_\nu^{\rm eff} = 0.68\,^{+0.8}_{-0.7}\,. \tag{9.9}$$

Given these large uncertainties, a very light neutralino is easily accommodated, and even favoured, by the BBN and CMB data. In the near future, the Planck mission [282] is foreseen to determine $N_\nu^{\rm eff}$ to a higher precision of about $\delta N_\nu^{\rm eff} = \pm 0.26$ [64], thus possibly constraining the light neutralino hypothesis.

Local SUSY models necessarily include a massive gravitino [283]. Depending on its mass, the gravitino can also contribute to $\Delta N_\nu^{\rm eff}$ as we discuss in § 9.2. This effect is only relevant for sub-eV mass gravitinos (for models see *e.g.* Ref. [284]). More commonly the gravitino has electroweak-scale mass and its decays into the light neutralino will result in photo-dissociation of light elements, in particular ^{4}He [62]. The resulting (over) production of ^{2}H and ^{3}He is strongly constrained observationally and we present the resulting bounds in § 9.3. In § 9.4 we examine under which conditions the gravitino itself can be a viable DM candidate in the presence of a very light neutralino.

9.1 Light neutralinos and nucleosynthesis

In global SUSY models, or local SUSY models with a non–relativistic gravitino, the sub–eV neutralino is the only relativistic particle present at the onset of nucleosynthesis apart from the usual photons, electrons and 3 types of neutrinos.

The contribution of the neutralino to the number of effective neutrino species is [62]:

$$\Delta N_\nu^{\rm eff}(\chi_1^0) = \frac{g_{\chi_1^0}}{2}\left(\frac{T_{\chi_1^0}}{T_\nu}\right)^4, \tag{9.10}$$

where $g_{\chi_1^0}$ is the number of internal degrees of freedom, equal to 2 due to the Majorana character of the neutralino. The ratio of temperatures is given by

$$\frac{T_{\chi_1^0}}{T_\nu} = \left[\frac{g^*(T_{\rm fr}^\nu)}{g^*(T_{\rm fr}^{\chi_1^0})}\right]^{1/3}, \tag{9.11}$$

where $T_{\rm fr}^i$ is the freeze–out temperature of particle i and

$$g^*(T) = \sum_{\rm bosons} g_i \cdot \left(\frac{T_i}{T}\right)^4 + \frac{7}{8}\sum_{\rm fermions} g_i \cdot \left(\frac{T_i}{T}\right)^4. \tag{9.12}$$

with g_i being the internal relativistic degrees of freedom at temperature T. Usually T_i for a decoupled particle species i is lower than the photon temperature T. because of subsequent

entropy generation.

The freeze-out temperature of $SU(2)$ doublet neutrinos is $T^{\nu}_{\rm fr} \sim 2$ MeV [285]. The interaction rate $\Gamma_{\chi^0_1}$ of the lightest neutralino is suppressed relative to that of neutrinos [77] because the SUSY mass scale $m_{\rm SUSY} > M_{\rm W}$, where $m_{\rm SUSY}$ denotes the relevant SUSY particle mass involved in the neutralino reactions. Hence the freeze-out temperature of the very light neutralino will generally be higher than $T^{\nu}_{\rm fr}$.

Estimating the thermally-averaged neutralino annihilation cross-section via an effective vertex, we obtain the approximate interaction rate

$$\Gamma_{\chi^0_1}(T) = 2\frac{3}{4}\frac{\zeta(3)}{\pi^2} G^2_{\rm SUSY}\, T^5_{\chi^0_1}, \tag{9.13}$$

where $G_{\rm SUSY}/\sqrt{2} = g^2/(8m^2_{\rm SUSY})$. Equating this to the Hubble expansion rate [62]

$$H(T) = \sqrt{\frac{4\pi^3 g^*(T)}{45}}\frac{T^2}{M_{\rm Pl}}, \tag{9.14}$$

where g^* counts the relativistic degrees of freedom, yields the approximate freeze-out temperature:

$$T^{\chi^0_1}_{\rm fr} \approx 3\,\left(\frac{m_{\rm SUSY}}{200\ {\rm GeV}}\right)^{4/3} T^{\nu}_{\rm fr}\,. \tag{9.15}$$

Thus, for sparticle masses below ~ 3 TeV, the neutralinos freeze–out below the temperature at which muons annihilate [77].

We now calculate the freeze–out temperature of a pure bino–like neutralino more carefully, considering all annihilation processes into leptons which are present at the time of neutralino freeze–out:

$$\chi^0_1\chi^0_1 \to \ell\bar{\ell}, \quad \ell = e, \nu_e, \nu_\mu, \nu_\tau. \tag{9.16}$$

Assuming that sleptons and sneutrinos have a common mass scale $m_{\rm slepton}$, the following relations hold

$$\begin{aligned}\sigma(\chi^0_1\chi^0_1 \to \ell_R\bar{\ell}_L) &= 16\sigma(\chi^0_1\chi^0_1 \to \ell_L\bar{\ell}_R)\\ &= 16\sigma(\chi^0_1\chi^0_1 \to \nu\bar{\nu}),\end{aligned} \tag{9.17}$$

so the total annihilation cross section into leptons is given by

$$\sigma(\chi^0_1\chi^0_1 \to \ell\bar{\ell}) = 20\sigma(\chi^0_1\chi^0_1 \to \ell_L\bar{\ell}_R)\,, \tag{9.18}$$

where we have taken the electron to be massless. The thermally-averaged cross-section is then given by

$$\langle\sigma(\chi^0_1\chi^0_1 \to \ell\bar{\ell})v\rangle = \frac{20}{9\zeta(3)^2}\frac{2^5}{3} I(1)^2\hat{\sigma}T^2, \tag{9.19}$$

where

$$I(n) = \int_0^\infty \frac{y^{n+2}}{\exp(y)+1} \tag{9.20}$$

and

$$\hat{\sigma} = \frac{e^4}{8\pi\cos^4\theta_W}\frac{1}{m^4_{\rm slepton}} \tag{9.21}$$

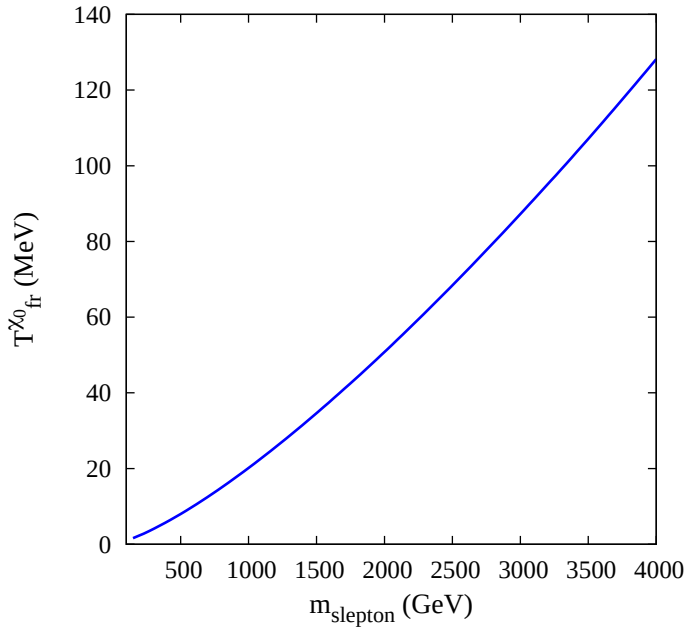

Figure 9.1: Freeze-out temperature of the pure bino–like neutralino as a function of the common mass scale $m_{\rm slepton}$.

for $m_{\rm slepton} \gg T$. In calculating the cross-section (9.19), we have neglected the Pauli blocking factors in the final state statistics [286].

Relating the reaction rate (9.19) to the Hubble expansion rate (9.14), we can now obtain the freeze–out temperature for a bino–like neutralino, shown in Fig. 9.1 as a function of the common mass scale $m_{\rm slepton}$. Note that for $m_{\rm slepton}$ below a few TeV, the neutralino decouples below the muon mass as noted earlier. Thus neutrinos and neutralinos will have the same temperature,

$$T_{\chi_1^0} = T_\nu \,, \tag{9.22}$$

hence during BBN,

$$\Delta N_\nu^{\rm eff}(\chi_1^0) = 1 \,. \tag{9.23}$$

However, for slepton masses above a few TeV, the neutralino freeze–out temperature is close to the muon mass, and muon annihilation will influence the neutralino and neutrino temperature differently. For $T_{\rm fr}^{\chi_1^0} \gtrsim m_\mu$, the neutrinos are heated by the muon annihilations, whereas this affects the neutralinos only marginally. Therefore $T_{\chi_1^0}/T_\nu$ is reduced due to the conservation of comoving entropy. The muons contribute to $g^*(T_{\chi_1^0})$, such that

$$\frac{T_{\chi_1^0}}{T_\nu} = \left[\frac{g_\gamma + \frac{7}{8}(g_e + 3g_\nu)}{g_\gamma + \frac{7}{8}(g_e + 3g_\nu + g_\mu)}\right]^{1/3} = \left(\frac{43}{57}\right)^{1/3} . \tag{9.24}$$

Thus employing Eq. (9.10) we obtain

$$\Delta N_\nu^{\rm eff}(\chi_1^0) = 0.69 \,, \tag{9.25}$$

which is interestingly close to the observationally inferred central value of 0.68 in Eq. (9.9). The LHC already restricts the masses of strongly coupled SUSY particles (squarks and gluinos) to be above several hundred GeV [287–289] and the supernova cooling argument requires the selectron mass to also be above a TeV for a massless neutralino [73], so the picture is consistent.

Even for a neutralino freeze–out temperature somewhat below the muon mass, the effects from muon annihilation are notable. We now determine the equivalent number of neutrino species more carefully using the Boltzmann equation as in Refs. [285, 290], in order to determine the effect for arbitrary slepton masses. Consider a fiducial relativistic fermion x which is decoupled during $\mu\bar{\mu}$ annihilation, so that its number density, n_x, satisfies

$$\dot{n}_x + \frac{3\dot{R}}{R} n_x = 0\,. \tag{9.26}$$

The Boltzmann equation controlling the number density of the lightest neutralino can then be written as

$$\frac{d}{dt}\left(\frac{n_{\chi_1^0}}{n_x}\right) = n_x \langle\sigma v\rangle \left[\left(\frac{n_\mu}{n_x}\right)^2 - f(T_{\chi_1^0})\left(\frac{n_{\chi_1^0}}{n_x}\right)^2\right], \tag{9.27}$$

where

$$f(T_{\chi_1^0}) = \left[\frac{n_\mu(T_{\chi_1^0})}{n_{\chi_1^0}(T_{\chi_1^0})}\right]^2_{\text{equilibrium}}\,. \tag{9.28}$$

The cross-section $\mu\bar{\mu} \to \chi_1^0\chi_1^0$ is given by

$$16\pi s^2 \quad \frac{\cos\theta_{\rm W}^4}{e^4}\,\sigma(\mu_R\bar{\mu}_L \to \chi_1^0\chi_1^0) = \tag{9.29}$$

$$2(m_{\tilde{\mu}}^2 - \quad m_\mu^2)\,\ln\left(\frac{2(m_{\tilde{\mu}}^2 - m_\mu^2) + s - \sqrt{s}\sqrt{s-4m_\mu^2}}{2(m_{\tilde{\mu}}^2 - m_\mu^2) + s + \sqrt{s}\sqrt{s-4m_\mu^2}}\right)$$
$$+\sqrt{s}\sqrt{s-4m_\mu^2}\,\frac{2(m_{\tilde{\mu}}^2 - m_\mu^2)^2 + m_{\tilde{\mu}}^2 s}{(m_{\tilde{\mu}}^2 - m_\mu^2)^2 + m_{\tilde{\mu}}^2 s}. \tag{9.30}$$

Since this involves a cancellation between the two terms, we Taylor expand to ensure numerical stability:

$$16\pi\frac{\cos\theta_{\rm W}^4}{e^4}\sigma(\mu_R\bar{\mu}_L \to \chi_1^0\chi_1^0) \;\approx\; \frac{\sqrt{1-\frac{4m_\mu^2}{s}}(s-m_\mu^2)}{3(m_{\tilde{\mu}}^2 - m_\mu^2)^2},$$

then take the thermal average $\langle\sigma v\rangle$ following Ref. [291].

In order to reformulate Eq. (9.27) in terms of dimensionless quantities, we define

$$\delta \equiv \frac{T_{\chi_1^0} - T_x}{T_x}, \quad \epsilon \equiv \frac{T_\gamma - T_x}{T_x}\,, \quad y \equiv \frac{m_\mu}{T_\gamma}\,. \tag{9.31}$$

Here δ measures the temperature difference between the decoupled particle x and the lightest neutralino and thus quantifies the heating of the lightest neutralino due to $\mu\bar{\mu}$ annihilation. We now evaluate n_μ/n_x numerically and expand $n_{\chi_1^0}/n_x \approx 1 + 3\delta$ so Eq. (9.27) can be written as

[285, 290]

$$\frac{d\delta}{dy} \approx a y^{-2}(\epsilon - \delta)\,, \tag{9.32}$$

for $\delta \ll 1$, *i.e.* for small temperature differences. The prefactor a depends on the size of the annihilation cross-section, and thus on y and the slepton mass:

$$a(y, m_{\tilde{l}}) = \frac{5.67 \times 10^{17}}{\sqrt{g^*}} \frac{\langle \sigma v \rangle}{\mathrm{GeV}^{-2}}\,. \tag{9.33}$$

We approximate the drop in g^* when the muons become non–relativistic by a step-function with $g^*(y < 1) = 16$ and $g^*(y > 1) = 12.34$.

Now T_x and the photon temperature T_γ are related through entropy conservation [62]:

$$\frac{T_x}{T_\gamma} = \left(\frac{43}{57}\right)^{1/3} [\zeta(y)]^{1/3}\,, \tag{9.34}$$

where

$$\zeta(y) = 1 + \frac{180}{43\pi^4} \times \int_0^\infty x^2 \frac{\sqrt{x^2+y^2} + \frac{x^2}{3\sqrt{x^2+y^2}}}{e^{\sqrt{x^2+y^2}} + 1}\,\mathrm{d}x. \tag{9.35}$$

We use Eqs. (9.34) and (9.35) to numerically evaluate $\epsilon(y)$ and then solve the differential equation (9.32) for $\delta(y, m_{\tilde{l}})$. The solution asymptotically approaches a limit [denoted by $\delta_{\max}(m_{\tilde{l}})$] for $y \gtrsim 10$ because for temperatures far below the muon mass there is no further heating of the neutralinos from muon annihilation. This improves our estimate (9.23) to:

$$\Delta N_\nu^{\mathrm{eff}}(\chi_1^0) = \left(\frac{T_{\chi_1^0}}{T_\nu}\right)^4 = 0.69\,[1 + \delta_{\max}(m_{\tilde{l}})]^4. \tag{9.36}$$

In Fig. 9.2, we show $\Delta N_\nu^{\mathrm{eff}}(\chi_1^0)$ as a function of the common slepton mass m_{slepton}. We see that for slepton masses above 3 TeV, our previous result of 0.69 in Eq.(9.25) is not modified. This is because if the interaction between the neutralinos and muons is too weak, then the neutralinos cannot stay in thermal contact with the muons. For slepton masses around 1 TeV, we get again 1 additional effective neutrino species. (Our numerical approximation is valid only for $\delta \ll 1$, so holds down to $m_{\mathrm{slepton}} = 0.5$ TeV when $\delta \simeq 0.1$.)

Summarizing, the neutralino contribution to the effective number of neutrinos lies between 0.69 and 1, depending on the slepton mass as seen in Fig. 9.2. Thus, a very light neutralino is easily accommodated by BBN and CMB data and is in fact favoured by the recent observational indication (9.9) that $N_\nu \gtrsim 3$.

9.2 A very light neutralino and a very light gravitino

A very light gravitino (as realized *e.g.* in some models of gauge-mediated SUSY breaking) can constitute HDM. For its relic density to be small enough to be consistent with the observed small–scale structure requires [292]:

$$m_{\tilde{G}} \lesssim 15 - 30\ \mathrm{eV}\,. \tag{9.37}$$

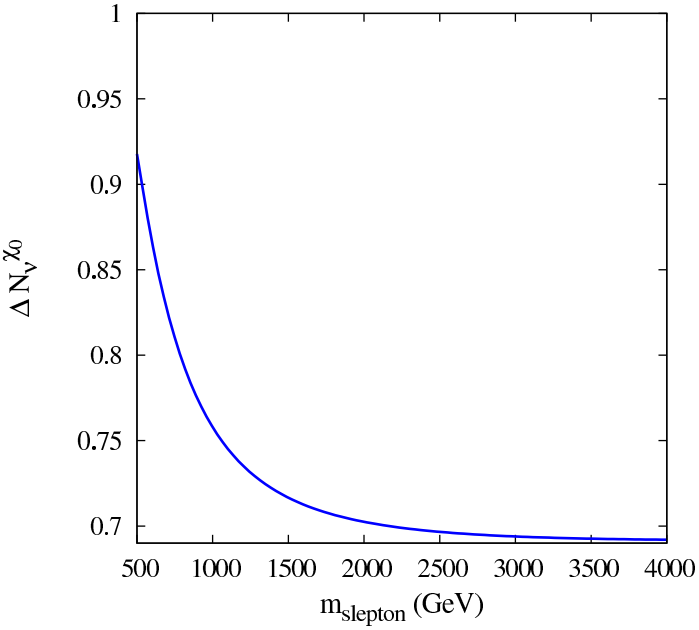

Figure 9.2: Contribution of the pure bino–like neutralino to the effective number of neutrinos versus the slepton mass.

If the gravitino is heavier than the (very light) neutralino it will decay into it plus a photon with a lifetime $\gtrsim 10^{38}$ s [see Eq. (9.44) below] which is well above the age of the universe $\sim 4\times 10^{17}$ s. Conversely if the gravitino is lighter than the neutralino, the latter will decay to a gravitino and a photon with lifetime [293]

$$\tau_{\chi_1^0} \simeq 7.3\times 10^{41}\ \mathrm{s}\left(\frac{m_{\chi_1^0}}{1\ \mathrm{eV}}\right)^{-5}\left(\frac{m_{\tilde{G}}}{0.1\ \mathrm{eV}}\right)^{2}, \tag{9.38}$$

assuming that there is no near–mass degeneracy between the neutralino and the gravitino. Again the lifetime is well above the age of the universe, therefore we can consider both the gravitino and the very light neutralino as effectively stable HDM.

The presence of a very light gravitino thus affects the primordial ^{4}He abundance analogously to a very light neutralino. However, the contribution of the gravitino to the expansion rate depends on its mass, since it couples to other particles predominantly via its helicity–1/2 components with the coupling strength $\Delta m^2/(m_{\tilde{G}} m_{\rm Pl})$, where Δm^2 is the squared mass splitting of the superpartners [294]. For a very light gravitino, the interaction cross-section can be of order the weak interaction, leading to later decoupling. Hence it can have a sizeable effect on BBN.

The freeze-out temperature of a very light gravitino can be estimated from the conversion process with cross-section [295]

$$\sigma(\tilde{G}e^\pm \to e^\pm\chi_1^0) = \frac{\alpha}{9}\frac{s}{m_{\rm Pl}^2 m_{\tilde{G}}^2}. \tag{9.39}$$

We neglect self–annihilations, $\tilde{G}\tilde{G}\to \ell\bar{\ell},\gamma\gamma$ since the annihilation rate into photons is $\propto m_{\chi_1^0}^4$ [286, 296] hence suppressed for a light neutralino, while the annihilation rate into leptons is

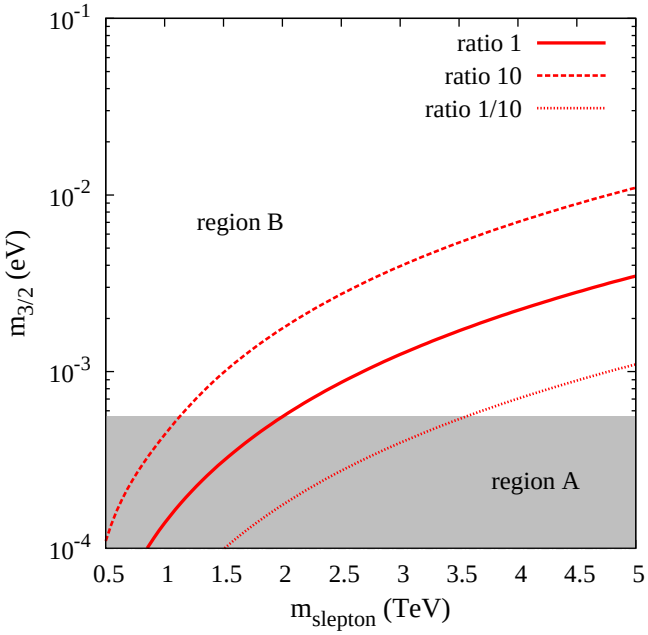

Figure 9.3: Contour lines for the ratio of cross-sections for neutralino self–annihilation (9.16) and conversion/co-annihilation (9.39), in the gravitino–slepton mass plane. The shaded area indicates where $\Delta N_\nu^{\rm total} = 2$.

$\propto T^6$ [286] so falls out of equilibrium much earlier than the conversions (similarily for the wino-like neutralino, where the annihilation rate is $\propto T^4 m_{\chi_2^0}^2$ [286]). If this process (9.39) is dominant over the neutralino self–annihilation process, neutralino and gravitino will co-annihilate, $\tilde{G}\chi_1^0 \to e^+e^-$, with a rate similar to Eq. (9.39).

After thermal averaging of the conversion rate (9.39) as before, we find

$$\begin{aligned} T_{\rm fr}^{\rm conversion} &\simeq 7.51\, m_{\tilde{G}}^{2/3} m_{\rm Pl}^{1/3} g^{*1/6} \\ &\approx 100\, g^{*1/6} \left(\frac{m_{\tilde{G}}}{10^{-3}\ {\rm eV}}\right)^{2/3}\ {\rm MeV}. \end{aligned} \tag{9.40}$$

Since the goldstino coupling is enhanced for decreasing gravitino mass, the freeze-out temperature of the gravitino increases with its mass. For a gravitino mass of 5.6×10^{-4} eV (7.8×10^{-4} eV) its freeze-out temperature equals the muon (pion) mass, so for heavier gravitinos the contribution to $\Delta N_\nu^{\rm eff}$ will decrease. We also consider the case $m_{\tilde{G}} = 10$ eV which gives a freeze-out temperature of $\mathcal{O}(100)$ GeV, thus a negligible effect on $\Delta N_\nu^{\rm eff}$. (Note however that $T_{\rm fr}^{\tilde{\rm G}}$ will now depend on the SUSY mass spectrum because above temperatures of a GeV or so other SUSY processses can also be in thermal equilibrium [297, 298] and Eq. (9.40) may not apply.)

We can now evaluate the contribution of the gravitino, in conjunction with the very light neutralino, to the effective number of neutrino species. We need to keep in mind that the gravitino can affect neutralino decoupling since for very large slepton masses and/or very light gravitinos, the neutralino annihilation process $\chi_1^0\chi_1^0 \to \ell\bar{\ell}$ becomes sub–dominant to the conversion process $\tilde{G}e^\pm \to e^\pm\chi_1^0$ and therefore neutralino and gravitino will co-annihilate with a rate similar to

Eq. (9.40).

In Fig. 9.3, we show contour lines for the ratio of the cross-sections for neutralino annihiliation (9.16), and the conversion process (9.39), in the slepton–gravitino mass plane. For a ratio less than 0.1, the freeze–out temperature of both particles is determined via the conversion process (9.39) and $T_{\tilde{G}} = T_{\chi_1^0}$. Hence $\Delta N_\nu^{\rm eff}(\tilde{G}, \chi_1^0) = 1/0.69/0.57$, the latter two cases corresponding to gravitino masses above 5.6×10^{-4} eV and 7.8×10^{-4} eV, respectively [corresponding to a freeze–out temperature below the muon and the pion mass, as determined from Eq. (9.40)]. The corresponding equivalent number of neutrino species is:

$$\Delta N_\nu^{\rm total} \equiv \Delta N_\nu^{\rm eff}(\tilde{G}) + \Delta N_\nu^{\rm eff}(\chi_1^0) = 2/1.38/1.14\,. \tag{9.41}$$

Thus a very light gravitino is strongly constrained by the BBN bound (9.9), a mass below 5.6×10^{-4} eV being excluded at 3σ. As the gravitino mass increases, $\Delta N_\nu^{\rm total}$ decreases because the gravitino and neutralino freeze-out earlier, hence are colder than the neutrinos at the onset of BBN.

One can see from Fig. 9.3 that a further increase of the gravitino mass (or smaller slepton mass) accesses parameter regions where the neutralino annihilation process dominates over the conversion process. When the ratio of their rates exceeds ~ 10, the freeze–out of the neutralino and the gravitino is governed by the processes (9.16) and (9.39) respectively. For a slepton mass above ~ 3 TeV, the lightest neutralino decouples above the muon mass hence yields $\Delta N_\nu^{\rm eff}(\chi_1^0) = 0.69$. Fig. 9.2 shows that with decreasing slepton mass, this increases to $\Delta N_\nu^{\rm eff}(\chi_1^0) = 1$ as before. Hence we obtain the same bounds on the gravitino mass for $\Delta N_\nu^{\rm eff}(\tilde{G}) = 1/0.69/0.57$.

In summary for a slepton mass below ~ 1 TeV

$$\Delta N_\nu^{\rm total} = 2/1.69/1.57\,, \tag{9.42}$$

while for a slepton mass above ~ 3 TeV

$$\Delta N_\nu^{\rm total} = 1.69/1.38/1.26\,; \tag{9.43}$$

for intermediate slepton masses, there is a continuous transition between the two cases.

If the gravitino mass increases further its effect on the expansion rate continues to decrease, *e.g.* for $m_{\tilde{G}} = 10$ eV (corresponding to $T_{\rm fr}^{\tilde{G}} \approx 100$ GeV), we find $g^* = 395/4$ or $\Delta N_\nu^{\rm eff}(\tilde{G}) \simeq 0.05$. Thus, gravitinos with mass $\gtrsim$ eV do not significantly affect the expansion rate.

Summarising, $\Delta N_\nu^{\rm total}$ is between 1.14 and 2 for scenarios with both a relativistic neutralino and a relativistic gravitino (when their freeze-out temperature lies between the freeze-out temperature of the neutrino and the pion mass). As before we can use the Boltzmann equation if necessary to obtain exact values for $\Delta N_\nu^{\rm eff}$ around the mass thresholds. From Eq. (9.9), $N_\nu^{\rm total} > 4.9$ is excluded at 3σ implying a lower bound on the gravitino mass of 5.6×10^{-4} eV, *cf.* Fig. 9.3. This bound is two orders of magnitude weaker than the one stated in Ref. [286] where a model with a very light gravitino but a heavy neutralino was considered. This is because the gravitino annihilation into di-photons or leptons is the relevant process when there is no light neutralino, also Ref. [286] assumed a more stringent BBN limit: $N_\nu^{\rm total} < 3.6$.

9.3 Decaying Gravitinos

So far we have considered the increase in the expansion rate caused by sub–eV neutralinos and gravitinos which are quasi–stable (*cf.* § 9.4). We now consider a gravitino with a mass above $\mathcal{O}(100\,\mathrm{GeV})$ as would be the case in gravity mediated SUSY breaking where the gravitino sets the mass scale of SUSY partners.

As the gravitino mass increases, the relative coupling strength of the helicity–1/2 components, $\Delta m^2/(m_{\tilde{G}} m_{\mathrm{Pl}})$ decreases and the helicity–3/2 components come to dominate. These are however also suppressed by $1/\mathrm{m_{Pl}}$ hence gravitinos decouple from thermal equilibrium very early. During reheating, gravitinos are produced thermally via two–body scattering processes (dominantly QCD interactions) and the gravitino abundance is proportional to the reheating temperature T_{R} [299]. The gravitino is unstable and will decay subsequently into the very light neutralino and a photon with lifetime [278, 299–301],

$$\tau_{\tilde{G}} \simeq 4.9 \times 10^8 \left(\frac{m_{3/2}}{100\,\mathrm{GeV}}\right)^{-3} \mathrm{s}\,, \tag{9.44}$$

where we have assumed for simplicity that the gravitino is the next–to–lightest SUSY particle (NLSP) while the neutralino is the LSP. If the gravitino decays around or after BBN, the light element abundances are affected by the decay products whether photons or hadrons. In particular there is potential overproduction of D and ^{3}He from photodissociation of (the much more abundant) ^{4}He [278, 300], while for short lifetimes, decays into hadrons have more effect [301].

Therefore, the observationally inferred light element abundances constrain the number density of gravitinos. For a gravitino lifetime of $\mathcal{O}(10^8\,\mathrm{sec})$ one obtains [302, 303] a severe bound on the abundance $Y_{3/2} \equiv n_{3/2}/s$:

$$Y_{3/2} \lesssim 10^{-14} \left(\frac{100\,\mathrm{GeV}}{m_{\tilde{G}}}\right). \tag{9.45}$$

This is proportional to the reheating temperature through [278, 299–301]

$$\left(\frac{T_{\mathrm{R}}}{10^{10}\,\mathrm{GeV}}\right) \approx 3.0 \times 10^{11}\; Y_{3/2}\,, \tag{9.46}$$

hence the latter is constrained to be

$$T_{\mathrm{R}} \lesssim 3.0 \times 10^7\ \mathrm{GeV} \times \left(\frac{100\,\mathrm{GeV}}{m_{3/2}}\right). \tag{9.47}$$

Note that a reheating temperature below $\mathcal{O}(10^8\ \mathrm{GeV})$ is not consistent with thermal leptogenesis, which typically requires $T_{\mathrm{R}} \sim 10^{10}$ GeV [304]. There are however other possible means to produce the baryon asymmetry of the universe at lower temperature [275–277].

The contribution to the present neutralino relic density from gravitino decays is

$$\Omega_{\chi_1^0}^{\mathrm{decay}} h^2 \approx 0.28\; Y_{3/2} \left(\frac{m_{\chi_1^0}}{1\,\mathrm{eV}}\right). \tag{9.48}$$

i.e. negligible, such that the Cowsik–McClelland bound on the neutralino mass is unaffected.

9.4 Quasi–stable Gravitinos

As mentioned in § 9.3, when the gravitino mass is below ~ 100 MeV its lifetime is longer than the age of the universe so it is quasi–stable and can constitute warm dark matter. Decaying gravitino DM is constrained by limits on the diffuse γ–ray background. For a mass between ~ 100 keV and ~ 100 MeV the gravitino decays to a photon and a neutralino, and the photon spectrum is simply

$$\frac{dN_\gamma}{dE} = \delta(E - \frac{m_{\tilde{G}}}{2})\,. \tag{9.49}$$

The γ–flux from gravitions decaying in our Milky Way halo dominates [305, 306] over the redshifted flux from gravitino decays at cosmological distances. Using a Navarro-Frenk-White profile for the distribution of DM in our galaxy, we obtain [307]

$$\begin{aligned} E^2 \quad \frac{\mathrm{d}J}{\mathrm{d}E}|_{\rm halo} &\equiv \frac{2E^2}{8\pi\tau_{\tilde{G}} m_{\tilde{G}}} \frac{\mathrm{d}N_\gamma}{\mathrm{d}E} \int_{\rm l.o.s} \langle \rho_{\rm halo}(\vec{\ell}) d\vec{\ell} \rangle / \Delta\Omega \\ &= 31.1 \left(\frac{m_{\tilde{G}}}{1\ \mathrm{MeV}}\right)^4 \delta(E - \frac{m_{\tilde{G}}}{2}) \frac{\mathrm{MeV}}{\mathrm{cm}^2\ \mathrm{str}\ \mathrm{s}}\,. \end{aligned} \tag{9.50}$$

We compare this to the measurements of the γ-ray background by COMPTEL, EGRET and Fermi [308–310] and extract a conservative upper bound of 3×10^{-2} cm^{-2}str^{-1}s^{-1}MeV on the γ-ray flux from the inner Galaxy in the relevant mass region below ~ 100 MeV. This implies that gravitinos with mass above ~ 250 keV would generate a flux exceeding the observed galactic γ-ray emission. On the other hand, constraints from small–scale structure formation set a lower mass bound on WDM of $\mathcal{O}$(keV) [311–313].

Now we consider the relic density of those gravitinos. Due to the presence of the very light neutralino, all sparticles will decay into the latter before the onset of BBN. Therefore the gravitino will only be produced thermally with relic density [314]

$$\Omega_{3/2} h^2 \approx \left(\frac{1\ \mathrm{keV}}{m_{\tilde{G}}}\right) \left(\frac{T_{\rm R}}{10\ \mathrm{TeV}}\right) \left(\frac{M_{\rm SUSY}}{200\ \mathrm{GeV}}\right)^2 . \tag{9.51}$$

This further restricts the gravitino mass and/or the reheating temperature in order not to exceed the observed value $\Omega_{\rm DM} h^2 \approx 0.11$. The least restrictive upper bound on the reheating temperature from Eq. (9.51) is $\mathcal{O}(10^5\,\mathrm{GeV})$ for gravitino and gaugino masses of order 100 keV and 100 GeV, respectively. This could be alleviated if the gravitino density is diluted by the decay of particles (such as moduli fields [301] or the saxion from the axion multiplet [315, 316]). In this context, there have been several detailed studies on gravitinos as light DM [317–321].

Chapter 10

Summary and Conclusion

After motivating and introducing our framework in chapters § 1 to § 3, we presented work on several aspects of a lepton–number violating minimal supersymmetric extension of the Standard Model, the B_3 cMSSM in chapters § 4 to § 7. Then, we discussed the discovery potential of light stops in the R_p–conserving MSSM in § 8 and finally we investigated bounds on a near massless neutralino in the R_p–conserving MSSM due to cosmological restrictions (§ 9). First, we analyzed in § 4 how the neutrino masses, which are naturally present in the B_3 cMSSM, depend on the input parameters at the unification scale, restricting ourselves to the case of one single LNV coupling for simplicity. We found that the tree–level neutrino mass depends strongly on the trilinear soft-breaking A_0–parameter (and also similarly on the gaugino masses). We conclude in § 4, that in regions of parameter space with $A_0 \approx 2M_{1/2}$ ($A_0 \approx M_{1/2}/2$) for $\lambda'_{ijk}|_{\rm GUT} \neq 0$ ($\lambda_{ijk}|_{\rm GUT} \neq 0$), a cancellation between the different contributions to the tree–level mass can occur. We have explained this effect in detail and have shown that such a cancellation is significant in large regions of the cMSSM parameter space. Although we concentrated in this work on the B_3 cMSSM model, the mechanisms described will also work in more general lepton–number violating models.

Keeping this effect in mind, we calculated upper bounds on single trilinear LNV couplings at the unification scale within the B_3 cMSSM, which result from the cosmological bound on the sum of neutrino masses (§ 5.3). We showed that these bounds on the couplings can be weaker by one to two orders of magnitude compared to the ones which were previously presented in the literature. In general, the bounds can be as weak as $\mathcal{O}(10^{-1})$. Thus other low energy bounds become competitive. The reason for these large effects is the above mentioned A_0 dependence of the tree–level neutrino mass. For example, the bounds can be weakened by one order of magnitude in A_0 intervals of up to $\mathcal{O}(100\ \text{GeV})$ around $A_0 \approx 2M_{1/2}$ ($A_0 \approx M_{1/2}/2$), see Fig. 5.1 (Fig. 5.2). Therefore, much weaker bounds (compared to previous ones) can occur without significant fine–tuning. In order to obtain the correct bounds in the vicinity of the tree–level neutrino mass minimum, we included the main 1–loop contributions as listed in § 3.

The work presented in § 4 can also help to find new supersymmetric scenarios that are consistent with the observed neutrino masses and mixings. We have shown how the (typically large) hierarchy between the tree–level and 1–loop neutrino masses can systematically be reduced by tuning (but not fine–tuning) the tri–linear soft breaking A_0 parameter. Together with additional LNV couplings, one can use this mechanism to match the ratio between tree–level and 1–loop induced masses to the observed neutrino mass hierarchy. We further develop this idea in § 6. However, in § 4.5 it was mentioned that loop corrections to the sneutrino vevs can lead to a seizable correction of the absolute value of the neutrino masses. Also, there are further contributions to 1–loop neutrino masses besides the dominant $\Lambda\Lambda$ and neutral scalar–neutralino loops discussed here. Hence, we implement a full 1–loop treatment of the neutrino sector within the spectrum calculator `SOFTSUSY`, described in § 6.1.2, in order to obtain a precise description of

neutrino masses for comparison with experimental data. We then analyze how phenomenologically viable neutrino mass and mixings can be obtained in the B_3 cMSSM for the cases of normal hierarchy (NH), inverted hierarchy (IH) and degenerate (DEG) neutrino masses. Furthermore we have mostly focused on one benchmark point to fix the other cMSSM parameters. We have implemented all the relevant low–energy bounds on the lepton number violating R–parity violating couplings. It turns out these kill a significant number of the best–fit solutions we find. We have then considered five different scenarios, labelled **S1** through **S5**. Scenarios **S1** through **S3** employ diagonal lepton number violating couplings Λ_{ijl} and the couplings are chosen to closely follow the structure of the tri–bi maximal mixing solutions. The three scenarios correspond to the three different possible generations $j = 1, 2, 3$. *Higher* generations lead to *smaller* lepton number violating couplings, because the corresponding Higgs Yukawa couplings which also enter the formulae are larger. In looking for solutions, we then fit a small number of lepton number violating couplings to the neutrino data. We need five couplings in the NH case, six in the IH case and eight couplings for the degenerate case. Our results are presented in Table 6.2. Solutions with large couplings, $\Lambda = \mathcal{O}(10^{-2})$, are mostly excluded by the low–energy bounds. In particular this kills all **S1** models, as well as the IH and DEG models in the **S2** scenarios. The NH **S2**, as well as the NH and DEG **S3** scenarios include $LL\bar{E}$ couplings of order 10^{-2}. All other remaining scenarios have couplings 10^{-3} or smaller. Possible alternatives to the scenarios **S1**, **S2** and **S3** are presented in scenarios **S4** and **S5**. The **S4** models assume ansätze with diagonal Λ couplings but alternative methods to obtain the neutrino masses, whereas the **S5** models employ off–diagonal Λ couplings. Despite the tension between the neutrino mass contribution and the low energy bounds, which favor large and small LNV couplings respectively, λ couplings of $\mathcal{O}(0.01)$ (e.g. **S2, S3** NH) involving only the first 2 lepton generations are allowed. However, simultaneous presence of (dominant) diagonal LNV couplings λ'_{i11} and λ_{j11} appears to be difficult, at least with the assumed mass spectrum BP. Single coupling dominance, which many collider studies usually assume, also appears to be consistent with neutrino oscillation data (**S5** DEG). It would therefore be interesting to study collider implications of these models in more detail.

For this purpose, we introduce in § 7 a hierarchical ansatz for the trilinear LNV couplings in the B_3 cMSSM, which corresponds to scenario **S5** NH of § 6. Here, the trilinear LNV Yukawa couplings are related to the Higgs Yukawa couplings via six independent complex numbers ℓ_i and ℓ'_i. We have then determined the best fit values of the ℓ_i and ℓ'_i in order to obtain phenomenologically viable neutrino masses and mixing angles. We find that we obtain phenomenologically viable neutrino masses and mixings only in the case of NH neutrino masses and that the LNV sector is unambiguously determined by neutrino oscillation data. We discuss the resulting collider signals for the case of a neutralino as well as a scalar tau lightest supersymmetric particle. We use the ATLAS searches for multi–jet events and large $\not{p}_T$ in the 0, 1 and 2 lepton channel with 7 TeV center–of–mass energy in order to derive exclusion limits on the parameter space of this R–parity violating supersymmetric model. We present the 95% and 68% CL exclusion limits in the M_0–$M_{1/2}$ plane for fixed $\mathrm{sgn}(\mu)$ and $\tan\beta$ in Figs. 7.6- 7.8. We can exclude squark masses below 800 GeV, and gluino masses below 700 GeV (for squark masses below 1 TeV) at 95%. These limits become more stringent at 68% CL by roughly 100 GeV. Compared to the case of the R–parity conserving cMSSM, we obtain weaker limits using the ATLAS searches (optimized for R_p–conserving models) because generally we have less $\not{p}_T$ and more jets and/or leptons.

Furthermore, we consider in § 8 light stops nearly degenerate with the lightest neutralino, with mass splitting of at most a few tens of GeV in the R_p–conserving MSSM. In such a

scenario the direct production of a pair of light stops in stop pair production is difficult to detect at a hadron collider like the LHC since the decay products of the stops are quite soft. One solution is to examine stop pair production in association with two $b-$jets, which could not only serve as a stop discovery channel, but could also be used to constrain Yukawa couplings of superparticles because mixed QCD–EW contributions are large. However, in order to determine the value of this coupling from future data, it is necessary to know the stop mass so that the QCD contribution can be subtracted. In this context, it is interesting to stop pair production in association with a hard jet because here EW contributions are negligible. We analyze this process with some significant improvements compared to previous publications. Firstly, we include the $t\bar{t}$ background, which had been neglected in previous works. Secondly, we simulate the signal and full SM background with the recent Monte Carlo simulations including a detector simulation. Finally, we optimize the selection cuts. We find that demanding a lot of missing transverse energy ($\not{p}_T \geq 450$GeV) and large transverse momentum of the hardest jet ($p_T(j_1) \geq 500$GeV) is not sufficient to see an excess above the SM background. However, additionally imposing a lepton veto and a veto on the second jet ($p_T(j_2) \leq 100$GeV) is very efficient for background suppression, the remaining dominant background process being the irreducible process $Z(\to \nu\bar{\nu}) + j$. Fortunately, this background can be determined experimentally from $Z(\to \ell\ell) + j$, although with reduced statistics. Here, we adopted a conservative estimate of the background uncertainty of the $Z(\to \nu\bar{\nu}) + j$ channel using $\delta B_{Z(\to\nu\bar{\nu})+j} = 5.3 B_{Z(\to\nu\bar{\nu})+j}$. On the remaining SM backgrounds we assum a systematic error of 10%. For our benchmark point, we show that we can have a total signal significance exceeding 8 for an integrated luminosity of 100 fb^{-1} at $\sqrt{s} = 14$ TeV, cf. Table 8.3. For the same cuts, we examine the discovery reach in the stop–neutralino mass plane and showed that this process can probe stop masses up to 290 GeV if the mass splitting to the LSP is very small, cf. Fig. 8.9.

Finally, we consider the effect of a stable very light neutralino on the effective number of neutrino species during big bang nucleosynthesis in § 9. Even a massless neutralino is compatible with all laboratory data, while the strictest astrophysical constraint is imposed by supernova cooling and requires selectrons to be heavy ($m_{\tilde{e}} \gtrsim 1\,\text{TeV}$). For slepton masses above ~ 3 TeV, we arrive at the result that $\Delta N_\nu^{\text{eff}}(\chi_1^0)$ is 0.69 and this increases as the slepton mass decreases, reaching 1 for slepton masses below ~ 0.5 TeV. We also consider constraints on the gravitino mass in the context of local SUSY with a very light neutralino. A very light gravitino will affect the expansion rate of the universe similarly to a light neutralino. We identify the mass range where a gravitino has a sizeable effect on the effective number of neutrino species as $\sim 10^{-4} - 10$ eV. Within this range, we obtain values for $\Delta N_\nu^{\text{eff}}(\chi_1^0 \,\&\, \tilde{G})$ between 0.74 and 1.69, depending on the gravitino and slepton masses. Values around 0.7 are favored by recent BBN measurements. However, the uncertainties in the determination of ^{4}He are still sufficiently large that we need to await data from Planck to pin down the allowed gravitino and slepton mass. If the gravitino is heavier than $\sim$ 100 MeV, it decays to the neutralino and a photon with a lifetime smaller than the age of the universe. This results in photo-dissociation of the light elements, which is strongly constrained observationally and translates into an upper bound on the reheating temperature of the universe of $\sim 10^7$ GeV for typical gravity mediated SUSY breaking models. Note that neither the neutralino nor the gravitino can constitute the complete dark matter in the scenarios considered so far. The mass range where the gravitino can constitute warm dark matter is constrained by bounds from the diffuse γ-ray background, from the formation of structure on small-scales, and from the observed DM abundance, leaving a small window of allowed gravitino mass between 1 and 100 keV for a reheating temperature below 10^5 GeV.

Appendix A

Abbreviations

B_3	Baryon Triality
BBN	Big Bang Nucleosynthesis
BNV	baryon number violating
CKM	Cabbibo–Kobayashi–Maskawa matrix
cMSSM	constrained Minimal Supersymmetric extension of the Standard Model
CPE	CP–even
CPO	CP–odd
DEG	degenerate
DM	dark matter
EW	electroweak
FCNC	flavor changing neutral currents
Fig.	Figure
HDM	hot dark matter
IH	Inverted Hierarchy
LEO	low energy observables
LEP	Large Electron–Positron Collider
LHC	Large Hadron Collider
LNV	lepton number violating
LSP	lightest supersymmetric particle
MSSM	Minimal Supersymmetric extension of the Standard Model
NH	Normal Hierarchy
NLSP	next–to–lightest supersymmetric particle
P_6	Proton Hexality
PMNS	Pontecorvo–Maki–Nakagaw–Sakata matrix
R_p	R–parity
$\not{R}_p$	R–parity violating
Ref.	Reference
REWSB	radiative electroweak symmetry breaking
RG(E)	Renormalization Group (Equations)
RHS	right hand side
SM	Standard Model of particle physics
SUSY	Supersymmetry
Tab.	Table
TBM	tri-bi maximal mixing
QCD	quantum chromodynamics
WDM	warm dark matter
WMAP	Wilkinson Microwave Anisotropy Probe

Appendix B

Softsusy code

We here present parts of the new SOFTSUSY-3.2 code where we implemented the $\not{R}_p$ tadpoles for REWSB. We only show the routines which calculate the 1–loop sneutrinoVEVs, not the code which does the same for the Higgs VEVs, since the calculation is similar. More details about the general procedure are given in Ref. [83]. We have checked that in the R_p–conserving limit our results agree with the internal results in SOFTSUSY-3.1.5.

```
DoubleVector RpvNeutrino::calculateSneutrinoVevs
(const DoubleVector & sneutrinoVevs, double tol, double snuSq, double v1, double v2) {

  double tb = displayTanb(), beta = atan(tb);
  double vSM = displayHvev();
  double mz = displayMzRun();
  double sinthDRbar = calcSinthdrbar();

  DoubleVector n(3);
  DoubleMatrix m(3, 3), mInverse(3, 3);
  DoubleMatrix i(3, 3);   i(1, 1) = i(2, 2) = i(3, 3) = 1.0; /// Identity matrix

  /// tree level sneutrino vevs
  n = displayDr() * v2 - displaySusyMu() * v1 * displayKappa()  - displayMh1lSquared() * v1;
  m = displaySoftMassSquared(mLl).transpose()  + (0.5 * sqr(mz) * cos(2.0 * beta)
       + sqr(sin(beta)) * sqr(mz) / sqr(vSM) * snuSq) * i
       + outerProduct(displayKappa(), displayKappa());

  mInverse = m.inverse();

  /// adding the 1-loop correction
  n = n + calculateSneutrinoTadpoles(sinthDRbar);

  return mInverse * n;
}


DoubleVector RpvNeutrino::calculateSneutrinoTadpoles(double sinthDRbar) {

  double g1 = displayGaugeCoupling(1) * sqrt(0.6), g2 = displayGaugeCoupling(2);
  double tanb = displayTanb(), beta = atan(tanb);

  double costhDRbar = sqrt(1.0 - sqr(sinthDRbar)),
         tanthDRbar = tan(asin(sinthDRbar)), tanthDRbar2 = sqr(tanthDRbar);

  double vSM = displayHvev();
```

```
DoubleVector vi = displaySneutrinoVevs();
double snuSq, v1, v2;
if (usefulVevs(vSM, vi, snuSq, v1, v2)) {
      cout << "sneutrino VEVs incompatible with MZ, MW!" << endl; }
double mw = displayMwRun();
double mz = displayMzRun();
double q = displayMu();

double smu = displaySusyMu();
DoubleVector kappa =  displayKappa();
DoubleVector Dr =  displayDr();

DoubleMatrix ye = displayYukawaMatrix(YE);
DoubleMatrix he = displayTrilinear(EA);
DoubleMatrix yd = displayYukawaMatrix(YD);
DoubleMatrix hd = displayTrilinear(DA);
DoubleMatrix yu = displayYukawaMatrix(YU);

/// CPE/CPO scalar couplings
DoubleMatrix CPECoupling(5,5), CPOCoupling(5,5);
vector<DoubleMatrix> CPECouplings, CPOCouplings;

for (int family=1; family <=3; family++) {
  for (int ii=1; ii<=5; ii++) {                    //initialise
    for (int jj=1; jj<=5; jj++) {
        CPECoupling(ii,jj) = 0.;
        CPOCoupling(ii,jj) = 0.;
  }}

  for (int ii=1; ii<=3; ii++) {  //sneutrinos
    CPECoupling(ii+2, ii+2) = sqr(g2 / costhDRbar) /8.0 * vi(family);
    CPOCoupling(ii+2, ii+2) = sqr(g2 / costhDRbar) /8.0 * vi(family);

    if ((ii)==family) {
       CPECoupling(1, ii+2) = - sqr(g2 / costhDRbar)/ 8.0 * v2;
       CPECoupling(2, ii+2) = sqr(g2 / costhDRbar)/ 8.0 * v1;
       CPECoupling(ii+2, 1) = CPECoupling(1, ii+2);
       CPECoupling(ii+2, 2) = CPECoupling(2, ii+2);

       for (int jj=1; jj<=3; jj++) {
         CPECoupling(family+2, jj+2) = CPECoupling(family+2, jj+2) +
                                       sqr(g2 / costhDRbar) /8.0 * vi(jj);
         CPECoupling(jj+2, family+2) = CPECoupling(jj+2, family+2) +
                                       sqr(g2 / costhDRbar) /8.0 * vi(jj);
  }}}

  /// snu-higgs1-higgs1 (down-type)
  CPECoupling(2, 2) = sqr(g2 / costhDRbar) / 8.0 * vi(family);
  CPOCoupling(2, 2) = sqr(g2 / costhDRbar) / 8.0 * vi(family);

  /// snu-higgs2-higgs2 (up-type)
  CPECoupling(1, 1) = - sqr(g2 / costhDRbar) / 8.0 * vi(family);
  CPOCoupling(1, 1) = - sqr(g2 / costhDRbar) / 8.0 * vi(family);
```

```
  CPECoupling = CPEscalarMixing.transpose() * CPECoupling * CPEscalarMixing;
  CPOCoupling = CPOscalarMixing.transpose() * CPOCoupling * CPOscalarMixing;

  CPECouplings.push_back(CPECoupling);
  CPOCouplings.push_back(CPOCoupling);
}

DoubleVector neutralCPEscalars(3), neutralCPOscalars(3);
for (int family=1; family <=3; family++) {
  for (int ii=1; ii<=5; ii++) {
    neutralCPEscalars(family) = neutralCPEscalars(family) +
         CPECouplings[family-1](ii, ii)  * a0(CPEmasses(ii), q);
    neutralCPOscalars(family) = neutralCPOscalars(family) +
         CPOCouplings[family-1](ii, ii)  * a0(CPOmasses(ii), q);
}}

CPECouplings.clear();
CPOCouplings.clear();

DoubleVector tadpole = neutralCPEscalars + neutralCPOscalars;

///charged higgs-slepton mass matrix - order: Hu1, Hd2, tildeLi, tildeEbarj
DoubleMatrix Sleptons = calculateLNVSleptonMassMatrix(sinthDRbar);

DoubleVector SleptonMasses(8);
DoubleMatrix SleptonMixing(8, 8);
Sleptons.diagonaliseSym(SleptonMixing, SleptonMasses);
SleptonMasses = SleptonMasses.apply(ccbSqrt);

///slepton couplings
DoubleMatrix SleptonCoupling(8, 8);
vector<DoubleMatrix> SleptonCouplings;

for (int family=1; family <=3; family++) {
  for (int ii=1; ii<=8; ii++) {       //initialise
    for (int jj=1; jj<=8; jj++) SleptonCoupling(ii, jj) = 0.;
  }

  SleptonCoupling(1, 1) = sqr(g2 / 2.0) * (1. - tanthDRbar2) * vi(family);
  SleptonCoupling(2, 2) = -sqr(g2 / 2.0) * (1. - tanthDRbar2) * vi(family);

  for (int ii=1; ii<=3; ii++) {
    if (family == ii) {
       SleptonCoupling(1, ii+2) = 0.25 * sqr(g2) * v2;
       SleptonCoupling(2, ii+2) = 0.25 * sqr(g2) * v1;
       SleptonCoupling(ii+2, 2) = 0.25 * sqr(g2) * v1;
    }
    SleptonCoupling(2, ii+5) = - he(family, ii) / root2;
    SleptonCoupling(ii+2, ii+2) = - sqr(g2 / 2.0) * (1. - tanthDRbar2) * vi(family);
    SleptonCoupling(ii+5, ii+5) = - 0.5 * sqr(g2) * tanthDRbar2 * vi(family);
    SleptonCoupling(1, ii+5) = SleptonCoupling(1, ii+5) - smu /  root2 * ye(family, ii);
```

```
      for (int jj=1; jj<=3; jj++) {
    if (family == jj) {
       SleptonCoupling(ii+2, family+2) = SleptonCoupling(ii+2, family+2)
                                         + sqr(g2) * 0.25 * vi(ii);
       SleptonCoupling(family+2, ii+2) = SleptonCoupling(family+2, ii+2)
                                         + sqr(g2) * 0.25 * vi(ii);
    }
    SleptonCoupling(1, ii+5) = SleptonCoupling(1, ii+5) +
          displayLam(family, jj, ii) / root2 * kappa(jj);
    SleptonCoupling(ii+2, 2) = SleptonCoupling(ii+2, 2) -
          ye(family, jj) * ye(ii, jj) * v1;
    SleptonCoupling(2, 2) = SleptonCoupling(2, 2) +
          ye(family, jj) * ye(ii, jj) * vi(ii);
    SleptonCoupling(ii+2, jj+5) = SleptonCoupling(ii+2, jj+5) +
          displayHr(LE).display(jj, family, ii) / root2;

    for (int kk=1; kk<=3; kk++) {
      SleptonCoupling(2, ii+2) = SleptonCoupling(2, ii+2) -
         ye(kk, jj) * displayLam(family, ii, jj) * vi(kk);
      SleptonCoupling(ii+2, 2) = SleptonCoupling(ii+2, 2) -
         ye(family, jj) * displayLam(kk, ii, jj) * vi(kk);
      SleptonCoupling(ii+2, jj+2) = SleptonCoupling(ii+2, jj+2) +
         ye(ii, kk)  * displayLam(family, jj, kk) * v1;
      SleptonCoupling(ii+5, jj+5) = SleptonCoupling(ii+5, jj+5) +
         ye(family, jj) * ye(kk, ii) * vi(kk)  +
        ye(kk, ii) * v1 * displayLam(family, kk, jj);

      for (int ll=1; ll<=3; ll++) {
         SleptonCoupling(ii+2, jj+2) = SleptonCoupling(ii+2, jj+2) +
       displayLam(kk, ii, ll) * displayLam(family, jj, ll) * vi(kk);
         SleptonCoupling(ii+5, jj+5) = SleptonCoupling(ii+5, jj+5) +
       displayLam(kk, ll, ii) * displayLam(family, ll, jj) * vi(kk);
      }}
      SleptonCoupling(jj+5, ii+2) = SleptonCoupling(ii+2, jj+5);
    }
    SleptonCoupling(ii+2, 1) = SleptonCoupling(1, ii+2);
    SleptonCoupling(ii+5, 1) = SleptonCoupling(1, ii+5);
    SleptonCoupling(ii+5, 2) = SleptonCoupling(2, ii+5);
 }
 SleptonCoupling = SleptonMixing.transpose() * SleptonCoupling * SleptonMixing;
 SleptonCouplings.push_back(SleptonCoupling);
}

DoubleVector sleptons(3), cgb(3), chiggs(3), sleps(3);
for (int family=1; family<=3; family++) {
   for (int II=1; II<=8; II++) {
      sleptons(family) = sleptons(family) +
                    SleptonCouplings[family-1](II, II) * a0(SleptonMasses(II), q);

      if (II>=2 && II<=7) sleps(family) = sleps(family) +
                    SleptonCouplings[family-1](II, II) * a0(SleptonMasses(II), q);
   }
   cgb(family) = cgb(family) + SleptonCouplings[family-1](1, 1) *
```

```
                        a0(SleptonMasses(1), q);
  chiggs(family) = chiggs(family) + SleptonCouplings[family-1](8, 8) *
                       a0(SleptonMasses(8), q);
}
tadpole = tadpole + sleptons;

SleptonCouplings.clear();

/// squark mass matrices
DoubleMatrix UpSquarks = calculateLNVUpSquarkMassMatrix(sinthDRbar),
DownSquarks = calculateLNVDownSquarkMassMatrix(sinthDRbar);

DoubleVector UpSquarkMasses(6), DownSquarkMasses(6);
DoubleMatrix UpSquarkMixing(6, 6), DownSquarkMixing(6, 6);
UpSquarks.diagonaliseSym(UpSquarkMixing, UpSquarkMasses);
DownSquarks.diagonaliseSym(DownSquarkMixing, DownSquarkMasses);

UpSquarkMasses = UpSquarkMasses.apply(ccbSqrt);
DownSquarkMasses = DownSquarkMasses.apply(ccbSqrt);

/// squark couplings
DoubleMatrix UpSquarkCoupling(6, 6), DownSquarkCoupling(6, 6);
vector<DoubleMatrix> UpSquarkCouplings, DownSquarkCouplings;

for (int family=1; family <=3; family++) {
   /// initialise
   for (int ii=1; ii<=6; ii++) {
     for (int jj=1; jj<=6; jj++) {
        UpSquarkCoupling(ii, jj) = 0.;
        DownSquarkCoupling(ii, jj) = 0.;
   }}
   for (int ii=1; ii<=3; ii++) {
      UpSquarkCoupling(ii, ii) = sqr(g2 / 2.0) * (1. - tanthDRbar2 / 3.0) * vi(family);
      UpSquarkCoupling(ii+3, ii+3) = sqr(g2) * tanthDRbar2 / 3.0 * vi(family);

      DownSquarkCoupling(ii,ii) = - sqr(g2 / 2.0) * (1. + tanthDRbar2 / 3.0) * vi(family);
      DownSquarkCoupling(ii+3,ii+3) = - sqr(g2) * tanthDRbar2 / 6.0 * vi(family);

      for (int jj=1; jj<=3; jj++) {
         UpSquarkCoupling(ii, jj+3) = - kappa(family) / root2 * yu(ii, jj);
         UpSquarkCoupling(jj+3, ii) = UpSquarkCoupling(ii, jj+3);
         DownSquarkCoupling(ii, jj+3) = displayHr(LD).display(jj, family, ii) / root2;
         DownSquarkCoupling(jj+3, ii) = DownSquarkCoupling(ii, jj+3);

         for (int kk=1; kk<=3; kk++) {
            DownSquarkCoupling(ii, jj) = DownSquarkCoupling(ii, jj) +
                                displayLamPrime(family, ii, kk) * yd(jj, kk) * v1;
            DownSquarkCoupling(ii+3, jj+3) = DownSquarkCoupling(ii+3, jj+3) +
                                 yd(kk, jj) * displayLamPrime(family, kk, ii) * v1;

            for (int ll=1; ll<=3; ll++) {
               DownSquarkCoupling(ii, jj) = DownSquarkCoupling(ii, jj) +
                      displayLamPrime(ll, jj, kk) * vi(ll) * displayLamPrime(family, ii, kk);
```

```
              DownSquarkCoupling(ii+3, jj+3) = DownSquarkCoupling(ii+3, jj+3) +
                 displayLamPrime(kk, ll, ii) * vi(kk) * displayLamPrime(family, ll, jj);
}}}}
UpSquarkCoupling = UpSquarkMixing.transpose() * UpSquarkCoupling * UpSquarkMixing;
DownSquarkCoupling = DownSquarkMixing.transpose() * DownSquarkCoupling * DownSquarkMixing;

UpSquarkCouplings.push_back(UpSquarkCoupling);
DownSquarkCouplings.push_back(DownSquarkCoupling);
}
DoubleVector squarks(3);
for (int II=1; II<=6; II++) {
   for (int family=1; family<=3; family++) {
      squarks(family) = squarks(family) + 3.0 *
                    UpSquarkCouplings[family-1](II, II) * a0(UpSquarkMasses(II),  q);
      squarks(family) = squarks(family) + 3.0 *
                    DownSquarkCouplings[family-1](II, II) * a0(DownSquarkMasses(II), q);
}}
tadpole = tadpole + squarks;

UpSquarkCouplings.clear();
DownSquarkCouplings.clear();

///Quarks
DoubleVector quarks(3), DownMasses(3);
DoubleMatrix DownMixingU(3, 3), DownMixingV(3, 3), DownCoupling(3, 3);
vector<DoubleMatrix> DownCouplings;

DoubleMatrix md = (yd * v1 + displayLambda(LD).dotProd(vi, 2)) / root2;
md.diagonalise(DownMixingU, DownMixingV, DownMasses);

for (int family=1; family<=3; family++) {
  for (int ii=1; ii<=3; ii++) {
    for (int jj=1; jj<=3; jj++) {
       DownCoupling(ii, jj) = displayLamPrime(family, ii,jj) / root2;
  }}
  DownCoupling = DownMixingU.transpose() * DownCoupling * DownMixingV;
  DownCouplings.push_back(DownCoupling);
}
for (int family=1; family<=3; family++) {
  for (int ii=1; ii<=3; ii++) {
    quarks(family) = quarks(family) - 6.0 * DownCouplings[family-1](ii, ii) *
                        DownMasses(ii) * a0(DownMasses(ii), q) * 2.0;
}}
tadpole = tadpole + quarks;
DownCouplings.clear();

/// Weak bosons
DoubleVector gaugeBosons(3);
gaugeBosons = vi * (3.0 * sqr(g2) / 4.0 * (2.0 * a0(mw, q) + a0(mz, q) / sqr(costhDRbar)));
tadpole = tadpole + gaugeBosons;

/// chargino-charged lepton mass matrix in basis (W-, Hd-, l-) M (W+, hu+, ebar+)
DoubleMatrix Charginos = chargedLeptons(vSM);
```

```
DoubleVector CharginoMasses(5);
DoubleMatrix CharginoMixingU(5, 5), CharginoMixingV(5, 5);
Charginos.diagonalise(CharginoMixingU, CharginoMixingV, CharginoMasses);

/// chargino couplings
DoubleMatrix CharginoCoupling(5, 5);
vector<DoubleMatrix> CharginoCouplings;

for (int family=1; family<=3; family++) {
  for (int ii=1; ii<=5; ii++) { for (int jj=1; jj<=5; jj++) {    //initialise
     CharginoCoupling(ii, jj) = 0.0; }
  }
  CharginoCoupling(family+2, 1) = 2.0 * g2 / root2;
  for (int ii=1; ii<=3; ii++) {
    CharginoCoupling(2, ii+2) = - 2.0 * ye(family, ii) / root2;
    for (int jj=1; jj<=3; jj++) {
       CharginoCoupling(ii+2, jj+2) = 2.0 * displayLam(family, ii, jj) / root2;
  }}
  CharginoCoupling = CharginoMixingU.transpose() * CharginoCoupling *  CharginoMixingV;
  CharginoCouplings.push_back(CharginoCoupling);
}
DoubleVector charginos(3);
for (int family=1; family<=3; family++) {
  for (int II=1; II<=5; II++) {
    charginos(family) = charginos(family) - 2.0 * CharginoCouplings[family-1](II, II) *
                          CharginoMasses(II) * a0(CharginoMasses(II),  q);
}}
tadpole = tadpole + charginos;

CharginoCouplings.clear();

/// neutralino-neutrino mass matrix
DoubleMatrix Neutralinos = neutralinoMassMatrix();

/// Swap rows and columns to the format (Bino, Wino,  Hu, Hd,  nui)
Neutralinos.swaprows(1, 4); Neutralinos.swapcols(1, 4);
Neutralinos.swaprows(2, 5); Neutralinos.swapcols(2, 5);
Neutralinos.swaprows(3, 7); Neutralinos.swapcols(3, 7);
Neutralinos.swaprows(6, 4); Neutralinos.swapcols(6, 4);
Neutralinos.swaprows(6, 5); Neutralinos.swapcols(6, 5);

DoubleVector NeutralinoMasses(7);
DoubleMatrix NeutralinoMixing(7, 7);
Neutralinos.diagonaliseSym(NeutralinoMixing, NeutralinoMasses);

/// neutralino couplings
DoubleMatrix NeutralinoCoupling(7, 7);
vector<DoubleMatrix> NeutralinoCouplings;

for (int family=1; family<=3; family++) {
  for (int ii=1; ii<=7; ii++) {
     for (int jj=1; jj<=7; jj++) {         //initialise
   NeutralinoCoupling(ii, jj) = 0.0;
```

```
    }}
    NeutralinoCoupling(1, family+4) = - g2 * tanthDRbar;
    NeutralinoCoupling(2, family+4) = g2;

    NeutralinoCoupling.symmetrise();
    NeutralinoCoupling = NeutralinoMixing.transpose() * NeutralinoCoupling *
                              NeutralinoMixing;

    NeutralinoCouplings.push_back(NeutralinoCoupling);
  }
  DoubleVector neutralinos(3);
  for (int family=1; family<=3; family++) {
    for (int II=1; II<=7; II++) {
      neutralinos(family) = neutralinos(family) - NeutralinoCouplings[family-1](II, II)
                                * NeutralinoMasses(II) * a0(NeutralinoMasses(II), q);
  }}
  tadpole = tadpole + neutralinos;

  NeutralinoCouplings.clear();

  for (int family = 1; family<=3; family++) {
    tadpole(family) = tadpole(family) / (16.0 * sqr(PI));
  }
  return tadpole;
}
```

Bibliography

[1] Y. Fukuda et al., 'Evidence for oscillation of atmospheric neutrinos', *Phys.Rev.Lett.* 81 (1998) 1562–1567, arXiv:hep-ex/9807003 [hep-ex].

[2] B. Cleveland et al., 'Measurement of the solar electron neutrino flux with the Homestake chlorine detector', *Astrophys.J.* 496 (1998) 505–526.

[3] Q. Ahmad et al., 'Direct evidence for neutrino flavor transformation from neutral current interactions in the Sudbury Neutrino Observatory', *Phys.Rev.Lett.* 89 (2002) 011301, arXiv:nucl-ex/0204008 [nucl-ex].

[4] M. Apollonio et al., 'Search for neutrino oscillations on a long baseline at the CHOOZ nuclear power station', *Eur.Phys.J.* C27 (2003) 331–374, arXiv:hep-ex/0301017 [hep-ex].

[5] M. Gonzalez-Garcia and M. Maltoni, 'Phenomenology with Massive Neutrinos', *Phys.Rept.* 460 (2008) 1–129, arXiv:0704.1800 [hep-ph].

[6] T. Schwetz, M. Tortola and J. Valle, 'Global neutrino data and recent reactor fluxes: status of three-flavour oscillation parameters', *New J.Phys.* 13 (2011) 063004, arXiv:1103.0734 [hep-ph].

[7] M. Tortola, J. Valle and D. Vanegas, 'Global status of neutrino oscillation parameters after recent reactor measurements' (2012), arXiv:1205.4018 [hep-ph].

[8] R. Barate et al., 'An Upper limit on the tau-neutrino mass from three-prong and five-prong tau decays', *Eur.Phys.J.* C2 (1998) 395–406.

[9] K. Assamagan et al., 'Upper limit of the muon-neutrino mass and charged pion mass from momentum analysis of a surface muon beam', *Phys.Rev.* D53 (1996) 6065–6077.

[10] J. Bonn et al., 'The Mainz neutrino mass experiment', *Nucl.Phys.Proc.Suppl.* 91 (2001) 273–279.

[11] V. Lobashev et al., 'Direct search for neutrino mass and anomaly in the tritium beta-spectrum: Status of 'Troitsk neutrino mass' experiment', *Nucl.Phys.Proc.Suppl.* 91 (2001) 280–286.

[12] M. Cirelli and A. Strumia, 'Cosmology of neutrinos and extra light particles after WMAP3', *JCAP* 0612 (2006) 013, arXiv:astro-ph/0607086 [astro-ph].

[13] A. Goobar et al., 'A new bound on the neutrino mass from the sdss baryon acoustic peak', *JCAP* 0606 (2006) 019, arXiv:astro-ph/0602155 [astro-ph].

[14] S. Hannestad et al., 'Neutrino and axion hot dark matter bounds after WMAP-7', *JCAP* 1008 (2010) 001, arXiv:1004.0695 [astro-ph.CO].

[15] P. Minkowski, 'mu to e gamma at a Rate of One Out of 1-Billion Muon Decays?', *Phys.Lett.* B67 (1977) 421.

[16] M. Jezabek and Y. Sumino, 'Neutrino mixing and seesaw mechanism', *Phys.Lett.* B440 (1998) 327–331, arXiv:hep-ph/9807310 [hep-ph].

[17] W. Rodejohann, 'The See-saw mechanism: Neutrino mixing, leptogenesis and lepton flavor violation', *Pramana* 72 (2009) 217–227, arXiv:0804.3925 [hep-ph].

[18] M. Magg and C. Wetterich, 'Neutrino Mass Problem And Gauge Hierarchy', *Phys.Lett.* B94 (1980) 61.

[19] G. Lazarides, Q. Shafi and C. Wetterich, 'Proton Lifetime and Fermion Masses in an SO(10) Model', *Nucl.Phys.* B181 (1981) 287.

[20] J. Schechter and J. Valle, 'Neutrino Masses in SU(2) x U(1) Theories', *Phys.Rev.* D22 (1980) 2227.

[21] R. N. Mohapatra and G. Senjanovic, 'Neutrino Masses and Mixings in Gauge Models with Spontaneous Parity Violation', *Phys.Rev.* D23 (1981) 165.

[22] R. Mohapatra, 'Mechanism For Understanding Small Neutrino Mass in Superstring Theories', *Phys.Rev.Lett.* 56 (1986) 561–563.

[23] R. Foot et al., 'Seesaw Neutrino Masses Induced By A Triplet Of Leptons', *Z.Phys.* C44 (1989) 441.

[24] H. K. Dreiner et al., 'Neutrino masses from gauge symmetries', *Nucl.Phys.* B436 (1995) 461–473, arXiv:hep-ph/9409369 [hep-ph].

[25] Y. Liao, Y. Liu and G.-Z. Ning, 'Radiative Neutrino Mass in Type III Seesaw Model', *Phys.Rev.* D79 (2009) 073003, arXiv:0902.1434 [hep-ph].

[26] J. Hisano and D. Nomura, 'Solar and atmospheric neutrino oscillations and lepton flavor violation in supersymmetric models with the right-handed neutrinos', *Phys.Rev.* D59 (1999) 116005, arXiv:hep-ph/9810479 [hep-ph].

[27] H. E. Haber and G. L. Kane, 'The Search for Supersymmetry: Probing Physics Beyond the Standard Model', *Phys.Rept.* 117 (1985) 75–263.

[28] S. P. Martin, 'A Supersymmetry primer' (1997), arXiv:hep-ph/9709356 [hep-ph].

[29] R. G. M. Drees and P. Roy, *Theory and Phenomenology of Sparticles*, World Scientific, 2004.

[30] S. R. Coleman and J. Mandula, 'All Possible Symmetries of the S Matrix', *Phys.Rev.* 159 (1967) 1251–1256.

[31] R. Haag, J. T. Lopuszanski and M. Sohnius, 'All Possible Generators of Supersymmetries of the s Matrix', *Nucl.Phys.* B88 (1975) 257.

[32] E. Gildener, 'Gauge Symmetry Hierarchies', *Phys.Rev.* D14 (1976) 1667.

[33] M. Veltman, 'The Infrared - Ultraviolet Connection', *Acta Phys.Polon.* B12 (1981) 437.

[34] N. Sakai, 'Naturalness in Supersymmetric Guts', *Z.Phys.* C11 (1981) 153.

[35] E. Witten, 'Dynamical Breaking of Supersymmetry', *Nucl.Phys.* B188 (1981) 513.

[36] M. Drees, 'An Introduction to supersymmetry' (1996), arXiv:hep-ph/9611409 [hep-ph].

[37] L. J. Hall and M. Suzuki, 'Explicit R-Parity Breaking in Supersymmetric Models', *Nucl.Phys.* B231 (1984) 419.

[38] A. S. Joshipura and M. Nowakowski, ''Just so' oscillations in supersymmetric standard model', *Phys.Rev.* D51 (1995) 2421–2427, arXiv:hep-ph/9408224 [hep-ph].

[39] E. Nardi, 'Renormalization group induced neutrino masses in supersymmetry without R-parity', *Phys.Rev.* D55 (1997) 5772–5779, arXiv:hep-ph/9610540 [hep-ph].

[40] Y. Grossman and H. E. Haber, 'Neutrino masses and sneutrino mixing in R-parity violating supersymmetry' (1999), arXiv:hep-ph/9906310 [hep-ph].

[41] S. Davidson and M. Losada, 'Basis independent neutrino masses in the R(p) violating MSSM', *Phys.Rev.* D65 (2002) 075025, arXiv:hep-ph/0010325 [hep-ph].

[42] A. Dedes, S. Rimmer and J. Rosiek, 'Neutrino masses in the lepton number violating MSSM', *JHEP* 0608 (2006) 005, arXiv:hep-ph/0603225 [hep-ph].

[43] B. Allanach and C. Kom, 'Lepton number violating mSUGRA and neutrino masses', *JHEP* 0804 (2008) 081, arXiv:0712.0852 [hep-ph].

[44] R. Barbier et al., 'R-parity violating supersymmetry', *Phys.Rept.* 420 (2005) 1–202, arXiv:hep-ph/0406039 [hep-ph].

[45] N. Sakai and T. Yanagida, 'Proton Decay in a Class of Supersymmetric Grand Unified Models', *Nucl.Phys.* B197 (1982) 533.

[46] A. Y. Smirnov and F. Vissani, 'Upper bound on all products of R-parity violating couplings lambda-prime and lambda-prime-prime from proton decay', *Phys.Lett.* B380 (1996) 317–323, arXiv:hep-ph/9601387 [hep-ph].

[47] G. R. Farrar and P. Fayet, 'Phenomenology of the Production, Decay, and Detection of New Hadronic States Associated with Supersymmetry', *Phys.Lett.* B76 (1978) 575–579.

[48] H. K. Dreiner, C. Luhn and M. Thormeier, 'What is the discrete gauge symmetry of the MSSM?', *Phys.Rev.* D73 (2006) 075007, arXiv:hep-ph/0512163 [hep-ph].

[49] L. E. Ibanez and G. G. Ross, 'Discrete gauge symmetries and the origin of baryon and lepton number conservation in supersymmetric versions of the standard model', *Nucl.Phys.* B368 (1992) 3–37.

[50] H. K. Dreiner et al.,
'Baryon triality and neutrino masses from an anomalous flavor U(1)',
Nucl.Phys. B774 (2007) 127–167, arXiv:hep-ph/0610026 [hep-ph].

[51] B. Allanach, A. Dedes and H. Dreiner, 'R parity violating minimal supergravity model',
Phys.Rev. D69 (2004) 115002, arXiv:hep-ph/0309196 [hep-ph].

[52] A. Abada and M. Losada, 'Constraints on a general three generation neutrino mass matrix from neutrino data: Application to the MSSM with R-parity violation',
Nucl.Phys. B585 (2000) 45–78, arXiv:hep-ph/9908352 [hep-ph].

[53] G. Bhattacharyya,
'R-parity violating supersymmetric Yukawa couplings: A Minireview',
Nucl.Phys.Proc.Suppl. 52A (1997) 83–88, arXiv:hep-ph/9608415 [hep-ph].

[54] H. K. Dreiner, 'An Introduction to explicit R-parity violation' (1997),
arXiv:hep-ph/9707435 [hep-ph].

[55] R. Hempfling, 'Neutrino masses and mixing angles in SUSY GUT theories with explicit R-parity breaking', *Nucl.Phys.* B478 (1996) 3–30, arXiv:hep-ph/9511288 [hep-ph].

[56] D. E. Kaplan and A. E. Nelson,
'Solar and atmospheric neutrino oscillations from bilinear R parity violation',
JHEP 0001 (2000) 033, arXiv:hep-ph/9901254 [hep-ph].

[57] J. Mira et al.,
'Bilinear R-parity violation and small neutrino masses: A Selfconsistent framework',
Phys.Lett. B492 (2000) 81–90, arXiv:hep-ph/0007266 [hep-ph].

[58] M. Hirsch et al., 'Neutrino masses and mixings from supersymmetry with bilinear R parity violation: A Theory for solar and atmospheric neutrino oscillations',
Phys.Rev. D62 (2000) 113008, arXiv:hep-ph/0004115 [hep-ph].

[59] M. Diaz et al., 'Solar neutrino masses and mixing from bilinear R parity broken supersymmetry: Analytical versus numerical results', *Phys.Rev.* D68 (2003) 013009,
arXiv:hep-ph/0302021 [hep-ph].

[60] M. Hirsch and J. Valle, 'Supersymmetric origin of neutrino mass',
New J.Phys. 6 (2004) 76, arXiv:hep-ph/0405015 [hep-ph].

[61] F. de Campos et al., 'Probing bilinear R-parity violating supergravity at the LHC',
JHEP 0805 (2008) 048, arXiv:0712.2156 [hep-ph].

[62] S. Sarkar, 'Big bang nucleosynthesis and physics beyond the standard model',
Rept.Prog.Phys. 59 (1996) 1493–1610, arXiv:hep-ph/9602260 [hep-ph].

[63] E. Komatsu et al., 'Seven-Year Wilkinson Microwave Anisotropy Probe (WMAP) Observations: Cosmological Interpretation', *Astrophys.J.Suppl.* 192 (2011) 18,
arXiv:1001.4538 [astro-ph.CO].

[64] J. Hamann et al., 'Cosmology seeking friendship with sterile neutrinos',
Phys.Rev.Lett. 105 (2010) 181301, arXiv:1006.5276 [hep-ph].

[65] V. Barger et al.,
'Effective number of neutrinos and baryon asymmetry from BBN and WMAP',
Phys.Lett. B566 (2003) 8–18, arXiv:hep-ph/0305075 [hep-ph].

[66] V. Simha and G. Steigman,
'Constraining The Early-Universe Baryon Density And Expansion Rate',
JCAP 0806 (2008) 016, arXiv:0803.3465 [astro-ph].

[67] Y. Izotov and T. Thuan,
'The primordial abundance of 4He: evidence for non-standard big bang nucleosynthesis',
Astrophys.J. 710 (2010) L67–L71, arXiv:1001.4440 [astro-ph.CO].

[68] E. Aver, K. A. Olive and E. D. Skillman, 'A New Approach to Systematic Uncertainties and Self-Consistency in Helium Abundance Determinations', *JCAP* 1005 (2010) 003, arXiv:1001.5218 [astro-ph.CO].

[69] D. Choudhury et al., 'A Supersymmetric solution to the KARMEN time anomaly',
Phys.Rev. D61 (2000) 095009, arXiv:hep-ph/9911365 [hep-ph].

[70] A. Dedes, H. K. Dreiner and P. Richardson,
'Attempts at explaining the NuTeV observation of dimuon events',
Phys.Rev. D65 (2001) 015001, arXiv:hep-ph/0106199 [hep-ph].

[71] I. Gogoladze et al., 'Implications of a massless neutralino for neutrino physics',
Phys.Rev. D68 (2003) 073004, arXiv:hep-ph/0211391 [hep-ph].

[72] V. Barger, P. Langacker and H.-S. Lee,
'Lightest neutralino in extensions of the MSSM', *Phys.Lett.* B630 (2005) 85–99,
arXiv:hep-ph/0508027 [hep-ph].

[73] H. Dreiner et al.,
'Supernovae and light neutralinos: SN1987A bounds on supersymmetry revisited',
Phys.Rev. D68 (2003) 055004, arXiv:hep-ph/0304289 [hep-ph].

[74] H. K. Dreiner, O. Kittel and U. Langenfeld,
'Discovery potential of radiative neutralino production at the ILC',
Phys.Rev. D74 (2006) 115010, arXiv:hep-ph/0610020 [hep-ph].

[75] H. K. Dreiner, O. Kittel and U. Langenfeld,
'The Role of Beam polarization for Radiative Neutralino Production at the ILC',
Eur.Phys.J. C54 (2008) 277–284, arXiv:hep-ph/0703009 [HEP-PH].

[76] H. Dreiner et al., 'Rare meson decays into very light neutralinos',
Phys.Rev. D80 (2009) 035018, arXiv:0905.2051 [hep-ph].

[77] H. K. Dreiner et al., 'Mass Bounds on a Very Light Neutralino',
Eur.Phys.J. C62 (2009) 547–572, arXiv:0901.3485 [hep-ph].

[78] J. R. Ellis et al., 'Low Mass Photinos And Supernova SN1987A',
Phys.Lett. B215 (1988) 404.

[79] J. Grifols, E. Masso and S. Peris, 'Photinos From Gravitational Collapse',
Phys.Lett. B220 (1989) 591.

[80] M. Kachelriess, 'The KARMEN anomaly, light neutralinos and supernova SN1987A',
JHEP 0002 (2000) 010, arXiv:hep-ph/0001160 [hep-ph].

[81] R. Cowsik and J. McClelland, 'An Upper Limit on the Neutrino Rest Mass',
Phys.Rev.Lett. 29 (1972) 669–670.

[82] B. de Carlos and P. White, 'R-parity violation effects through soft supersymmetry breaking terms and the renormalization group', *Phys.Rev.* D54 (1996) 3427–3446, URL: hep-ph/9602381.

[83] B. Allanach, C. Kom and M. Hanussek, 'Computation of Neutrino Masses in R-parity Violating Supersymmetry: SOFTSUSY3.2', *Comput.Phys.Commun.* 183 (2012) 785–793, arXiv:1109.3735 [hep-ph].

[84] G. Aad et al., 'Search for squarks and gluinos using final states with jets and missing transverse momentum with the ATLAS detector in sqrt(s) = 7 TeV proton-proton collisions', *Phys.Lett.* B710 (2012) 67–85, arXiv:1109.6572 [hep-ex].

[85] G. Aad et al., 'Search for new phenomena in final states with large jet multiplicities and missing transverse momentum using sqrt(s)=7 TeV pp collisions with the ATLAS detector', *JHEP* 1111 (2011) 099, arXiv:1110.2299 [hep-ex].

[86] A. Collaboration, 'Search for squarks and gluinos using final states with jets and missing transverse momentum with the ATLAS detector in sqrt(s) = 7 TeV proton-proton collisions', *Conference Note* ATLAS-CONF-2012-033 (2012), URL: https://cdsweb.cern.ch/record/1432199.

[87] C. Collaboration, 'Search for supersymmetry in all-hadronic events with MT2', *Physics Analysis Summaries* CMS-PAS-SUS-11-005 (2011), URL: http://cdsweb.cern.ch/record/1377032.

[88] C. Collaboration, 'Search for supersymmetry in all-hadronic events with MET', *Physics Analysis Summaries* CMS-PAS-SUS-11-004 (2011), URL: http://cdsweb.cern.ch/record/1378478.

[89] S. Chatrchyan et al., 'Search for Supersymmetry at the LHC in Events with Jets and Missing Transverse Energy', *Phys.Rev.Lett.* 107 (2011) 221804, arXiv:1109.2352 [hep-ex].

[90] G. Aad et al., 'Search for supersymmetry in final states with jets, missing transverse momentum and one isolated lepton in sqrt(s) = 7 TeV pp collisions using 1 inv fb of ATLAS data', *Phys.Rev.* D85 (2012) 012006, arXiv:1109.6606 [hep-ex].

[91] A. collaboration, 'Further search for supersymmetry at sqrt(s)=7 TeV in final states with jets, missing transverse momentum and one isolated lepton', *Conference Note* ATLAS-CONF-2012-041 (2012), URL: https://cdsweb.cern.ch/record/1435195.

[92] C. Collaboration, 'Search for supersymmetry with single-leptons at the LHC', *Physics Analysis Summaries* CMS-PAS-SUS-11-015.Updated plots at https://twiki.cern.ch/twiki/bin/view/CMSPublic/PhysicsResultsSUS12010 (2012), URL: http://cdsweb.cern.ch/record/1380922.

[93] G. Aad et al., 'Searches for supersymmetry with the ATLAS detector using final states with two leptons and missing transverse momentum in sqrt(s) = 7 TeV proton-proton collisions', *Phys.Lett.* B709 (2012) 137–157, arXiv:1110.6189 [hep-ex].

[94] C. Collaboration, 'Search for new physics in events with opposite-sign dileptons and missing transverse energy', *Physics Analysis Summaries* Updated plots for 5 inv fb at https://twiki.cern.ch/twiki/bin/view/CMSPublic/PhysicsResultsSUS110115fb.CMS-PAS-SUS-11-011 (2012),
URL: http://cdsweb.cern.ch/record/1370065.

[95] C. Collaboration, 'Search for new physics in events with same-sign dileptons and missing transverse energy', *Physics Analysis Summaries* Updated plots for 5 inv fb at https://twiki.cern.ch/twiki/bin/view/CMSPublic/PhysicsResultsSUS110105fb.CMS-PAS-SUS-11-010 (2011),
URL: http://cdsweb.cern.ch/record/1370064.

[96] J. R. Ellis et al., 'Supersymmetric Relics from the Big Bang', *Nucl.Phys.* B238 (1984) 453–476.

[97] B. Allanach et al., 'Mass Spectrum in R-Parity Violating mSUGRA and Benchmark Points', *Phys.Rev.* D75 (2007) 035002, arXiv:hep-ph/0609263 [hep-ph].

[98] A. Akeroyd et al., 'Charged Higgs boson and Stau phenomenology in the simplest R parity breaking model', *Nucl.Phys.* B529 (1998) 3–22, arXiv:hep-ph/9707395 [hep-ph].

[99] H. Dreiner and S. Grab, 'All Possible Lightest Supersymmetric Particles in R-Parity Violating mSUGRA Models and their Signals at the LHC', *AIP Conf.Proc.* 1200 (2010) 358–361, arXiv:0909.5407 [hep-ph].

[100] H. Dreiner, S. Grab and T. Stefaniak, 'Constraining Selectron LSP Scenarios with Tevatron Trilepton Searches', *Phys.Rev.* D84 (2011) 015005, arXiv:1103.1883 [hep-ph].

[101] K. Desch et al., 'Stau as the Lightest Supersymmetric Particle in R-Parity Violating SUSY Models: Discovery Potential with Early LHC Data', *Phys.Rev.* D83 (2011) 015013, arXiv:1008.1580 [hep-ph].

[102] J. Butterworth and H. K. Dreiner, 'R-parity violation at HERA', *Nucl.Phys.* B397 (1993) 3–34, arXiv:hep-ph/9211204 [hep-ph].

[103] J. Erler, J. L. Feng and N. Polonsky, 'A Wide scalar neutrino resonance and b anti-b production at LEP', *Phys.Rev.Lett.* 78 (1997) 3063–3066, arXiv:hep-ph/9612397 [hep-ph].

[104] H. K. Dreiner, P. Richardson and M. H. Seymour, 'Resonant slepton production in hadron hadron collisions', *Phys.Rev.* D63 (2001) 055008, arXiv:hep-ph/0007228 [hep-ph].

[105] H. Dreiner et al., 'Supersymmetric NLO QCD corrections to resonant slepton production and signals at the Tevatron and the CERN LHC', *Phys.Rev.* D75 (2007) 035003, arXiv:hep-ph/0611195 [hep-ph].

[106] I. Jack, D. Jones and A. Kord, 'Two-loop beta-functions and their effects for the R-parity violating MSSM', *Phys.Lett.* B632 (2006) 703–709, arXiv:hep-ph/0505238 [hep-ph].

[107] H. D. M.A. Bernhardt S.P. Das and S. Grab, 'Sneutrino as Lightest Supersymmetric Particle in Baryon Triality mSUGRA Models and Signals at the LHC', *Phys.Rev.* D79 (2009) 035003, arXiv:0810.3423 [hep-ph].

[108] H. Dreiner, S. Grab and T. Stefaniak, 'Discovery Potential of Selectron or Smuon as the Lightest Supersymmetric Particle at the LHC', *Phys.Rev.* D84 (2011) 035023, arXiv:1102.3189 [hep-ph].

[109] A. Collaboration, 'Search for supersymmetry in events with four or more leptons and missing transverse momentum in pp collisions at sqrt(s)=7 TeV with the ATLAS detector', *Conference Note* ATLAS-CONF-2012-001 (2012), URL: https://cdsweb.cern.ch/record/1418920.

[110] A. collaboration, 'Constraining R-parity violating Minimal Supergravity with stau LSP in a four lepton final state with missing transverse momentum', *Conference Note* ATLAS-CONF-2012-035 (2012), URL: https://cdsweb.cern.ch/record/1432202.

[111] G. e. a. Aad, 'Search for a heavy neutral particle decaying into an electron and a muon using 1 inverse fb of ATLAS data', *Eur.Phys.J.* C71 (2011) 1809, arXiv:1109.3089 [hep-ex].

[112] G. Aad et al., 'Search for displaced vertices arising from decays of new heavy particles in 7 TeV pp collisions at ATLAS', *Phys.Lett.* B707 (2012) 478–496, arXiv:1109.2242 [hep-ex].

[113] S. Chatrchyan et al., 'Search for Physics Beyond the Standard Model Using Multilepton Signatures in pp Collisions at sqrt(s)=7 TeV', *Phys.Lett.* B704 (2011) 411–433, arXiv:1106.0933 [hep-ex].

[114] S. Chatrchyan et al., 'Study of high-pT charged particle suppression in PbPb compared to pp collisions at sqrt(sNN)=2.76 TeV', *Eur. Phys. J.* C (2012) 72:1945, arXiv:1202.2554 [nucl-ex].

[115] P. W. Graham et al., 'Displaced Supersymmetry' (2012), arXiv:1204.6038 [hep-ph].

[116] H. Dreiner and T. Stefaniak, 'Bounds on R-parity Violation from Resonant Slepton Production at the LHC' (2012), arXiv:1201.5014 [hep-ph].

[117] H. K. Dreiner, J. Soo Kim and M. Thormeier, 'A Simple baryon triality model for neutrino masses' (2007), arXiv:0711.4315 [hep-ph].

[118] X.-J. Bi, S. Yan and P.-F. Yin, 'Probing Light Stop Pairs at the LHC', *Phys.Rev.* D85 (2012) 035005, arXiv:1111.2250 [hep-ph].

[119] C. Brust et al., 'SUSY, the Third Generation and the LHC', *JHEP* 1203 (2012) 103, arXiv:1110.6670 [hep-ph].

[120] N. Desai and B. Mukhopadhyaya, 'Constraints on supersymmetry with light third family from LHC data' (2011), arXiv:1111.2830 [hep-ph].

[121] M. Papucci, J. T. Ruderman and A. Weiler, 'Natural SUSY Endures' (2011), arXiv:1110.6926 [hep-ph].

[122] S. Sekmen et al., 'Interpreting LHC SUSY searches in the phenomenological MSSM', *JHEP* 1202 (2012) 075, arXiv:1109.5119 [hep-ph].

[123] G. Aad et al., 'Search for scalar bottom pair production with the ATLAS detector in pp Collisions at sqrt(s) = 7 TeV' (2011), arXiv:1112.3832 [hep-ex].

[124] H. Baer and X. Tata, *Weak scale supersymmetry: From superfields to scattering events*, Cambridge University Press, 2006.

[125] K. Griest and D. Seckel, 'Three exceptions in the calculation of relic abundances', *Phys.Rev.* D43 (1991) 3191–3203.

[126] C. Boehm, A. Djouadi and M. Drees, 'Light scalar top quarks and supersymmetric dark matter', *Phys.Rev.* D62 (2000) 035012, arXiv:hep-ph/9911496 [hep-ph].

[127] K.-i. Hikasa and M. Kobayashi, 'Light Scalar Top at e+ e- Colliders', *Phys.Rev.* D36 (1987) 724.

[128] M. Muhlleitner and E. Popenda, 'Light Stop Decay in the MSSM with Minimal Flavour Violation', *JHEP* 1104 (2011) 095, arXiv:1102.5712 [hep-ph].

[129] C. Boehm, A. Djouadi and Y. Mambrini, 'Decays of the lightest top squark', *Phys.Rev.* D61 (2000) 095006, arXiv:hep-ph/9907428 [hep-ph].

[130] M. Carena, A. Freitas and C. Wagner, 'Light Stop Searches at the LHC in Events with One Hard Photon or Jet and Missing Energy', *JHEP* 0810 (2008) 109, arXiv:0808.2298 [hep-ph].

[131] G. Arnison et al., 'Experimental Observation of Events with Large Missing Transverse Energy Accompanied by a Jet Or a Photon(s) in p anti-p Collisions at s**(1/2)=540-GeV', *Phys.Lett.* B139 (1984) 115.

[132] L. Vacavant and I. Hinchliffe, 'Model independent extra dimension signatures with ATLAS' (2000), arXiv:hep-ex/0005033 [hep-ex].

[133] S. Bornhauser et al., 'Light Stop Searches at the LHC in Events with two b-Jets and Missing Energy', *Phys.Rev.* D83 (2011) 035008, arXiv:1011.5508 [hep-ph].

[134] H. Dreiner, M. Hanussek and S. Grab, 'Bounds on R-parity Violating Couplings at the Grand Unification Scale from Neutrino Masses', *Phys.Rev.* D82 (2010) 055027, arXiv:1005.3309 [hep-ph].

[135] H. K. Dreiner et al., 'Neutrino masses and mixings in the baryon triality constrained minimal supersymmetric standard model', *Phys.Rev.* D84 (2011) 113005, arXiv:1106.4338 [hep-ph].

[136] M. Hanussek and J. Kim, 'Testing neutrino masses in the R-parity violating minimal supersymmetric standard model with LHC results', *to be published in Phys. Rev.* (2012), arXiv:1205.0019 [hep-ph].

[137] M. Drees, M. Hanussek and J. S. Kim, 'Light Stop Searches at the LHC with Monojet Events' (2012), arXiv:1201.5714 [hep-ph].

[138] H. K. Dreiner et al., 'Gravitino cosmology with a very light neutralino' (2011), arXiv:1111.5715 [hep-ph].

[139] S. Weinberg, 'Supersymmetry at Ordinary Energies. 1. Masses and Conservation Laws', *Phys.Rev.* D26 (1982) 287.

[140] S. Weinberg, 'Baryon and Lepton Nonconserving Processes', *Phys.Rev.Lett.* 43 (1979) 1566–1570.

[141] B. Allanach, 'SOFTSUSY: a program for calculating supersymmetric spectra', *Comput.Phys.Commun.* 143 (2002) 305–331, arXiv:hep-ph/0104145 [hep-ph].

[142] B. Allanach and M. Bernhardt, 'Including R-parity violation in the numerical computation of the spectrum of the minimal supersymmetric standard model: SOFTSUSY', *Comput.Phys.Commun.* 181 (2010) 232–245, arXiv:0903.1805 [hep-ph].

[143] F. Wilczek and A. Zee, 'Operator Analysis of Nucleon Decay', *Phys.Rev.Lett.* 43 (1979) 1571–1573.

[144] H. E. Haber, 'The Status of the minimal supersymmetric standard model and beyond', *Nucl.Phys.Proc.Suppl.* 62 (1998) 469–484, arXiv:hep-ph/9709450 [hep-ph].

[145] L. E. Ibanez and G. G. Ross, 'SU(2)-L x U(1) Symmetry Breaking as a Radiative Effect of Supersymmetry Breaking in Guts', *Phys.Lett.* B110 (1982) 215–220.

[146] H. K. Dreiner and M. Thormeier, 'Supersymmetric Froggatt-Nielsen models with baryon and lepton number violation', *Phys.Rev.* D69 (2004) 053002, arXiv:hep-ph/0305270 [hep-ph].

[147] N. Cabibbo, 'Unitary Symmetry and Leptonic Decays', *Phys.Rev.Lett.* 10 (1963) 531–533.

[148] M. Kobayashi and T. Maskawa, 'CP Violation in the Renormalizable Theory of Weak Interaction', *Prog.Theor.Phys.* 49 (1973) 652–657.

[149] K. Agashe and M. Graesser, 'R-parity violation in flavor changing neutral current processes and top quark decays', *Phys.Rev.* D54 (1996) 4445–4452, arXiv:hep-ph/9510439 [hep-ph].

[150] H. Dreiner, S. Grab and M. Trenkel, '$\tilde{\tau}$ LSP Phenomenology: Two versus Four-Body Decay Modes. Example: Resonant Single Slepton Production at the LHC', *Phys.Rev.* D79 (2009) 016002, arXiv:0808.3079 [hep-ph].

[151] M. Nowakowski and A. Pilaftsis, 'W and Z boson interactions in supersymmetric models with explicit R-parity violation', *Nucl.Phys.* B461 (1996) 19–49, arXiv:hep-ph/9508271 [hep-ph].

[152] E. J. Chun and S. K. Kang, 'One loop corrected neutrino masses and mixing in supersymmetric standard model without R-parity', *Phys.Rev.* D61 (2000) 075012, arXiv:hep-ph/9909429 [hep-ph].

[153] S. Davidson, M. Losada and N. Rius, 'Neutral Higgs sector of the MSSM without R(p)', *Nucl.Phys.* B587 (2000) 118–146, arXiv:hep-ph/9911317 [hep-ph].

[154] A. Dedes and P. Slavich,
'Two loop corrections to radiative electroweak symmetry breaking in the MSSM',
Nucl.Phys. B657 (2003) 333–354, arXiv:hep-ph/0212132 [hep-ph].

[155] M. Drees and S. P. Martin, 'Implications of SUSY model building' (1995),
arXiv:hep-ph/9504324 [hep-ph].

[156] H. K. Dreiner, H. E. Haber and S. P. Martin, 'Two-component spinor techniques and Feynman rules for quantum field theory and supersymmetry',
Phys.Rept. 494 (2010) 1–196, arXiv:0812.1594 [hep-ph].

[157] Y. Grossman and H. E. Haber, 'Sneutrino mixing phenomena',
Phys.Rev.Lett. 78 (1997) 3438–3441, arXiv:hep-ph/9702421 [hep-ph].

[158] Y. Grossman and H. E. Haber, 'Basis independent analysis of the sneutrino sector in R-parity violating supersymmetry', *Phys.Rev.* D63 (2001) 075011,
arXiv:hep-ph/0005276 [hep-ph].

[159] J. Gunion and H. E. Haber, 'Higgs Bosons in Supersymmetric Models. 1.',
Nucl.Phys. B272 (1986) 1.

[160] A. Denner, 'Techniques for calculation of electroweak radiative corrections at the one loop level and results for W physics at LEP-200', *Fortsch.Phys.* 41 (1993) 307–420,
arXiv:0709.1075 [hep-ph].

[161] B. Pontecorvo, 'Mesonium and anti-mesonium', *Sov.Phys.JETP* 6 (1957) 429.

[162] Z. Maki, M. Nakagawa and S. Sakata,
'Remarks on the unified model of elementary particles',
Prog.Theor.Phys. 28 (1962) 870–880.

[163] B. Pontecorvo,
'Neutrino Experiments and the Problem of Conservation of Leptonic Charge',
Sov.Phys.JETP 26 (1968) 984–988.

[164] K. Nakamura et al., 'Review of particle physics', *J.Phys.G* G37 (2010) 075021.

[165] M. Gonzalez-Garcia, M. Maltoni and J. Salvado,
'Updated global fit to three neutrino mixing: status of the hints of nonzero theta13',
JHEP 1004 (2010) 056, arXiv:1001.4524 [hep-ph].

[166] F. An et al., 'Observation of electron-antineutrino disappearance at Daya Bay',
Phys.Rev.Lett. 108 (2012) 171803, arXiv:1203.1669 [hep-ex].

[167] J. Ahn et al., 'Observation of Reactor Electron Antineutrino Disappearance in the RENO Experiment' (2012), arXiv:1204.0626 [hep-ex].

[168] J. Lagoda, 'The T2K experiment: First results and future plans',
Acta Phys.Polon. B42 (2011) 2389–2398.

[169] A. Bakalyarov et al.,
'Results of the experiment on investigation of Germanium-76 double beta decay: Experimental data of Heidelberg-Moscow collaboration November 1995 - August 2001',
Phys.Part.Nucl.Lett. 2 (2005) 77–81, arXiv:hep-ex/0309016 [hep-ex].

[170] H. Klapdor-Kleingrothaus et al.,
'Latest results from the Heidelberg-Moscow double beta decay experiment',
Eur.Phys.J. A12 (2001) 147–154, arXiv:hep-ph/0103062 [hep-ph].

[171] C. Arnaboldi et al.,
'Results from a search for the 0 neutrino beta beta-decay of Te-130',
Phys.Rev. C78 (2008) 035502, arXiv:0802.3439 [hep-ex].

[172] C. Aalseth et al., 'The IGEX Ge-76 neutrinoless double beta decay experiment: Prospects for next generation experiments', *Phys.Rev.* D65 (2002) 092007, arXiv:hep-ex/0202026 [hep-ex].

[173] H. Klapdor-Kleingrothaus et al., 'Evidence for neutrinoless double beta decay', *Mod.Phys.Lett.* A16 (2001) 2409–2420, arXiv:hep-ph/0201231 [hep-ph].

[174] D. Spergel et al., 'Wilkinson Microwave Anisotropy Probe (WMAP) three year results: implications for cosmology', *Astrophys.J.Suppl.* 170 (2007) 377, arXiv:astro-ph/0603449 [astro-ph].

[175] M. Tegmark et al., 'Cosmological parameters from SDSS and WMAP', *Phys.Rev.* D69 (2004) 103501, arXiv:astro-ph/0310723 [astro-ph].

[176] M. Tegmark et al., 'The 3-D power spectrum of galaxies from the SDSS', *Astrophys.J.* 606 (2004) 702–740, arXiv:astro-ph/0310725 [astro-ph].

[177] S. Cole et al., 'The 2dF Galaxy Redshift Survey: Power-spectrum analysis of the final dataset and cosmological implications', *Mon.Not.Roy.Astron.Soc.* 362 (2005) 505–534, arXiv:astro-ph/0501174 [astro-ph].

[178] M. Colless et al., 'The 2dF Galaxy Redshift Survey: Final data release' (2003), arXiv:astro-ph/0306581 [astro-ph].

[179] A. G. Riess et al., 'Type Ia supernova discoveries at z abc 1 from the Hubble Space Telescope: Evidence for past deceleration and constraints on dark energy evolution', *Astrophys.J.* 607 (2004) 665–687, arXiv:astro-ph/0402512 [astro-ph].

[180] P. Astier et al., 'The Supernova legacy survey: Measurement of omega(m), omega(lambda) and W from the first year data set',
Astron.Astrophys. 447 (2006) 31–48, arXiv:astro-ph/0510447 [astro-ph].

[181] P. Harrison, D. Perkins and W. Scott,
'Tri-bimaximal mixing and the neutrino oscillation data', *Phys.Lett.* B530 (2002) 167, arXiv:hep-ph/0202074 [hep-ph].

[182] S. Schael et al., 'Search for neutral MSSM Higgs bosons at LEP',
Eur.Phys.J. C47 (2006) 547–587, arXiv:hep-ex/0602042 [hep-ex].

[183] R. Barate et al., 'Search for the standard model Higgs boson at LEP',
Phys.Lett. B565 (2003) 61–75, arXiv:hep-ex/0306033 [hep-ex].

[184] E. Barberio et al., 'Averages of b-hadron and c-hadron Properties at the End of 2007' (2008), arXiv:0808.1297 [hep-ex].

[185] T. Besmer and A. Steffen, 'R-parity violation and the decay b to s gamma',
Phys.Rev. D63 (2001) 055007, arXiv:hep-ph/0004067 [hep-ph].

[186] S. P. Martin and M. T. Vaughn,
'Two loop renormalization group equations for soft supersymmetry breaking couplings',
Phys.Rev. D50 (1994) 2282, arXiv:hep-ph/9311340 [hep-ph].

[187] G. Belanger et al., 'MicrOMEGAs 2.0: A Program to calculate the relic density of dark matter in a generic model', *Comput.Phys.Commun.* 176 (2007) 367–382, arXiv:hep-ph/0607059 [hep-ph].

[188] B. Allanach et al., 'The Snowmass points and slopes: Benchmarks for SUSY searches', *Eur.Phys.J.* C25 (2002) 113–123, arXiv:hep-ph/0202233 [hep-ph].

[189] V. D. Barger, G. Giudice and T. Han, 'Some New Aspects of Supersymmetry R-Parity Violating Interactions', *Phys.Rev.* D40 (1989) 2987.

[190] B. Allanach, A. Dedes and H. K. Dreiner, 'Bounds on R-parity violating couplings at the weak scale and at the GUT scale', *Phys.Rev.* D60 (1999) 075014, arXiv:hep-ph/9906209 [hep-ph].

[191] B. Allanach, C. Kom and H. Pas, 'LHC and B physics probes of neutrinoless double beta decay in supersymmetry without R-parity', *JHEP* 0910 (2009) 026, arXiv:0903.0347 [hep-ph].

[192] M. Hirsch, H. Klapdor-Kleingrothaus and S. Kovalenko, 'Supersymmetry and neutrinoless double beta decay', *Phys.Rev.* D53 (1996) 1329–1348, arXiv:hep-ph/9502385 [hep-ph].

[193] A. Faessler, S. Kovalenko and F. Simkovic, 'Pions in nuclei and manifestations of supersymmetry in neutrinoless double beta decay', *Phys.Rev.* D58 (1998) 115004, arXiv:hep-ph/9803253 [hep-ph].

[194] A. Faessler and F. Simkovic, 'Double beta decay', *J.Phys.G* G24 (1998) 2139–2178, arXiv:hep-ph/9901215 [hep-ph].

[195] J. E. Kim, P. Ko and D.-G. Lee, 'More on R-parity and lepton family number violating couplings from muon(ium) conversion, and tau and pi0 decays', *Phys.Rev.* D56 (1997) 100–106, arXiv:hep-ph/9701381 [hep-ph].

[196] B. Allanach, S. Kraml and W. Porod, 'Theoretical uncertainties in sparticle mass predictions from computational tools', *JHEP* 0303 (2003) 016, arXiv:hep-ph/0302102 [hep-ph].

[197] G. Degrassi et al., 'Towards high precision predictions for the MSSM Higgs sector', *Eur.Phys.J.* C28 (2003) 133–143, arXiv:hep-ph/0212020 [hep-ph].

[198] B. Allanach et al., 'Precise determination of the neutral Higgs boson masses in the MSSM', *JHEP* 0409 (2004) 044, arXiv:hep-ph/0406166 [hep-ph].

[199] J. Prades, 'Standard Model Prediction of the Muon Anomalous Magnetic Moment', *Acta Phys.Polon.Supp.* 3 (2010) 75–86, arXiv:0909.2546 [hep-ph].

[200] G. Bennett et al., 'Final Report of the Muon E821 Anomalous Magnetic Moment Measurement at BNL', *Phys.Rev.* D73 (2006) 072003, arXiv:hep-ex/0602035 [hep-ex].

[201] F. Jegerlehner and A. Nyffeler, 'The Muon g-2', *Phys.Rept.* 477 (2009) 1–110, arXiv:0902.3360 [hep-ph].

[202] J. P. Miller, E. de Rafael and B. L. Roberts, 'Muon (g-2): Experiment and theory', *Rept.Prog.Phys.* 70 (2007) 795, arXiv:hep-ph/0703049 [hep-ph].

[203] A. Dedes, H. K. Dreiner and U. Nierste,
'Correlation of Bs to mu+ mu- and (g-2) (mu) in minimal supergravity',
Phys.Rev.Lett. 87 (2001) 251804, arXiv:hep-ph/0108037 [hep-ph].

[204] H. K. Dreiner and S. Grab,
'All Possible Lightest Supersymmetric Particles in R-Parity Violating mSUGRA',
Phys.Lett. B679 (2009) 45–50, arXiv:0811.0200 [hep-ph].

[205] H. Dreiner, M. Kramer and B. O'Leary, 'Bounds on R-parity violating supersymmetric couplings from leptonic and semi-leptonic meson decays',
Phys.Rev. D75 (2007) 114016, arXiv:hep-ph/0612278 [hep-ph].

[206] H. K. Dreiner, G. Polesello and M. Thormeier,
'Bounds on broken R parity from leptonic meson decays',
Phys.Rev. D65 (2002) 115006, arXiv:hep-ph/0112228 [hep-ph].

[207] D. K. Ghosh, S. Raychaudhuri and K. Sridhar,
'Bounds from t tbar production on R-parity violating models of supersymmetry',
Phys.Lett. B396 (1997) 177–182, arXiv:hep-ph/9608352 [hep-ph].

[208] G. Bhattacharyya and D. Choudhury,
'D and tau decays: Placing new bounds on R-parity violating supersymmetric coupling',
Mod.Phys.Lett. A10 (1995) 1699–1704, arXiv:hep-ph/9503263 [hep-ph].

[209] Y. Kao and T. Takeuchi,
'Single-Coupling Bounds on R-parity violating Supersymmetry, an update' (2009),
arXiv:0910.4980 [hep-ph].

[210] H. Dreiner et al., 'Testing the CP-violating MSSM in stau decays at the LHC and ILC',
Phys.Rev. D83 (2011) 095012, arXiv:1011.2449 [hep-ph].

[211] A. Akeroyd, C. Liu and J.-H. Song,
'Stau LSP and comparison with H+- phenomenology', *Phys.Rev.* D65 (2002) 015008,
arXiv:hep-ph/0107218 [hep-ph].

[212] P. Dey et al.,
'Two-loop neutrino masses with large R-parity violating interactions in supersymmetry',
JHEP 0812 (2008) 100, arXiv:0808.1523 [hep-ph].

[213] H. K. Dreiner, P. Richardson and M. H. Seymour,
'Parton shower simulations of R-parity violating supersymmetric models',
JHEP 0004 (2000) 008, arXiv:hep-ph/9912407 [hep-ph].

[214] A. collaboration,
'Tracking Studies for b-tagging with 7 TeV Collision Data with the ATLAS Detector',
35th Presented at the 35th Int. Conf. on High Energy Physics, Paris, France, Jul 2010
ATLAS-CONF-2010-070 (2010),
URL: http://cdsweb.cern.ch/record/1281352?ln=en.

[215] H. K. Dreiner, M. Guchait and D. Roy, 'Like sign dilepton signature for gluino production at CERN LHC with or without R conservation',
Phys.Rev. D49 (1994) 3270–3282, arXiv:hep-ph/9310291 [hep-ph].

[216] S. Kolb et al., 'Sneutrino induced like sign dilepton signal with conserved R parity',
Phys.Rev. D64 (2001) 115006, arXiv:hep-ph/0102175 [hep-ph].

[217] F. Abe et al., 'Search for R-parity violating supersymmetry using like-sign dielectrons in p pbar collisions at sqrt(s) = 1.8 TeV', *Phys.Rev.Lett.* 83 (1999) 2133–2138, arXiv:hep-ex/9908063 [hep-ex].

[218] M. Guchait and D. Roy, 'Like sign dilepton signature for R-parity violating SUSY search at the Tevatron collider', *Phys.Rev.* D54 (1996) 3276–3282, arXiv:hep-ph/9603219 [hep-ph].

[219] F. James and M. Roos, 'Minuit: A System for Function Minimization and Analysis of the Parameter Errors and Correlations', *Comput.Phys.Commun.* 10 (1975) 343–367.

[220] F. E. Paige et al., 'ISAJET 7.69: A Monte Carlo event generator for pp, anti-p p, and e+e- reactions' (2003), arXiv:hep-ph/0312045 [hep-ph].

[221] W. Porod and F. Staub, 'SPheno 3.1: Extensions including flavour, CP-phases and models beyond the MSSM' (2011), arXiv:1104.1573 [hep-ph].

[222] A. Sherstnev and R. Thorne, 'Parton Distributions for LO Generators', *Eur.Phys.J.* C55 (2008) 553–575, arXiv:0711.2473 [hep-ph].

[223] G. Corcella et al., 'HERWIG 6: An Event generator for hadron emission reactions with interfering gluons (including supersymmetric processes)', *JHEP* 0101 (2001) 010, arXiv:hep-ph/0011363 [hep-ph].

[224] W. Beenakker, R. Hopker and M. Spira, 'PROSPINO: A Program for the production of supersymmetric particles in next-to-leading order QCD' (1996), arXiv:hep-ph/9611232 [hep-ph].

[225] S. Ovyn, X. Rouby and V. Lemaitre, 'DELPHES, a framework for fast simulation of a generic collider experiment' (2009), arXiv:0903.2225 [hep-ph].

[226] R. Brun and F. Rademakers, 'ROOT: An object oriented data analysis framework', *Nucl.Instrum.Meth.* A389 (1997) 81–86.

[227] W. A. Rolke, A. M. Lopez and J. Conrad, 'Limits and confidence intervals in the presence of nuisance parameters', *Nucl.Instrum.Meth.* A551 (2005) 493–503, arXiv:physics/0403059 [physics].

[228] G. Aad et al., 'Search for events with large missing transverse momentum, jets, and at least two tau leptons in 7 TeV proton-proton collision data with the ATLAS detector', *ATLAS Collaboration* arXiv:1203.6580 (2012).

[229] G. Aad et al., 'Search for supersymmetry in pp collisions at sqrt(s) = 7 TeV in final states with missing transverse momentum and b-jets with the ATLAS detector', *ATLAS Collaboration* arXiv:1203.6193 (2012).

[230] A. collaboration, 'An update to the combined search for the Standard Model Higgs boson with the ATLAS detector at the LHC using up to 4.9 inv fb of pp collision data at sqrt(s) = 7 TeV', *Conference Note* ATLAS-CONF-2012-019 (2012), URL: http://cdsweb.cern.ch/record/1430033.

[231] S. Chatrchyan et al., 'Combined results of searches for the standard model Higgs boson in pp collisions at sqrt(s) = 7 TeV' (2012), arXiv:1202.1488 [hep-ex].

[232] U. Ellwanger, C. Hugonie and A. M. Teixeira,
'The Next-to-Minimal Supersymmetric Standard Model', *Phys.Rept.* 496 (2010) 1–77, arXiv:0910.1785 [hep-ph].

[233] D. A. Vasquez et al., 'The 125 GeV Higgs in the NMSSM in light of LHC results and astrophysics constraints' (2012), arXiv:1203.3446 [hep-ph].

[234] U. Ellwanger and C. Hugonie,
'Higgs bosons near 125 GeV in the NMSSM with constraints at the GUT scale' (2012), arXiv:1203.5048 [hep-ph].

[235] R. Barbieri and L. Maiani,
'Renormalization of the Electroweak rho Parameter from Supersymmetric Particles', *Nucl.Phys.* B224 (1983) 32.

[236] M. Drees and K. Hagiwara,
'Supersymmetric Contribution to the Electroweak rho Parameter',
Phys.Rev. D42 (1990) 1709–1725.

[237] J. Grifols and J. Sola,
'Radiative Corrections to Weak Boson Masses from Supersymmetry',
Phys.Lett. B137 (1984) 257.

[238] C. Lim, T. Inami and N. Sakai, 'The Rho Parameter in Supersymmetric Models',
Phys.Rev. D29 (1984) 1488.

[239] G. Hiller, J. S. Kim and H. Sedello,
'Collider Signatures of Minimal Flavor Mixing from Stop Decay Length Measurements',
Phys.Rev. D80 (2009) 115016, arXiv:0910.2124 [hep-ph].

[240] W. Porod, 'SPheno, a program for calculating supersymmetric spectra, SUSY particle decays and SUSY particle production at e+ e- colliders',
Comput.Phys.Commun. 153 (2003) 275–315, arXiv:hep-ph/0301101 [hep-ph].

[241] J. Pumplin et al.,
'New generation of parton distributions with uncertainties from global QCD analysis',
JHEP 0207 (2002) 012, arXiv:hep-ph/0201195 [hep-ph].

[242] F. Maltoni and T. Stelzer, 'MadEvent: Automatic event generation with MadGraph',
JHEP 0302 (2003) 027, arXiv:hep-ph/0208156 [hep-ph].

[243] T. Sjostrand, S. Mrenna and P. Z. Skands, 'A Brief Introduction to PYTHIA 8.1',
Comput.Phys.Commun. 178 (2008) 852–867, arXiv:0710.3820 [hep-ph].

[244] M. Dobbs and J. B. Hansen,
'The HepMC C++ Monte Carlo event record for High Energy Physics',
Comput.Phys.Commun. 134 (2001) 41–46.

[245] M. Cacciari, 'FastJet: A Code for fast kt clustering, and more' (2006) 487–490, arXiv:hep-ph/0607071 [hep-ph].

[246] S. Franchino, 'Measurement of the muon inclusive cross section in pp collisions at sqrt(s) = 7 TeV with the ATLAS detector' (2011), arXiv:1111.4928 [hep-ex].

[247] G. Aad et al.,
'Expected Performance of the ATLAS Experiment - Detector, Trigger and Physics' (2009), arXiv:0901.0512 [hep-ex].

[248] R. Bonciani et al.,
'NLL resummation of the heavy quark hadroproduction cross-section',
Nucl.Phys. B529 (1998) 424–450, arXiv:hep-ph/9801375 [hep-ph].

[249] H. Ita et al., 'Precise Predictions for Z + 4 Jets at Hadron Colliders',
Phys.Rev. D85 (2012) 031501, arXiv:1108.2229 [hep-ph].

[250] G. A. e. a. ATLAS Collaboration, 'Early supersymmetry searches in channels with jets and missing transverse momentum with the ATLAS detector',
ATLAS-CONF-2010-065 (2010).

[251] B. C. Allanach, S. Grab and H. E. Haber,
'Supersymmetric Monojets at the Large Hadron Collider', *JHEP* 1101 (2011) 138,
arXiv:1010.4261 [hep-ph].

[252] V. Abazov et al., 'Search for scalar top quarks in the acoplanar charm jets and missing transverse energy final state in p pbar collisions at sqrt(s) = 1.96 TeV',
Phys.Lett. B665 (2008) 1–8, arXiv:0803.2263 [hep-ex].

[253] C. Collaboration, 'Search for Scalar top decaying into Charm and Neutralino',
CDF note 9834 (2009).

[254] P. Achard et al., 'Search for scalar leptons and scalar quarks at LEP',
Phys.Lett. B580 (2004) 37–49, arXiv:hep-ex/0310007 [hep-ex].

[255] M. Drees and O. J. Eboli,
'Strong interaction effects in stop pair production at e+ e- colliders',
Eur.Phys.J. C10 (1999) 337–345, arXiv:hep-ph/9902391 [hep-ph].

[256] M. Martinez and f. t. A. Collaboration,
'Search for new phenomena in events with a monojet and large missing transverse momentum at the LHC using the ATLAS detector'
(2012), Presented at the 2011 Hadron Collider Physics symposium (HCP-2011), Paris, France, November 14-18 2011, 3 pages, 3 figures, arXiv:1202.0158 [hep-ex].

[257] J. Conley, H. Dreiner and P. Wienemann, 'Measuring a Light Neutralino Mass at the ILC: Testing the MSSM Neutralino Cold Dark Matter Model',
Phys.Rev. D83 (2011) 055018, arXiv:1012.1035 [hep-ph].

[258] N. M. Silvestri et al., 'A catalog of spectroscopically selected close binary systems from the Sloan Digital Sky Survey data release four', *Astron.J.* 131 (2006) 1674–1686.

[259] J. Isern et al., 'Axions and the white dwarf luminosity function',
J.Phys.Conf.Ser. 172 (2009) 012005, arXiv:0812.3043 [astro-ph].

[260] B. W. Lee and S. Weinberg, 'Cosmological Lower Bound on Heavy Neutrino Masses',
Phys.Rev.Lett. 39 (1977) 165–168.

[261] P. Hut, 'Limits on Masses and Number of Neutral Weakly Interacting Particles',
Phys.Lett. B69 (1977) 85.

[262] K. Sato and M. Kobayashi,
'Cosmological Constraints on the Mass and the Number of Heavy Lepton Neutrinos',
Prog.Theor.Phys. 58 (1977) 1775.

[263] M. Vysotsky, A. Dolgov and Y. Zeldovich,
'Cosmological Restriction on Neutral Lepton Masses', *JETP Lett.* 26 (1977) 188–190.

[264] D. Hooper and T. Plehn, 'Supersymmetric dark matter: How light can the LSP be?', *Phys.Lett.* B562 (2003) 18–27, arXiv:hep-ph/0212226 [hep-ph].

[265] G. Belanger et al.,
'A Lower limit on the neutralino mass in the MSSM with nonuniversal gaugino masses' (2002) 919–924, arXiv:hep-ph/0212227 [hep-ph].

[266] G. Belanger et al., 'Lower limit on the neutralino mass in the general MSSM', *JHEP* 0403 (2004) 012, arXiv:hep-ph/0310037 [hep-ph].

[267] A. Bottino et al., 'Lower bound on the neutralino mass from new data on CMB and implications for relic neutralinos', *Phys.Rev.* D68 (2003) 043506, arXiv:hep-ph/0304080 [hep-ph].

[268] D. A. Vasquez et al.,
'Can neutralinos in the MSSM and NMSSM scenarios still be light?', *Phys.Rev.* D82 (2010) 115027, arXiv:1009.4380 [hep-ph].

[269] D. Albornoz Vasquez, G. Belanger and C. Boehm,
'Revisiting light neutralino scenarios in the MSSM', *Phys.Rev.* D84 (2011) 095015, arXiv:1108.1338 [hep-ph].

[270] N. Fornengo, S. Scopel and A. Bottino,
'Discussing direct search of dark matter particles in the Minimal Supersymmetric extension of the Standard Model with light neutralinos', *Phys.Rev.* D83 (2011) 015001, arXiv:1011.4743 [hep-ph].

[271] S. Choi et al., 'Search at the CERN LHC for a light neutralino of cosmological interest', *Phys.Rev.* D85 (2012) 035009, arXiv:1108.2190 [hep-ph].

[272] R. Bernabei et al., 'New results from DAMA/LIBRA', *Eur.Phys.J.* C67 (2010), presented at the Int. Conf. Beyond the Standard Models of Particle Physics, Cosmology and Astrophysics, 1-6 February 2010, Cape Town, South Africa 39–49, arXiv:1002.1028 [astro-ph.GA].

[273] C. Aalseth et al., 'Results from a Search for Light-Mass Dark Matter with a P-type Point Contact Germanium Detector', *Phys.Rev.Lett.* 106 (2011) 131301, arXiv:1002.4703 [astro-ph.CO].

[274] S. Profumo, 'Hunting the lightest lightest neutralinos', *Phys.Rev.* D78 (2008) 023507, arXiv:0806.2150 [hep-ph].

[275] R. Allahverdi, B. Dutta and K. Sinha, 'Baryogenesis and Late-Decaying Moduli', *Phys.Rev.* D82 (2010) 035004, arXiv:1005.2804 [hep-ph].

[276] K. Kohri, A. Mazumdar and N. Sahu,
'Inflation, baryogenesis and gravitino dark matter at ultra low reheat temperatures', *Phys.Rev.* D80 (2009) 103504, arXiv:0905.1625 [hep-ph].

[277] S. Davidson, M. Losada and A. Riotto, 'A New perspective on baryogenesis', *Phys.Rev.Lett.* 84 (2000) 4284–4287, arXiv:hep-ph/0001301 [hep-ph].

[278] J. R. Ellis, D. V. Nanopoulos and S. Sarkar, 'The Cosmology of Decaying Gravitinos', *Nucl.Phys.* B259 (1985) 175.

[279] J. Preskill, M. B. Wise and F. Wilczek, 'Cosmology of the Invisible Axion', *Phys.Lett.* B120 (1983) 127–132.

[280] K. Rajagopal, M. S. Turner and F. Wilczek, 'Cosmological implications of axinos', *Nucl.Phys.* B358 (1991) 447–470.

[281] R. H. Cyburt et al.,
'New BBN limits on physics beyond the standard model from He-4',
Astropart.Phys. 23 (2005) 313–323, arXiv:astro-ph/0408033 [astro-ph].

[282] P. Ade et al., 'Planck Early Results: The Planck mission' (2011),
arXiv:1101.2022 [astro-ph.IM].

[283] D. Z. Freedman, P. van Nieuwenhuizen and S. Ferrara,
'Progress Toward a Theory of Supergravity', *Phys.Rev.* D13 (1976) 3214–3218.

[284] A. Brignole, F. Feruglio and F. Zwirner,
'On the effective interactions of a light gravitino with matter fermions',
JHEP 9711 (1997) 001, arXiv:hep-th/9709111 [hep-th].

[285] D. A. Dicus et al., 'Primordial Nucleosynthesis Including Radiative, Coulomb, and Finite Temperature Corrections to Weak Rates', *Phys.Rev.* D26 (1982) 2694.

[286] T. Gherghetta, 'Goldstino decoupling in spontaneously broken supergravity theories', *Nucl.Phys.* B485 (1997) 25–37, arXiv:hep-ph/9607448 [hep-ph].

[287] G. Aad et al.,
'Search for squarks and gluinos using final states with jets and missing transverse momentum with the ATLAS detector in sqrt(s) = 7 TeV proton-proton collisions',
Phys.Lett. B701 (2011) 186–203, arXiv:1102.5290 [hep-ex].

[288] S. Chatrchyan et al.,
'Inclusive search for squarks and gluinos in pp collisions at sqrt(s) = 7 TeV',
Phys.Rev. D85 (2012) 012004, arXiv:1107.1279 [hep-ex].

[289] P. Bechtle et al.,
'What if the LHC does not find supersymmetry in the sqrt(s)=7 TeV run?',
Phys.Rev. D84 (2011) 011701, arXiv:1102.4693 [hep-ph].

[290] J. R. Ellis et al., 'Primordial Nucleosynthesis, Additional Neutrinos and Neutral Currents from the Superstring', *Phys.Lett.* B167 (1986) 457.

[291] P. Gondolo and G. Gelmini, 'Cosmic abundances of stable particles: Improved analysis', *Nucl.Phys.* B360 (1991) 145–179.

[292] J. L. Feng, M. Kamionkowski and S. K. Lee,
'Light Gravitinos at Colliders and Implications for Cosmology',
Phys.Rev. D82 (2010) 015012, arXiv:1004.4213 [hep-ph].

[293] L. Covi et al., 'Gravitino Dark Matter and general neutralino NLSP',
JHEP 0911 (2009) 003, arXiv:0908.3399 [hep-ph].

[294] P. Fayet,
'Mixing Between Gravitational and Weak Interactions Through the Massive Gravitino',
Phys.Lett. B70 (1977) 461.

[295] P. Fayet,
'Scattering Cross-Sections of the Photino and the Goldstino (Gravitino) on Matter',
Phys.Lett. B86 (1979) 272.

[296] T. Bhattacharya and P. Roy, 'Role of Chiral Scalar and Pseudoscalar in Two Photon Production of a Superlight Gravitino', *Phys.Rev.* D38 (1988) 2284.

[297] P. Fayet, 'Phenomenology of Supersymmetry' (1982).

[298] D. J. Chung, G. R. Farrar and E. W. Kolb, 'On the relic abundance of light photinos', *Phys.Rev.* D56 (1997) 6096–6106, arXiv:astro-ph/9703145 [astro-ph].

[299] J. R. Ellis, J. E. Kim and D. V. Nanopoulos, 'Cosmological Gravitino Regeneration and Decay', *Phys.Lett.* B145 (1984) 181.

[300] J. R. Ellis et al., 'Astrophysical constraints on massive unstable neutral relic particles', *Nucl.Phys.* B373 (1992) 399–437.

[301] M. Kawasaki, K. Kohri and T. Moroi, 'Big-Bang nucleosynthesis and hadronic decay of long-lived massive particles', *Phys.Rev.* D71 (2005) 083502, arXiv:astro-ph/0408426 [astro-ph].

[302] K. Kohri, T. Moroi and A. Yotsuyanagi, 'Big-bang nucleosynthesis with unstable gravitino and upper bound on the reheating temperature', *Phys.Rev.* D73 (2006) 123511, arXiv:hep-ph/0507245 [hep-ph].

[303] R. H. Cyburt et al., 'Nucleosynthesis Constraints on a Massive Gravitino in Neutralino Dark Matter Scenarios', *JCAP* 0910 (2009) 021, arXiv:0907.5003 [astro-ph.CO].

[304] M. Fukugita and T. Yanagida, 'Baryogenesis Without Grand Unification', *Phys.Lett.* B174 (1986) 45.

[305] W. Buchmuller et al., 'Gravitino Dark Matter in R-Parity Breaking Vacua', *JHEP* 0703 (2007) 037, arXiv:hep-ph/0702184 [HEP-PH].

[306] G. Bertone et al., 'Gamma-Rays from Decaying Dark Matter', *JCAP* 0711 (2007) 003, arXiv:0709.2299 [astro-ph].

[307] N. Bernal and S. Palomares-Ruiz, 'Constraining Dark Matter Properties with Gamma-Rays from the Galactic Center with Fermi-LAT', *Nucl.Phys.* B857 (2012) 380–410, arXiv:1006.0477 [astro-ph.HE].

[308] A. Strong, I. Moskalenko and O. Reimer, 'A new determination of the extragalactic diffuse gamma-ray background from egret data', *Astrophys.J.* 613 (2004) 956–961, arXiv:astro-ph/0405441 [astro-ph].

[309] A. W. Strong et al., 'Gamma-ray continuum emission from the inner galactic region as observed with integral/spi', *Astron.Astrophys.* 444 (2005) 495, arXiv:astro-ph/0509290 [astro-ph].

[310] A. Abdo et al., 'The Spectrum of the Isotropic Diffuse Gamma-Ray Emission Derived From First-Year Fermi Large Area Telescope Data', *Phys.Rev.Lett.* 104 (2010) 101101, arXiv:1002.3603 [astro-ph.HE].

[311] M. Viel et al., 'How cold is cold dark matter? Small scales constraints from the flux power spectrum of the high-redshift Lyman-alpha forest', *Phys.Rev.Lett.* 100 (2008) 041304, arXiv:0709.0131 [astro-ph].

[312] H. de Vega and N. Sanchez, 'Model independent analysis of dark matter points to a particle mass at the keV scale', *Mon.Not.Roy.Astron.Soc.* 404 (2010) 885, arXiv:0901.0922 [astro-ph.CO].

[313] A. Boyarsky, O. Ruchayskiy and D. Iakubovskyi,
'A Lower bound on the mass of Dark Matter particles', *JCAP* 0903 (2009) 005, arXiv:0808.3902 [hep-ph].

[314] J. Pradler, 'Electroweak Contributions to Thermal Gravitino Production' (2007), arXiv:0708.2786 [hep-ph].

[315] J. Hasenkamp and J. Kersten,
'Leptogenesis, Gravitino Dark Matter and Entropy Production',
Phys.Rev. D82 (2010) 115029, arXiv:1008.1740 [hep-ph].

[316] J. Pradler and F. D. Steffen,
'Constraints on the Reheating Temperature in Gravitino Dark Matter Scenarios',
Phys.Lett. B648 (2007) 224–235, arXiv:hep-ph/0612291 [hep-ph].

[317] M. Kawasaki, N. Sugiyama and T. Yanagida,
'Gravitino warm dark matter motivated by the CDF e e gamma gamma event',
Mod.Phys.Lett. A12 (1997) 1275–1282, arXiv:hep-ph/9607273 [hep-ph].

[318] E. A. Baltz and H. Murayama, 'Gravitino warm dark matter with entropy production', *JHEP* 0305 (2003) 067, arXiv:astro-ph/0108172 [astro-ph].

[319] K. Jedamzik, M. Lemoine and G. Moultaka,
'Gravitino dark matter in gauge mediated supersymmetry breaking',
Phys.Rev. D73 (2006) 043514, arXiv:hep-ph/0506129 [hep-ph].

[320] D. Gorbunov, A. Khmelnitsky and V. Rubakov,
'Is gravitino still a warm dark matter candidate?', *JHEP* 0812 (2008) 055, arXiv:0805.2836 [hep-ph].

[321] J. J. Heckman, A. Tavanfar and C. Vafa, 'Cosmology of F-theory GUTs', *JHEP* 1004 (2010) 054, arXiv:0812.3155 [hep-th].

List of Figures

List of Tables